



## DOCTORAL THESIS

# Behavior of Embankment Dams in Earthquake Conditions and Numerical Analysis

Doctoral Program in Civil Engineering

Thesis Advisor: Univ. Prof. Dipl.-Ing. Dr. techn. Peter Tschernutter  
[Institute of Hydraulic Engineering and Water Resources Management]  
[Vienna University of Technology]

Second Advisor: Univ. Prof. Dipl.-Ing. Dr. techn. Miroslav Marenc  
[Institute for Water Education]  
[UNESCO – IHE]

A Thesis Submitted to Vienna University of Technology  
Faculty of Civil Engineering

By

Author: DI Hans-Martin Leitner

Matriculation number: 0326313

1230 Vienna, Anton – Krieger - Gasse 130

Vienna, the 1st of September, 2016

Signature



## **Abstract**

Within this thesis various numerical methods for prediction of an embankment dam's dynamic behavior were compared by back-calculation of three case studies that suffered severe earthquake shaking.

These three case studies namely are:

- The Aratozawa dam, a 85m high Clay Core Rockfill dam that was shaken by the Mw=6,9 Iwate 7 Miyagi earthquake resulting in an measured peak ground acceleration of 0,85g.
- The Zigingpu dam, a 156m high Concrete Face Rockfill dam shaken by the Mw=7,9 Wenchuan earthquake resulting in severe damage to the concrete slabs.
- The Fujinuma dam, a 18m high earthfill dam that was shaken by the Mw=9,0 Tohoku earthquake resulting in crest overflow and dam breach.

State of the art numerical methods as recommended by ICOLD Bulletin 155 were compared to newly developed models. State of the art numerical models as defined by ICOLD Bulletin 155 are the well-known Equivalent – Linear analysis accompanied by 2<sup>nd</sup> step Newmark or Makdisi- Seed deformation type analysis. “Newly” developed models in this case are Nonlinear dynamic analysis. The analyses were performed by use of Software GeoStudio 2012 and Plaxis 2015.

## **Acknowledgement**

I would like to express my appreciation to my first advisor Univ.Prof. Dipl.-Ing. Dr.techn. Peter Tschernutter, thanks for giving me the opportunity to make use of the institutes' software licenses and special thanks for the technical guidance, no matter what time or day of the week.

Thanks to my second Advisor Prof. Miroslav Marenc for your worthwhile help. My gratitude also goes to Dr. Martin Wieland, thank you for giving me valuable tips in modeling, literature references and technical input.

Special thanks to GeoSlope for providing me with a free version of GeoStudio 2012 software and the friendly and straight forward cooperation.

Thanks to Mr. Bernhard Mayer for his support in handling raw earthquake data.

The most special thanks go to my wife Daniela for your love and patience. Without your constant support, writing this thesis would have been impossible.

To my parents Andrea and Hans-Georg, to my children Amelie and Jakob.

## Table of Content

<b>1</b>	<b>Scope and Outline .....</b>	<b>29</b>
<b>2</b>	<b>Executive Summary .....</b>	<b>30</b>
<b>3</b>	<b>Historic Performance of Embankment Dams .....</b>	<b>32</b>
<b>4</b>	<b>Observed Damage of Embankment Dams due to Earthquake Loading .....</b>	<b>35</b>
<b>5</b>	<b>Earthquake Hazard and Seismicity .....</b>	<b>38</b>
5.1	<i>General.....</i>	<i>38</i>
5.2	<i>Plate Boundaries .....</i>	<i>38</i>
5.3	<i>Fault Types.....</i>	<i>43</i>
5.4	<i>Hypocenter – Epicenter.....</i>	<i>46</i>
5.5	<i>Earthquake Statistics .....</i>	<i>46</i>
5.6	<i>Epicentral Distance - Acceleration at Dam Base.....</i>	<i>48</i>
5.7	<i>Seismic Waves.....</i>	<i>49</i>
5.8	<i>Earthquake magnitude .....</i>	<i>50</i>
5.9	<i>Strong Motion Recording and Processing.....</i>	<i>51</i>
5.10	<i>Accelerograms –Effects and Application in Dam Engineering.....</i>	<i>54</i>
<b>6</b>	<b>Factors affecting the Dynamic Behavior of Embankments .....</b>	<b>60</b>
6.1	<i>Earthquake induced failure modes .....</i>	<i>60</i>
6.2	<i>Valley Shape.....</i>	<i>61</i>
6.3	<i>Foundation Characteristics .....</i>	<i>61</i>
6.4	<i>Stress-Deformation Characteristics of Fill Materials .....</i>	<i>62</i>
6.5	<i>Soil Liquefaction.....</i>	<i>65</i>
6.5.1	<i>General.....</i>	<i>65</i>

6.5.2	Liquefiable soils .....	66
6.5.3	Concepts to stabilize liquefiable soils .....	67
6.5.4	Assessment Liquefaction Potential .....	67
6.5.5	Surface Acceleration on Liquefied Soil Deposits.....	69
<b>7</b>	<b>Engineering Parameters of Dams subject to strong ground motion .....</b>	<b>71</b>
7.1	<i>Natural period of embankment dams.....</i>	71
7.2	<i>Crest amplification .....</i>	71
7.3	<i>Simplified Methods for Estimating Permanent Settlements.....</i>	74
<b>8</b>	<b>Risk Mitigation in Dam Design – Lessons Learned .....</b>	<b>80</b>
8.1	<i>Selection of Seismic Design Parameters.....</i>	80
8.2	<i>Earthquake and Flooding .....</i>	83
8.3	<i>Adequate Freeboard and Camber Arrangement .....</i>	83
8.4	<i>Crest Width.....</i>	84
8.5	<i>Filter Design in Earthquake prone Areas.....</i>	85
8.6	<i>Soils Susceptible to Liquefaction .....</i>	86
<b>9</b>	<b>Calibration of Model Codes on Monitoring data obtained during strong earthquakes .....</b>	<b>88</b>
9.1	<i>Japan’s seismic observation networks KiK-Net &amp; K-Net.....</i>	88
9.2	<i>Selected Observation Stations.....</i>	91
9.2.1	Seismic Observation Station FSKH08 .....	96
9.2.2	Seismic Observation Station FKSH09 .....	104
9.2.3	Seismic Observation Station FSKH10 .....	112
9.3	<i>Conclusions.....</i>	120
<b>10</b>	<b>Case Studies .....</b>	<b>125</b>
10.1	<i>General.....</i>	125

10.2	<i>Aratozawa Dam (ECRD)</i> .....	126
10.2.1	Dam and site characterization .....	126
10.2.2	Causative earthquake .....	128
10.2.3	Material parameters and construction details .....	129
10.2.4	Dam behavior during Iwate – Miyagi earthquake .....	131
10.3	<i>Zipingpu Dam (CFRD)</i> .....	133
10.3.1	Dam and site characterization .....	133
10.3.2	Causative earthquake .....	134
10.3.3	Dam behavior during Wenchuan earthquake .....	135
10.4	<i>Fujinuma Dam (Homogeneous)</i> .....	141
10.4.1	Dam and site characterization .....	141
10.4.2	Causative earthquake .....	142
10.4.3	Material parameters and construction details .....	144
10.4.4	Dam behavior during / after Tohoku earthquake .....	147
<b>11</b>	<b>Modeling Procedure</b> .....	<b>149</b>
11.1	<i>Aratozawa Dam (ECRD)</i> .....	149
11.1.1	Meshing .....	149
11.1.2	Seismic Input Motion .....	150
11.1.3	Stepped Construction & Boundary Conditions .....	151
11.1.4	Equivalent number of Cycles vs. Rupture Distance .....	156
11.1.5	Best Fit Input Parameter Sets .....	157
11.2	<i>Zipingpu Dam (CFRD)</i> .....	163
11.2.1	Meshing .....	163
11.2.2	Seismic Input Motion .....	164
11.2.3	Stepped Construction & Boundary Conditions .....	168
11.2.4	Equivalent number of Cycles vs. Rupture Distance .....	172
11.2.5	Best Fit Input Parameter Sets .....	172
11.3	<i>Fujinuma Dam (Homogeneous)</i> .....	176

11.3.1	Meshing.....	176
11.3.2	Seismic Input Motion .....	178
11.3.3	Stepped Construction & Boundary Conditions .....	180
11.3.4	Equivalent number of Cycles vs. Rupture Distance .....	183
11.3.5	Best Fit Input Parameter Sets.....	184
<b>12</b>	<b>Results and Comparison .....</b>	<b>193</b>
12.1	<i>Aratozawa Dam (ECRD).....</i>	<i>193</i>
12.2	<i>Zipingpu Dam (CFRD) .....</i>	<i>221</i>
12.3	<i>Homogeneous Embankment.....</i>	<i>241</i>
<b>13</b>	<b>Conclusions.....</b>	<b>269</b>
<b>14</b>	<b>Research .....</b>	<b>275</b>
<b>15</b>	<b>References .....</b>	<b>276</b>
<b>16</b>	<b>Certification .....</b>	<b>287</b>



## Table of Figures

Figure 1 Observed damage of earth core rockfill dams vs. magnitude and epicentral distance (Matsumoto 2010).....	34
Figure 2 Observed damage of concrete face rockfill dams vs. magnitude and epicentral distance (Matsumoto 2010).....	34
Figure 3 Observed damage of earthfill dams vs. magnitude and epicentral distance (Matsumoto 2010) .....	34
Figure 4 Horizontal construction joint of Zipingpu CFRD (Chen and Sheng-Shui n.d.) ..	35
Figure 5 Slides close to the crest of Colbun dam (Noguera 2010) .....	35
Figure 6 Spalling at joints of Zipingpu CFRD (Chen and Sheng-Shui n.d.) .....	35
Figure 7 “Near” failure of Lower San Fernando Dam (Wieland 2013) .....	35
Figure 8 Upstream slip surface Wenchuan earthquake 2008 (Wieland 2013) .....	36
Figure 9 Failure of Fujinuma-ike dam after the Tohoku earthquake (Matsumoto 2011) .....	36
Figure 10 Damage class vs. magnitude and pga (Pells and Fells, 2003) .....	37
Figure 11 The major tectonic plates, mid-oceanic ridges, trenches and transformation faults of the earth (Fowler 1990, reproduced from Day,2002) .....	38
Figure 12 Seafloor spreading, divergent boundary (USGS 2000) .....	40
Figure 13 Development of a rift valley, divergent boundary (USGS 2000) .....	40
Figure 14 Oceanic-continental subduction zone, convergent boundary (USGS 2000) ..	41
Figure 15 Oceanic-oceanic subduction zone, convergent boundary (USGS 2000) .....	41
Figure 16 Continental-continental subduction zone, convergent boundary (USGS 2000) .....	41
Figure 17 Strike – slip fault (Namson and Davis 1988) .....	45
Figure 18 Normal fault (Namson and Davis 1988, reproduced from Day 2002).....	45
Figure 19 Reverse fault (Namson and Davis 1988, reproduced from Day 2002) .....	45
Figure 20 Illustration of hypocenter and epicenter of an earthquake (Penn n.d., reproduced from Kamalesh 2008) .....	46
Figure 21 Attenuation of horizontal PGA component vs. fault distance.....	49

Figure 22 Digital strong motion record (Michigan Tech n.d., reproduced from Kamalesh 2008).....	50
Figure 23 Approximate relationship between moment magnitude and other magnitude scales (developed by Heaton et al. 1982, reproduced from Day 2002).....	51
Figure 24 Digital accelerograph (Mateo 2009) .....	52
Figure 25 Analogue accelerograph (Dadisp 2014) .....	52
Figure 26 Bracketed duration vs. epicentral distance and magnitude for a specific fault mechanism (Chang and Krinitzsky 1977) .....	56
Figure 27 Base accelerations recorded at Aratozawa dam site during Iwate-Miyagi earthquake 14.06.2008 (Ohmachi 2011) .....	57
Figure 28 Crest to gallery spectral ratios in stream axis (Ohmachi 2011) .....	58
Figure 29 Running spectral ratios from crest to gallery records in stream direction (Ohmachi 2011) .....	58
Figure 30 Mid-crest amplification for three different $V_{dam} / V_{Base}$ ratios.....	61
Figure 31 Construction method vs. base acceleration and occurrence of crest settlement (Okamoto 2004).....	63
Figure 32 Cyclic resistance ratio based on SPT (Seed et al., 1985, reproduced from Day 2002).....	68
Figure 33 Range of Magnitude scaling factor (Youd and Noble, 1997) .....	68
Figure 34 Accelerogram of a station located on fully liquefied soil deposits (reproduced from Kramer, 1996) .....	69
Figure 35 Recorded amplification of rockfill dams (Matsumoto 2010).....	72
Figure 36 Recorded amplification of earthfill dams (Matsumoto 2010) .....	72
Figure 37 Peak ground acceleration [g] vs. amplification factor (Yu et al. 2012) .....	73
Figure 38 Crest settlement vs. PGA and magnitude (corrected from Swaisgood 2003) 76	
Figure 39 Observed crest settlement vs. PGA (Swaisgood 2003).....	77
Figure 40 Observed crest settlement vs. base acceleration (Okamoto 2010).....	77
Figure 41 Earthquake severity index vs. crest settlement [%] (Bureau et al. 1985).....	78
Figure 42 Isawa dam during construction after Iwate /Miyagi earthquake in 2008 (Ohmachi 2008) .....	84

Figure 43 Close up of cracks in Isawa dam (Shimamoto et.al. 2008) .....	84
Figure 44 Strong-motion stations in Japan (a) K-Net and (b) KiK-Net (Fujiwara, 2003). 89	
Figure 45 Setup of a KiK-Net seismic observation station (Fujiwara, 2003) .....	90
Figure 46 Location of KiK-Net stations in Fukushima prefecture (modified from NIED) 91	
Figure 47 FSKH08 acceleration data monitored during the Great Eastern Earthquake (NIED) .....	92
Figure 48 FSKH09 acceleration data monitored during the Great Eastern Earthquake (NIED) .....	93
Figure 49 FSKH10 acceleration data monitored during the Great Eastern Earthquake (NIED) .....	94
Figure 50 Modelling initial stress conditions .....	97
Figure 51 Model for dynamic analysis .....	97
Figure 52 $G_{max}$ reduction sets applied to FKSH08 analysis (equivalent linear).....	98
Figure 53 Damping sets applied to FKSH08 analysis (equivalent linear).....	98
Figure 54 Monitored vs. calculated horizontal surface accelerogram FKSH08.....	99
Figure 55 Monitored vs. calculated vertical surface accelerogram FKSH08 .....	100
Figure 56 FKSH08 horizontal spectral acceleration .....	102
Figure 57 FKSH08 horizontal spectral acceleration (logarithmic scale) .....	102
Figure 58 FKSH08 vertical spectral acceleration.....	103
Figure 59 FKSH08 vertical spectral acceleration (logarithmic scale).....	103
Figure 60 Modelling initial stress conditions .....	105
Figure 61 Model for dynamic analysis .....	105
Figure 62 $G_{max}$ reduction sets applied to FKSH09 analysis (equivalent linear).....	106
Figure 63 Damping sets applied to FKSH09 analysis (equivalent linear).....	106
Figure 64 Monitored vs. calculated horizontal surface accelerogram FKSH09.....	107
Figure 65 Monitored vs. calculated vertical surface accelerogram FKSH09 .....	108
Figure 66 FKSH09 horizontal spectral acceleration .....	109
Figure 67 FKSH09 horizontal spectral acceleration (logarithmic scale) .....	109
Figure 68 FKSH09 vertical spectral acceleration.....	110
Figure 69 FKSH09 vertical spectral acceleration (logarithmic scale).....	110

Figure 70 Modelling initial stress conditions .....	112
Figure 71 Model for dynamic analysis .....	112
Figure 72 $G_{max}$ reduction sets applied to FKSH10 analysis (equivalent linear) .....	114
Figure 73 Damping sets applied to FKSH10 analysis (equivalent linear) .....	114
Figure 74 Monitored vs. calculated horizontal surface accelerogram FKSH10 .....	116
Figure 75 Monitored vs. calculated vertical surface accelerogram FKSH10.....	117
Figure 76 FKSH10 horizontal spectral acceleration .....	118
Figure 77 FKSH10 horizontal spectral acceleration (logarithmic scale).....	118
Figure 78 FKSH10 vertical spectral acceleration .....	119
Figure 79 FKSH10 vertical spectral acceleration (logarithmic scale) .....	119
Figure 80 Plan view of Aratozawa dam (Ohmachi and Tahara 2011).....	126
Figure 81 Maximum cross section of Aratozawa dam (Ohmachi and Tahara 2011) ....	127
Figure 82 Location of accelerographs in longitudinal section of Aratozawa dam (Ohmachi and Tahara 2011) .....	127
Figure 83 Pre- and post-earthquake aerial photo of Aratozawa dam, reservoir and landslide (Kayen et al. 2008) .....	128
Figure 84 Back-calculated shear-modulus reduction of Aratozawa clay core [-] (Ohmachi and Tahara 2011) .....	130
Figure 85 Shear-modulus reduction of various plasticity clays [%] (Vucetic and Dobry 1991).....	130
Figure 86 Shear-wave velocity measured at three locations of Aratozawa dam after Iwate – Miyagi earthquake (Kayen et al. 2008) .....	131
Figure 87 Pore water pressure development prior (a), immediately after (b) and past earthquake (Ohmachi and Tahara 2011) .....	132
Figure 88 Layout of Zipingpu dam (Chen 2008) .....	133
Figure 89 Typical section of Zipingpu dam (Chen 2008) .....	134
Figure 90 Location of Zipingpu dam, epicenter of Wenchuan earthquake and known fault systems (Zou 2012) .....	135
Figure 91 Rupture and spalling of parapet to slab joint (Guan 2009) .....	136
Figure 92 Dislocation of pavement at the crest's ds edge (Guan 2009) .....	136

Figure 93 Repair works at vertical slab joints (Guan 2009) .....	136
Figure 94 Massive spalling off of concrete edges at vertical slab joints (Chen 2008)..	136
Figure 95 Repair works at cold joint slip over of 3 <sup>rd</sup> phase slab after concrete removal (Guan 2009).....	136
Figure 96 Cold joint failure and slip over of 3 <sup>rd</sup> phase slab (Chen 2008).....	136
Figure 97 Vertical crest settlement taken from top of parapet wall readings (Guan 2009) .....	137
Figure 98 Horizontal displacement taken from top of parapet wall readings (+ = towards ds, Guan 2009) .....	137
Figure 99 Horizontal displacement vectors of ds shoulder and crest surface monuments until July 20 <sup>th</sup> (Guan 2009) .....	138
Figure 100 Internal fill settlement of Zipingpu CFRD (excluding settlements prior earthquake, Chen 2008).....	139
Figure 101 Internal fill displacement of Zipingpu CFRD (excluding deformations prior earthquake, Chen 2008).....	139
Figure 102 Leakage of Zipingpu dam before and after Wenchuan earthquake (Zeping, 2009) .....	140
Figure 103 Aerial view of Fujinuma irrigation reservoir (Harder et al, 2011) .....	141
Figure 104 Typical cross section of main Fujinuma earthfill dam [m] (Matsumoto, N., Sasaki, T. and Ohmachi, T., 2001) .....	142
Figure 105 Accelerograms recoded by FKHS08 station situated in bedrock (courtesy NIED database).....	143
Figure 106 Accelerograms recoded by FKSH09 station situated in bedrock (courtesy NIED database).....	143
Figure 107 View towards left abutment of breached Fujinuma dam (Harder et al., 2011) .....	145
Figure 108 The “Chinese criteria” plotted against results of laboratory testing (Bray et all. 2004).....	146
Figure 109 Criteria for judgement of liquefiable soils (Bray et all. 2004) .....	146
Figure 110 Overtopped crest of Fujinuma dam (EERI, 2011) .....	147

Figure 111 Mapping of rip rap and concrete blocks (JCOLD, 2012).....	148
Figure 112 Aratozawa dam model after impounding, general view .....	149
Figure 113 Aratozawa dam model after impounding, dam cross section .....	150
Figure 114 Horizontal base acceleration Aratozawa dam model (adapted from JCOLD 2014).....	151
Figure 115 Vertical base acceleration Aratozawa dam model (adapted from JCOLD 2014).....	151
Figure 116 Aratozawa dam model – initial stresses .....	154
Figure 117 Aratozawa dam model – layered construction – placement of 6 <sup>th</sup> layer ...	154
Figure 118 Aratozawa dam model – layered construction – last layer .....	154
Figure 119 Aratozawa dam model – impounding.....	155
Figure 120 Aratozawa dam model – earthquake analysis .....	155
Figure 121 Aratozawa dam model – post-earthquake deformation - Newmark analysis .....	155
Figure 122 Empirical relationship of moment magnitude, equivalent number of cycles and rupture plane distance .....	156
Figure 123 Shear modulus reduction vs. shear strain applied to embankment fill material in GeoStudio EL analysis .....	158
Figure 124 Damping ratio vs. shear strain applied to embankment fill material in GeoStudio EL analysis .....	159
Figure 125 Shear modulus vs. vertical stress applied to embankment fill material in GeoStudio EL and NL analysis.....	159
Figure 126 Pore water pressure built up vs. cyclic number ratio applied to the clay core in GeoStudio EL analysis .....	160
Figure 127 Shear stress ratio vs. actual cyclic number applied to embankment fill material in GeoStudio EL analysis .....	160
Figure 128 Recoverable modulus vs. vertical effective stress applied to embankment fill material in GeoStudio NL analysis .....	161
Figure 129 Accumulated vs. incremental volumetric strain functions applied to embankment fill material in GeoStudio NL analysis .....	161

Figure 130 Zipingpu dam model after impounding, general view .....	163
Figure 131 Zipingpu dam model after impounding, dam cross section .....	163
Figure 132 Accelerograph recordings at dam crest mid at the crest's downstream edge (Guan 2009).....	165
Figure 133 Crest accelerograph hit by destroyed unreinforced concrete guard elements (Zou 2012) .....	165
Figure 134 Horizontal base acceleration Zipingpu dam model .....	166
Figure 135 Vertical base acceleration Zipingpu dam model .....	167
Figure 136 Spectral response of generated input acceleration Zipingpu CFRD .....	167
Figure 137 Zipingpu dam model – initial stresses .....	169
Figure 138 Zipingpu dam model – layered construction – placement of 2 <sup>nd</sup> layer .....	169
Figure 139 Zipingpu dam model – layered construction – placement of 3 <sup>rd</sup> layer .....	169
Figure 140 Zipingpu dam model – layered construction – placement of concrete slab and parapet wall .....	170
Figure 141 Zipingpu dam model – layered construction – last layer + 1A material placement .....	170
Figure 142 Zipingpu dam model – impounding – boundary conditions .....	171
Figure 143 Zipingpu dam model – earthquake analysis .....	171
Figure 144 Zipingpu dam model – post-earthquake deformation - Newmark analysis .....	171
Figure 145 Shear modulus reduction vs. shear strain applied to embankment fill material in GeoStudio EL analysis .....	173
Figure 146 Damping ratio vs. shear strain applied to embankment fill material in GeoStudio EL analysis .....	174
Figure 147 Shear modulus vs. vertical stress applied to embankment fill material in GeoStudio EL and NL analysis .....	174
Figure 148 Fujinuma dam model after impounding, general view .....	178
Figure 149 Fujinuma dam model after impounding, dam cross section .....	178
Figure 150 Fujinuma dam model close up view cohesive to non-cohesive materials .	178
Figure 151 Horizontal base acceleration Fujinuma dam model .....	179

Figure 152 Vertical base acceleration Fujinuma dam model.....	180
Figure 153 Fujinuma dam model – initial stresses.....	182
Figure 154 Fujinuma dam model – layered construction – first layer.....	182
Figure 155 Fujinuma dam model – layered construction – last layer.....	182
Figure 156 Fujinuma dam model – impounding.....	183
Figure 157 Fujinuma dam model – earthquake analysis .....	183
Figure 158 Shear modulus reduction vs. shear strain applied to embankment fill material in GeoStudio EL analysis .....	185
Figure 159 Damping ratio vs. shear strain applied to embankment fill material in GeoStudio EL analysis.....	186
Figure 160 Pore water pressure built up vs. cyclic number ratio applied to embankment fill material in GeoStudio EL analysis.....	186
Figure 161 Shear stress ratio vs. actual cyclic number applied to embankment fill material in GeoStudio EL analysis .....	187
Figure 162 Recoverable modulus vs. vertical effective stress applied to embankment fill material in GeoStudio EL analysis .....	188
Figure 163 Accumulated vs. incremental volumetric strain functions applied to embankment fill material in GeoStudio NL analysis .....	189
Figure 164 Discontinuity of accumulated vs. incremental volumetric strain .....	189
Figure 165 Pore water pressure distribution after impounding (prior earthquake) of Aratozawa dam.....	193
Figure 166 Effective vertical stresses after impounding and prior earthquake of Aratozawa dam [kN/m <sup>2</sup> ].....	194
Figure 167 Cyclic shear strain at 4,82 sec during the earthquake analysis of Aratozawa dam [-] .....	194
Figure 168 Effective minimum stresses within the clay core after impounding of Aratozawa dam [kN/m <sup>2</sup> ].....	195
Figure 169 Horizontal peak acceleration due to Iwate / Miyagi earthquake [g] (EL GeoStudio).....	196



Figure 170 Vertical peak acceleration due to Iwate / Miyagi earthquake [g] (EL GeoStudio) .....	196
Figure 171 Horizontal crest acceleration calculated from Iwate / Miyagi earthquake – SMA 3 [g] (EL GeoStudio) .....	197
Figure 172 vertical crest acceleration calculated from Iwate / Miyagi earthquake – SMA 3 [g] (EL GeoStudio) .....	197
Figure 173 Pore water pressure distribution after Iwate / Miyagi earthquake [kN/m <sup>2</sup> ] (EL GeoStudio).....	199
Figure 174 Pore water pressure development during Iwate / Miyagi earthquake [kN/m <sup>2</sup> ] (EL GeoStudio).....	199
Figure 175 Distribution of effective minimum stresses after Iwate / Miyagi earthquake [kN/m <sup>2</sup> ] (EL GeoStudio).....	199
Figure 176 Vertical crest vs. base displacement [m] (EL GeoStudio) .....	200
Figure 177 Vertical crest settlement from post-earthquake stress – redistribution analysis[m] (EL GeoStudio) .....	200
Figure 178 Downstream slip circle resulting in a deformation of 0,38m (EL GeoStudio) .....	202
Figure 179 Downstream slip circle resulting in the highest deformation of 11,6m (EL GeoStudio) .....	202
Figure 180 Downstream slip circle resulting in a deformation of 0,061m (EL GeoStudio) .....	203
Figure 181 Downstream deep seated slip circle resulting in a deformation of 0,00m (EL GeoStudio) .....	203
Figure 182 Upstream slip circle resulting in highest deformation of 0,15m (EL GeoStudio) .....	203
Figure 183 Upstream deep seated slip circle resulting in a deformation of 0,04m (EL GeoStudio) .....	203
Figure 184 General view of slip surface resulting in approximately 0,00m of deformation (EL GeoStudio) .....	204

Figure 185 Effective vertical stresses after Iwate / Miyagi earthquake [kN/m <sup>2</sup> ] (EL GeoStudio).....	204
Figure 186 Horizontal crest acceleration calculated from Iwate / Miyagi earthquake – SMA 3 [g] (NL GeoStudio).....	205
Figure 187 Vertical crest acceleration calculated from Iwate / Miyagi earthquake – SMA 3 [g] (NL GeoStudio) .....	206
Figure 188 Pore water pressure distribution after Iwate / Miyagi earthquake [kN/m <sup>2</sup> ] (NL GeoStudio) .....	207
Figure 189 Pore water pressure development during Iwate / Miyagi earthquake [kN/m <sup>2</sup> ] (NL GeoStudio).....	208
Figure 190 Distribution of effective minimum stresses after Iwate / Miyagi earthquake [kN/m <sup>2</sup> ] (NL GeoStudio).....	208
Figure 191 Vertical crest vs. base displacement [m] (NL GeoStudio) .....	208
Figure 192 Vertical crest settlement, permanent deformation as a result of dynamic analysis [m] (NL GeoStudio) .....	209
Figure 193 Vertical crest settlement, permanent deformation as a result of post-earthquake stress redistribution analysis [m] (NL GeoStudio) .....	209
Figure 194 Downstream slip circle resulting in a deformation of 1,45m (NL GeoStudio) .....	210
Figure 195 Downstream slip circle resulting in the highest deformation of 54m (NL GeoStudio).....	210
Figure 196 Downstream slip circle resulting in a deformation of 0,10m (NL GeoStudio) .....	210
Figure 197 Downstream deep seated slip circle resulting in a deformation of 0,00m (NL GeoStudio).....	210
Figure 198 Upstream slip circle resulting in highest deformation of 0,02m (NL GeoStudio).....	211
Figure 199 Upstream deep seated slip circle resulting in a deformation of 0,00m (NL GeoStudio).....	211

Figure 200 Effective vertical stresses after Iwate / Miyagi earthquake [kN/m <sup>2</sup> ] (NL GeoStudio) .....	211
Figure 201 Effective vertical stresses prior earthquake analysis of Aratozawa dam [kN/m <sup>2</sup> ] (NL Plaxis) .....	212
Figure 202 Effective vertical stress distribution after earthquake analysis [kN/m <sup>2</sup> ] (NL Plaxis) .....	212
Figure 203 Horizontal crest acceleration calculated from Iwate / Miyagi earthquake – SMA 3 [g] (NL Plaxis) .....	213
Figure 204 Vertical crest acceleration calculated from Iwate / Miyagi earthquake – SMA 3 [g] (NL Plaxis).....	214
Figure 205 Pore water pressure distribution after Iwate / Miyagi earthquake [kN/m <sup>2</sup> ] (NL Plaxis).....	216
Figure 206 Pore water pressure development during Iwate / Miyagi earthquake [kN/m <sup>2</sup> ] (NL Plaxis) .....	216
Figure 207 Development of effective minimum stresses during Iwate / Miyagi earthquake [kN/m <sup>2</sup> ] (NL Plaxis).....	217
Figure 208 Vertical crest vs. base displacement [m] (NL Plaxis) .....	217
Figure 209 Vertical crest settlement, permanent deformation as a result of dynamic analysis [m] (NL Plaxis).....	218
Figure 210 Vertical crest settlement, permanent deformation as a result of post-earthquake stress redistribution analysis [m] (NL Plaxis).....	218
Figure 211 Failure points (red dots) where the yield criterion was reached during or at end of the dynamic calculation of Iwate / Miyagi earthquake (NL code, Plaxis) .....	219
Figure 212 Pore water pressure distribution after impounding (prior earthquake) of Zipingpu dam.....	221
Figure 213 Effective vertical stress distribution after impounding and shortly prior earthquake of Zipingpu dam.....	221
Figure 214 Horizontal peak acceleration due to Wenchuan earthquake [g] (EL GeoStudio) .....	223

Figure 215 Horizontal peak acceleration in crest region [g] (EL GeoStudio) .....	223
Figure 216 Vertical peak acceleration due to Wenchuan earthquake [g] (EL GeoStudio) .....	223
Figure 217 Vertical peak acceleration in crest region [g] (EL GeoStudio).....	223
Figure 218 Horizontal crest acceleration calculated from Wenchuan earthquake [g] (EL GeoStudio).....	224
Figure 219 Vertical crest acceleration calculated from Wenchuan earthquake [g] (EL GeoStudio).....	224
Figure 220 Effective vertical stresses after Wenchuan earthquake [kN/m <sup>2</sup> ] (EL GeoStudio).....	225
Figure 221 Vertical crest vs. base displacement [m] (EL GeoStudio).....	226
Figure 222 Vertical crest settlement, permanent deformation as a result of post- earthquake stress-redistribution analysis [m] (EL GeoStudio).....	226
Figure 223 Downstream slip circle resulting in the largest deformation of 1,19m (EL GeoStudio).....	228
Figure 224 Downstream slip circle resulting in a deformation of 0,06m (EL GeoStudio) .....	228
Figure 225 General view of slip surface resulting in approximately 0,00m deformation (EL GeoStudio) .....	228
Figure 226 Upstream slip circle resulting in highest deformation of 0,26m (EL GeoStudio).....	229
Figure 227 Upstream “deep” seated slip circle resulting in a deformation of 0,02m (EL GeoStudio).....	229
Figure 228 Upstream slip surface resulting in approximately 0,00m of deformation (EL GeoStudio).....	229
Figure 229 Horizontal crest acceleration calculated from Wenchuan earthquake [g] (NL GeoStudio).....	230
Figure 230 vertical crest acceleration calculated from Wenchuan earthquake [g] (NL GeoStudio).....	230

Figure 231 Vertical delta crest settlement as a result of plasticity conditions reached during shaking [m]. (NL GeoStudio) .....	231
Figure 232 Vertical crest settlement, permanent deformation as a result of post-earthquake stress-redistribution analysis [m] (NL GeoStudio) .....	231
Figure 233 Downstream slip circle resulting in the largest deformation of 0,69m (NL GeoStudio) .....	232
Figure 234 Downstream slip circle first one including the whole crest and resulting in a deformation of 0,04m (NL GeoStudio) .....	233
Figure 235 Downstream slip surface resulting in approximately 0,00m deformation (NL GeoStudio) .....	233
Figure 236 Upstream slip circle resulting in highest deformation of 1,37m (NL GeoStudio) .....	233
Figure 237 Upstream “deep” seated slip circle resulting in a deformation of 0,025m (NL GeoStudio) .....	234
Figure 238 Upstream slip surface resulting in approximately 0,00m of deformation (NL GeoStudio) .....	234
Figure 239 Effective vertical stresses after Wenchuan earthquake [kN/m <sup>2</sup> ] (NL GeoStudio) .....	234
Figure 240 Effective vertical stress distribution prior earthquake analysis [kN/m <sup>2</sup> ] (NL Plaxis) .....	235
Figure 241 Effective vertical stress distribution after earthquake analysis [kN/m <sup>2</sup> ] (NL Plaxis) .....	235
Figure 242 Horizontal crest acceleration calculated from Wenchuan earthquake [m/sec <sup>2</sup> ] (NL Plaxis) .....	236
Figure 243 vertical crest acceleration calculated from Wenchuan earthquake [m/sec <sup>2</sup> ] (NL Plaxis) .....	236
Figure 244 Vertical crest vs. base displacement [m] (NL Plaxis) .....	237
Figure 245 Vertical crest settlement, permanent deformation as a result of post-earthquake stress-redistribution analysis [m] (NL Plaxis) .....	238

Figure 246 Horizontal crest displacement, permanent deformation as a result of post-earthquake stress-redistribution analysis [m] (NL Plaxis).....	238
Figure 247 Failure points (red dots) where the yield criterion was reached during or at end of the dynamic calculation of Wenchuan earthquake (NL code, Plaxis) ...	239
Figure 248 DS global factor of safety, prior earthquake static conditions .....	241
Figure 249 US global factor of safety, prior earthquake static conditions .....	241
Figure 250 Effective vertical stress distribution after impounding shortly prior earthquake analysis of Fujinuma dam .....	242
Figure 251 DS global factor of safety after check earthquake (slope stability based on EL analysis, GeoStudio).....	243
Figure 252 DS local factor of safety after check earthquake (slope stability based on EL analysis, GeoStudio) .....	243
Figure 253 US local factor of safety after check earthquake (slope stability based on EL analysis, GeoStudio) .....	243
Figure 254 US local factor of safety after check earthquake (slope stability based on EL analysis, GeoStudio) .....	244
Figure 255 US local factor of safety after check earthquake (slope stability based on EL analysis, GeoStudio) .....	244
Figure 256 Liquefaction plot after check earthquake (liquefied material would be marked in yellow color, EL analysis, GeoStudio).....	244
Figure 257 Post-earthquake deformations after check earthquake [m] (EL analysis, GeoStudio).....	245
Figure 258 DS local stability after Tohoku earthquake (slope stability based on EL analysis, GeoStudio) .....	245
Figure 259 DS local stability after Tohoku earthquake (slope stability based on EL analysis, GeoStudio) .....	246
Figure 260 DS local stability after Tohoku earthquake (slope stability based on EL analysis, GeoStudio) .....	246
Figure 261 DS local stability after Tohoku earthquake (slope stability based on EL analysis, GeoStudio) .....	246

Figure 262 US local stability after Tohoku earthquake (slope stability based on EL analysis, GeoStudio).....	246
Figure 263 US local stability after Tohoku earthquake (slope stability based on EL analysis, GeoStudio).....	247
Figure 264 US local stability after Tohoku earthquake (slope stability based on EL analysis, GeoStudio).....	247
Figure 265 Liquefied zones within Fujinuma embankment after Tohoku earthquake (EL analysis, GeoStudio).....	247
Figure 266 Post-earthquake xy - displacements after Tohoku earthquake (EL analysis, GeoStudio) .....	249
Figure 267 Post-earthquake settlement after Tohoku earthquake (EL analysis, GeoStudio) .....	249
Figure 268 Vertical crest settlement vs. vertical model base settlement at end of dynamic calculation [m] (EL analysis, GeoStudio) .....	249
Figure 269 Peak horizontal crest acceleration during Tohoku earthquake [g] (EL analysis, GeoStudio).....	250
Figure 270 Peak vertical crest acceleration during Tohoku earthquake [g] (EL analysis, GeoStudio) .....	250
Figure 271 Pore water pressure development vs. dynamic time (EL analysis, GeoStudio) .....	251
Figure 272 Effective vertical stresses after Tohoku earthquake (EL analysis, GeoStudio) .....	251
Figure 273 DS global factor of safety after check earthquake (slope stability based on NL analysis, GeoStudio).....	252
Figure 274 DS local factor of safety after check earthquake (slope stability based on NL analysis, GeoStudio).....	252
Figure 275 US local of safety after check earthquake (slope stability based on NL analysis, GeoStudio).....	252
Figure 276 US local of safety after check earthquake (slope stability based on NL analysis, GeoStudio).....	253

Figure 277 local of safety after check earthquake (slope stability based on NL analysis, GeoStudio).....	253
Figure 278 Liquefaction plot after check earthquake (liquefied material would be marked in yellow color, NL code, GeoStudio) .....	254
Figure 279 Post-earthquake deformations after check earthquake [m] (NL code, GeoStudio).....	254
Figure 280 DS local stability after Tohoku earthquake (slope stability based on NL analysis, GeoStudio) .....	254
Figure 281 DS local stability after Tohoku earthquake (slope stability based on NL analysis, GeoStudio) .....	255
Figure 282 DS local stability after Tohoku earthquake (slope stability based on NL analysis, GeoStudio) .....	255
Figure 283 DS local stability after Tohoku earthquake (slope stability based on NL analysis, GeoStudio) .....	255
Figure 284 US local stability after Tohoku earthquake (slope stability based on NL analysis, GeoStudio) .....	256
Figure 285 US local stability after Tohoku earthquake (slope stability based on NL analysis, GeoStudio) .....	256
Figure 286 US local stability after Tohoku earthquake (slope stability based on NL analysis, GeoStudio) .....	256
Figure 287 Liquefied zones within Fujinuma embankment after Tohoku earthquake (NL code, GeoStudio).....	257
Figure 288 Post-earthquake xy - displacements after Tohoku earthquake (NL code, GeoStudio).....	257
Figure 289 Post-earthquake settlement after Tohoku earthquake (NL code, GeoStudio) .....	258
Figure 290 Post-earthquake settlement after Tohoku earthquake, deformed mesh 1:1 (NL code, GeoStudio).....	258
Figure 291 Vertical crest settlement vs. vertical model base settlement at end of dynamic calculation [m] (NL code, GeoStudio) .....	258



Figure 292 Horizontal crest acceleration vs. horizontal model base acceleration during Tohoku earthquake [g] (NL code, GeoStudio) .....	259
Figure 293 Vertical crest acceleration vs. vertical model base acceleration during Tohoku earthquake [g] (NL code, GeoStudio) .....	259
Figure 294 Pore water pressure development vs. dynamic time (NL code, GeoStudio) .....	260
Figure 295 Effective vertical stresses after Tohoku earthquake (NL code, GeoStudio) .....	260
Figure 296 Pre-earthquake stability analysis (Plaxis) .....	261
Figure 297 Effective vertical stresses prior earthquake analysis (Plaxis) .....	261
Figure 298 Effective vertical stresses after earthquake analysis -> pore water pressure built up (Plaxis).....	262
Figure 299 Effective minimum stresses prior check earthquake (NL code, Plaxis) .....	262
Figure 300 Effective minimum stresses after check earthquake (NL code, Plaxis) .....	263
Figure 301 Settlement at end of Check earthquake (NL code, Plaxis) .....	263
Figure 302 Post-earthquake settlement from Check earthquake (NL code, Plaxis) ....	263
Figure 303 Liquefaction of fill zones within Fujinuma embankment after Tohoku earthquake (NL code, Plaxis).....	264
Figure 304 Liquefaction of fill zones within Fujinuma embankment after Tohoku earthquake (NL code, Plaxis).....	264
Figure 305 Failure points (red dots) where the yield criterion was reached during or at end of the dynamic calculation of Tohoku earthquake (NL code, Plaxis) .....	265
Figure 306 Settlement after Tohoku earthquake (NL code, Plaxis).....	266
Figure 307 Settlement at end of Tohoku earthquake, deformed mesh 1:1 (NL code, Plaxis) .....	266
Figure 308 Horizontal crest acceleration vs. horizontal model base acceleration during Tohoku earthquake [g] (NL code, Plaxis) .....	267
Figure 309 Vertical crest acceleration vs. vertical model base acceleration during Tohoku earthquake [g] (NL code, Plaxis) .....	267

## List of Tables

Table 1 Damage class system acc. to Pells and Fell (2003) .....	36
Table 2 Plate boundary types, related typical earthquake types and exemplarily faults (Day 2002) .....	42
Table 3 Frequency of earthquake occurrence worldwide (USGS 2000) .....	47
Table 4 Ranking of the 5 largest earthquakes from 1900 to 2014, (USGS 2014) .....	47
Table 5 Approximate correlations of descriptive earthquake parameters (reproduced from Day 2002) .....	47
Table 6 Correlation of rupture area and magnitude (Penn n.d., reproduced from Kamalesh 2008) .....	48
Table 7 Bracketed duration [sec] vs. earthquake magnitude (Bolt 1973) .....	56
Table 8 Risk factors for calculation of total risk factor (Hawaii Dam Safety Guideline 2004) .....	82
Table 9 Total risk factor vs. risk class (Hawaii Dam Safety Guideline 2004) .....	82
Table 10 Risk class vs. design earthquake (Hawaii Dam Safety Guideline 2004) .....	82
Table 11 P and S-wave profile of FSKH08 / FSKH09 and FSKH10 boreholes (NIED) .....	95
Table 12 Material parameter sets applied to FKSH08 analysis (equivalent linear) .....	98
Table 13 Material parameter sets applied to FKSH09 analysis (equivalent linear) .....	105
Table 14 Material parameter sets applied to FKSH10 analysis (equivalent linear) .....	113
Table 15 Rise of pore water pressure within clay core material .....	132
Table 16 Triaxial test results of samples taken at Fujinuma dam embankment after failure (Charatpangoon et al, 2014) .....	145
Table 17 Material parameter sets applied to embankment fill material in GeoStudio EL and NL analysis .....	157
Table 18 Material parameter sets applied to embankment fill material in Plaxis NL analysis .....	162
Table 19 Material parameter sets applied to embankment fill material in GeoStudio EL and NL analysis .....	172

Table 20 Material parameter sets applied to embankment fill material in Plaxis NL analysis.....	175
Table 21 Material parameter sets applied to embankment fill material in GeoStudio EL and NL analysis.....	184
Table 22 Material parameter sets applied to embankment fill material in Plaxis NL analysis.....	191

## List of Abbreviations

CFRD	Concrete faced Rockfill Dam
ECRD	Earth Core Rockfill Dam
US	Upstream
DS	Downstream
PGA	Peak Ground Acceleration
MC	Mohr Coulomb constitutive model
HSS	Hardening Soil Small Strain constitutive model
UBC2D	UBC Sand constitutive model
GHS	Generalized Hardening Soil Small Strain constitutive model
EL	Equivalent Linear
NL	Nonlinear

## 1 Scope and Outline

Recently, extensive engineering emphasis was put on development of constitutive models better reproducing the real stress – strain behavior of coarse grained fill materials. Simultaneously, increasing computation capacities enable solving more and more complex dynamic calculations. However, engineering practice lacks for examples making use of those beneficial developments. Still the behavior of embankment dams is commonly assessed mainly by empirically driven formulae.

Having in mind recent magnitude 9 earthquake events and the international trend to verify adequate dam behavior for 10000 year or sometimes higher deterministic events, a state of the art approach might reach its limit or might overestimate the dynamic effects. This trend in deed raises the need for more sophisticated calculation methods. This thesis follows the research appeal of ICOLD as stated in Bulletin 155 (Guideline for use of numerical models in dam engineering). Especially in case of embankment dams, the use of recently developed numerical models is generally questioned. Their use in practice is not recommended.

The general scope of this thesis is to compare the proved - state of the art - calculation methods with more sophisticated numerical approaches. Their results will be cross checked on observed dam behavior on three dams recently hit by high magnitude earthquakes. This shall bring more light into the potential of these models, their sensitivity to input parameters and the potential in accurately predicting the seismic behavior.

In a first step, three Japanese dynamic observation stations will be back—calculated. These stations consist of a pair of 3D seismographs were the lower one is located in rock inside a borehole and the upper one is placed at the borehole's upper end on top of shallow soil deposits.

In a second step plain strain dynamic time history analysis shall verify a numerical model's applicability to a surface lined, a central earth core and a homogeneous dam that were hit by an severe earthquake.

## 2 Executive Summary

Within this thesis state of the art analysis on dynamic behavior of embankment dams were cross checked by back calculation of three case studies that have suffered severe earthquake shaking.

These three case studies namely are:

- The Aratozawa dam, a 85m high Clay Core Rockfill dam that was shaken by the Mw=6,9 Iwate 7 Miyagi earthquake resulting in an measured peak ground acceleration of 0,85g.
- The Zigingpu dam, a 156m high Concrete Face Rockfill dam shaken by the Mw=7,9 Wenchuan earthquake resulting in severe damage to the concrete slabs.
- The Fujinuma dam, a 18m high earthfill dam that was shaken by the Mw=9,0 Tohoku earthquake resulting in crest overflow and dam breach.

State of the art numerical methods as recommended by ICOLD Bulletin 155 were compared to newly developed models.

In general it was found that the Equivalent Linear (GeoStudio 2012) and the Nonlinear (Plaxis 2015) model were or might be able to accurately reproduce observed peak accelerations.

In accordance with ICOLD Bulletin 155, it was found that Nonlinear models shall be used in cases where significant pore water pressure increase or liquefaction develop.

In general contrast to ICOLD Bulletin 155 it was found that state of the art methods (i.e. the Linear – Equivalent method combined with Newmark's double integration or Makdisi – Seed deformation analysis) fail in accurately predicting the permanent deformation of all selected case studies. It was found that the theoretical background of Newmark' double integration as well as Makdisi – Seed deformation analysis are not in accordance with the physical behavior of rockfill embankments during dynamic shaking.

Furthermore it was found that none of the applied constitutive models could accurately predict the dynamic settlements of rockfill dams. The most trustable prediction could be achieved from sophisticated Nonlinear models that do realistically reproduce the stress – deformation behavior of rockfill embankments. However, as none of the applied soil models accounts for cyclic energy dependent strain softening the accurate prediction of dynamic rockfill densification was underestimated in all cases.

Analysis on earthfill dams shall be excluded from the previously stated as all constitutive models resulted in observed dam behavior. However, the Nonlinear models of

software Plaxis resulted in inherently stable and reliable prediction of the dam breach. These constitutive models provide a closed form where a realistic stress – strain behavior is directly linked to realistic pore water pressure generation, without intermediate simplifications that enable to manipulate the results. Thus it was found that the time needed from setup of the model to the achievement of reliable realistic and stable results was significantly less than needed for the other methods. Hence the increased number of input parameters should not scare the Engineer in most cases as they finally will save time.

### **3 Historic Performance of Embankment Dams**

ICOLD (1995) has performed statistical analysis on dam failures. Within bulletin 99 in total 4 embankment dams are reported to have failed due to earthquake effects.

Three out of these failed dams were earthfill dams, one was a rockfill dam. The causative mechanisms were reported to be liquefaction in two cases and abrupt crest settlement for the two other cases.

It is interesting to note that a so called dam failure is uncontrolled release of stored water hence the classification is in many cases dependent on a reporter's judgment. The failure of gates or bottom outlets is often termed a dam failure even though the dam itself was not subject to untypical behavior. The near failure of Upper San Fernando dam for example is not listed as a dam failure in ICOLD (1995). Having in mind aerial pictures of the Upper San Fernando dam it is hard to state that this dam did not fail (Figure 7).

This bulletin sums up dams exceeding 15m in total height. Even though, this bulletin does not (and clearly cannot) list all dams that failed worldwide the low number of failed dams indirectly reflects the high inherent resistance of embankment dams to earthquake induced ground motion. This inherent resistance is mainly resulting from the distinct nonlinear dynamic behavior of earth or rock fillings in cyclic excitation. Most irrigation dams for example have heights not exceeding 15m in total and hence are often not in accordance with international state of the art design regulations. As a consequence the before mentioned number of four failed dams has to be increased by unknown or unreported cases. Liquefaction is often estimated to be the causative mechanism of failure especially for small (rural) dams that have failed directly after earthquake events.

Wieland (n.d.) points out that the Bhuj earthquake from January 2001 has shown that rural dams are prone to earthquake related settlements and the reported cases would



have resulted in catastrophic situations if the earthquake happened at end of monsoon in reservoir full conditions.

USSD (2014) summarizes the observed performance of dams worldwide during earthquake events and highlights numerous case histories. Summarizing the behavior of embankment dams, the authors conclude: *'From a detailed review of past experience records, it is apparent that embankment dams have fared both satisfactorily and poorly when subjected to strong earthquake motion. Their performance has generally been closely related to the nature of the materials used for construction. Most well-built earthfill dams are capable of withstanding substantial earthquake shaking with no detrimental effects. Dams built of compacted clayey materials on clay or bedrock foundations have historically withstood extremely strong levels of ground motion, even when obsolete or inefficient compaction procedures were used (Coiheuco Dam may be an exception to this trend.). In contrast, older embankments built on sandy materials or of insufficiently compacted sands and silts and tailings dams represent nearly all the known cases of failures, primarily as a result of the liquefiability of these materials. Therefore, hydraulic fill dams, a type of construction now abandoned, and tailings dams represent the most hazardous types of embankment dams. Conversely, rockfill dams or concrete face rockfill dams (CFRD's) are generally considered to be inherently stable under extreme earthquake loading, and represent desirable types of dams in highly seismic areas. However, the Zipingpu Dam experience shows that concrete face slabs can crack.'*

Matsumoto (2010) summarizes the behavior of Japanese dams and concludes that none of the embankment dams was damaged when moment magnitude  $M_w$  was smaller than 6.9 even for dams close to the epicenter. Moderate damage to embankment dams was observed for dams within a 30 km distance to epicenter when  $M_w$  exceeded 7.6. In this case embankment dams suffered cracks in the crest as well as shallow slope failures. Figure 1 to Figure 3 show the observed damage of earth core rockfill dams, concrete face rockfill dams and earthfill dams in respect to  $M_J$  and epicentral distance. Where  $M_J$  is related to moment magnitude  $M_w$  as follows:

$$M_w = 0.78M_J + 1.08$$

[1]

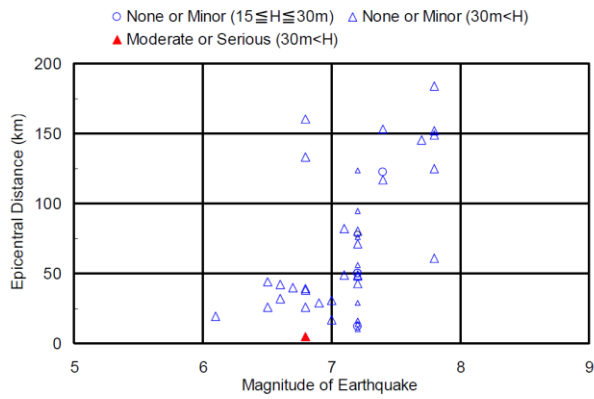


Figure 1 Observed damage of earth core rockfill dams vs. magnitude and epicentral distance (Matsumoto 2010)

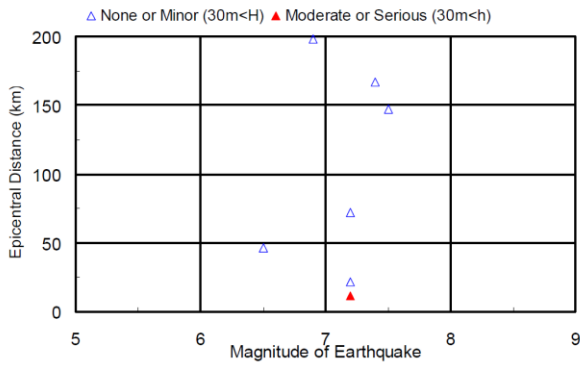


Figure 2 Observed damage of concrete face rockfill dams vs. magnitude and epicentral distance (Matsumoto 2010)

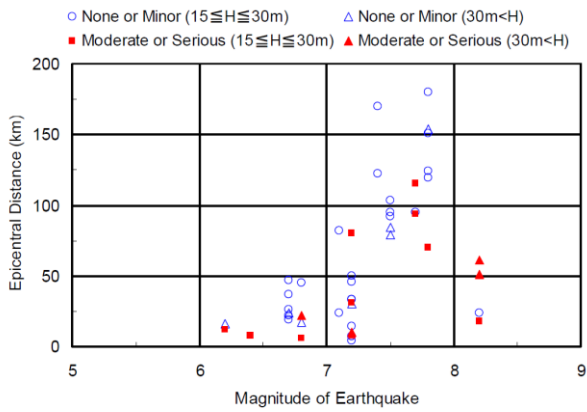


Figure 3 Observed damage of earthfill dams vs. magnitude and epicentral distance (Matsumoto 2010)

## 4 Observed Damage of Embankment Dams due to Earthquake Loading

Figure 4 to Figure 9 provide a comprehensive view on typical damage of embankment dams after being subject to strong motion acceleration. Figure 4 and Figure 6 show joint detail close ups of Zipingpu CFRD, a 156m high dam that was severely shaken by the  $M_w=7,9$  Wenchuan earthquake. Figure 7 shows the “near failure” of Lower San Fernando dam after the 1971 San Fernando earthquake. The 85m high hydraulic fill dam suffered severe damage due to liquefaction of the embankment, but luckily did not breach. This situation is characteristic for several other smaller dams that suffered extensive sliding failures after an earthquake but did not breach due to lucky combinations as low reservoir levels or other factors.

Figure 9 shows the 18m high Fujinuma-ike dam that unfortunately breached during the 2011 Tohoku earthquake. Liquefaction of the embankment fill resulting in crest settlement and overtopping is deemed to be the most likely cause for the failure.



Figure 4 Horizontal construction joint of Zipingpu CFRD (Chen and Sheng-Shui n.d.)



Figure 5 Slides close to the crest of Colbun dam (Nogueira 2010)



Figure 6 Spalling at joints of Zipingpu CFRD (Chen and Sheng-Shui n.d.)



Figure 7 “Near” failure of Lower San Fernando Dam (Wieland 2013)



Figure 8 Upstream slip surface Wenchuan earthquake 2008 (Wieland 2013)



Figure 9 Failure of Fujinuma-ike dam after the Tohoku earthquake (Matsumoto 2011)

Pells and Fell (2003) introduced a damage classification system based on observed performance of 305 dams. They report that cracking of fill dams in longitudinal direction was observed quite often. Transversal cracks were not observed that often, whilst they conclude that slope failures are uncommon.

They found out that visible longitudinal cracks were observed when the pga exceeds 0,3g and magnitude exceeds 6,5 or when pga exceeds 0,15g and magnitude exceeds 7,0.

<i>Damage class</i>		<i>Max. longitudinal crack width (mm) †</i>	<i>Max. relative crest settlement (%)‡</i>
No.	Description		
0	No or slight	<10mm	<0.03
1	Minor	10-30	0.03-0.2
2	Moderate	30-80	0.2-0.5
3	Major	80-150	0.5-1.5
4	Severe	150-500	1.5-5
5	Collapse	>500	>5

† *Max. crack width is taken as the maximum width, in millimeters, of any longitudinal cracking that occurs.*

‡ *Max. relative crest settlement is expressed as a percentage of the maximum dam height (from general foundation to dam crest).*

**Table 1 Damage class system acc. to Pells and Fell (2003)**

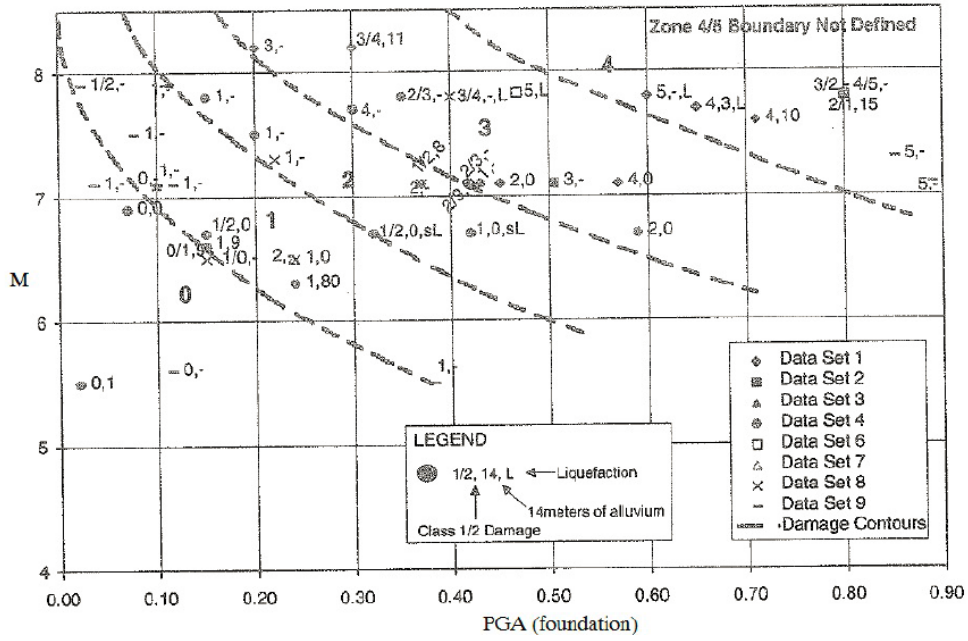


Figure 10 Damage class vs. magnitude and pga (Pells and Fells, 2003)

## 5 Earthquake Hazard and Seismicity

### 5.1 General

Earthquakes are the result of confined shear deformation releasing the accumulated energy in abrupt rupturing of the earth's crust. Figure 11 shows the earth's major tectonic plates and the type of plate boundaries. Arrows show the overall direction of plate movement. These plate movements are hindered at their boundaries unless the accumulated stresses exceed the shear capacity of existing fault planes. The accumulated energy is released abruptly in a fault rupture resulting in residual deformations. These deformations increase stepwise with each earthquake (Day 2002).

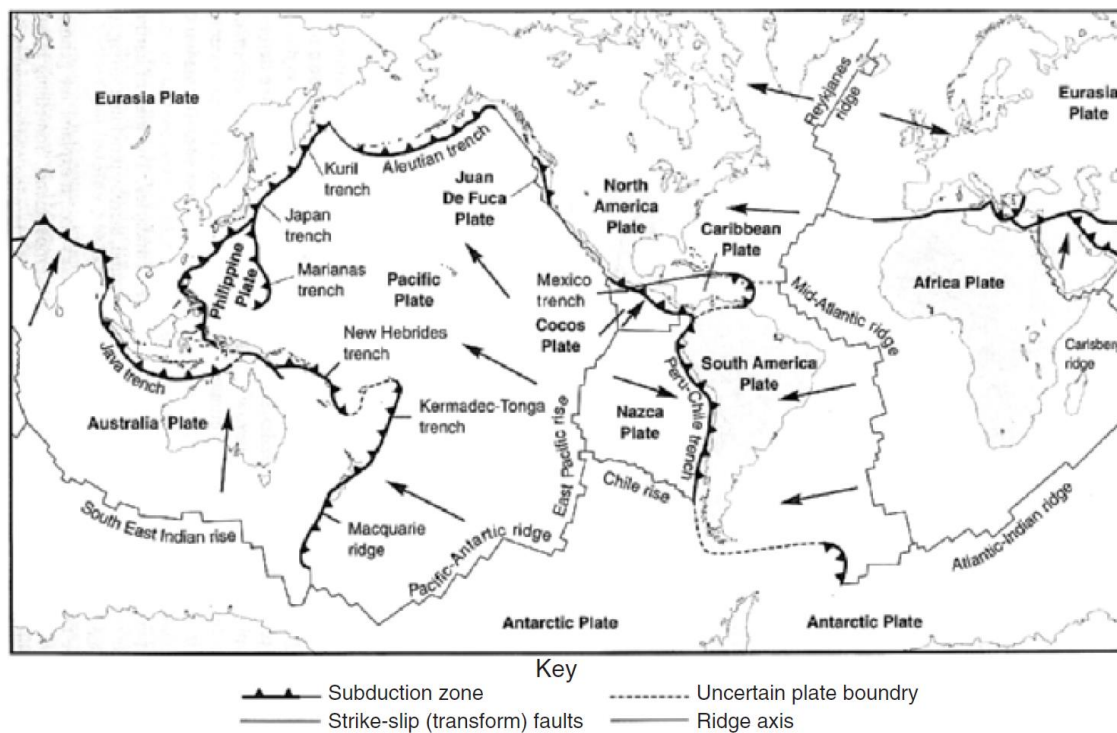


Figure 11 The major tectonic plates, mid-oceanic ridges, trenches and transformation faults of the earth (Fowler 1990, reproduced from Day,2002)

### 5.2 Plate Boundaries

In general, the plate boundaries may be classified in divergent, convergent and transform boundaries (Day 2002). As indicated by its names, divergent boundaries tend to separate from each other whilst convergent boundaries collide. Transform boundaries

name deformation mechanisms where the plate movement is essentially parallel to the fault without destruction or built up of crust material.

Kamalesh (2008) states that divergent boundaries tend to produce earthquakes smaller than magnitude 8 whilst transform boundaries produce shallow earthquakes not exceeding magnitude 8.5. Furthermore he points out that the world's largest earthquakes result from compressional boundaries exceeding magnitude 9, resulting from brittle failure of the sub-ducting zone.

Pacheco and Sykes (1992) define more precisely that the largest earthquakes (in terms of released seismic energy) are estimated to result from oceanic – oceanic subduction zone plate boundaries.

Figure 12 and Figure 13 show illustrations of divergent boundaries. Figure 14, Figure 15 and Figure 16 show illustrations of convergent boundaries.

Table 2 summarizes the three tectonic plate boundaries, the related types of earthquakes and exemplary fault names (Day 2002). Table 2 in combination with Figure 12 to Figure 16, provide a comprehensive insight to plate tectonics and causative mechanisms triggering earthquake events.

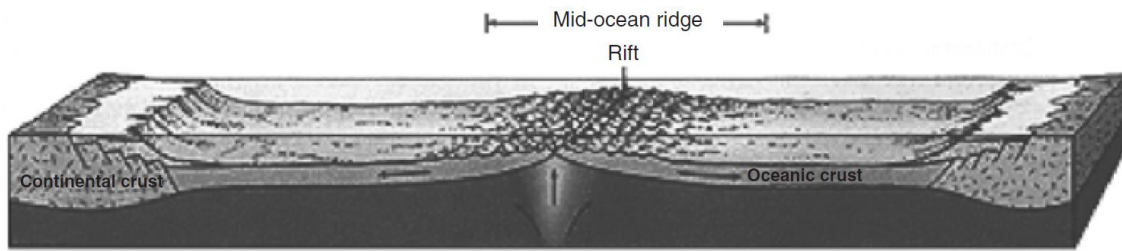
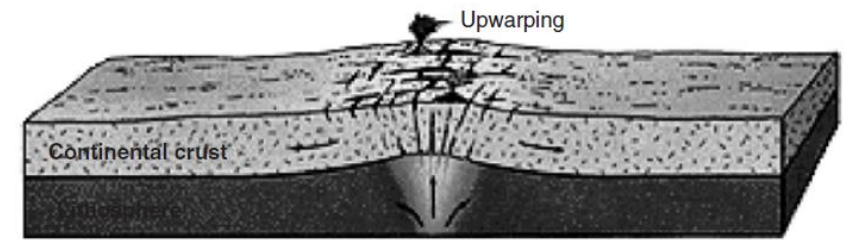
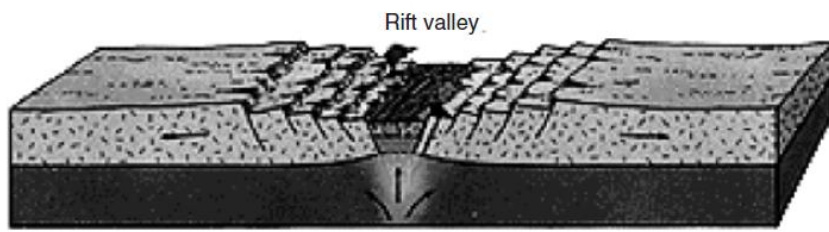


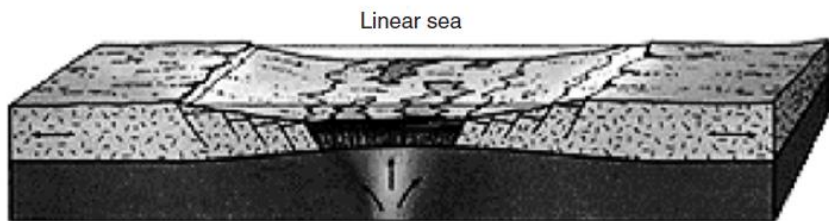
Figure 12 Seafloor spreading, divergent boundary (USGS 2000)



A.



B.



C.

Figure 13 Development of a rift valley, divergent boundary (USGS 2000)



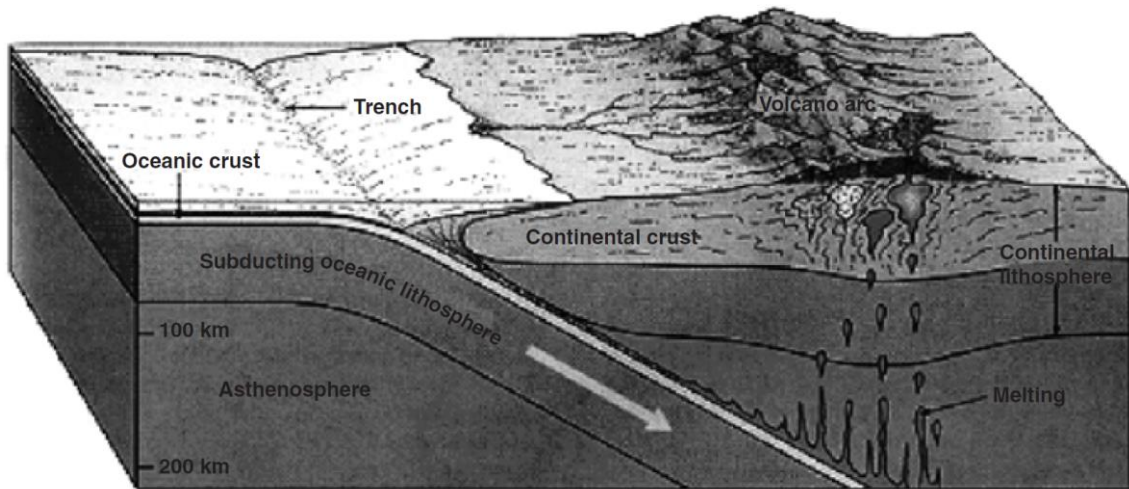


Figure 14 Oceanic-continental subduction zone, convergent boundary (USGS 2000)

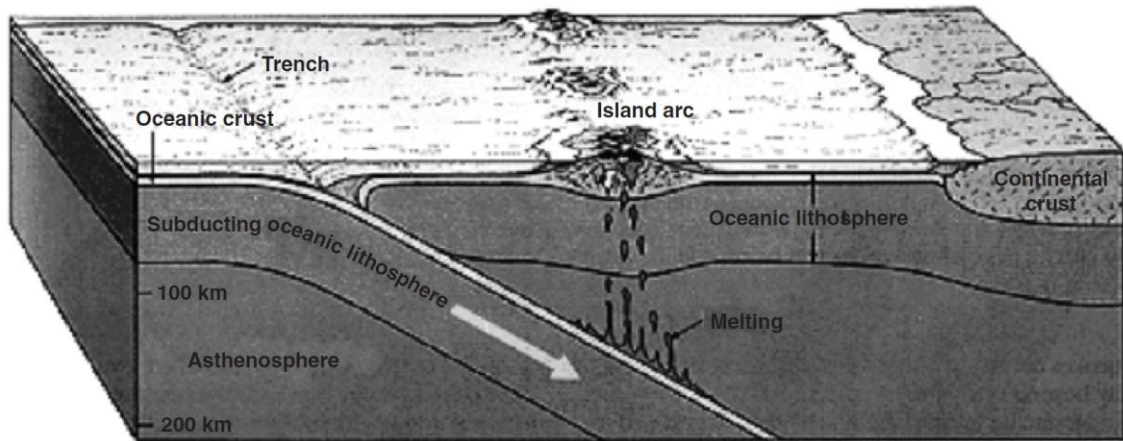


Figure 15 Oceanic-oceanic subduction zone, convergent boundary (USGS 2000)

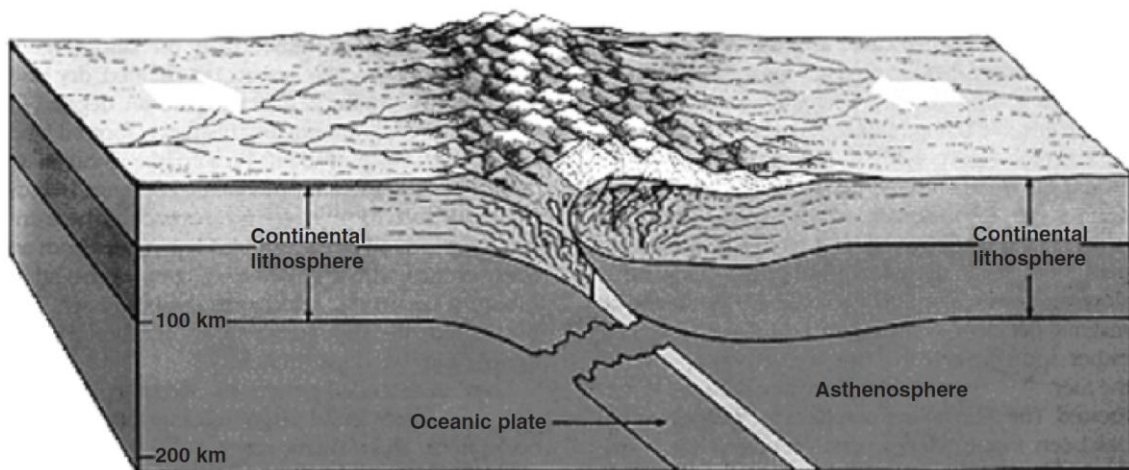


Figure 16 Continental-continental subduction zone, convergent boundary (USGS 2000)

Plate boundary type	Type of plate movement	Categories	Types of earthquakes	Examples
Divergent boundary	Relative movement of the two plates is away from each other	Sea floor spreading (Figure 12)	Earthquakes on spreading ridges are limited to the ridge crest, where new crust is being formed. These earthquakes tend to be relatively small and occur at shallow depths.	Mid-Atlantic ridge
		Continental rift valley (Figure 13)	Earthquakes generated along normal faults in the rift valley.	East African rift
Convergent boundary	Relative movement of the two plates is towards each other	Oceanic-continental subduction zone (Figure 14)	<ol style="list-style-type: none"> <li>1.) Shallow interplate thrust events caused by failure of the interface between the down-going plate and the overriding plate.</li> <li>2.) Shallow earthquakes caused by deformation within the upper plate.</li> <li>3.) Earthquakes at depths of 40 to 700 km within the down-going plate.</li> <li>4.) Earthquakes that are seaward of the trench, caused mainly by the flexing of the down-going plate, but also by compression of the plate.</li> </ol>	Peru – Chile trench
		Oceanic-oceanic subduction zone (Figure 15)		Aleutian Island chain
		Continental-continental collision zone (Figure 16)	Earthquakes generated at the collision zone, such as at reverse faults and thrust faults.	Himalaya Mountains
Transform boundary	Plates slide past each other without the construction or destruction of the earth's crust.	Strike-slip fault zone	Earthquakes often generated on strike – slip faults.	San Andreas fault

**Table 2 Plate boundary types, related typical earthquake types and exemplarily faults (Day 2002)**

### 5.3 Fault Types

Day 2002 summarizes: “A fault is defined as a fracture or a zone of fractures in rock along which displacement has occurred. The fault length can be defined as the total length of the fault or fault zone. The fault length could also be associated with a specific earthquake, in which case it would be defined as the actual rupture length along a fault or fault zone. The rupture length could be determined as the distance of observed surface rupture. In order to understand the terminology associated with faults, the terms “strike” and “dip” must be defined. The “strike” of a fault plane is the azimuth of a horizontal line drawn on the fault plane. The dip is measured in a direction perpendicular to the strike and is the angle between the inclined fault plane and a horizontal plane. “

Kamalesh (2008) states that the majority of earthquakes and active faulting occurs on tectonic plate boundaries, however it is not restricted to, as active faults are found in the middle of plates too. Furthermore the mechanism of brittle failure is restricted to the upper top 10 to 15 km of the earth’s crust. During an earthquake only a localized part of the fault is involved in the rupture. The total rupture area is determined from aftershocks.

According to Day 2002, faults may be classified depending on the residual deformation and offset characteristics as follows:

- **Strike-Slip Fault:** *fault on which the movement is parallel to the strike of the fault. A strike-slip fault is illustrated in Figure 17.*
- **Transform Fault:** *A fault that is located at a transform boundary. Yeats et al. (1997) define a transform fault as a strike-slip fault of plate-boundary dimensions that transforms into another plate-boundary structure at its terminus.*
- **Normal Fault:** *Figure 18 illustrates a normal fault. The “hangingwall” is defined as the overlying side of a nonvertical fault. Thus, in Figure 18, the “hangingwall” block is that part of the ground on the right side of the fault and the “footwall”*

*block is that part of the ground on the left side of the fault. A normal fault would be defined as a fault where the hanging wall block has moved downward with respect to the footwall block.*

- **Reverse Fault:** *Figure 19 illustrates a reverse fault. A reverse fault would be defined as a fault where the hanging wall block has moved upward with respect to the footwall block.*
- **Thrust Fault:** *A thrust fault is defined as a reverse fault where the dip is less than or equal to 45°.*
- **Blind Fault:** *A blind fault is defined as a fault that has never extended upward to the ground surface. Blind faults often terminate in the upward region of an anticline.*
- **Blind Thrust Fault:** *A blind reverse fault where the dip is less than or equal to 45°.*
- **Longitudinal Step Fault:** *A series of parallel faults. These parallel faults develop when the main fault branches upward into several subsidiary faults.*
- **Dip-Slip Fault:** *A fault which experiences slip only in the direction of its dip, or in other words, the movement is perpendicular to the strike. Thus a fault could be described as a “dip-slip normal fault,” which would indicate that it is a normal fault (see Figure 18) with the slip only in the direction of its dip.*
- **Oblique-Slip Fault:** *A fault which experiences components of slip in both its strike and dip directions. A fault could be described as a “oblique-slip normal fault,” which would indicate that it is a normal fault (see Figure 18) with components of slip in both the strike and dip directions.*

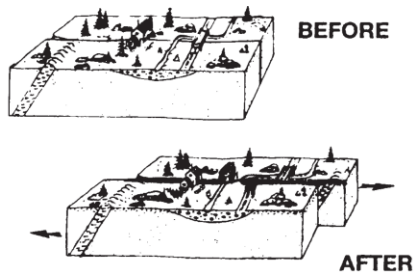


Figure 17 Strike – slip fault (Namson and Davis 1988)

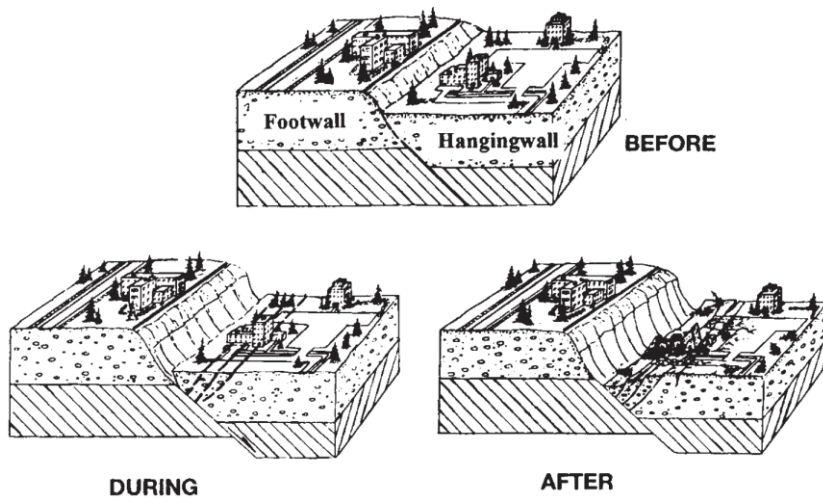


Figure 18 Normal fault (Namson and Davis 1988, reproduced from Day 2002)

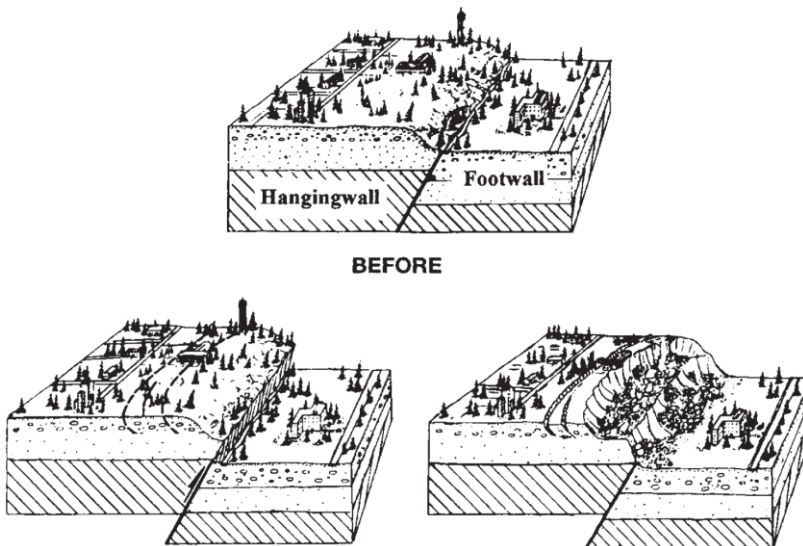


Figure 19 Reverse fault (Namson and Davis 1988, reproduced from Day 2002)

## 5.4 Hypocenter - Epicenter

Figure 20 illustrates the commonly used phrases epicenter and hypocenter. Hypocenter is the point on the fault surface where the earthquake initiates. Epicenter is the point where a vertical axis to earth center penetrates the surface (Kamalesh 2008).

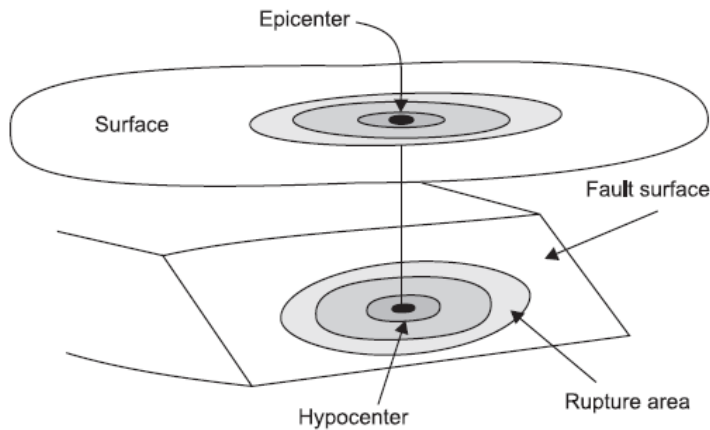


Figure 20 Illustration of hypocenter and epicenter of an earthquake (Penn n.d., reproduced from Kamalesh 2008)

## 5.5 Earthquake Statistics

Table 3 shows the frequency of earthquake occurrence worldwide (USGS 2000). It can be seen that an earthquake having a magnitude larger than 8 can be expected to occur once per year whereas magnitudes of 7 to 7.9 can be expected to occur 15 times per year (worldwide). This shall be stated in contrast to the limited strong motion records of dams if having in mind that many rivers have developed along planes weakened by faults.

Table 4 shows a ranking of the 5 largest earthquakes from 1900 to 2014. It shows that the catastrophic earthquakes from 2004 and 2011 rank place 3 and 4 (ranked by moment magnitude).

Magnitude	Average annularity
8 and higher	1
7 - 7.9	15
6 - 6.9	134
5 - 5.9	1319
4 - 4.9	13000 (estimated)
3 - 3.9	130000 (estimated)
2 - 2.9	1300000 (estimated)

**Table 3 Frequency of earthquake occurrence worldwide (USGS 2000)**

Ranking	Location	Year	Moment magnitude Mw
1	Chile	1960	9.5
2	Alaska	1964	9.2
3	Indonesia - Thailand	2004	9.1
4	Japan	2011	9.0
5	Russia	1952	9.0

**Table 4 Ranking of the 5 largest earthquakes from 1900 to 2014, (USGS 2014)**

Table 5 shows a helpful but rough correlation of important earthquake parameters as the local magnitude  $M_L$ , peak ground acceleration, ground shaking duration and modified Mercalli intensity scale for near fault / rupture locations (reproduced from Day 2002). For practical uses, this table is important as it provides a general trend for judging seismic design values from site specific hazard reports.

The magnitude of earthquakes and hence the damage potential increase with rupture area. Table 6 shows a correlation of magnitude and rupture area.

Local magnitude $M_L$	Typical peak ground acceleration $a_{max}$ near the vicinity of the fault rupture	Typical duration of ground shaking near the vicinity of the fault rupture	Modified Mercalli intensity level near the vicinity of the fault rupture
$\leq 2$	-	-	1-2
3	-	-	3
4	-	-	4-5
5	0.09g	2s	5-6
6	0.22g	12s	7-9
7	0.37g	24s	9-10
$\geq 8$	$\geq 0.50g$	$\geq 34s$	11-12

**Table 5 Approximate correlations of descriptive earthquake parameters (reproduced from Day 2002)**

Magnitude	Fault dimensions (length x depth, in km)
4.0	1.2 x 1.2
5.0	3.3 x 3.3
6.0	10 x 10
6.5	16 x 16, 25 x 10
7.0	40 x 20, 50 x 15
7.5	140 x 15, 100 x 20, 72 x 30, 50 x 40, 45 x 45
8.0	300 x 20, 200 x 30, 150 x 40, 125 x 50

Table 6 Correlation of rupture area and magnitude (Penn n.d., reproduced from Kamalesh 2008)

## 5.6 Epicentral Distance - Acceleration at Dam Base

The destructive energy is biggest in the closer vicinity to the hypocenter (or the epicenter). Due to damping effects, the propagating energy reduces with increasing distance to the hypocenter.

Sommerville (n.d.) states: '*Near-fault ground motions are different from ordinary ground motions in that they often contain strong coherent dynamic long period pulses and permanent ground displacements. The dynamic motions are dominated by a large long period pulse of motion that occurs on the horizontal component perpendicular to the strike of the fault, caused by rupture directivity effects.*'

Matsumoto (2010) published a formula relating fault distance to observed horizontal pga at Japanese dam sites. Figure 21 plots the formulas basic data to show its wide scatter.

The wide scatter is clear if having in mind the shear velocities of various types of rocks. However, if judging ground motions such a formula is an important Engineering tool.

$$PGA = \frac{k}{(R+\Delta)^b} \cdot M_J \quad [2]$$

PGA = horizontal peak ground acceleration in gals (= cm/s<sup>2</sup>)

k = 1.18 x 10<sup>5</sup> for dam foundations

Δ = 20 km

b = 2.0

M<sub>w</sub> = 0.78M<sub>J</sub> + 1.08

M<sub>w</sub> = Moment magnitude



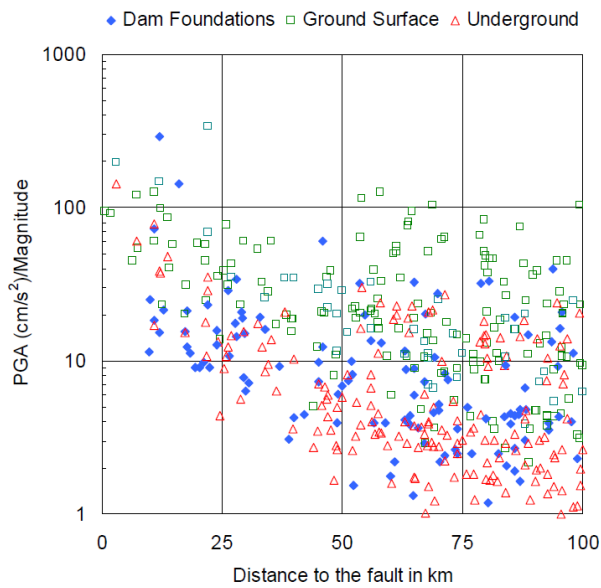


**Figure 21 Attenuation of horizontal PGA component vs. fault distance**

## 5.7 Seismic Waves

During an earthquake, the released energy propagates along the earth's crust and its interior. Seismic waves may be separated by their particle motion, their propagation velocity in various media and their ability to propagate in fluids. They are classified in P-waves (compressional, primary, longitudinal), S-waves (shear, secondary, transvers), L-waves (love, surface, long waves) and R-waves (Rayleigh, surface, long). Detailed information about wave characteristic can be found in Day (2002) or Kamalesh (2008).

Day (2002) states that it is typically the surface waves highly contributing to the peak ground acceleration at a specific site. However, he does also point out that distinguishing the different wave types is not of engineering interest as the maximum ground acceleration is a combination of all wave types and forms.

Figure 22 shows a typical strong motion record from a digital accelerograph. Typically it's the P-waves arriving at the instrument triggering the storage of the data.

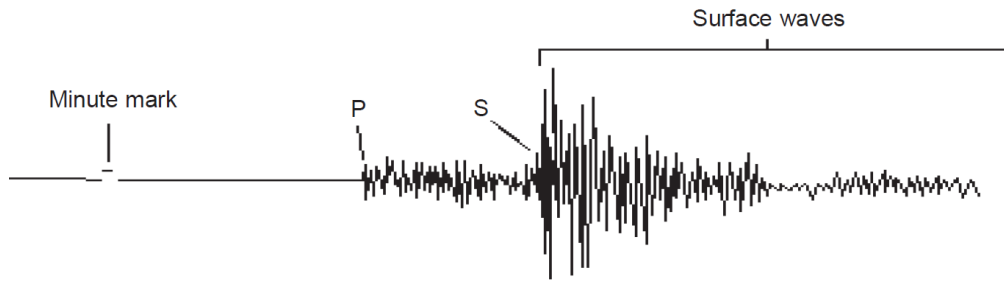


Figure 22 Digital strong motion record (Michigan Tech n.d., reproduced from Kamalesh 2008)

## 5.8 Earthquake magnitude

The destructive energy of a specific earthquake event needs to be classified and ranked. This classification is mainly done by specifying earthquake magnitudes. Earthquake magnitudes are measured and described by use of varying systems. This is to a large extent due to the fact that these systems were developed with varying cultural background. Nowadays the word is connected and the engineer very often has to convert magnitudes from one system to the other. It is not the purpose of this chapter to plot the varying ranking systems and their theoretical background. The aim was to enable fast and easy magnitude conversion within this document for practical use.

Figure 23 plots the approximate relation between moment magnitude ( $M_W$ ) and other magnitude scales whereas  $M_L$  represents the local magnitude,  $m_b$  = the short period body wave magnitude scale,  $m_B$  = the long period body wave magnitude scale,  $M_{JMA}$  = the Japan meteorological magnitude scale and finally  $M_s$ , representing the surface wave magnitude scale (Heaton et al. 1982).

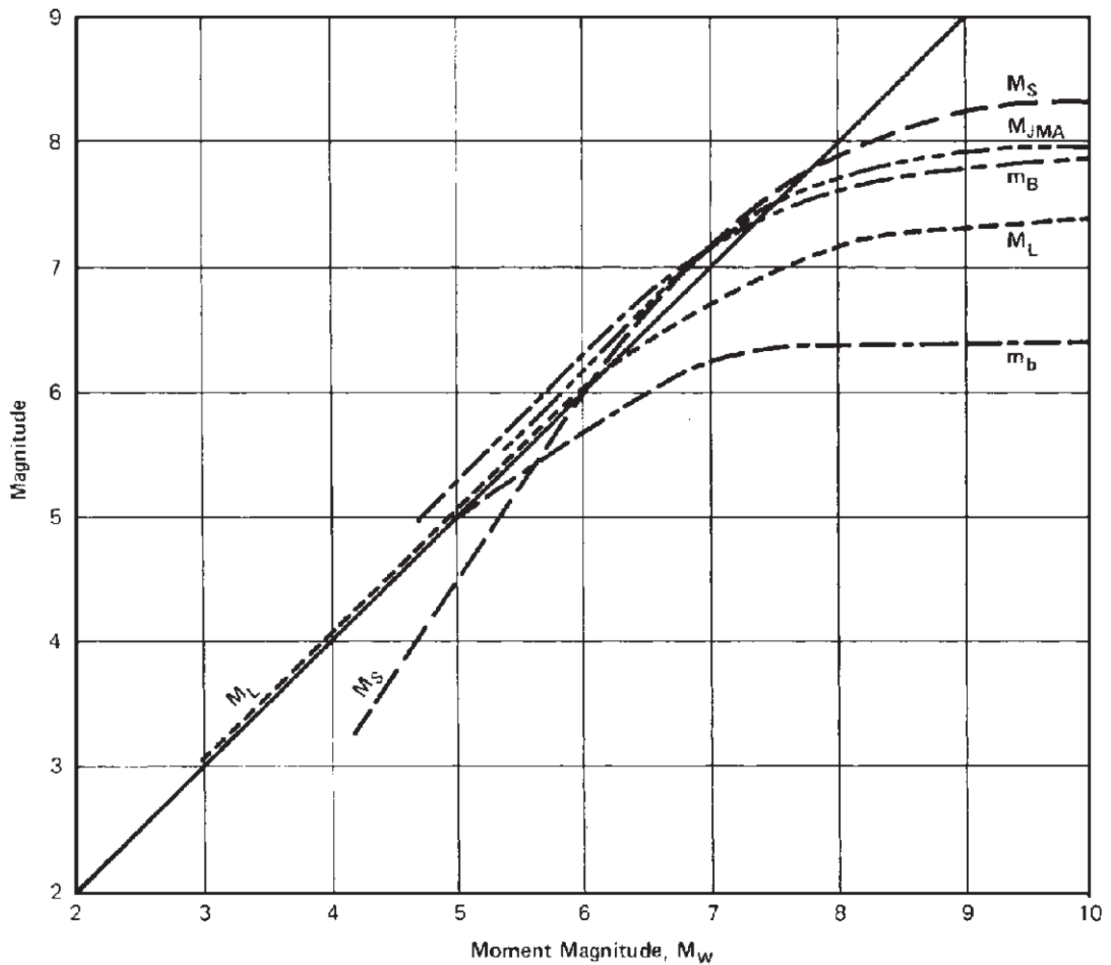


Figure 23 Approximate relationship between moment magnitude and other magnitude scales (developed by Heaton et al. 1982, reproduced from Day 2002)

## 5.9 Strong Motion Recording and Processing

Earthquakes are recorded by either analogue or digital accelerographs. The majority of the data available now is recorded by digital accelerometers. However especially in case of dam engineering a lot of recorded strong motions originate from dams in operation for more than 50 years and hence analogue data is quite usual in that field. Figure 24 and Figure 25 show digital and analogue accelerographs.

Ambraseys et al. (2002) states that an analogue accelerometer records: ‘... the ground motion in the form of either a photographic trace on film or paper, or a scratch trace on waxed paper. They do not record all the time but are triggered by a minimum level

*of ground acceleration, usually of the order of 0.005 to 0.01g in the vertical direction. Therefore they do not record the entire ground motion, which occurred during the earthquake.’ Whilst digital accelerometers: ‘... record on reusable media (magnetic or solid state) and so are able to record continuously. If the threshold trigger level is exceeded then the record is retained together with the ground motion which occurred in the seconds before the instrument triggered (pre-event time). Therefore they record the entire ground motion which occurred during the earthquake as long as the post-event time is sufficient.’*

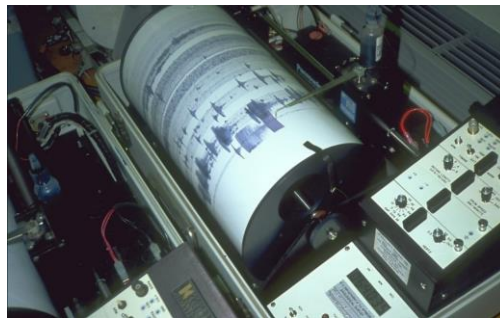


**Figure 24 Digital accelerograph (Mateo 2009)      Figure 25 Analogue accelerograph (Dadisp 2014)**

Records of both, analogue and digital recorders are prone to errors and hence have to be corrected to fit as input for engineering purposes. Such corrections involve simple exclusion of unrealistic parts as backward time loops or filtering processes in the high and low frequency range as well as base line corrections. Correction methods vary largely and correction technics especially in case of filtering processes are subject to harsh discussions within the international literature. However, it is commonly agreed that corrections need to be made and it seems that filtering in the high frequency range enjoy higher popularity than filtering in the low frequency range.

Ambraseys et al. (2002) sum up typical errors in strong motion records:

***Instrumental errors***

- *Transducer distortions of amplitude and phase*
- *Imperfections of the transducer design: most existing transducers are not true single-degree-of-freedom (SDOF) systems*
- *Transverse play of the recording paper/film causing variations up to several*

*millimeters*

- *Non-uniform velocity of the record-driving mechanism*
- *Non-uniform time marks*
- *Misalignment of the transducers*
- *Clipping: if sensitivity setting of instrument is too high, the largest peaks may go off scale*
- *Variable trace thickness: influences accuracy of digitisation*
- *Sensitivity calibration*
- *Drift: over long time intervals, temperature and humidity effects can cause drift but for periods of minutes this is not important*
- *Instrument slip*

### **Photographic processing errors**

- *Warping of film negatives caused by chemical processing and ageing*
- *Errors from optical enlargement during printing of film negatives resulting from lens imperfection and non-parallelism of the planes of original film and projected image*
- *Poisson effect in film processing because during film copying, the original and copy are held together under longitudinal tension*

### **Digitisation errors**

- *Digitisation rate: the greater the number of digitised points, the better the accuracy with which the digital data approximates the continuous function of the accelerogram*
- *Inadequate resolution of the digitising equipment*
- *Low-pass filtering effects of optical-mechanical digitisation because digitisation approximates a continuous function by a sequence of discrete points*

### **Systematic and random digitisation errors**

- *Imperfections in the mechanical traverse mechanism of the digitiser creates systematic long period errors*
- *Human "imperfection" introduces random intermediate and high frequency errors*
- *Baseline shifts (translations and/or rotations relative to the digitiser axes) during digitisation can be considered as random long period errors*

Javelaud et al. (2011) adds an further error found in recorded strong ground motions that needs to be corrected. Residual tilt of the instrument results in permanent acceleration (due to gravity) at the end of the recorded ground motion of both horizontal accelerometers.

Ambraseys et al. (2002) point out that filtering in the high frequency range ( $\geq 20$  Hz) and filtering in the low frequency range ( $\leq 5$  Hz) does not affect the periods of normal engineering interest (0.1 to 2 sec).

Baseline correction needs to be done especially in case of analogue records as the start acceleration and sometimes the final acceleration are not included in the recorded ground motion. However, Sommerville (n.d.) points out that especially in case of design of near fault structures, the residual static displacement resulting from double integration of the accelerogram is of highest interest.

There are several methods used for baseline correction. They have in common that the residual displacement at the end of the record is zeroed.

### **5.10 Accelerograms –Effects and Application in Dam Engineering**

Recorded ground motions are ideal input motion for time history analysis of civil structures. If the faults mechanisms and the related magnitude in respect to the design recurrence periods are known (or estimated) from each fault, civil structures may be calculated by a set of recorded accelerograms that are scaled to design pga. In fact the character of earthquake motions and its descriptive engineering parameters as number of peaks close to pga, duration and envelope shape are randomly distributed itself and hence the above mentioned approach is not accepted by all engineers. In this case artificially generated earthquakes strictly following prescribed design spectra may be used alternatively. This approach guaranties that the periods of the artificial ground motions meet a specific structure's natural periods and excitation at natural period lasts long enough.

#### **5.10.1.1 Accurate Modeling of Artificial Input Motions**

EN 1998-1 (2004, chapter 3.2.3.1.2) provides detailed advises for artificial time history generation for a reoccurrence period of 475 years. Generated time histories have to be in accordance with the prescribed design spectrum varying with a sites specific foundation soil type (including 5% viscous damping). Further demands for artificial time histories are calculation with a minimum of three independent sets of artificial ground motion, the average of the three maximum ground accelerations shall not undercut the prescribed maximum ground acceleration fixed in accordance to the site specific foundation soils characteristics. Additionally, the average minimum spectral ordinate of a set of three artificial ground motions shall not undercut 90% of the prescribed design spectrum within a range of 0.2 to 2 times the structures natural period.

Hawaii Dam Safety Guidelines (2004) claim the maximum time steps to be less or equal to 0.02 sec for dynamic dam analysis making use of artificial or recorded ground motions.

The authors of ICOLD (2010) state: *'Embankment dams have fundamental periods of vibration that typically range between 0.5 and 1.5 s and, for use in finite element analyses, a digitization interval longer than that recommended for concrete dams may be sufficient; time-steps up to 0.05 s have been shown to be quite acceptable in some cases. However, if an explicit formulation of the equations of motion is used, such as for nonlinear finite difference analyses, an extremely short digitization time-step is required (typically 0.001 s, or less)'*.

In general, the duration of an earthquake is of highest importance especially in case of embankment dams and the calculation of crest settlements.

EN 1998-1 specifies the duration of artificially generated time histories. The duration has to fit the design reoccurrence period and hence has to increase with design magnitude. Table 5 provides help for selecting adequate durations in respect to magnitude. If additional information is not present, the claimed minimum duration is 10 seconds. 10 seconds in this case are related to a design reoccurrence period of 475 years, which is obviously related to a Magnitude 6 event according to Table 5).

According to Bolt (1973) the most important part of a time history is that between the first and the last acceleration peak of 0.05g with special focus on frequencies exceeding 2 Hz. He termed this part “bracketed”. Table 7 summarizes Bolt’s findings for the relation of bracketed duration and Richter magnitude.

Mag Δ	5.5	6.0	6.5	7.0	7.5	8.0	8.5
10	8	12	19	26	31	34	35
25	4	9	15	24	28	30	32
50	2	3	10	22	26	28	29
75	1	1	5	10	14	16	17
100	0	0	1	4	5	6	7
125	0	0	1	2	2	3	3
150	0	0	0	1	2	2	3
175	0	0	0	0	1	2	2
200	0	0	0	0	0	1	2

Table 7 Bracketed duration [sec] vs. earthquake magnitude (Bolt 1973)

Chang and Krinitzsky (1977) developed more specific relations of fault mechanism, site foundation conditions, epicentral distance and magnitude (Richter magnitude). The findings are too extensive to be plotted in total, hence Figure 26 plots an exemplary extract for M6.5 to M7.5 for hard sites and events having a focal depth smaller than 19 km.

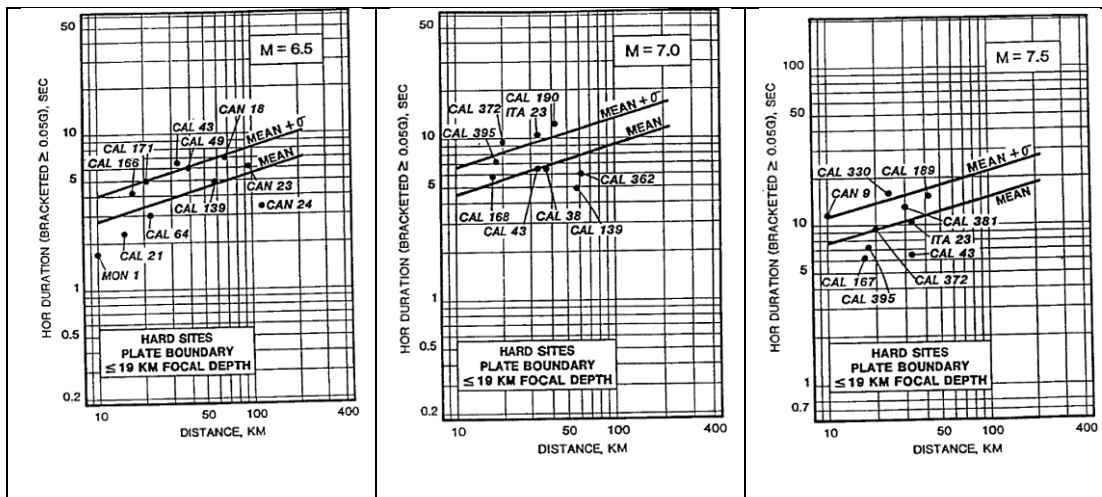


Figure 26 Bracketed duration vs. epicentral distance and magnitude for a specific fault mechanism (Chang and Krinitzsky 1977)



### 5.10.1.2 Peak Ground Acceleration – Predominant vs. Natural Period

The recorded accelerations of Aratozawa dam site shall be discussed as an exemplary case history (Midorikawa et al. n.d.). Figure 27 plots the recorded base acceleration in North-South, East-West and Up-Down direction at Aratozawa dam site during Iwate-Miyagi earthquake dated June 14<sup>th</sup> 2008. The intensity at dam site was judged to be magnitude 6.0  $M_j$ . The maximum recorded peak ground acceleration slightly exceeded 1g in UD direction (instrument limit = 1.024g). The recorded horizontal peak ground accelerations resulted in 0.87g and 0.81g in NS and EW direction.

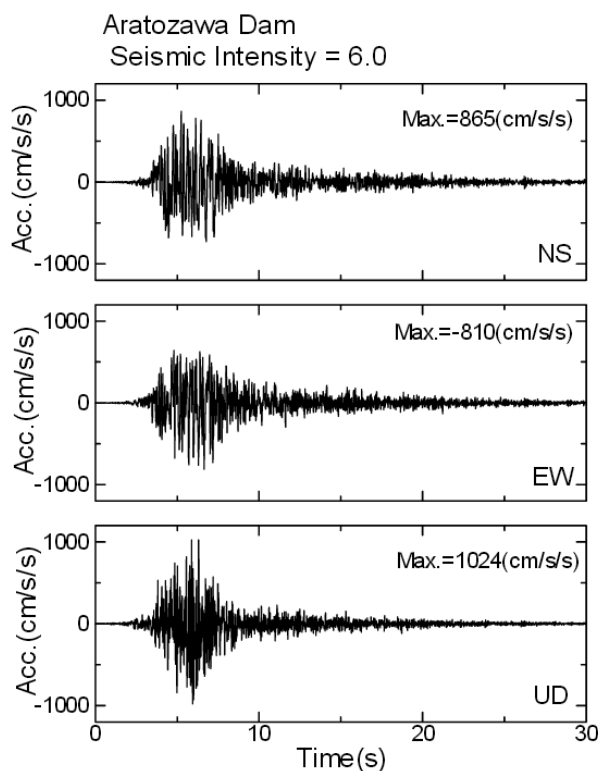


Figure 27 Base accelerations recorded at Aratozawa dam site during Iwate-Miyagi earthquake 14.06.2008 (Ohmachi 2011)

Ohmachi (2011) evaluated the seismic behavior of Aratozawa dam in detail. He stated that single peaks of the vertical acceleration recorded within the dam's base gallery exceeded the instrument limits, but this will not have an important influence on the final accuracy reached. Ohmachi has evaluated the spectral ratios of crest record to gallery record for three earthquakes observed in 1996 and Iwate-Miyagi earthquake. Figure 28 shows his findings in stream axis direction. The natural periods of Aratozawa dam for the three shocks in 1996 result in 0.32 to 0.35 sec. The natural period during

the main shock of Iwate-Miyagi earthquake results in 0.65 sec. Hence the natural period has significantly elongated during the main shock which is a result of the distinctive nonlinear behavior of the dam. This effect is also reported by Gazetas and Dakoulas (1991) from results of numerical analysis.

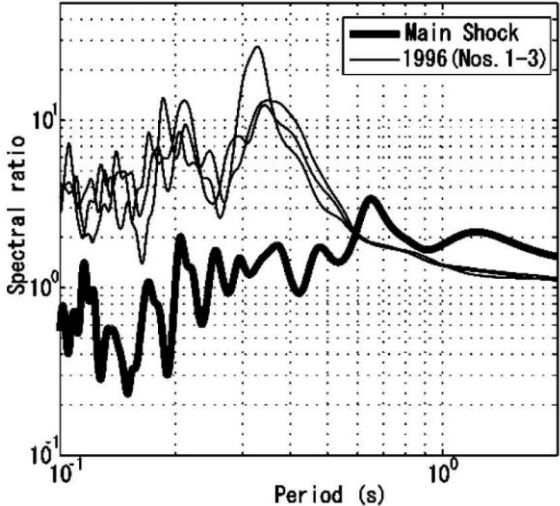


Figure 28 Crest to gallery spectral ratios in stream axis (Ohmachi 2011)

Ohmachi (2011) furthermore stepwise calculated the spectral ratios of crest to gallery record in time steps of 5.12 sec. Figure 29 shows the resulting predominant periods within the dam during the Iwate-Miyagi earthquake. He states that the predominant periods were close to the dam’s natural period and suddenly elongated when the intense shaking arrived at approximately 4 sec.

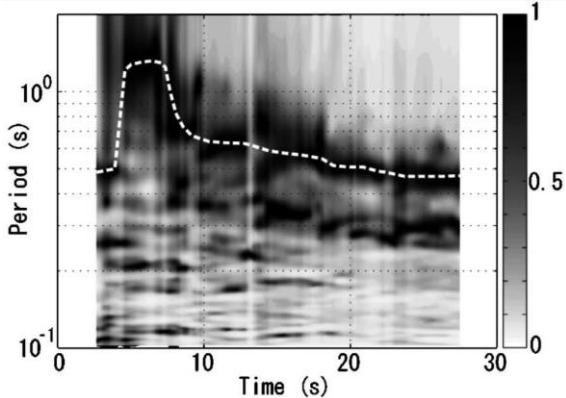


Figure 29 Running spectral ratios from crest to gallery records in stream direction (Ohmachi 2011)



## **6 Factors affecting the Dynamic Behavior of Embankments**

### **6.1 Earthquake induced failure modes**

In general, seismic ground acceleration might contribute to the following failure modes of embankment dams. The below mentioned failure types refer to case histories and theoretical failure modes (Wieland n.d.; ICOLD 1995 and 2011; USSD 2014)

#### **Breach of the dam due to overtopping resulting from crest settlement**

- Due to loss of shear strength, liquefaction of embankment or foundation
- Due to reduction of shear strength, buildup of excess pore water pressures within the embankment soils
- Due to slumping of the crest due to dynamic compaction of embankment material
- Due to reservoir landslides and tsunami wave
- Due to inoperable spilling capacities
- Due to massive rockfall, reducing the crest height locally

#### **Piping and backward erosion**

- Due to hydraulic cracking of cohesive soils
- Due to sheared filters protecting core material
- Through cracks resulting from differential settlements along dam axis or stream direction or close to the abutments or concrete structures
- Rockfall on impermeable surface linings close to the crest in shallow water
- Differential movements in faults within the dam base

## 6.2 Valley Shape

Gazetas and Dakoulas (1991) performed 2D and 3D numerical analysis and investigated the effect of narrow canyons on the dynamic behavior of rockfill dams. They conclude that a narrow valley approximately doubles the crest acceleration compared to a dam located in a wide valley.

## 6.3 Foundation Characteristics

### 6.3.1.1 Rock

The shear velocity respectively the shear modulus of the foundation significantly influences the dynamic behavior of rockfill dams. Figure 30 plots the findings of Gazetas and Dakoulas (1991). It shows the amplification of a dam located in a valley with a crest length to dam height ratio of 3 for three different combinations of shear wave velocity ratios ( $V_{\text{canyon}} / V_{\text{dam}} = 3, 10$  and  $\infty$ ). They point out that the assumption of a rigid base is conservative in 3D calculations.

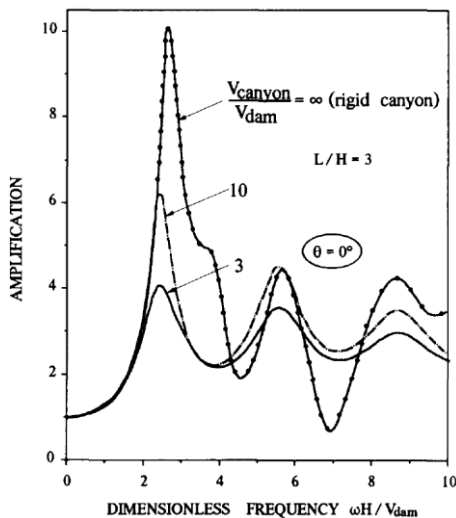


Figure 30 Mid-crest amplification for three different  $V_{\text{dam}} / V_{\text{Base}}$  ratios

### **6.3.1.2 Alluvial Layers**

Gazetas and Dakoulas (1991) discuss the effect of alluvial foundations on embankment dams and point out that their effect is closely related to other factors as valley shape and dam height. Whilst shallow alluvial layers, not prone to liquefaction have a limited effect on rockfill dams in narrow valleys, the influence in other combinations may be guiding. In general alluvial fillings may significantly amplify the base rock's peak ground acceleration at their surface (e.g. Mexico City earthquake 1985). This is of special interest for homogeneous embankment dams (typical liquefaction failure modulus) but also affecting the behavior of high rockfill dams in wide valleys.

## **6.4 Stress-Deformation Characteristics of Fill Materials**

### **6.4.1.1 Particle Shape, Gradation and Shear Strength**

Marshal (1973) has performed several large scale triaxial tests on rockfill material. He concluded that the particle shape of the grains significantly contributes to the stress-deformation characteristics of rockfill. Rounded particles for example will result in higher deformation moduli compared to angular grains. The stress in edges of angular particles concentrates and the edges break down, thus resulting in an overall lower modulus compared to angular shaped grains (e.g. alluvial sand gravel fill).

The gradation of the rockfill material influences the stress-deformation behavior. Uniformly graded rockfill results in a reduced number of particle contacts and a high pore volume (Marshal 1973). Consequently particle breakage is governing the deformation behavior when stresses exceed a certain level.

Douglas (2002) investigated the shear strength of rockfill materials and concluded that it is highly dependent on the uniaxial compression strength of the rock it originates from. However other factors as grain shape, grain diameter, gradation and especially compaction do also influence the shear strength to large extends. In general, the shear strength increases with increasing grain size, angularity and compaction, whilst it decreases with increasing uniformity and decreasing intact rock strength.

### 6.4.1.2 Compaction Effort

Compaction of embankment dams is mainly connected to developments in the field of compactor equipment. Despite other influences like design practice and acceptance of new developments in design the compaction effort is mainly related to the construction period of a dam. Dumped rockfill embankments or rockfill dumping in high lifts was common practice in the first half of the 19<sup>th</sup> century whilst compaction in medium to small lifts is state of the art now. Hence the construction method does not only effect the embankments settlement at end of construction and the creeping settlement, the seismically induced settlement is also highly influenced. All three above mentioned settlements reduce with increase of compaction effort and decrease of layer thickness.

Okamoto (2004) relates construction method and completed year to observed settlements during the event of ground shaking. Obviously, dumped embankments settle in case of low amplitude acceleration, whilst recently constructed dams suffered little settlements even they were intensively shaken.

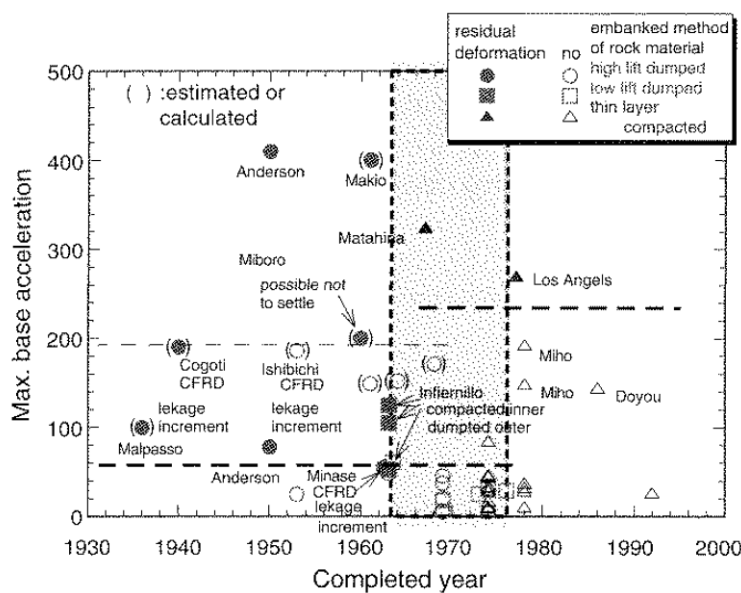


Figure 31 Construction method vs. base acceleration and occurrence of crest settlement (Okamoto 2004)

This effect is mainly resulting from high particle point loads. Those increase with maximum grain size and uniformity coefficient. Dumped rockfill tends to segregate during placement and maximum grain sizes that are related to transportation capacity only.

Hence, the particle contact loads are comparatively high and significant particle breakage is the consequence even in case of high strength rockfill (Douglas 2002, Marshal 1973, Hall 1963).

The deformation modulus of earthfill is generally more related to overall compaction effort than to grain shape, gradation and shear strength. However, the boundaries between the two terms rockfill and earthfill is transient especially in case of clean sands and gravel mixtures. Hence the influence of grain shape, gradation and shear strength increases with decreasing amount of fine particles.

In general, the shear wave velocity of solid materials increases with increasing density. Hence a high compaction will result in higher shear moduli, which is of special interest in case of CFRD's in narrow valleys.

#### **6.4.1.3 Dilatancy**

Dilatancy has an important effect on dynamic behavior of dams as it is directly related to pore-water pressure buildup under saturated conditions. This is valid for both cohesive and non-cohesive soils. Dilatant soils tend to expand when sheared. Hence a dilatant soil will produce negative (stabilizing) pore water pressures whilst the opposite is the case for compressible soils. Dilatancy is directly related to compaction effort and to potential liquefaction.

#### **6.4.1.4 Deformability and Effects on Dynamic Dam Behavior**

As previously stated particle shape, shear strength, gradation and compaction effort affect the deformability of embankment dams and are linked to each other vice versa. A low deformation modulus is mainly affected by particle strength and particle point loads. High deformability during and at end of construction will result in high creeping settlements of the crest as well as increased residual settlements due to earthquake excitation.



## 6.5 Soil Liquefaction

### 6.5.1 General

Soil liquefaction caused the majority of all embankment dam failures and near failures bound to earthquake excitation. Nearly all seismically induced failures of embankment dams resulted from liquefaction or partial liquefaction. Rural dams, tailing dams and especially hydraulic fill dams are prone to liquefaction failure.

In general one can state that liquefiable soils are saturated soils of low or no cohesion that tend to compact when excited to dynamic motions. During dynamic compaction the grain skeleton densifies and hence transmits loads to the pore water pressure as the pore water cannot dissipate fast enough for whatever reason for. As liquids do not have any shear resistance, the shear resistance is abruptly reduced when the total load from the grain skeleton is transmitted to the pore water. In a state of liquefaction the particle forces (theoretically) reduce to zero. Speaking in terms of Mohr – Coulomb failure criterion, the internal friction angle reduces to 0. The residual shear resistance of liquefied materials is often simulated by use of residual cohesion mainly derived from back-analysis. However, applying residual cohesion is questionable and largely depending in a soil's dilatancy which again is highly dependent in estimated residual deformation.

Boulanger (2007) summarized published data from back calculated residual shear strength of liquefied slopes resulting in a general shear strength (i.e. cohesion) range of 0 to 36 kN/m<sup>2</sup>.

In design practice of new structures, the presence of liquefiable soils has to be excluded by suitable measures taken.

Typical evidences that liquefaction occurred at a specific site are so called sand boils. At local spots, the pressurized (excess) pore water breaks through to the surface spilling up fine particles of the liquefied zone (Rauch 1997).

Commonly cyclic mobility is distinguished from liquefaction in engineering practice (Kamalesh 2008). The term cyclic mobility is used for soils that tend to dilate during

shearing. Although the basic principles of liquefaction are the same for these soils, the overall results are completely different. During cyclic loading the soil is liquefied at first resulting in an abrupt increase of shear strain, as the soil dilates during shearing, the pore pressure decreases and the soil stabilizes. Cyclic mobile slopes tend to move whilst slopes subject to liquefaction collapse.

### 6.5.2 Liquefiable soils

Kamalesh (2008) summarizes: *'Fortunately, areas susceptible to liquefaction can be readily identified and the hazard can often be mitigated. Because of the relative ease of identifying hazardous areas, numerous liquefaction maps have been made by government agencies. Liquefiable sediments are young, loose, water saturated, and well sorted. They are either fine sands or silts. The sediments are seldom older than Holocene, and are usually only present on the modern floodplains of creeks and rivers.'*

Kamalesh (2008) points out 12 factors that govern liquefaction in the field:

- A peak ground acceleration of 0.1g and local site magnitude 5 are reported to be the threshold for potential start of liquefaction.
- Soil deposits deeper than 15m below ground surface are usually not prone to liquefaction. However, experience is needed to judge the proper depth.
- Locations with near surface ground water table are most susceptible.
- Cohesive soils (= slightly cohesive soils) are only susceptible to liquefaction if the following characteristics are present  $d_{15} < 0,005\text{mm}$ , liquid limit  $< 35\%$  and the water content  $> 0.9 \times$  liquid limit. This criterion will be discussed again in chapter 10.4.3 Fujinuma Dam Material parameters and construction details.
- Cohesionless loose soils that show contractive behavior during cyclic shaking are most susceptible to liquefaction.
- Uniformly graded non plastic soils are more susceptible to liquefaction as widely graded soils are, as they tend to form unstable particle arrangements during natural or human placement.
- Soils deposited under water are highly susceptible to liquefaction. Segregation and loose placement under uplift forms unstable particle arrangements.
- The presence of highly permeable wrapping or crossing drainage layers reduces a soils liquefaction potential as excess pore water pressures dissipate rapidly.
- Particle shape affects the liquefaction potential as rounded particles tend to form denser arrangements more easily than angular shaped grains.
- The older a soil the less prone it is to liquefaction. Potential reasons are the higher overburden stresses that force particles to a denser grain skeleton, slight cementation of the grains or simply as they have already been compacted by previous earthquakes of design magnitude.
- A soils liquefaction potential increases with increasing over-consolidation ratio.

- Surcharge from civil construction decreases a soil's potential for liquefaction as the shear stresses are increased in contrast to the original state of the soil. Hence cyclic shear stresses needed for liquefaction reduce in contrast to the original state.

### 6.5.3 Concepts to stabilize liquefiable soils

Kamlesh (2008) summarizes anti-liquefaction measures:

- Compaction of loose material either by dynamic soil compaction, vibrofloating, excavation and backfilling in small compacted lifts or pile compaction.
- Injection of cement grout or other chemical stabilizers.
- Placement of temporary surcharge.
- Drainage by vertical or horizontal gravel drains.

### 6.5.4 Assessment Liquefaction Potential

Seed and Idriss (1971) developed a simplified method to judge if a soil is subject to liquefaction for a given design magnitude by use of standard penetration test results.

In principle liquefaction may be excluded if the factor of safety exceeds 1. Whereas the factor of safety is calculated by dividing the cyclic stress ratio (CSR) via the cyclic resistance ratio (CRR).

$$CSR = 0.65 \cdot r_d \cdot \left(\frac{\sigma_{v0}}{\sigma'_{v0}}\right) \cdot \left(\frac{a_{max}}{g}\right) \quad [3]$$

$$r_d = 1 - 0.012 \cdot z \quad [4]$$

CSR = Cyclic stress ratio [-]

$r_d$  = Correction factor [-]

$z$  = Depth below surface [m]

$a_{max}$  = Maximum site specific acceleration [m/sec<sup>2</sup>]

$g = 9.81$  [m/sec<sup>2</sup>]

$\sigma_{v0}$  = Total vertical overburden stress

$\sigma'_{v0}$  = Effective vertical overburden stress

CRR is taken from Figure 32 and multiplied by a magnitude scaling factor (Figure 33) to adjust the CRR for design magnitudes other than 7.5. Where  $(N_1)_{60}$  is the  $N_{60}$  corrected for overburden pressure.

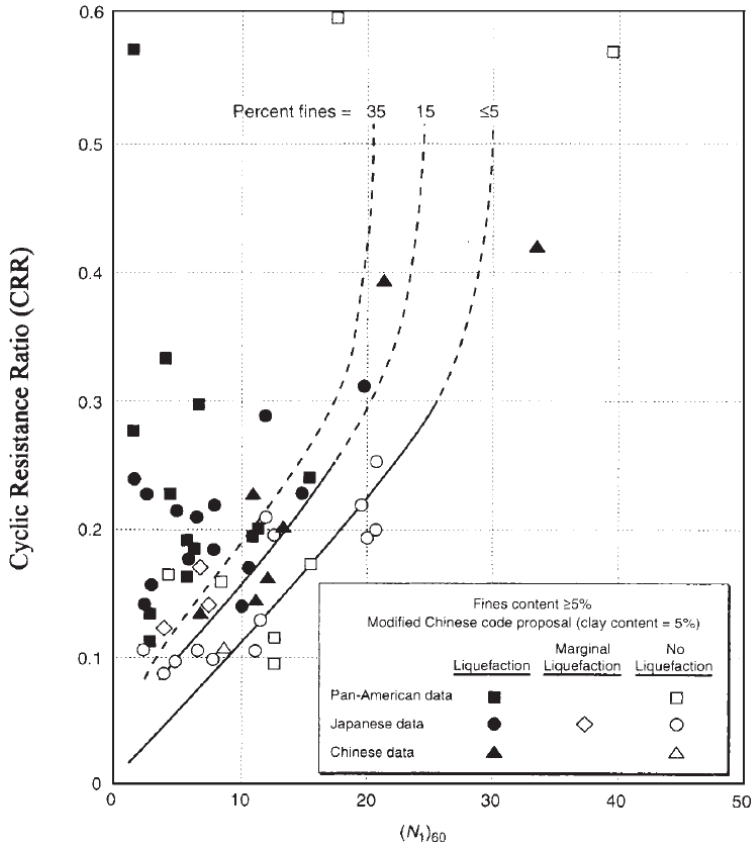


Figure 32 Cyclic resistance ratio based on SPT (Seed et al., 1985, reproduced from Day 2002)

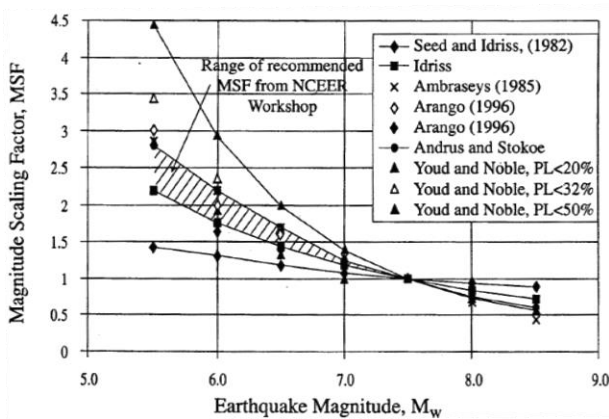


Figure 33 Range of Magnitude scaling factor (Youd and Noble, 1997)

Kamalesh (2008) points out that the above mentioned approach is based on quite a lot of corrections and hence engineering judgment and experience in the field is obligatory for judging a soils susceptibility to liquefaction.

### 6.5.5 Surface Acceleration on Liquefied Soil Deposits

Figure 34 plots seismograph data recorded during Niigata earthquake in 1964 (reproduced from Kramer 1996). Approximately at 6 seconds of recording time, the data drastically changes. It is assumed that this is due to the liquefaction of underlying soil deposits. The recording station was located near buildings that failed due to the loss of bearing capacity as a result of wide spread liquefaction.

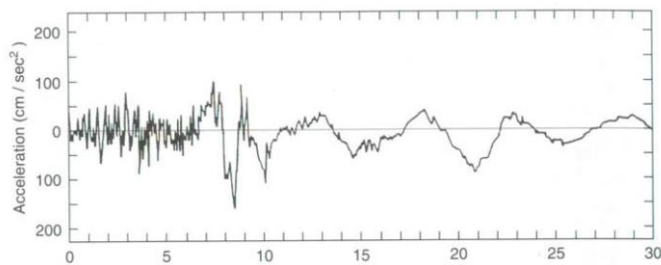


Figure 34 Accelerogram of a station located on fully liquefied soil deposits (reproduced from Kramer, 1996)



## 7 Engineering Parameters of Dams subject to strong ground motion

### 7.1 Natural period of embankment dams

For engineering purposes it is important to know or to localize a structures natural period. In case of earthquake resistant design, this is done to judge if the design earthquake or a specific recorded earthquake contains periods close to the natural period.

Matsumoto (2010) investigated the recorded accelerograms of several Japanese dam sites and plots formulae for rough calculation of a dam's natural period. The formulae foot on recorded data of 32 rockfill and 19 earthfill dams. The natural period was calculated from frequency response functions ratios of the Fourier-amplitude spectra of a pair of accelerograms.

The natural period is estimated to be the first peak from recorded base to crest Fourier-amplitude ratios (Ohmachi 2011). He adds that the natural period of dams change with ground shaking intensity due to the typical nonlinear material behavior.

$$\text{Natural period of rockfill dams: } T = \frac{0.45}{100} \cdot H \pm 0.11 \quad [5]$$

$$\text{Natural period of earthfill dams: } T = \frac{0.94}{100} \cdot H \pm 0.12 \quad [6]$$

### 7.2 Crest amplification

According to Gazetas and Dakulas (1991) crest acceleration of a dam is mainly affected by the three parameters valley shape, material stiffness and shear strain (i.e. damping).

Matsumoto (2010) has evaluated the pairwise base and crest accelerograph records from numerous Japanese and US dams. Despite other factors as valley shape, Figure 35 and Figure 36 clearly show that the crest amplification decreases rapidly with increasing base acceleration, thus evidencing the drastic increase of damping in nonlinear material range.

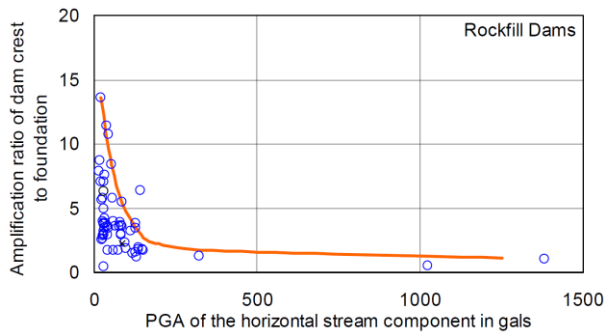


**Figure 35 Recorded amplification of rockfill dams (Matsumoto 2010)**

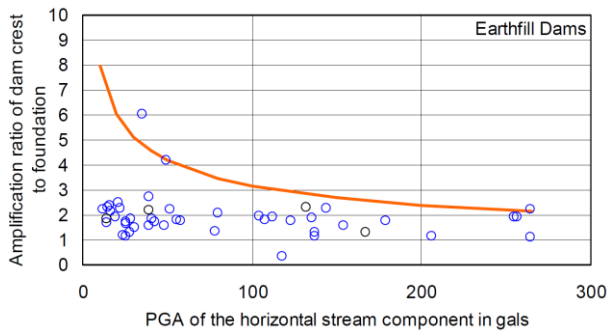


**Figure 36 Recorded amplification of earthfill dams (Matsumoto 2010)**

Yu et al. (2012) present a formula for the rough calculation of crest acceleration for rockfill dams. Figure 37 shows the base data the formula foots on (Eqn. (3.1) referenced in Figure 37).

$$AFC = \frac{PCA}{PGA} = \frac{0.5}{\sqrt{PGA}} + 1 \quad [7]$$

AFC = Amplification factor at crest elevation

PGA = Peak ground acceleration [g]

DH = Dam height [m]



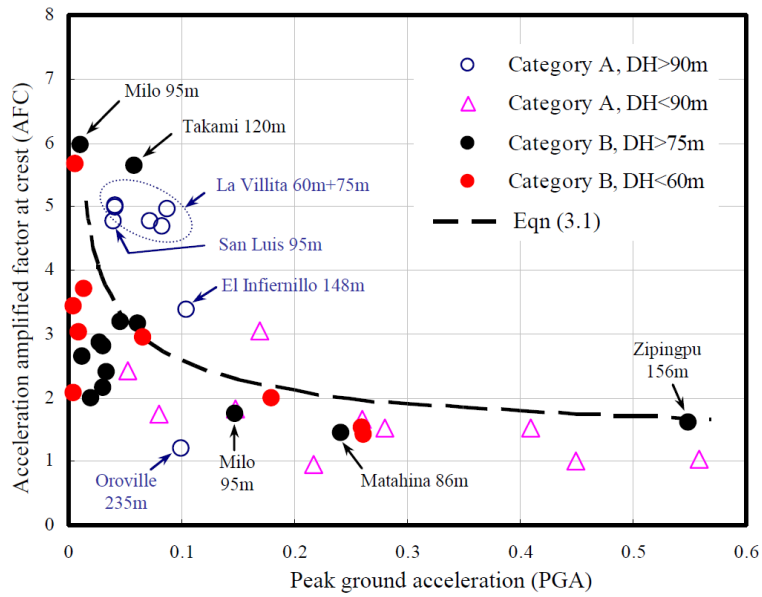


**Figure 37 Peak ground acceleration [g] vs. amplification factor (Yu et al. 2012)**

Yu et al. (2012) state that the crest acceleration decreases slightly with increasing dam height. Furthermore they varied the dam slopes within their numerical calculations in a range of 1:1.4 to 1:2.0 [V:H] and point out that the slope inclination has a minor effect on a dam's crest acceleration.

### **7.3 Simplified Methods for Estimating Permanent Settlements**

Empirical formulae were developed by several authors in order to provide tools for rapid judgment of a dam's residual settlement due to the design earthquake. An extract of these empirical formulae shall be reported herein. It shall be pointed out that these formulae provide useful help in judging the result of detailed calculations, but they do not account for site and project specific details (i.e. valley shape, material type, strength and compaction, slopes etc.). Hence care should be exercised when applying these formulae in the field.

On the other hand the author is the opinion that theses empirical formulae provide the most reliable forecast for a dam's crest settlement. This will be discussed and underlined by comparative case studies presented in chapter: 0



Results and Comparison. To the authors opinion the best estimation would result from single comparative dams selected in accordance to those factors mainly affecting the dynamic behavior. Unfortunately and as previously stated, real observation data from severe earthquake excitation is rare and hence selecting a suitable example is possible with restrictions only for most project sites.

Swaigood (2003) developed a formula wide spread in international dam engineering practice.

$$\% \text{ Settlement} = e^{(6.07 \text{ PGA} + 0.57 \text{ M} - 8.00)} \tag{8}$$

% Settlement = Crest settlement [m] divided by dam height [m] plus the thickness of the alluvial layer [m]

PGA = horizontal peak ground acceleration (on rock) [g]

M = M<sub>S</sub> = surface wave scale magnitude of the earthquake

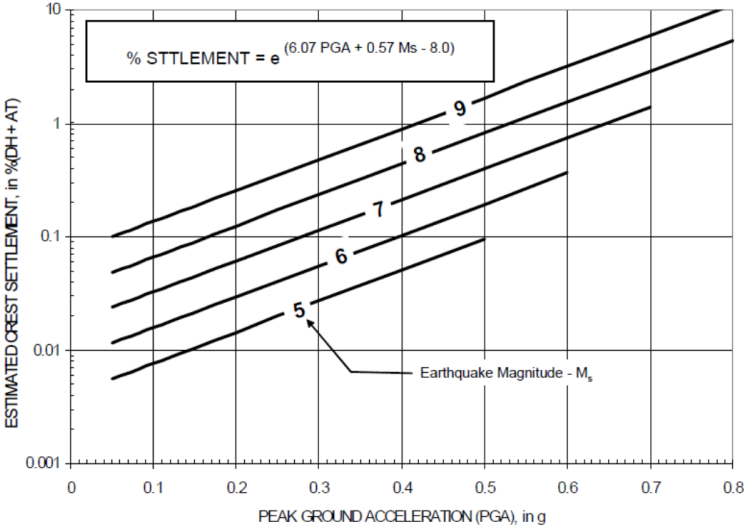


Figure 38 Crest settlement vs. PGA and magnitude (corrected from Swaisgood 2003)

Figure 39 provides additional information on observed crest settlements vs. PGA vs. embankment dam type. Were CFRD, ECRD and HF stand for concrete faced rockfill dam, earth core rockfill dam and hydraulic fill dam. This figure shows the wide spread

of the formula's basic data. It can be seen from Figure 39 that there is no clear trend separating typical settlements for different embankment dam types.

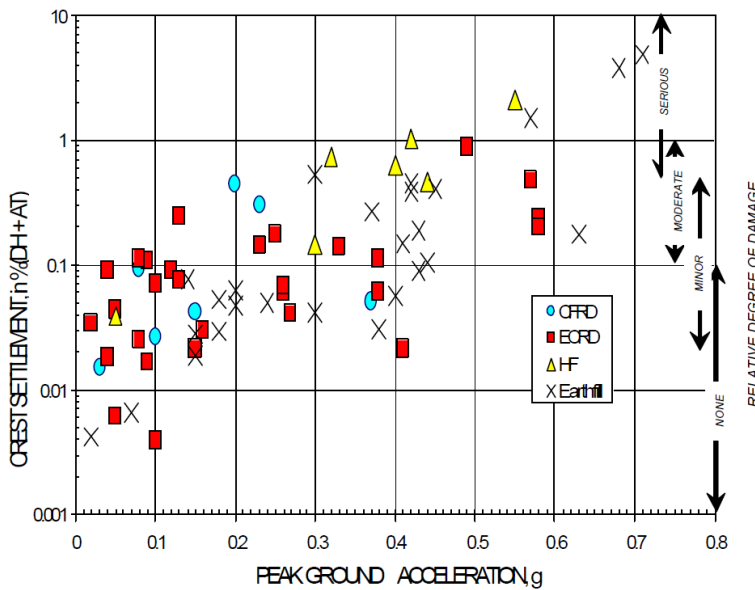


Figure 39 Observed crest settlement vs. PGA (Swaisgood 2003)

Okamoto (2010) evaluated the residual crest settlement of ECRD's and CFRD's vs. peak ground acceleration at dam base ( $1\text{gal} = 1\text{cm/s}^2$ ). Where  $A_b$  = maximum base acceleration and  $A_c$  = maximum crest acceleration. He concludes that results may be split up in three general regions, no-residual deformation corresponding to  $A_b \leq 0,1\text{g} / A_c \leq 0,2\text{g}$ , no and sometimes residual deformation corresponding to  $A_b \leq 0,2\text{g} / A_c \leq 0,5\text{g}$  and all residual deformation corresponding to  $A_b \geq 0,2\text{g} / A_c \leq 0,5\text{g}$ .

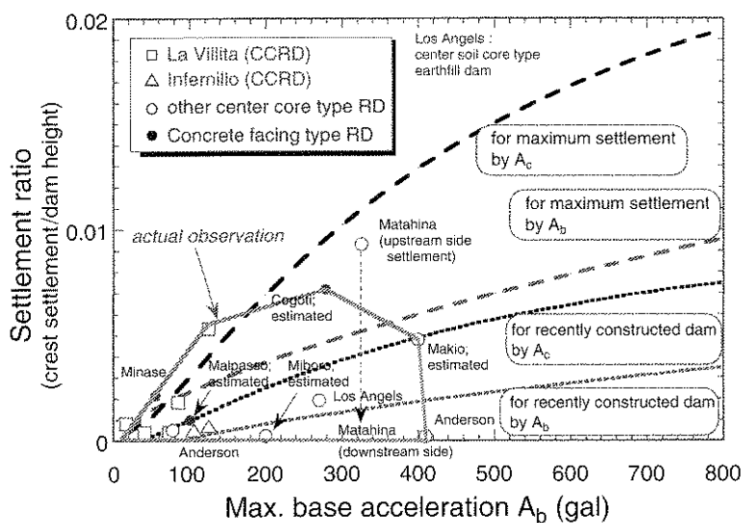


Figure 40 Observed crest settlement vs. base acceleration (Okamoto 2010)

Bureau et al. developed an empirical relationship for crest settlements of concrete face rockfill dams based on the 'Earthquake Severity Index (ESI)'.

$$ESI = PGA \cdot (M - 4,5)^3 \tag{9}$$

Where PGA is the peak ground acceleration on rock in g. The dam's settlement is calculated as a percentage of its total height based on Figure 41.

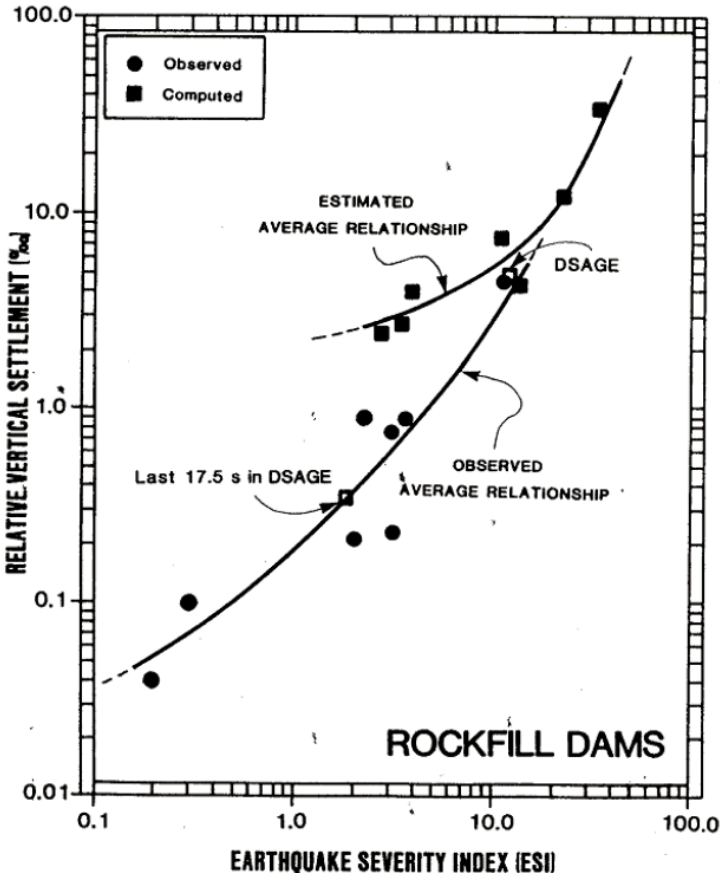


Figure 41 Earthquake severity index vs. crest settlement [%] (Bureau et al. 1985)



## **8 Risk Mitigation in Dam Design – Lessons Learned**

Design of dams was based on empirically gained knowledge in the early stages. This approach was still standard praxis until the 1970's to 1990's. Knowledge was and often still is typically gained by observed damages and dam failures. Generally design concepts and standards for the design of large dams are a living and developing field. National authorities developed design standards largely varying from each other. In the beginning and until mid of last century, the number of major dam failures increased and the trust in dam safety was widely discussed and concerned in the media. ICOLD (International Commission on Large Dams) was founded 1928 to maintain a non-governmental platform for discussion and exchange of knowhow in the field of dam safety. Since then, the number of member states continuously increased as the authorities realized that the positive effects exceeded the national interests.

### **8.1 Selection of Seismic Design Parameters**

The selection of design earthquake parameters has changed in nearly all countries in the last century. From engineering point of view it is clear that the design earthquake of a small bridge in rural area and those of major dams have to differ from each other. This is of course based on the largely varying damage potential of both cases on the one hand, and on the other hand it is also based on protection of investment costs.

Nationally the design earthquake for major dams and its generation vary strongly. Design earthquake within this paragraph is termed as that earthquake the dam has to withstand without jeopardizing the safe capability for reservoir regulation. The recurrence period of such design earthquakes varies between 100 and 10000+ years. Furthermore it shall be pointed out that the recurrence periods themselves are is not comparable as long as the background in probabilistic generation is not coherent. The author is aware of examples in the field where the official recurrence period is named to be 2475 years (probabilistic approach) whilst the standard deviation in generating this value is selected as 2% (compared to 1% in international praxis). One may be the opinion this is just a little difference but it resulted in an approximate plus 30% increase of the design peak ground acceleration.



ICOLD (2010) provides a guideline for the selection of adequate design earthquakes for large dams and appurtenant structures. A large dam in that respect is a dam that exceeds 15m height, or in the case it is between 10 to 15m, fulfills one of the following criteria:

- More than 500m long
- Reservoir capacity exceeding  $1 \times 10^6 \text{ m}^3$
- Spillway capacity exceeding  $2000 \text{ m}^3/\text{sec}$

ICOLD (2010) terms the previously stated design earthquake SEE (safety evaluation earthquake). The SEE is the bigger one of the probabilistically and the deterministically generated ground motion. Whereas the deterministically generated ground motion results from judgment of the damage potential of active faults in a minimum of 100 km (up to 300km) radial distance to the dam site. The effect on the dam site is calculated by attenuation functions.

The probabilistically generated ground motion refers to a reoccurrence period of 10000 years (great risk on human life) increased by one time the standard deviation. The reoccurrence period may be reduced in cases where there is no great risk to human life and limited other consequences of a dam failure. For moderate consequence dams ICOLD recommends a minimum return period of 3000 years, whilst a minimum return period of minimum 1000 years is recommended in case of low consequence dams.

The Hawaii dam safety guideline provides a practical risk classification system that is closely related to ICOLD requirements, linking reservoir capacity, dam height, number of persons to be evacuated and potential downstream economic damage. A total risk factor is calculated by summing up risk factors of each category. The minimum return period of the MDE (= maximum design earthquake, now termed SEE in updated ICOLD bulletin) is fixed according to the risk class that is depending on the total risk factor. It shall be noted that Hawaii Dam Safety Guideline allows for return periods as low as 100 years in case of low risk class.

	RISK			
	Extreme	High	Significant	Low
Capacity (Ac-ft)	> 5000 (6)	5000 – 500 (4)	500 – 50 (2)	< 50 (0)
Height (ft)	> 120 (6)	120 – 60 (4)	60 – 25 (2)	< 25 (0)
Evacuation Requirements (No. of persons)	> 1000 (12)	1000 – 100 (8)	100 – 10 (4)	< 10 (0)
Potential Downstream Economic Damage	High (12)	Moderate (8)	Significant (4)	None (0)

Weighting factors are indicated in parenthesis.

**Table 8 Risk factors for calculation of total risk factor (Hawaii Dam Safety Guideline 2004)**

Total Risk Factor	Risk Class
(0-6)	I (Low)
(7-18)	II (Significant)
(19-30)	III (High)
(31-35)	IV (Extreme)

**Table 9 Total risk factor vs. risk class (Hawaii Dam Safety Guideline 2004)**

RISK CLASS <sup>a</sup>	MAXIMUM DESIGN EARTHQUAKE (MDE)	
	DETERMINISTICALLY DERIVED	PROBABILISTICALLY DERIVED AEP <sup>b</sup>
Extreme, High (III, IV)	CMCE <sup>c</sup>	1/10,000 <sup>c</sup>
Significant (II)	50% to 100% of CMCE <sup>d,e</sup>	1/1,000 to 1/10,000 <sup>e</sup>
Low (I)	50% of CMCE or less <sup>f</sup>	1/100 to 1/1,000 <sup>f</sup>

**Table 10 Risk class vs. design earthquake (Hawaii Dam Safety Guideline 2004)**

## **8.2 Earthquake and Flooding**

Extreme flood conditions and design earthquakes are normally not assumed to happen simultaneously and hence are not combined in dam safety calculation. However, Wieland (n.d.) points out that even in the event of an SEE earthquake, floods in the order of 200 year return period have to be manageable in a safe manner. This is important especially in case of embankment dams.

A safe performance of an embankment dam during a severe earthquake is worth nothing if the spilling capacity is inoperable and an uncontrolled raising reservoir level causes overtopping.

## **8.3 Adequate Freeboard and Camber Arrangement**

The freeboard in highly seismic areas should be increased in order to account for dynamic crest settlement as well as for seismically induced landslides and seiches (ICOLD 2001). Wieland (n.d.) provides an easy rule. He states that the top of an embankment dam's impervious element shall not settle below the reservoir level.

Turkish Dam Design Guideline (2012) recommends designing a dam's camber arrangement for the calculated dynamic crest displacement increased by the estimated time-dependent crest settlements. If the calculated dynamic crest settlement exceeds 2% of dam height, the difference of 2% and the calculated dynamic settlement may take place within the freeboard.

Hawaii Dam Design Guideline (2004) specifies maximum residual crest displacements. A deformation between 0 to 1.5m is assumed to be sustainable as long as the deformation is still less than 10% of the dam height. Deformations in the order of 1.5 to 3.1m are assumed to be serious. The closer the calculated deformation is to 3.1m, the more unreliable the result is. In this case freeboard, crest width, zoning, remaining freeboard and embankment slopes should be checked if the design can accommodate such displacements. Deformations exceeding 3.1m are assumed to have post-earthquake safety factors of less than 1 and call for a structural redesign.

## 8.4 Crest Width

ICOLD (2001) states that the crest width should be increased in highly seismic areas in order to provide elongated seepage paths along potential transverse cracks.

However, this is controversially discussed, as widening the crest has substantial economic effects whilst its benefit is limited. Especially for high dams, there are cheaper methods to elongate the seepage path or to increase erosion resistance in potential transverse cracks. To the author's opinion, there is no sign that wider crests have significant influence on crack reduction. Shimamoto et.al. (2008) report the deformations of Isawa dam that might act as an interesting case study for the discussion of crest width. Isawa dam was under construction when it was shaken by the M 7,2 Iwate / Miyagi earthquake in 2008 (Figure 42). Figure 43 shows a close up view of a crack in longitudinal (i.e. dam axis) direction at the core to critical filter interface. Figure 42 shows that the intermediate "crest" width was untypically wide when the earthquake occurred. The dam was shaken during construction; hence the "crest width" was the temporary width of the dam at that time. Having in mind state of the art concepts where deformations are caused by sliding masses one might state that this example demonstrates that Makdisi – Seed and Newmark procedure cannot reproduce Isawa dam deformation. And in a wider sense they cannot explain the development of the cracks that obviously occurred.



Figure 42 Isawa dam during construction after Iwate /Miyagi earthquake in 2008 (Ohmachi 2008)



Figure 43 Close up of cracks in Isawa dam (Shimamoto et.al. 2008)

## **8.5 Filter Design in Earthquake prone Areas**

The general purpose of filter material is to protect fine material from getting washed away. Hence they shall protect against the development of piping and backward erosion, ensuring a safe storage of the reservoir. As a result of severe ground shaking, even well designed and constructed embankment dams will show shallow slides, compaction settlements and the related lateral spreading at crest location. Filters have to have a thickness that ensures that they are not sheared off due to permanent crest deformations. This criterion is typically kept in moderate and low seismic hazard zones as the minimum filter width needed for construction purposes exceeds potential permanent seismic displacements. However this is not necessarily the case in high seismic hazard zones.

BWG (2003) claims that 50% of the initial thickness of each filter or transition zone has to be available after an earthquake to preclude the start of internal erosion.

The BWG (2003) criterion clearly makes sense but the major question is how to calculate the horizontal crest displacement. In practice, the Engineer will have significant problems to find guidelines that do make sense (to the opinion of the author).

ICOLD (2001) specifies that high capacity internal drainage zones have to be provided in embankment dams. Such zones shall be designed for the presence of transverse cracks to ensure that the downstream shoulder remains unsaturated. It is furthermore specified that wider than normal filter zones have to be applied to account for zone offset due to slides at crest location. Transition zones should be self-healing and graded in a way to heal a transverse crack within the impermeable element. Filter zones should be placed along the entire footprint where embankment material might be washed through cracks in the foundation that might open during the earthquake.

The horizontal width of vertical filter zones is under constant discussion in international dam society as state of the art dimensioning based on Newmark or Makdisi – Seed calculations very often results in excessive filter widths. It is the author's conviction that whether Newmark, nor Makdisi – Seed procedure are able to reflect realistic dam behavior. This is in good agreement with other international researchers (Swaigood

2003 or Zou 2012). Dynamic crest deformations seem to be overwhelmingly guided by dynamic compaction of its fill materials and as long as liquefaction does not occur, sharp horizontal offsets in filter zones have not been observed even though the number of dams shaken by severe earthquakes increased in recent time. If significant horizontal offset was observed it has always been concentrated to the dam's outer surface only. Local failure has been observed in rip rap, at the concrete face slabs or local failure of crest edges. The inner zones of rockfill dams tend to compact / densify due to severe shaking while the outer zones might but do not necessarily have to be subject to loosening. Excluding local surface effects, the overall crest behavior is governed by the inner fill compaction and not by sliding masses of various depths.

Thus making embankment dams, having a flexible internal core, the favorable selection for highly seismic areas. Earth core rockfill dams have proven to show adequate behavior during severe shaking. If adequately designed against high seepage values, Concrete faced rockfill dams seem to resist severe shaking without catastrophic failure too. Their big advantage is that the impermeable element is easily accessible (above minimum water level). However it may be stated that such kind of repair works are likely even in case of medium earthquakes were internal core dams would not show any deficiencies. The same applies to asphalt lined rockfill dams. Geomembrane lined dams are a promising development but their seismic behavior still remains untested by real earthquakes and hence is based on theoretic assumptions.

## **8.6 Soils Susceptible to Liquefaction**

ICOLD (2001) states: '*Fill materials which tend to build significant pore water pressures during strong shaking must not be used upstream from the water barrier, or below the water table, ...*' It is further stated that dams in high seismic hazard zones have to be founded on very dense material or on rock. If the embankment has to be founded on loose material, these materials should either be densified or replaced by compacted material to avoid a potential loss of shear strength or liquefaction.



## **9 Calibration of Model Codes on Monitoring data obtained during strong earthquakes**

Earthquake engineering methods, as all other fields of engineering interest too, need to be proved by physical reality. Data observed and monitored in the field provides important information for checking a calculation method's suitability. Within this chapter, ground motions observed during the Great Eastern Earthquake (Tohoku earthquake, Japan, March 11<sup>th</sup> 2011) shall be compared to results obtained from numerical model codes. The Great Eastern Earthquake is among the largest ever monitored by mankind and caused the disaster of Fukushima Daiichi Nuclear Power Plant. By use of this reality check, guidelines for the built up of numerical models will be derived. Questions like which boundary conditions shall be used, effects of the models outer dimensions, wave damping and reflection at model boundaries will be discussed as well as model assumptions for competent rock masses.

### **9.1 Japan's seismic observation networks KiK-Net & K-Net**

The nation of Japan is vulnerable to multiple natural hazards. It is among the seismically most active areas of this planet. Japanese Engineers have put enormous effort on developing the field of earthquake engineering.

Figure 44 shows the distribution of strong motion observation stations in Japan (Fujiwara 2003).

It is obvious that Japan has spent enormous effort in the development of a dense seismic observation grid. Each of these blue or red dots consists of one or two 3D accelerometers located either at ground surface or the first seismograph is placed at ground surface and a second one is placed at the bottom of a borehole. Within the last two decades, these instruments have recorded the vast majority of all earthquakes. The recorded data as well as important information about the ground profile below each station is published online with free access to everyone.



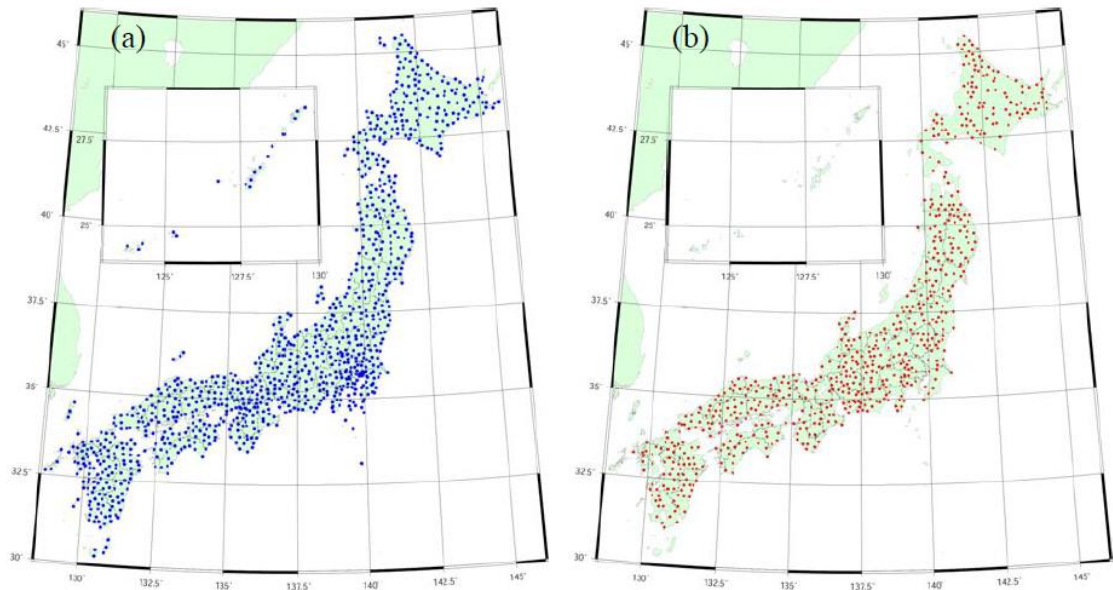


**Figure 44 Strong-motion stations in Japan (a) K-Net and (b) KiK-Net (Fujiwara, 2003)**

A typical set up of a KiK-Net station is shown in Figure 45 (Fujiwara, 2003). The threshold value for data recording of the lower accelerometer is set to 0,0002g for a minimum duration of 30sec (interval is elongated for another 120sec if 0,0001g is still exceeded). The data is sampled and stored at a frequency of 200 Hz. The majority of all KiK-net sites are located at shallow sedimentary deposits with 100 to 200m deep boreholes. Shear wave profiles are available and have been derived from downhole seismic investigations. The observation station is equipped with three component accelerometers at ground surface. The bottom of the borehole is equipped with a three component accelerometer, a three component velocity seismometer and two tiltmeters.

The seismic observation networks were installed and are operated by NIED - National Research Institute for Earth Science and Disaster Prevention.

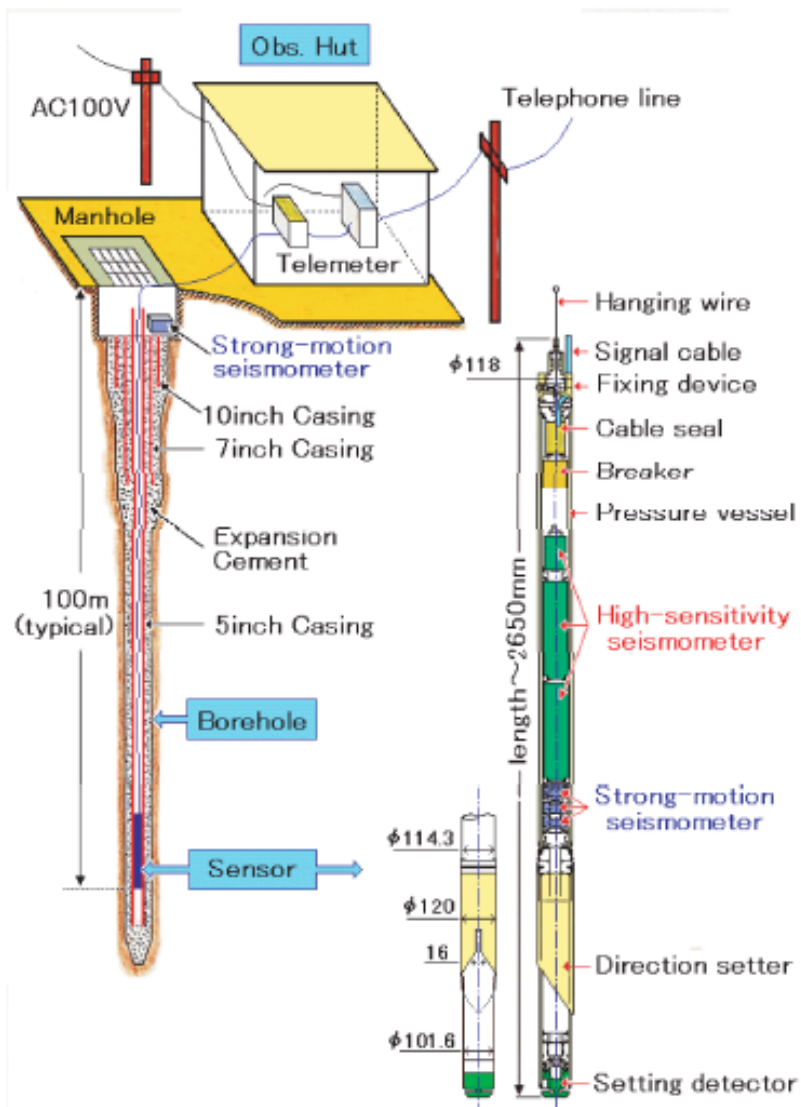


Figure 45 Setup of a KiK-Net seismic observation station (Fujiwara, 2003)

## 9.2 Selected Observation Stations

Figure 46 shows the location of all KiK-Net observation stations within Fukushima Prefecture. The pink colored triangle shows the location of Fujinuma dam that will play an important role in the later conducted seismic analysis of dam structures.

Three observation stations have been selected for the reality check, namely: FKSH08, FKSH09 and FKSH10.



Figure 46 Location of KiK-Net stations in Fukushima prefecture (modified from NIED)

Figure 47 to Figure 49 show the acceleration time histories that were monitored during the Tohoku earthquake on March 11<sup>th</sup> in 2011 at 14:46:43 local time. The six data sets of each observation station represent the three directions monitored at ground surface and at borehole bottom.

Set Number (1) refers to North – South direction at borehole bottom.

Set Number (2) refers to East – West direction at borehole bottom.

Set Number (3) refers to Up – Down (i.e. vertical) direction at borehole bottom.

Set Number (4) refers to North – South direction at ground surface.

Set Number (5) refers to East – West direction at ground surface.

Set Number (6) refers to Up – Down (i.e. vertical) direction at ground surface.

$$100[\text{gal}] = 100[\text{cm}/\text{sec}^2] = 1[\text{m}/\text{sec}^2] = 0,102[\text{g}]$$

2011/03/11-14:46 38.103N 142.860E 24km M9.0(FKSH08)

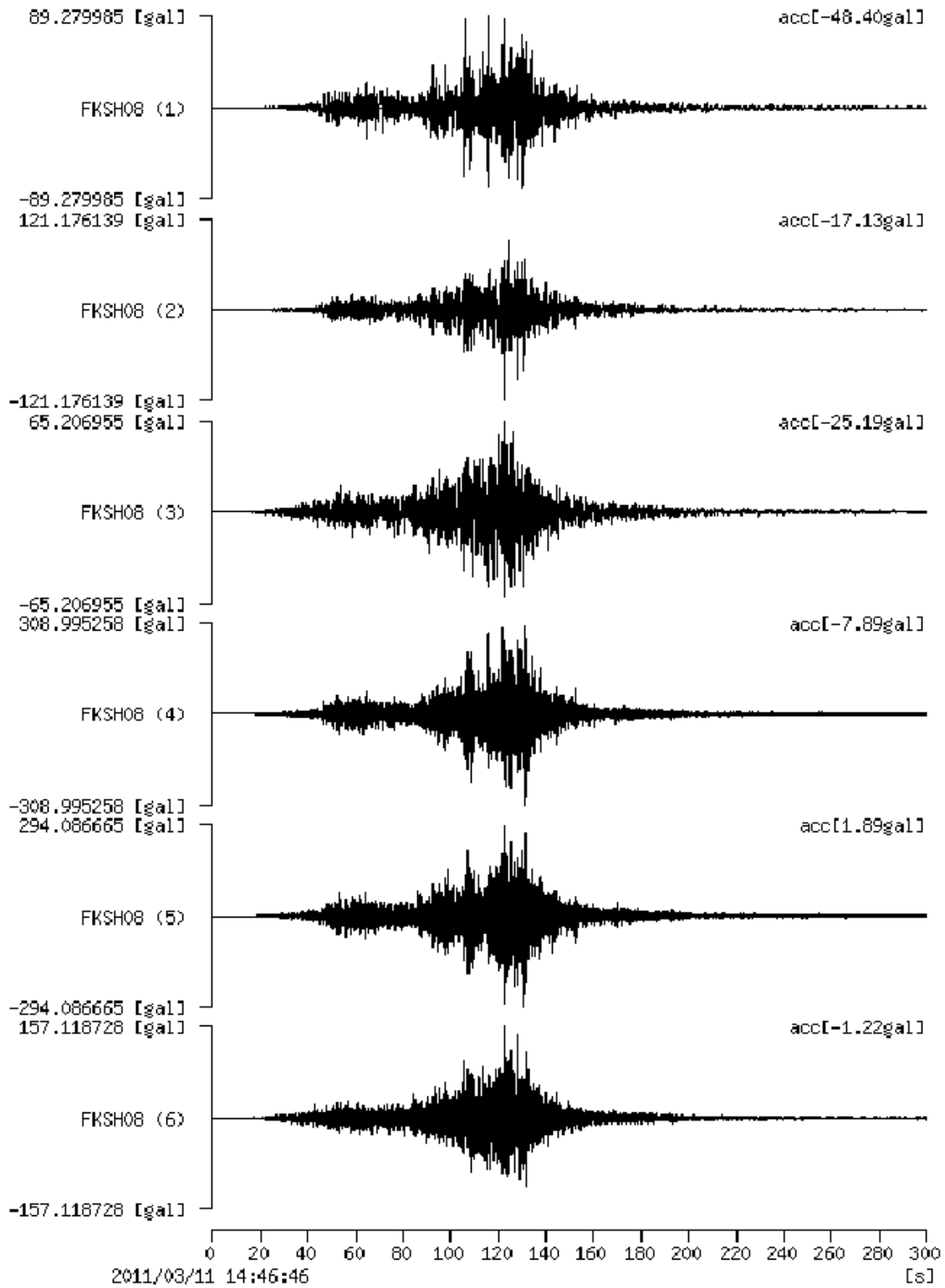


Figure 47 FSKH08 acceleration data monitored during the Great Eastern Earthquake (NIED)

2011/03/11-14:46 38.103N 142.860E 24km M9.0(FKSH09)

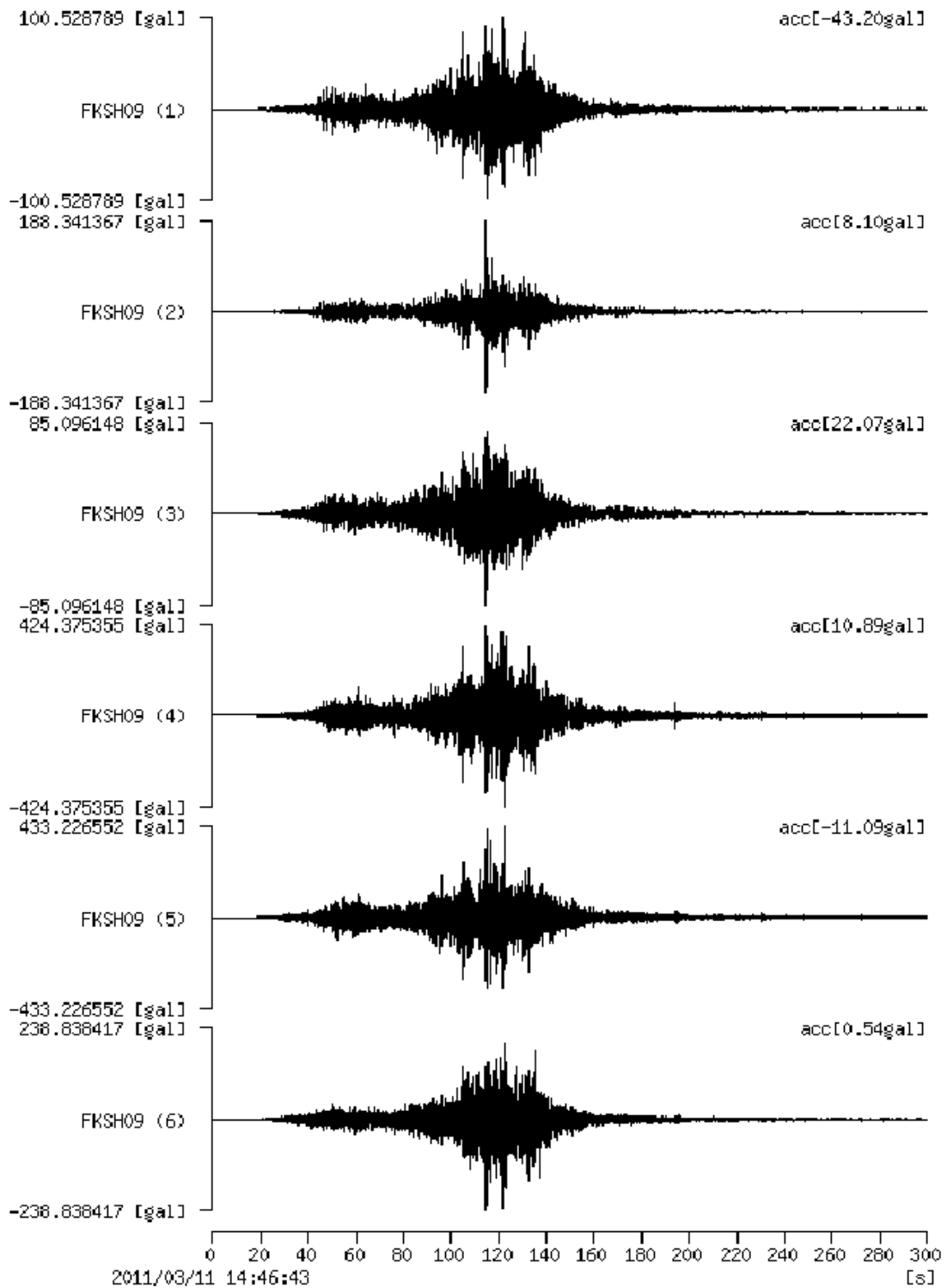


Figure 48 FSKH09 acceleration data monitored during the Great Eastern Earthquake (NIED)

2011/03/11-14:46 38.103N 142.860E 24km M9.0(FKSH10)

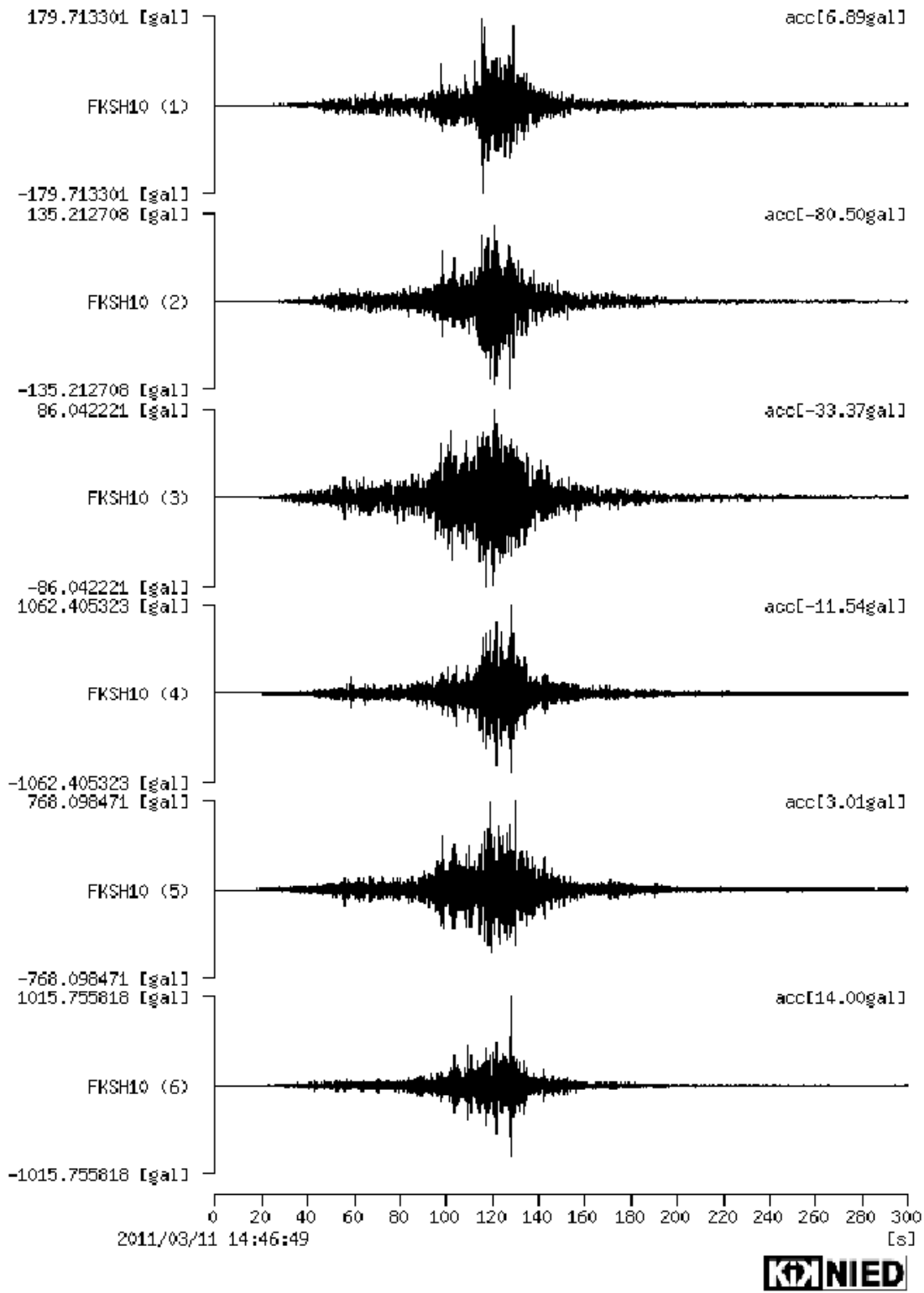


Figure 49 FSKH10 acceleration data monitored during the Great Eastern Earthquake (NIED)

Table 11 shows the results of downhole borehole seismic investigations at observation stations FSKH08 / FSKH09 and FSKH10. It can be seen that borehole depths are 48m (FSKH08), 170m (FSKH09) and 146m (FSKH10). Unfortunately no further material information is available and hence the other material parameters had to be estimated from available shear wave velocity and rough descriptions of local geology only.

No	Thickness (m)	Depth (m)	Vp (m/s)	Vs (m/s)	No	Thickness (m)	Depth (m)	Vp (m/s)	Vs (m/s)	No	Thickness (m)	Depth (m)	Vp (m/s)	Vs (m/s)
1,	4.00,	4.00,	1420.00,	200.00	1,	2.00,	2.00,	450.00,	140.00	1,	4.00,	4.00,	300.00,	150.00
2,	4.00,	8.00,	2620.00,	450.00	2,	8.00,	10.00,	1500.00,	300.00	2,	12.00,	16.00,	1500.00,	650.00
3,	40.00,	48.00,	2620.00,	900.00	3,	34.00,	44.00,	3480.00,	1930.00	3,	16.00,	32.00,	1700.00,	850.00
4,	-----,	-----,	3310.00,	1470.00	4,	126.00,	170.00,	4950.00,	2540.00	4,	34.00,	66.00,	2400.00,	1100.00
					5,	-----,	-----,	4950.00,	1960.00	5,	20.00,	86.00,	2900.00,	1300.00
										6,	60.00,	146.00,	2100.00,	940.00
										7,	-----,	-----,	2100.00,	870.00

**Table 11 P and S-wave profile of FSKH08 / FSKH09 and FSKH10 boreholes (NIED)**

From shear wave velocity it is possible to directly calculate the Small Strain Shear-modulus ( $G_{max}$ ). All other material parameters needed for the Equivalent –Linear and pure Nonlinear material models were in a first step estimated from literature and in a second step varied to obtain the best fit result.

$$V_s = \sqrt{\frac{G_{max}}{\rho}}$$

Where:

$G_{max}$  is the small strain shear modulus

$V_s$  is the shear wave velocity

$\rho$  is the mass density of the material defined as the dry unit weight divided by g (gravity acceleration)

## 9.2.1 Seismic Observation Station FSKH08

### 9.2.1.1 Model Geometry / Model Assumptions

Figure 50 shows the model for calculation of initial stress conditions. Boundary conditions are fixed in horizontal and vertical direction at model base. The left and right side model boundaries do not allow for horizontal deformation whilst the vertical deformation is not restricted. According to information from p-wave investigations (see Table 11), the phreatic surface was observed at ground surface ( $V_{p,water} = 1500\text{m/sec}$ ).

Figure 51 shows the model used for seismic analyses. In contrast to the initial static conditions, the vertical boundaries are free to deform in all directions. For the dynamic analysis, damping elements have been added at left and right model edge. These damping elements have the same material parameters as their horizontal neighbor regions with the only exception of a constant damping ratio of 99% applied to the full shear strain range. Observation points have been placed at the symmetry axis at surface and base elevation. The location represents the location of the strong motion accelerographs in reality. These observation points store and plot the full range of data obtained during the analysis.

The analyses have been performed using GeoStudio 2012 software comparing the well-known Equivalent Linear vs. the Nonlinear model code. The time history accelerograms obtained from FSKH08 borehole bottom were applied as input motion to the base of the model. In GeoStudio, the input motion is automatically applied to the fixed boundary at model base. No further adjustments have to be done.

The width of the model was selected to 14 times the height. In general it may be stated that the model width is of specific interest as the left and right model edge are free to move in all directions. During dynamic loading the free deforming edges influence the result and hence the model width has to be increased until the result does not change anymore. The effect of damping regions at left and right side decreases with increasing model width. Damping regions are suitable to exclude wave reflection on left and right side model edge, however, compared to other parameters their effect was found to be small. In case of FSKH08 analysis, the calculated peak ground accelera-



tion increased in the order of 8 to 7% if no damping was applied to left and right side edges. Wave reflection at the model base cannot be avoided as the lower base needs to transmit the input excitation. However this assumption is fully correct in case of FSKH08 station as competent rock underlies the seismograph at borehole bottom.

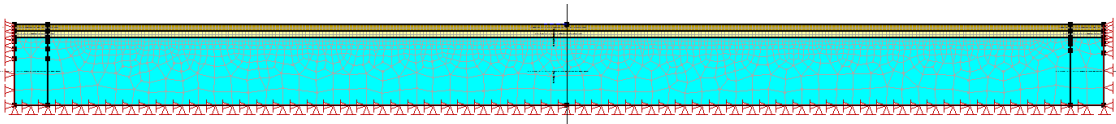


Figure 50 Modelling initial stress conditions

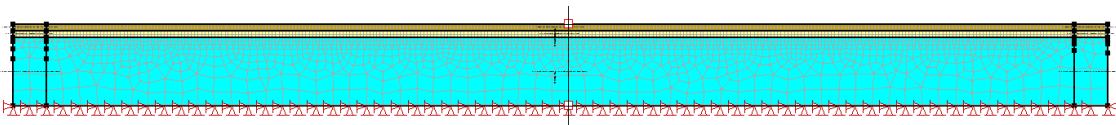


Figure 51 Model for dynamic analysis

### 9.2.1.2 Best Fit Parameter-Sets

Table 12 summarizes the material parameter sets that resulted in the best fit for the calculation of the monitored surface accelerations. The result of the calculated surface acceleration is highly affected by  $G_{max}$ ,  $G_{max}$  reduction, weight and Poisson's ratio. Other input parameters were found to have minor influence. Figure 52 and Figure 53 show the selected  $G_{max}$  reduction curves and damping graphs. These parameters vary with increasing shear strain. Selected functions were published by Vucetic and Doby (1991, Figure 85) and by Jeon (2008).

Jeon (2008) has conducted extensive investigations on Tuff specimens. Depending on the type of welding and amount of pore inclusions, the general unit weight of the investigated Tuff samples is between 12 to 23,5 kN/m<sup>3</sup>. Due to the wide spread of investigated samples the work of Jeon provides an important insight to the dynamic behavior of competent and weak sedimentary rocks too.

Analyses have been conducted comparing the material codes of the equivalent linear and the nonlinear method. Nonlinear analysis have been performed using the same set

of material parameters as shown in Table 12, whereas minimum and maximum damping have been selected same as the left and right boundary values shown in Figure 53.

Estimated material type	Shear wave velocity [m/sec]	Depth [m]	Colour in calculation	Plasticity index [-]	Saturated Weight [kN/m <sup>3</sup> ]	Poisson's ratio [-]	G <sub>max</sub> [kN/m <sup>2</sup> ]	Internal angle of friction [°]	Cohesion [kN/m <sup>2</sup> ]
Silty - Sand	200	0 - 4		0	21	0.4	84000	30	30
Sand - high density	450	4 - 8		0	22.5	0.3	455625	33	100
Rock (moderately welded Tuff)	900	8 - 48		0	13	0.13	650000	40	500

**Table 12 Material parameter sets applied to FKSH08 analysis (equivalent linear)**

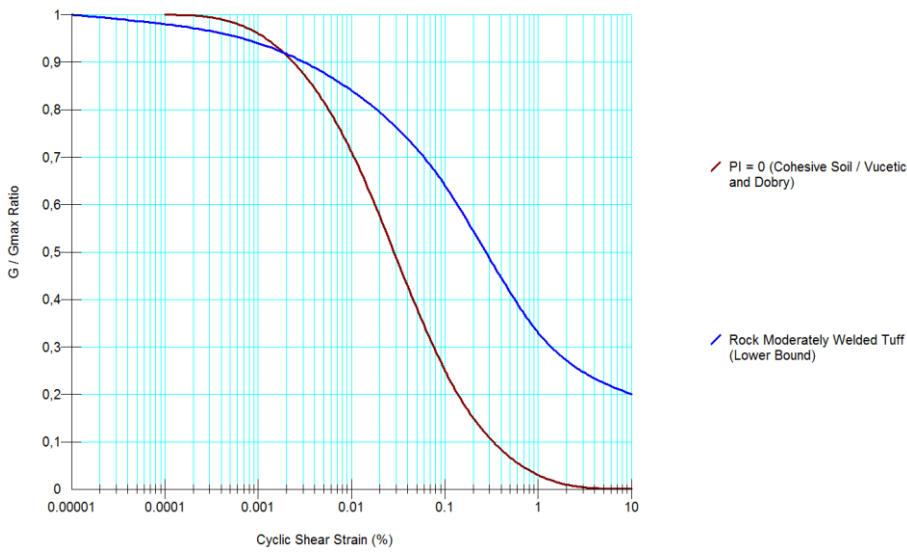


**Figure 52 G<sub>max</sub> reduction sets applied to FKSH08 analysis (equivalent linear)**

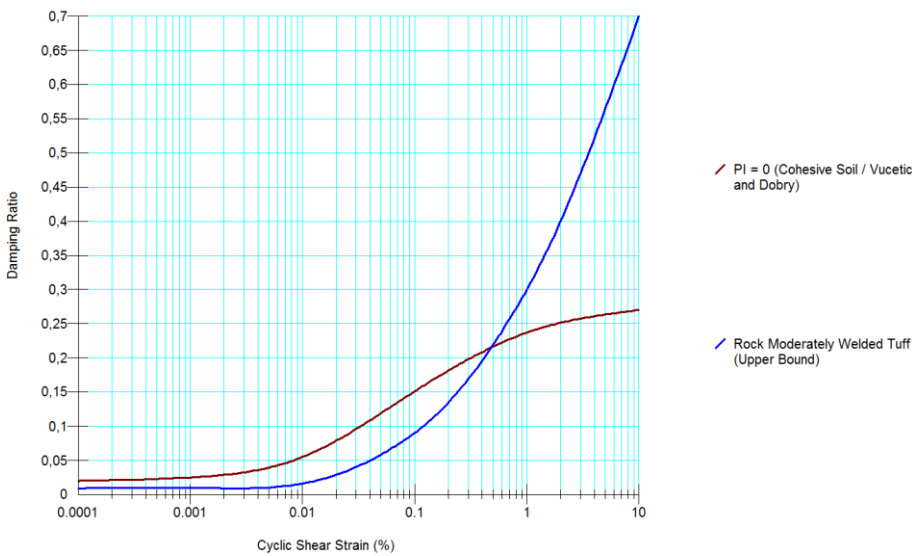


**Figure 53 Damping sets applied to FKSH08 analysis (equivalent linear)**

### 9.2.1.3 Results and Comparison

Figure 47 shows the accelerations obtained from station FKSH08 during the Tohoku earthquake in March 2011. The horizontal acceleration observed in East – West direction resulted in a peak of 0,124g (i.e. 121,2gal) at borehole bottom and 0,3g (i.e. 294,09gal) at ground surface. In vertical direction a peak acceleration of 0,066g (i.e. 65,21gal) at borehole bottom and 0,16g (i.e. 157,12gal) at ground surface was monitored.

The parameter set presented in Table 12 resulted in the best fit calibrated for the Equivalent Linear Method. The calculations resulted in a horizontal peak acceleration of 0,293g and a vertical peak acceleration of 0,166g. Hence the result seems to be quite good if referring to the peak acceleration only. Figure 54 shows the result, i.e. the calculated horizontal acceleration, in contrast to the monitored acceleration for each time step. By visual judgement and by having in mind the lack of knowledge about material investigation, the result surprises by its high accuracy. The green line shows the calculated results whilst the red line shows the monitored data. The general shape of the data record is reproduced in very good agreement by the Equivalent Linear Method. Direction and size of the peak ground acceleration fit the monitored data.

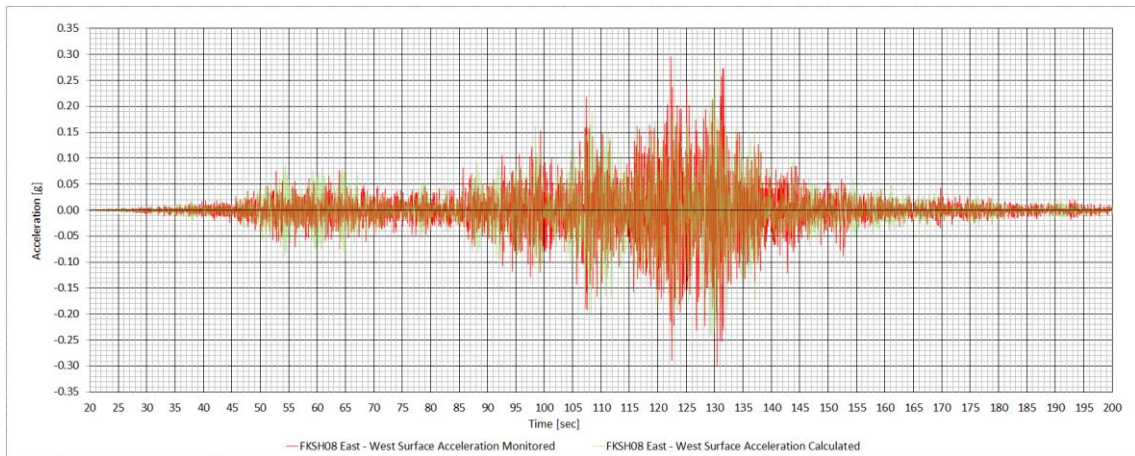


**Figure 54 Monitored vs. calculated horizontal surface accelerogram FKSH08**

Figure 55 shows the calculated vertical acceleration in contrast to the monitored acceleration for each time step. It can be seen that the calculated result in general over-

estimates the measured one for the majority of all time steps. Better accuracy could not be met in a large number of parameter set variations.

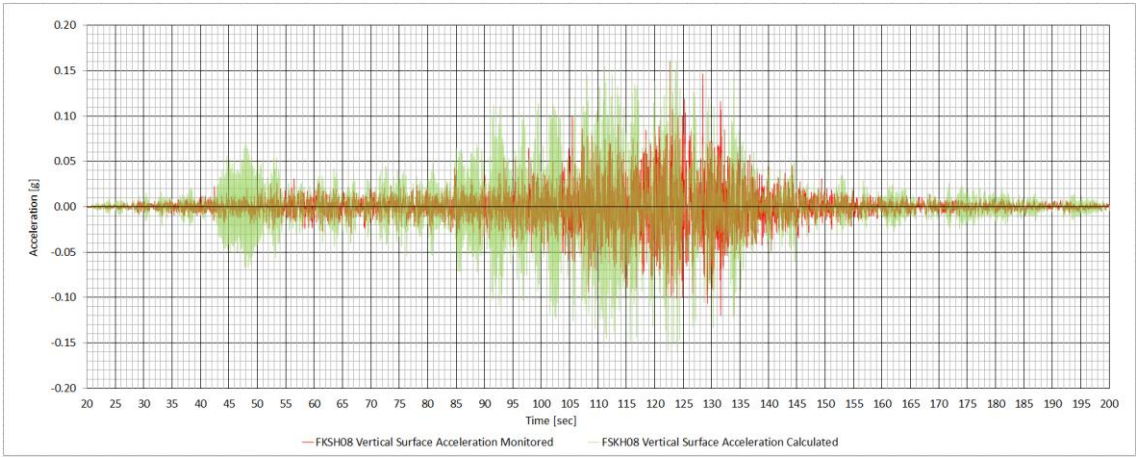


**Figure 55 Monitored vs. calculated vertical surface accelerogram FKSH08**

In contrast to the Equivalent Linear Method the Nonlinear method resulted in a horizontal peak acceleration of 0,300g and a vertical peak acceleration of 0,162g. In case of station FKSH08 the difference of Equivalent Linear and Nonlinear method is negligible. If the focus is on peak acceleration, both methods produce comparable results.

But, it is not the peak acceleration only that is of engineering interest. If calculation of realistic dynamic deformations is of special interest it is more important to meet the soil – structure interaction for all periods than to exactly meet the exact peak acceleration. Figure 56 and Figure 57 show the horizontal spectral accelerations in normal respectively in logarithmic scale. It can be seen that the base input motions (monitored and calculated) do not vary in significant ranges. This is an important check. Obviously the software (i.e. GeoStudio 2012 in this case) enables the engineer to accurately apply measured data to the numerical model. Furthermore it can be seen that the Equivalent Linear Method fits the monitored data for periods smaller than 0,1 seconds in an acceptable range. However the Nonlinear method provides a better estimate within that range. The result for periods between 0,1 to 0,2 seconds is underestimated by both methods, again the Nonlinear method provides the better estimation. EL method overestimates the observed data in periods ranging from 0,25 to 0,4 seconds. Nonlin-

ear method does the same approximately in the same range but again provides the better estimate.

In case of EL method, the monitored spectral acceleration at period 0,3 seconds, is approximately 2 times higher than the calculated one. Nonlinear method results in a maximum factor of 1,6 exceedance.

EL method provides much better accuracy for periods exceeding 0,4 to 1 sec. For dam engineering and structural interaction in general it is of highest interest to accurately describe the base soils response within this range as the natural periods of most dams (80 to 120m) would approximately plot within that range. In case of Nonlinear analysis, the result obtained for periods exceeding 0,45 seconds clearly follows the input motion. In other words, the numerical model tends to significantly underestimate the amplification at lower frequencies (i.e. long periods). It is nearly impossible to describe the dynamic behavior of a ground perfectly stepping through all periods and in all directions. The result achieved for FKSH08 is judged to be good to very good.

The logarithmic scale (Figure 57) is plotted to visualize its effect only. Logarithmic plots are quite famous in site specific seismic hazard reports as they indicate that the submitted time history records fit the resulting site specific response spectrum quite well. Here, we still have the maximum mismatch of 2,0 in our case and logarithmic plots should always be judged in detail and with good skeptical sense.

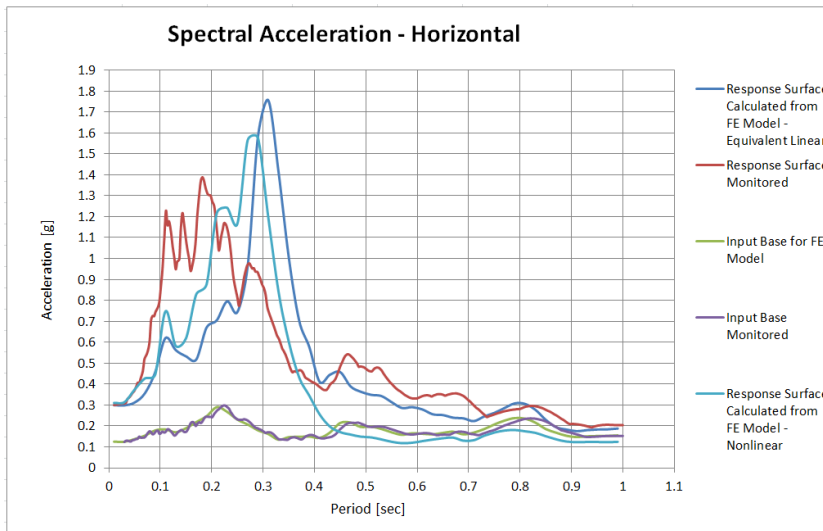


Figure 56 FKSH08 horizontal spectral acceleration

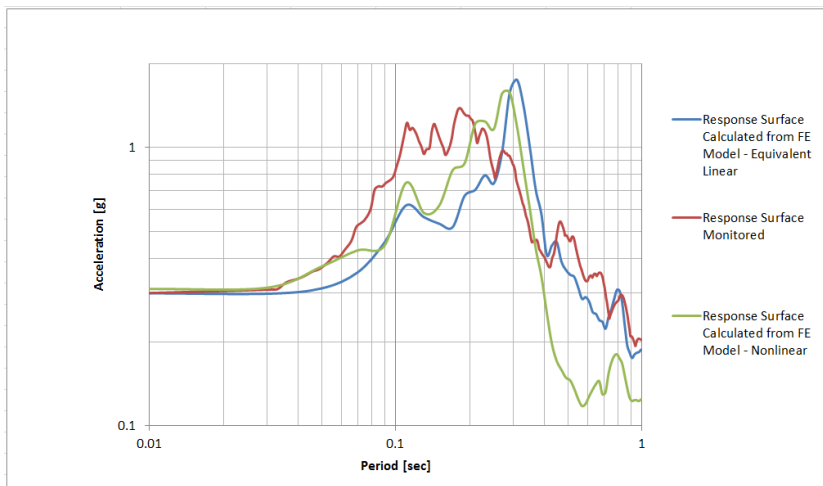
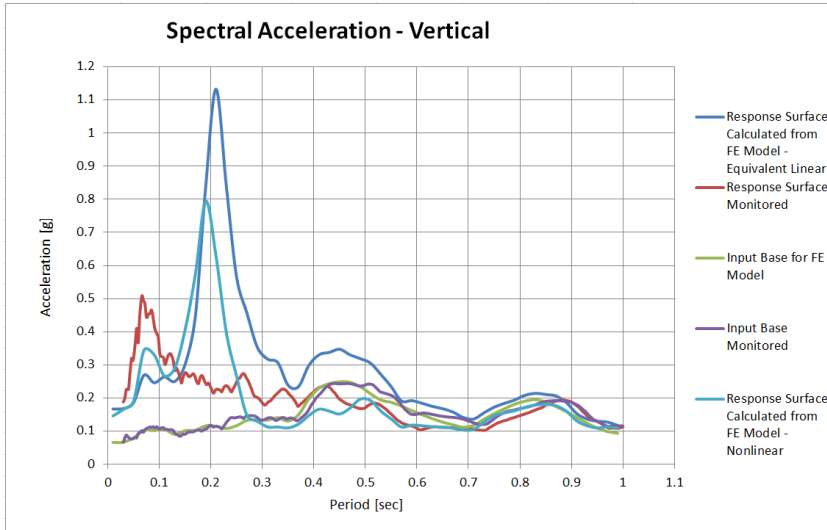
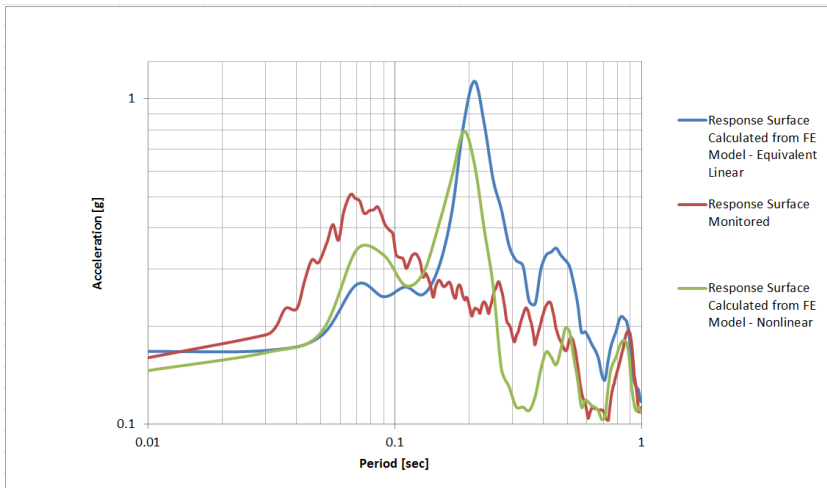


Figure 57 FKSH08 horizontal spectral acceleration (logarithmic scale)

Figure 58 and Figure 59 show the vertical spectral accelerations in normal respectively in logarithmic scale. Again it can be seen that the base input motions (monitored and calculated) do not vary in significant ranges. It can be seen that the Nonlinear Method better fits the monitored data for periods smaller than 0,12 seconds whilst the result of the Equivalent Linear Method results in a mismatch of approximately 2 in the same range. The result for periods from 0,12 to 0,25 seconds varies significantly from observed data. The maximum mismatch at that range is approximately 5 and 3,5 for EL and NL analysis respectively. Better accuracy is met for periods exceeding 0,35 seconds.



**Figure 58 FKSH08 vertical spectral acceleration**



**Figure 59 FKSH08 vertical spectral acceleration (logarithmic scale)**

From Figure 56 to Figure 59 it is clear that the results of the Equivalent Linear Method and the Nonlinear method are able to roughly reproduce the materials dynamic behavior. The result was calibrated to the peak ground acceleration in Equivalent Linear Method only. It is assumed that the result accuracy obtained for the Nonlinear Method would increase if more effort was put on calibration. However the sense of the analysis herein was to visualize the differences of these two methods. Hence similar input parameters are essential in this case.

## 9.2.2 Seismic Observation Station FKSH09

### 9.2.2.1 Model Geometry / Model Assumptions

Figure 60 shows the model for initial stress conditions. Boundary conditions are the same as selected for FKSH08 model. Following observations, the phreatic surface was fixed 2m below ground surface ( $V_{p,water} = 1500\text{m/sec}$ ). Station FKSH09 was built on shallow deposits overlaying high strength rock formations (see Table 11 b). Borehole seismic investigations revealed a shear wave velocity exceeding 1900m/sec in depths deeper than 10m below ground. The lower accelerograph is located at bottom of a 170m deep borehole in stable rock. Within high strength rock formations well offside the hypo center or active movements the acceleration may be presumed evenly distributed. FKSH09 is located in a distance exceeding 100km from the epicenter of the Great Eastern Earthquake and hence the high strength rock was not foreseen within the numerical model.

In general, evenly distributed acceleration within a high strength rock mass might be modelled by applying rigid body material parameters, a no mass approach (not possible in GeoStudio) or by simply applying the monitored accelerograph data at the top of the high strength rock. For the present analysis the high strength rock was deleted from the numerical model and the observed monitoring data was directly applied to the upper boundary of the rigid rock (i.e. the base of the modeled zones).

Figure 61 shows the model used for seismic analyses. Boundary conditions, observation points and damping elements were applied same as described for FKSH08 model. The analyses have been performed using GeoStudio 2012 software. The time history accelerograms obtained from FKSH09 borehole bottom were applied as input acceleration at the base of the model.

The width of the model was selected 22 times its height. In fact the model width might have been selected smaller to exclude effects from left and right side model edge.



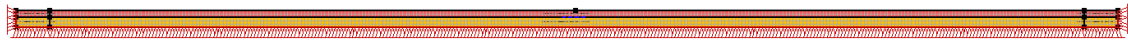


Figure 60 Modelling initial stress conditions

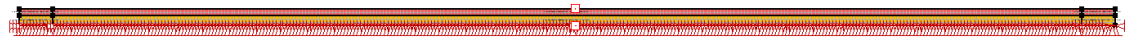


Figure 61 Model for dynamic analysis

### 9.2.2.2 Best Fit Parameter-Sets

Table 13 summarizes the material parameter sets that resulted in the best fit for the calculation of the monitored surface accelerations. The result of the calculated surface acceleration is highly affected from  $G_{max}$ ,  $G_{max}$  reduction, weight and Poission's ratio. Figure 62 and Figure 63 show the selected  $G_{max}$  reduction curves and damping graphs. These parameters vary with increasing shear strain. Selected functions were published or estimated from data published by Vucetic and Doby (1991, Figure 85).

Analyses have been conducted comparing the material codes of the equivalent linear and the nonlinear method. Nonlinear analysis were performed using the same set of material parameters as shown in Table 13, whereas minimum and maximum damping were selected same as the left and right boundary values shown in Figure 63.

Estimated material type	Shear wave velocity [m/sec]	Depth [m]	Colour in calculation	Plasticity index [-]	Weight above water table (dry) [kN/m <sup>3</sup> ]	Starated Weight [kN/m <sup>3</sup> ]	Poission's ratio [-]	$G_{max}$ [kN/m <sup>2</sup> ]	Internal angle of friction [°]	Cohesion [kN/m <sup>2</sup> ]
Sandy Silt - weak	140	0 - 2		0	20.5	-	0.35	46125	30	30
Clay - stiff	300	2 - 10		10	-	19	0.4	171000	30	200

Table 13 Material parameter sets applied to FKSH09 analysis (equivalent linear)

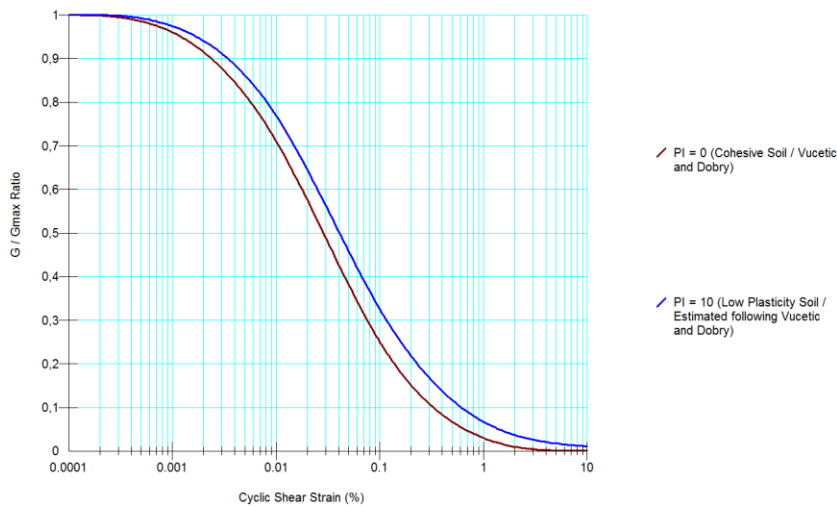


Figure 62  $G_{max}$  reduction sets applied to FKSH09 analysis (equivalent linear)

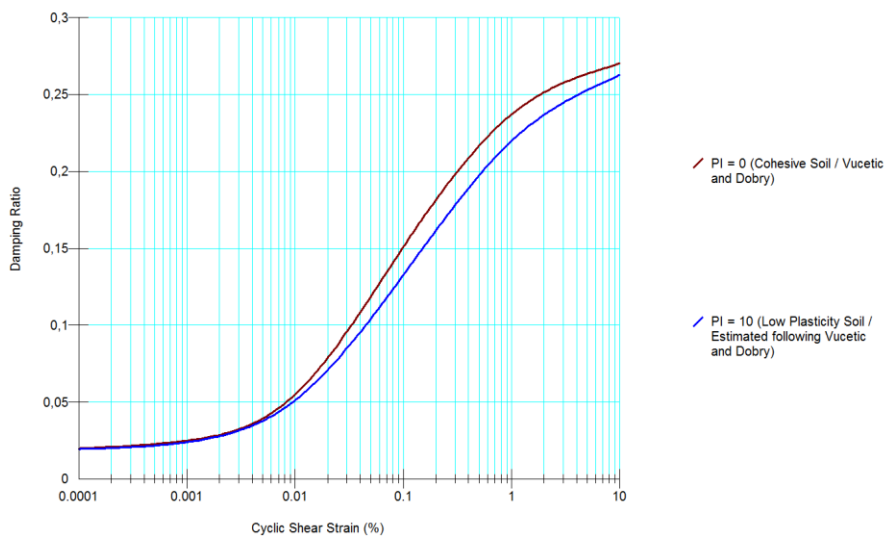
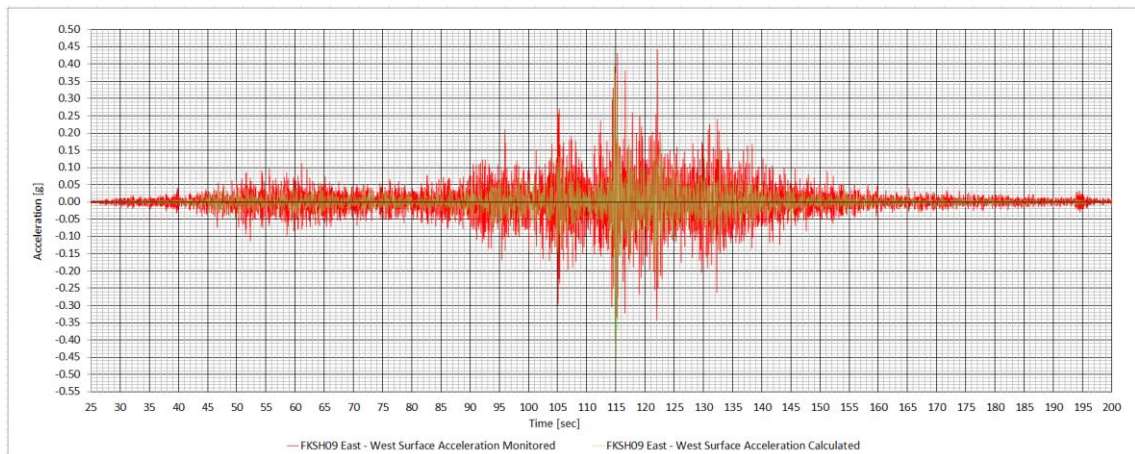


Figure 63 Damping sets applied to FKSH09 analysis (equivalent linear)

### 9.2.2.3 Results and Comparison

Figure 48 shows the accelerations obtained from station FKSH09 during the Tohoku earthquake in March 2011. The horizontal acceleration observed in East – West direction resulted in a peak of 0,192g (i.e. 188,3gal) at borehole bottom and 0,442g (i.e. 433,2gal) at ground surface. In vertical direction a peak acceleration of 0,087g (i.e. 85,1) at borehole bottom and 0,243g (i.e. 238,8gal) at ground surface was monitored.

The parameter set presented in Table 13 resulted in the best fit calibrated for the Equivalent Linear Method. The calculations resulted in a horizontal peak acceleration of 0,46g and a vertical peak acceleration of 0,24g. Hence the result seems to be quite good if referring to the peak acceleration only. Figure 64 shows the calculated horizontal acceleration in contrast to the monitored acceleration for each time step. The green line shows the calculated results whilst the red line shows the monitored data. The general shape of the data record may be reproduced by the Equivalent Linear Method. Compared to the results obtained for station FKSH08, the numerical model for FKSH09 seems to underestimate the recorded data for the majority of all time steps. The calculated peak acceleration fits the observed data quite well in location, direction and size.



**Figure 64 Monitored vs. calculated horizontal surface accelerogram FKSH09**

Figure 65 shows the calculated vertical acceleration compared to the monitored acceleration for each time step. The calculated vertical surface acceleration matches the observed data in general shape and size of peak acceleration. The exact direction and location of the peak acceleration could not be met. Nevertheless the obtained result is judged to be in good agreement with the observed data.

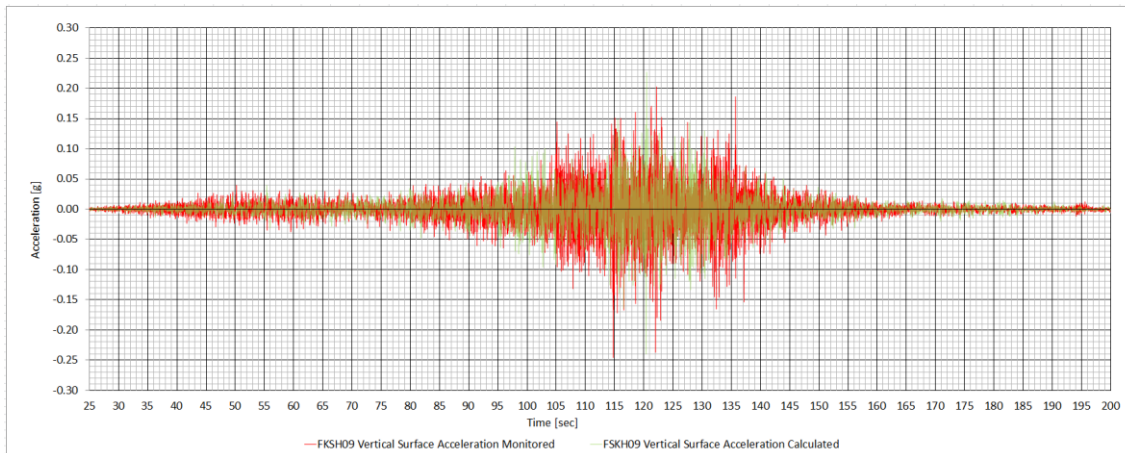


**Figure 65 Monitored vs. calculated vertical surface accelerogram FKSH09**

In contrast to the Equivalent Linear Method the Nonlinear method resulted in a horizontal peak acceleration of 0,61g and a vertical peak acceleration of 0,17g. In case of station FKSH09 the difference of Equivalent Linear and Nonlinear method is noticeable. Poisson's ratio has already been selected comparably low. A further decrease in Poisson's ratio is deemed to be unrealistic but would positively affect the results of the vertical peak acceleration in Nonlinear analyses.

As mentioned before, it is not only the peak acceleration that is of engineering interest. Figure 66 and Figure 67 show the horizontal spectral accelerations in normal respectively in logarithmic scale. It can be seen that the Equivalent Linear Method fits the monitored data for periods smaller than 0,18 seconds whilst the result for periods in the range of 0,18 to 0,3 seconds overestimates the observed data. Even though the model slightly overestimates the response for periods smaller than 0,05 seconds, and significantly exceeds observed data in the range of 0,18 to 0,3 the approximation is deemed to be acceptable. But, the monitored spectral acceleration at 0,24 seconds, still is 2,2 times higher than the calculated one. Much better accuracy is met for periods exceeding 0,3 seconds.

Again the logarithmic scale (Figure 67) is plotted to visualize its misleading effect only. If having an unprecise and quick look on Figure 67 one might think that the calculated results of Equivalent Linear Method perfectly fit the observed ones for all periods.

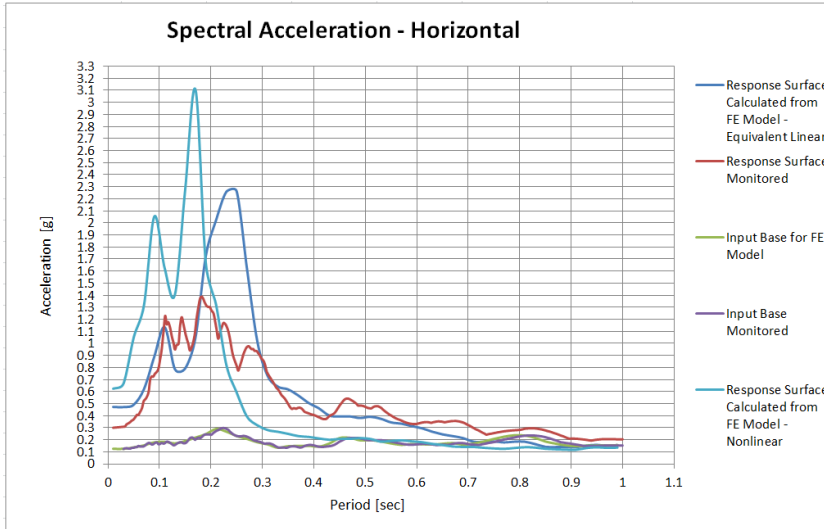


Figure 66 FKSH09 horizontal spectral acceleration

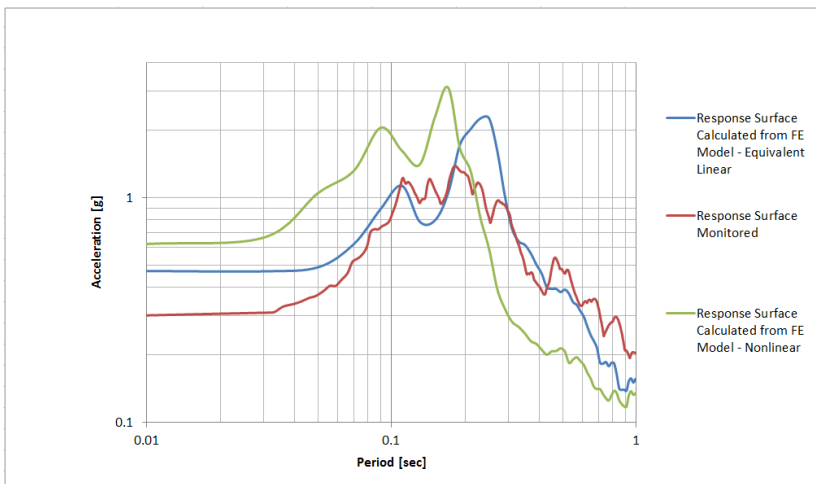


Figure 67 FKSH09 horizontal spectral acceleration (logarithmic scale)

Figure 68 and Figure 69 show the vertical spectral accelerations in normal respectively in logarithmic scale. This time it can be seen that the Equivalent Linear Method underestimates the observed data for periods smaller than 0,08sec whilst it significantly overestimates the amplification between 0,08 to 0,25 seconds. The reproduction of the vertical response spectrum may be termed weak in case of FKSH09 station even though the vertical peak acceleration is perfectly simulated.

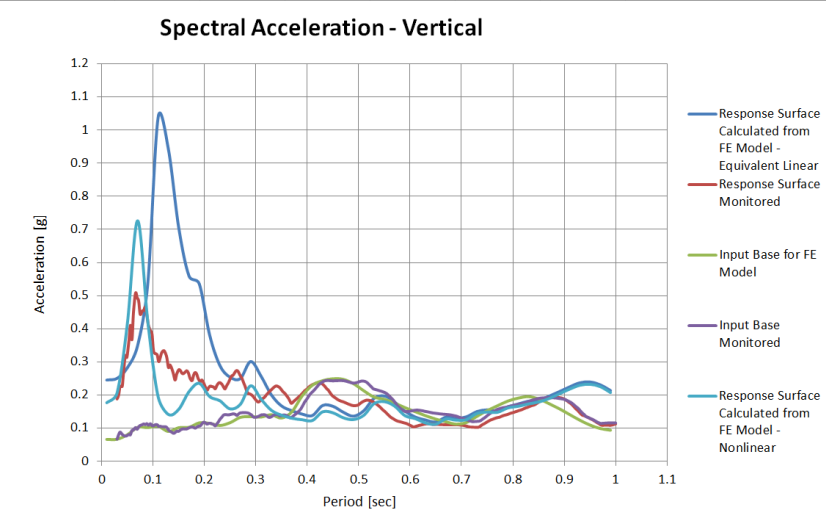


Figure 68 FKSH09 vertical spectral acceleration

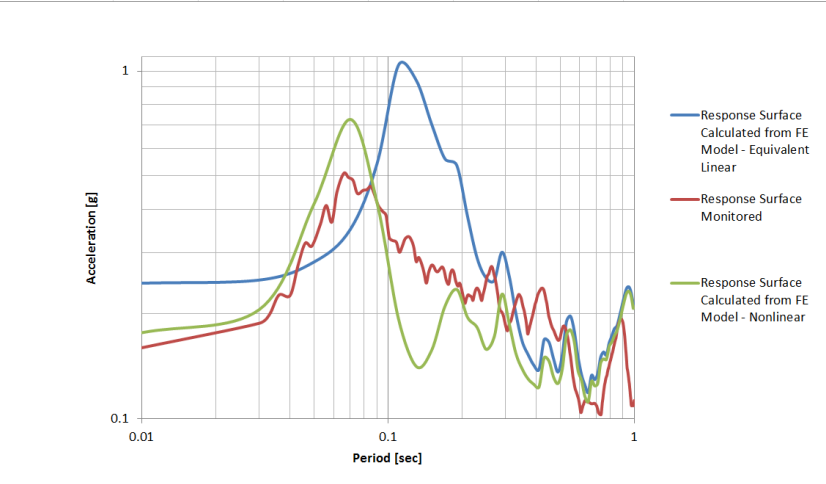


Figure 69 FKSH09 vertical spectral acceleration (logarithmic scale)

From Figure 66 to Figure 69 it is clear that the results of the Equivalent Linear Method better reproduce the structural behavior than the Nonlinear method does. The Nonlinear method in case of FKSH09 produces results that do not satisfactorily represent the observed behavior. A slightly better calibration of the Nonlinear method might be possible but would call for unrealistic parameter sets.

In general, the Equivalent Linear method provides better possibility for calibration if compared to the Nonlinear method. This is mainly due to constraints of less input parameters. Both methods call for minimum 7 input parameters, but damping and  $G_{\max}$  reduction may be fully specified within Equivalent Linear Method whilst they are bound to fixed mathematical formulas in Nonlinear method.

### 9.2.3 Seismic Observation Station FSKH10

#### 9.2.3.1 Model Geometry / Model Assumptions

Figure 70 shows the model for initial stress conditions. Boundary conditions are the same as selected for FSKH08 respectively for FSKH09 model. Based on  $V_p$  wave investigations the phreatic surface was fixed 4m below ground surface ( $V_{p,water} = 1500\text{m/sec}$ ). Station FSKH10 was built on shallow deposits overlaying low strength rock formations (see Table 11 c). Borehole seismic investigations revealed shear wave velocities in the range of 850 to 1300m/sec at depths deeper than 12m below ground. The lower accelerometer is located at bottom of a 146m deep borehole. Rock formations with higher shear wave velocity are present approximately in borehole middle. This higher strength rock is interbedded in lower strength rock formations above and below. As the observed shear velocities indicate weak rock conditions all rock formations need to be described within the numerical model.

Figure 71 shows the model used for seismic analyses. Boundary conditions, observation points and damping elements were applied the same way as described for FSKH08 and FSKH09 model. The analyses have been performed using GeoStudio 2012 software. The time history accelerograms obtained from FSKH10 borehole bottom were applied as input motion to the base of the model.

The width of the model was selected to 12 times its height to exclude effects from left and right side model edge.

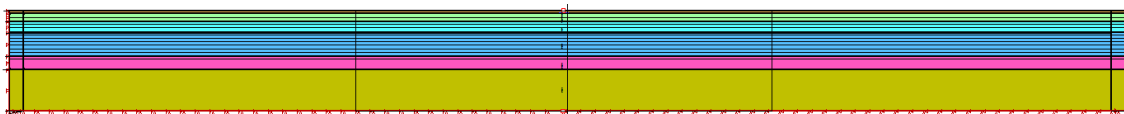


Figure 70 Modelling initial stress conditions

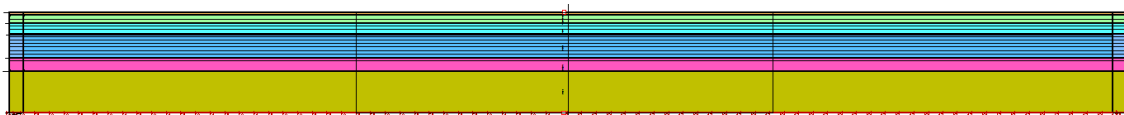


Figure 71 Model for dynamic analysis



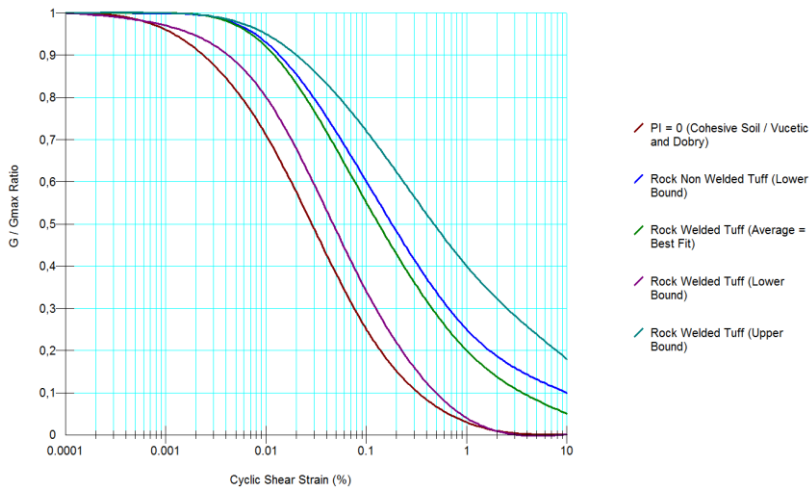
### 9.2.3.2 Best Fit Parameter-Sets

Table 14 summarizes the material parameter sets that resulted in the best fit for the back-calculation of the monitored surface accelerations. Again the result of the calculated surface acceleration is highly affected from  $G_{max}$ ,  $G_{max}$  reduction, weight and Poisson's ratio. Figure 72 and Figure 73 show the selected  $G_{max}$  reduction and damping graphs. Selected functions were published by Vucetic and Doby (1991, Figure 85) and by Jeon (2008). It has to be stated that unrealistic high parameter deviation was used for all rock formations. Extreme parameter sets in a sense of upper limit or lower limit in weight,  $G_{max}$  or damping had to be applied to come as close as possible to the observed seismic data on ground surface. Although extreme parameter sets have been used, they still are in accordance with test results published from Jeon (2008).

Analyses have been conducted comparing the material codes of the equivalent linear and the nonlinear method. Nonlinear analysis have been performed using the same set of material parameters as shown in Table 14, whereas minimum and maximum damping have been selected same as the left and right boundary values shown in Figure 73

Estimated material type	Shear wave velocity [m/sec]	Depth [m]	Colour in calculation	Plasticity index [-]	Weight above water table (saturated by matrix suction) [kN/m <sup>3</sup> ]	Saturated Weight [kN/m <sup>3</sup> ]	Poisson's ratio [-]	$G_{max}$ [kN/m <sup>2</sup> ]	Internal angle of friction [°]	Cohesion [kN/m <sup>2</sup> ]
Fine Sand - loose	150	0 - 4		0	20	-	0.25	45000	28	30
Rock (non welded Tuff)	650	4 - 12		0	-	12.5	0.2	400000	35	200
Rock (non welded Tuff)	850	12 - 32		0	-	10.5	0.17	500000	40	500
Rock (moderately welded Tuff)	1100	32 - 66		0	-	17.8	0.11	3600000	42	1000
Rock (moderately welded Tuff)	1300	66 - 86		0	-	18.5	0.1	4700000	45	1500
Rock (moderately welded Tuff)	940	86 - 146		0	-	14	0.16	2600000	40	500

**Table 14 Material parameter sets applied to FKSH10 analysis (equivalent linear)**



**Figure 72  $G_{max}$  reduction sets applied to FKSH10 analysis (equivalent linear)**

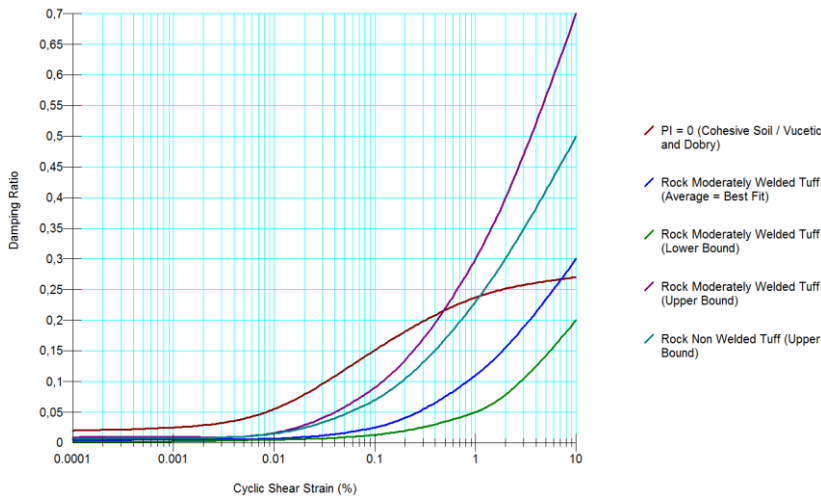


**Figure 73 Damping sets applied to FKSH10 analysis (equivalent linear)**

### **9.2.3.3 Results and Comparison**

Figure 49 shows the accelerations obtained from station FKSH10 during Tohoku earthquake in March 2011. The horizontal acceleration observed in East – West direction resulted in a peak of 0,138g (i.e. 135,2gal) at borehole bottom and 0,783g (i.e. 768,1gal) at ground surface. In vertical direction a peak acceleration of 0,088g (i.e. 86gal) at borehole bottom and 1,036g (i.e. 1016gal) at ground surface was monitored. The read out is a little unexpected. The horizontal acceleration at borehole bottom is 35% higher than the vertical one. However, at ground surface, the horizontal peak acceleration is less than the vertical one (i.e. 20% smaller).

The parameter set presented in Table 14 resulted in the best fit calibrated for the Equivalent Linear Method. The calculations resulted in a horizontal peak acceleration of 1,22g and a vertical peak acceleration of 0,73g. Compared to the results obtained for station FKSH08 and FKSH09 the peak accelerations it was impossible to match the observed data.

The main reason for this is assumed to be due to the inter-bedded stiffer rock formations. The borehole was drilled into low strength rock formations with varying shear velocity. The read out was taken at borehole bottom with stiffer rock formations overlying the seismograph. It is likely that the surface acceleration is mainly affected by the excitation within the stiff rock layers which might be significantly different from the acceleration monitored underneath it. The natural ground seems to have highly anisotropic behavior.

A further reason for the mismatch might be that the shear wave velocity of the rock underneath the seismograph is constant (i.e. same type and quality of rock underneath the seismograph). As a result the input motion would have to be applied to a transient boundary at the lower model edge. Unfortunately this is impossible in GeoStudio 2012 software. The input motion is always applied to the models lower fixed boundary resulting in full reflection of incoming waves. This type of boundary is absolutely correct if the input data was monitored at a stratigraphic boundary where two types of materials with significantly varying parameters adjoin to each other. But this is not the case

for FKSH10 bottom seismograph. Referring to the lower boundary of FSKH08 it may be stated that the assumption of a fully reflecting lower boundary exactly meets the natural site conditions as the shear wave velocity increases significantly below the seismograph (Table 11). FSKH09 indirectly meets this condition as the data was recorded in high strength rock. Due to the high strength rock the excitation may be assumed evenly distributed within this rock formation, which indeed was the reason why the rock formation was not modelled. In other words application of a fully reflecting boundary is correct for FSKH09 too as the lower model edge simulates the transition from soil like material to high strength rock (i.e. a natural boundary where incoming waves are reflected).

Figure 74 shows the calculated horizontal acceleration of FKSH10 in contrast to the monitored acceleration for each time step. The green line shows the calculated result whilst the red line shows the monitored data. By visual judgement and excluding the range from 120 to 125 seconds, it may be stated that the calculated data seems to match the observed one quite good. This is true for general shape and to some extent for the location and size of the horizontal peaks. However, in the 120 to 125 seconds range, the calculated result by far does not match the observed data.

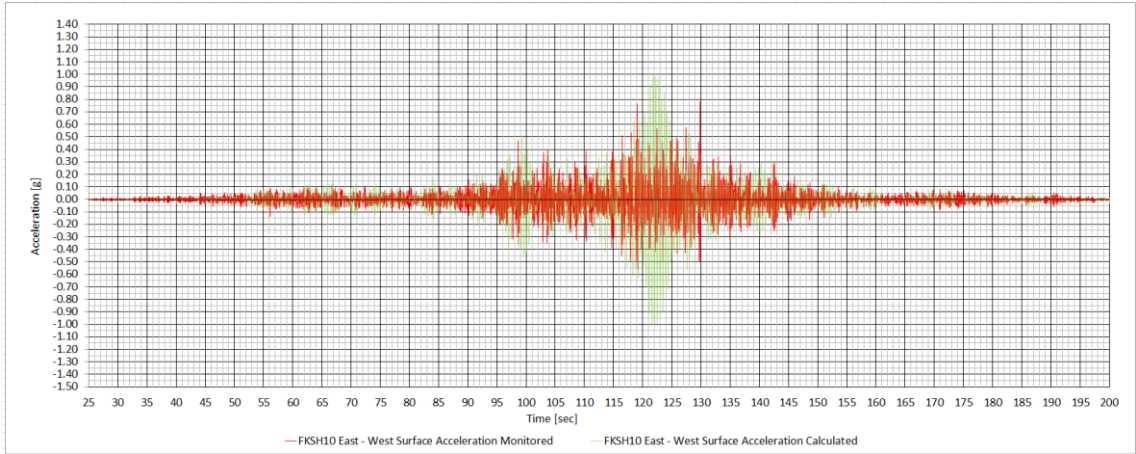


**Figure 74 Monitored vs. calculated horizontal surface accelerogram FKSH10**

Figure 75 shows the calculated vertical acceleration in contrast to the monitored acceleration for each time step. In general it may be stated that the calculated acceleration does not match the observed at all. The result highly overestimates the surface

acceleration between 112 to 123 seconds, but can't reproduce the real peaks between 127 to 129 seconds.

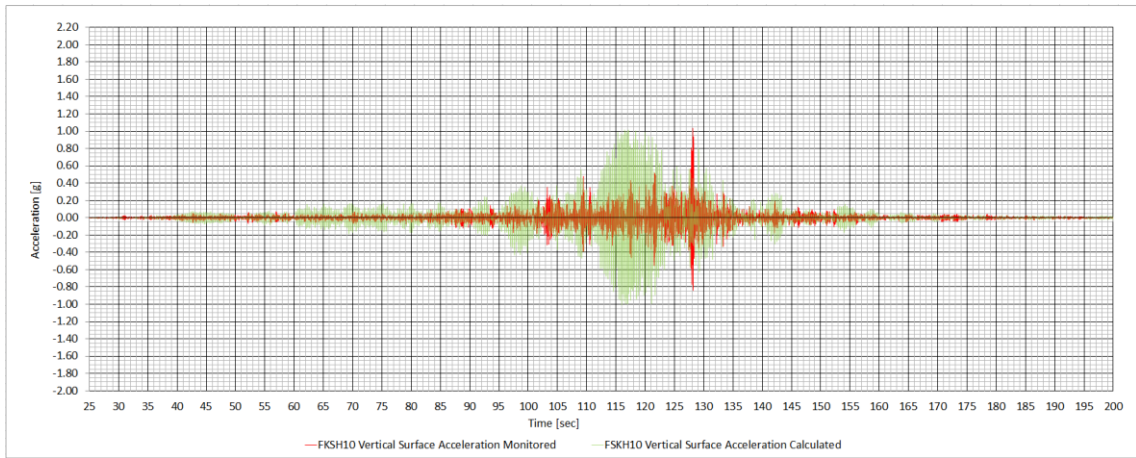


**Figure 75 Monitored vs. calculated vertical surface accelerogram FKSH10**

In contrast to the Equivalent Linear Method the Nonlinear method resulted in a horizontal peak acceleration of 0,54g and a vertical peak acceleration of 0,36g. In case of station FKSH10 the difference of Equivalent Linear and Nonlinear method is significant in number but both methods have in common that they can't reproduce the observed data.

Figure 76 and Figure 77 show the horizontal spectral accelerations in normal respectively in logarithmic scale. It can be seen that the Equivalent Linear Method completely mismatches the monitored data for all periods smaller than 0,9 seconds.

Again the logarithmic scale (Figure 77) is plotted to visualize its misleading effect only.

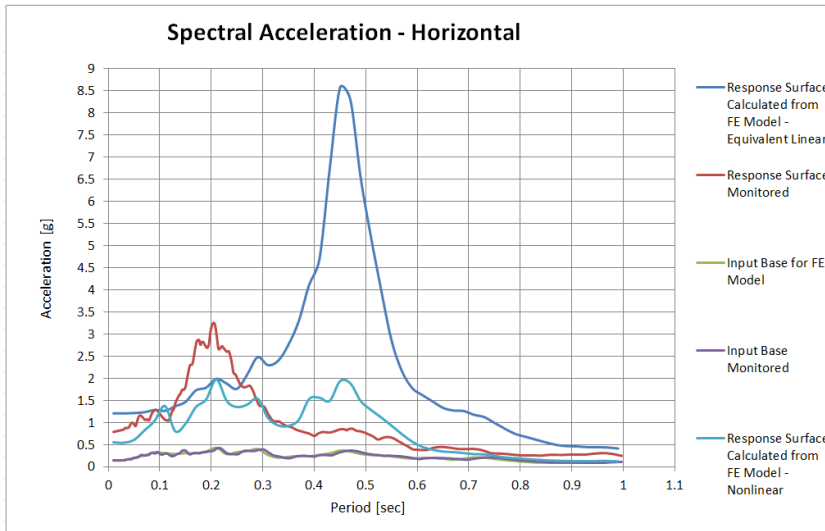


Figure 76 FKSH10 horizontal spectral acceleration

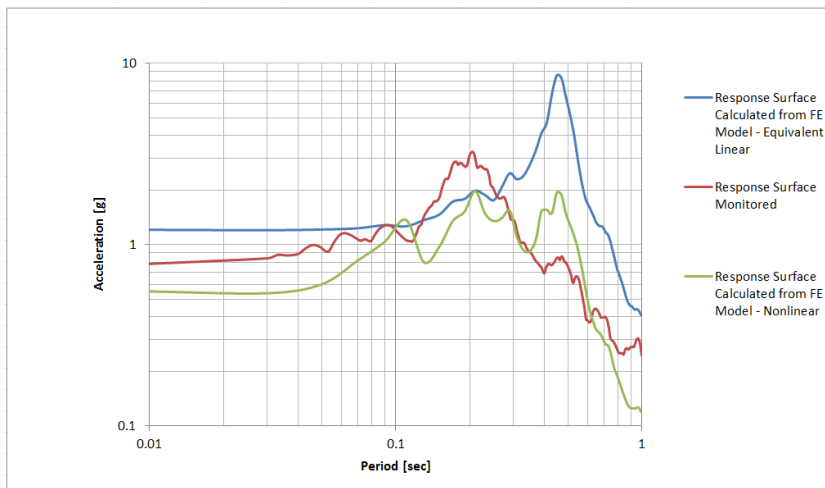


Figure 77 FKSH10 horizontal spectral acceleration (logarithmic scale)

Figure 78 and Figure 79 show the vertical spectral accelerations in normal respectively in logarithmic scale. The same comments as stated for the horizontal spectral acceleration keeps true for the vertical spectral acceleration. The observed data can't be reproduced, not even approximated.

From Figure 76 to Figure 79 it becomes clear that the results of both, the Equivalent Linear and the Nonlinear method cannot reproduce the surface response spectrum in case of complex ground profiles. However this is thought to be mainly due to the fact that the dominating input motion and its location are unknown in case of FSKH10.

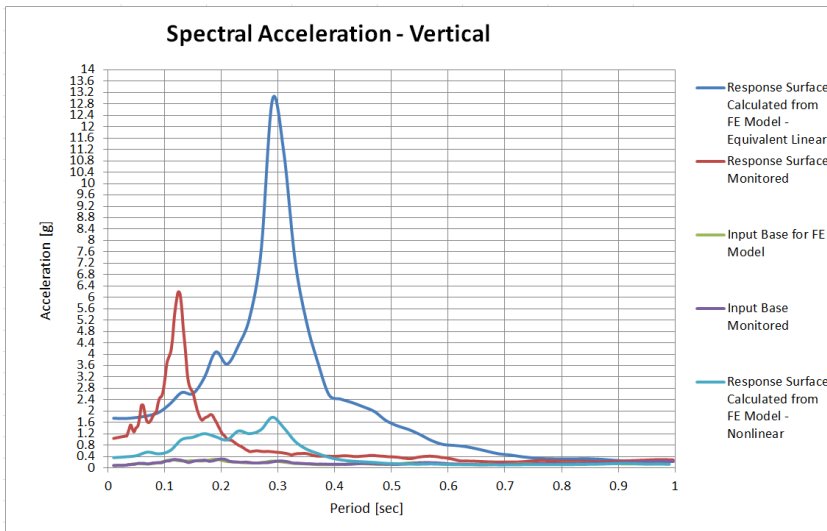


Figure 78 FKSH10 vertical spectral acceleration

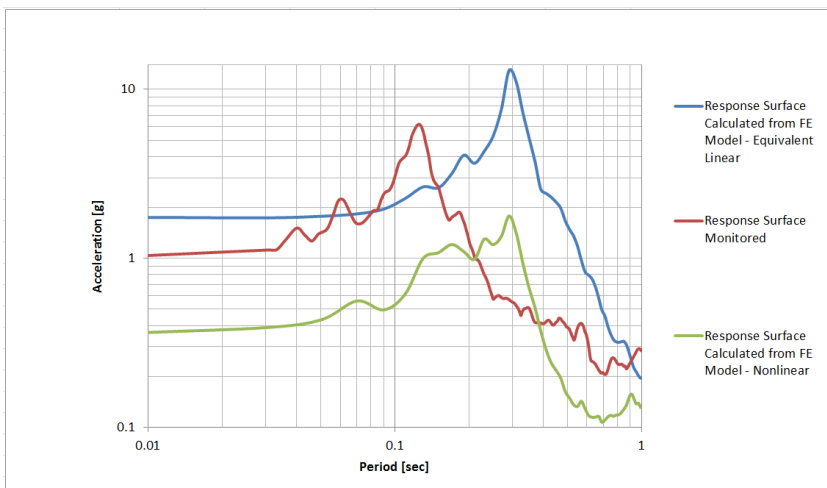


Figure 79 FKSH10 vertical spectral acceleration (logarithmic scale)

It has to be pointed out that this is particularly not the fault of the numerical model; it is the Engineer that has to take care about site specific conditions and needs to decide how to deal with it. FKSH10 demonstrates the effect of complex ground conditions and boundary assumption in numerical modelling. It furthermore shall draw the attention to Engineers to foresee weak rock conditions within their numerical model if they are present in reality and site specific input acceleration is available for high strength rock only.

## 9.3 Conclusions

### 9.3.1.1 *Guideline for Buildup of Numerical Models*

#### Effect of damping edge elements, boundary conditions and model dimensions:

The effect of damping boundary elements located at left and right hand side model edge has been studied. Application of such damping elements is often recommended in international literature to overcome potential effects of wave reflection at the model boundaries. The same material parameters have been applied to the damping elements as for their horizontal neighbor regions with the only exception of a constant damping ratio of 99% applied over the full range of shear strain. The damping elements could only be applied to the left and right hand side boundaries as the horizontal (i.e. lower) model base needs to be undamped to facilitate correct application of input motions.

The effect of such elements was found to decrease with increasing ratio of horizontal to vertical model dimension. In order to overcome influences from the freely deforming left and right hand side model boundaries, the horizontal width of the model has to be selected in a range of 10 to 15 times the vertical one anyway. This is true if compressible material is part of the foundation. The base width may be reduced significantly if high strength rock is simulated. If the selected ratio of model dimension exceeds 15, no positive effect of damping elements could be found anymore. No deviation between damped and undamped models could be observed in case of FSKH09. In cases where the horizontal width was less than 10 times the vertical one, damping elements had positively influenced the calculation results. In case of FSKH08, the calculated surface pga varied by 8% between damped and undamped boundary analysis.

Vertical and horizontal input acceleration need to be applied at same time if accurately modelling reality. In dam design, the input acceleration is typically applied to the lower model base. In order to study the effect of wave reflection, two cases were investigated. At first the horizontal input motion (no vertical excitation) was applied only. In a second step the vertical input motion (no horizontal excitation) was applied only.



If the model width is selected in sufficient ratio to the model depth, the horizontal input does not cause significant wave reflection at the model boundaries.

However, the vertical input might cause a noticeable effect. Within the presented analysis the calculated horizontal surface peak acceleration grew up to 10% of the vertical input peak (although no horizontal input motion was applied). If damping boundaries were applied at left and right hand side, this effect decreased to 5%.

Furthermore it is the Engineers decision if the application of a fully reflecting lower model boundary fits the real site conditions.

Accurate modelling of dynamic behavior calls for the application of damping boundaries or for very wide models. However the effect is small compared to other factors that might affect the calculated results.

### **9.3.1.2 Discussion on Material Parameter-Sets**

#### **Sensitivity Analysis – Factors largely influencing the Calculation Results:**

In order to find out those parameters that would strongly affect the result, sensitivity analysis have been carried out by manually changes of each material parameter within its typical ranges.

Material weight, poisson's ratio,  $G_{max}$  and  $G_{max}$  reduction were found to have the biggest effects on calculation results. Unfortunately most of these parameters vary largely under changing stress – strain conditions.

**Poission's ratio** – can be calculated from seismic site investigations ( $V_s, V_p$ ). However such seismic investigations describe a material's behavior in small strain conditions. In case of a severe earthquake, noticeable shear strains may develop and application of small strain poisson's ratios would significantly underestimate the vertical surface acceleration. Poission's ratio by nature is linked to  $G_{max}$  value. Within the analysis  $G_{max}$  may change dramatically due to its depth and shear strain dependence. While changes of  $G_{max}$  are simulated within the model, poisson's ration has to be selected as a constant.

### **Layered structure of natural soil deposits and weak sedimentary rock formation –**

Natural materials do normally show anisotropic behavior. Clear isotropic material behavior is found extremely seldom in the field. This statement is essentially true if thinking in dimensions needed to investigate a structures dynamic ground interaction. Unfortunately, isotropic material behavior has to be assumed for most dynamic models.

**$G_{max} / G_{max}$  reduction** –  $G_{max}$  is highly stress-dependent and may be back calculated from shear wave velocity investigations. Several methods for measuring the shear wave velocity in the field are applicable (cross-, down-, up-hole) but in many cases their results vary in a noticeable range.  $G_{max}$  reduces with increasing shear strain. This reduction may be “accurately “(size effects, compaction, membrane effects) tested within the laboratory for small shear strain ranges only. Data for shear strains exceeding 0,1% is rare and if available it varies strongly. Back-analysis and observed behavior during severe earthquakes indicate a drastic  $G_{max}$  reduction at higher strain ranges, much more than estimated from laboratory testing. This comment is valid for material damping too. Information within the 1% to 10% strain range often relies on pure estimation. The sudden and permanent decrease in material compaction when a specific acceleration is exceeded as well as the accompanying effect on damping and  $G_{max}$  reduction cannot be described satisfactorily neither by the Nonlinear nor by the Equivalent Linear method. Nevertheless it may be stated that if the calculation results in dynamic shear strain of 1% plus there are other problems then accurate modelling of damping ratio.

**Material weight** – material weight may be assumed to be one of the parameters that are the best to describe. However, the effect of material weight is enormous and adequate data is typically not available as the materials that need to be modelled for identification of the soil – structure interaction is those that do not show constant material weight. In case of alluvial deposits, material weight may vary largely within decimeters of depth, thus making it impossible to describe the 3 dimensional layering within a 2D model. Such material may only be described by applying average parameters per layer. Material weight above phreatic surface (i.e. matric suction) as well as the exact location of the phreatic level during the earth quake is of essential interest too. If the upper layers close to ground surface are saturated, saturated by matric suction or if they are dry will largely change the dynamic behavior at ground surface.

Information accurate enough to simulate the 3 dimensional behavior of wave propagation through 3 dimensional anisotropic materials is typically not available for engineering projects. However, it is again the Engineers job to select, simplify and change the model assumption in a way that a safe result is produced. In the end the aim is to produce an economic and safe structure. It is not the aim to reproduce the exact structural response in all time steps.

### ***9.3.1.3 Comparison of Linear Equivalent and pure Nonlinear Method***

For the analysis performed the result is quite clear, the Equivalent Linear Method provides much more possibilities to change the material parameters and hence it is the better method to approximate the monitored behavior by numerical models.

This comment might also be written in other words. The Equivalent Linear Method provides much more possibilities to produce a result that is wanted and accepted. As long as the parameter sets that are used as an input for such calculations were taken from laboratory tests and have not been derived from back-calculations on observed behavior during strong motions, everyone is able to produce every result.

This comment will not hold true for all aspects when the results of the dam case studies are discussed. In case of liquefaction analysis, Nonlinear models linked to more sophisticated soil models should be the Engineers preferred selection.

Additionally it may be stated that international literature in laboratory test results is rich in case of the EL method. The results of such laboratory test may be used for Non-linear analysis too, but to the authors opinion cannot be simulated as good as this is the case in EL analysis.

## **10 Case Studies**

### **10.1 General**

The number of recorded data from dams that suffered severe ground shaking is limited. Compared to the number of suitable recordings, the number of dams hit by major earthquakes is high, but it seems that recording systems are prone to failures. Even though digital accelerations are state of the art for modern rockfill dam instrumentation, it seems that accurate site adjustments as foundation, recording time, mutual triggering, unsuitable threshold acceleration, instrument protection, safe energy supply and many other factors have in many cases prevent the documentation of accurate recordings and so delayed the increase of know how in dam society.

In fact many dam types lack for the proof of truth as they have not been shaken by earthquakes of a magnitude they are typically designed for. There are lots of recordings for earth core rockfill dams. This may be contributed to the large number ECRD's built over the world as well as to the fact that this dam type is the preferred dam type in seismic active areas. Homogeneous dams in contrast, are typically of a height where the need for seismic instrumentation is underestimated in design or it is later cancelled during construction. Hence there are many homogeneous embankments that suffered severe ground shaking but the number of recorded accelerographs is limited. Concrete face rockfill dams enjoy increasing popularity and the number of dams built all over the world increased significantly in recent time. Due to their typical height, CFRD's are normally equipped with strong motion accelerographs, however up to now the number of dams shaken by large magnitude earthquakes is very, very low and the observed performance of a high CFRD that suffered severe ground shaking is at least alarming.

## 10.2 Aratozawa Dam (ECRD)

### 10.2.1 Dam and site characterization

Aratozawa dam is a 74m high central clay core rockfill dam located in Miyagi Prefecture, Japan. The dam was severely shaken by the so called Iwate – Miyagi Nairiku earthquake in June 14<sup>th</sup> 2008 at 08:43 o clock. With a crest width of approximately 410m, the crest length to height ratio results in 5.5. Thus Aratozawa dam is located in a wide, symmetric valley indicating that 2D plain strain analysis should result in sufficient accuracy without adaption of the shear moduli. The epicenter of Iwate – Miyagi earthquake is located in a 15km distance to Aratozawa dam. Figure 80 to Figure 82 plot Aratozawa dam's plan view, maximum cross section and longitudinal section. Three digital accelerographs located at the dam base, the dam's middle and crest elevation have recorded the behavior during Iwate – Miyagi earthquake.

Maximum acceleration recorded inside of the base gallery had a peak of 1.024g (Ohmachi and Tahara 2011). The reservoir water level during the earthquake was at elevation 268.60masl which is 6.40m below maximum operation water level.

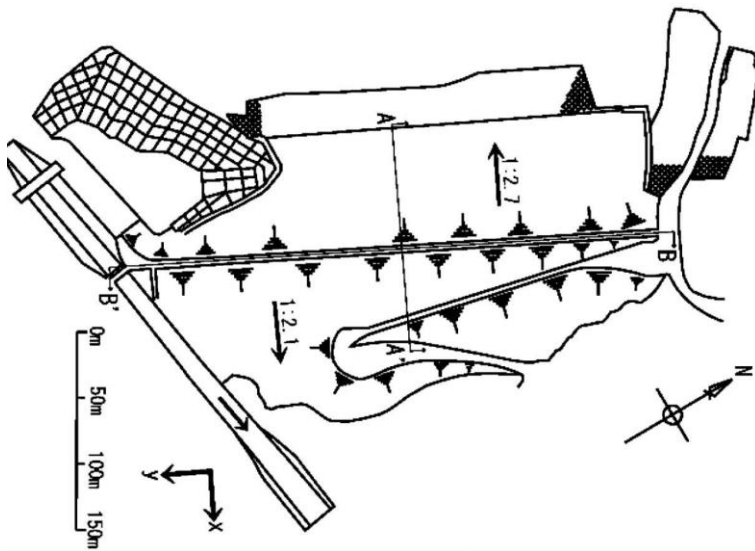


Figure 80 Plan view of Aratozawa dam (Ohmachi and Tahara 2011)

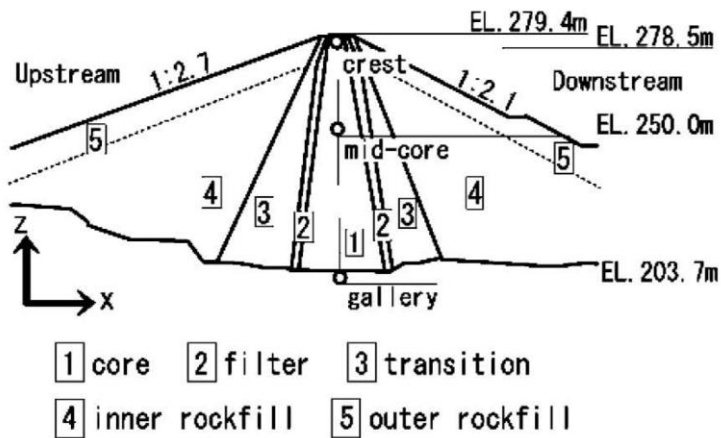


Figure 81 Maximum cross section of Aratozawa dam (Ohmachi and Tahara 2011)

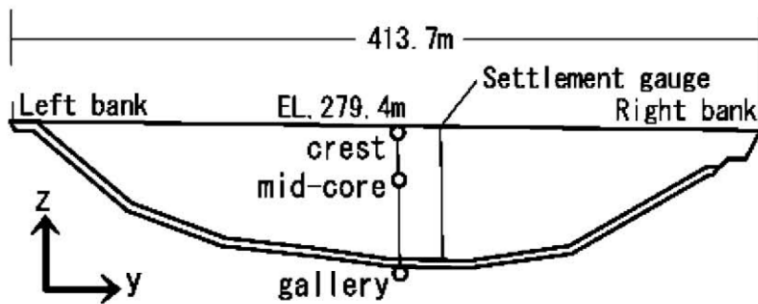


Figure 82 Location of accelerographs in longitudinal section of Aratozawa dam (Ohmachi and Tahara 2011)

Kayen et al. (2008) report that Iwate – Miyagi earthquake caused an major landslide with a total volume of 50 million  $m^3$  whereas an estimated amount of 1.5 million  $m^3$  slid into the reservoir causing a tsunami with a maximum wave height of 10m at the entries reverse slope. The tsunami did not overtop the dam crest but was partly spilled over the crest of the un-gated concrete spillway. Figure 83 shows pre- and post-earthquake aerial photos of Aratozawa dam, the reservoir and the massive landslide.

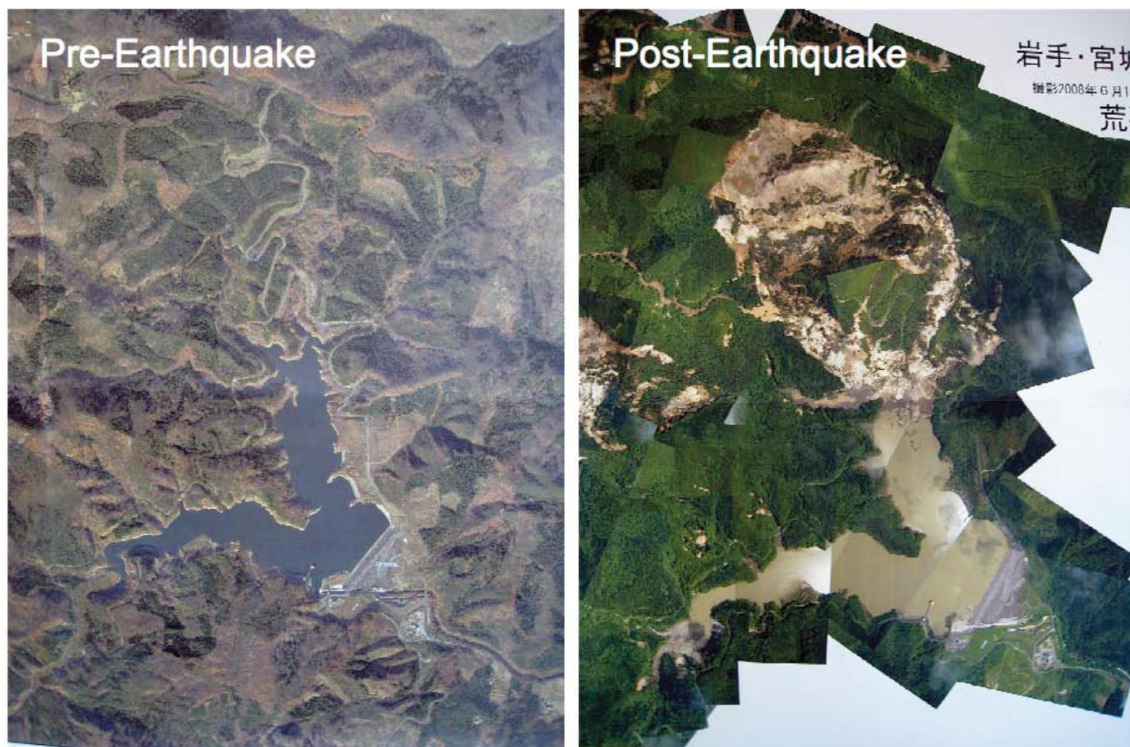


Figure 83 Pre- and post-earthquake aerial photo of Aratozawa dam, reservoir and landslide (Kayen et al. 2008)

Ohmachi and Tahara (2011) described the behavior of Aratozawa dam during the Iwate – Miyagi earthquake. Figure 27 plots the accelerograms recorded in stream direction at Aratozawa base gallery. Ohmachi and Tahara state that the dam was designed by the seismic coefficient method by use of a coefficient equal to 0.15.

### 10.2.2 Causative earthquake

On June 14<sup>th</sup> local time, Iwate – Miyagi Nairiku 2008 earthquake shook the boarder of Miyagi and Iwate prefecture killing 23 persons. The earthquake was one of the largest inland earthquakes in Japanese history and had a magnitude  $M_{JMA}$  of 7.2. The hypocentral depth was 8km. The epicenter was estimated to be located above the middle of the fault plane (Kazama et al. 2012).

Midorikawa et al. (n.d) report that the 6.9  $M_w$  (moment magnitude) earthquake was caused by a fault striking north-northeast. The mechanism was reverse faulting and



the fault plane was estimated to have a 30° dip down to the west, a length of 20km and a width of 12km resulting in a ruptured area of approximately 240km<sup>2</sup>. The average slip of the fault was 3.50m. No active fault was observed before the earthquake.

### **10.2.3 Material parameters and construction details**

Ohmachi and Tahara give a short summary of Aratozawa dam materials. They report that the dam construction was completed in 1998. The clay core may be specified as mixed gravel clay core (GC to GM) having a plasticity index of  $I_p = 32$ . The permeability coefficient of the clay core was continuously tested and resulted in values smaller than  $10^{-7}$ m/sec (Oh-ishi 1975).

Ohmachi and Tahara back-calculated the shear modulus reduction of Aratozawa dam from accelerograph readings. Figure 84 shows the published findings.

It is good to see, that the general shape of shear modulus reduction follows well known reduction curves from laboratory testing (Figure 85). However Ohmachi and Tahara found out that the dams initial shear moduli remain reduced directly after an earthquake (60% of initial small strain shear modulus). The initial shear modulus will slightly increase with time reaching its original start value again. They estimated the time span for full initial shear modulus recovery to be approximately one year.

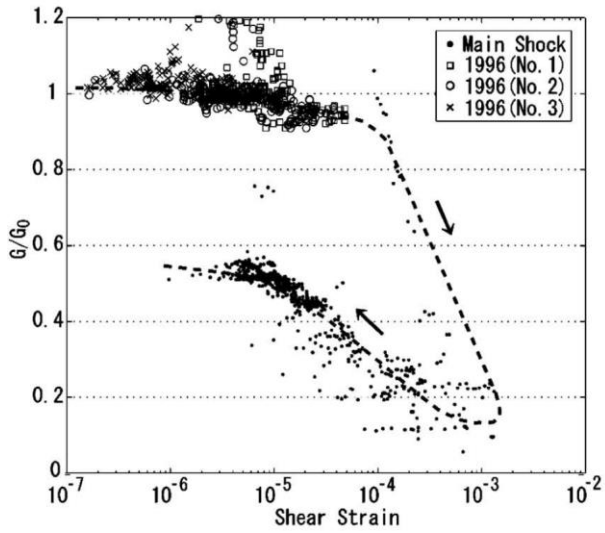


Figure 84 Back-calculated shear-modulus reduction of Aratozawa clay core [-] (Ohmachi and Tahara 2011)

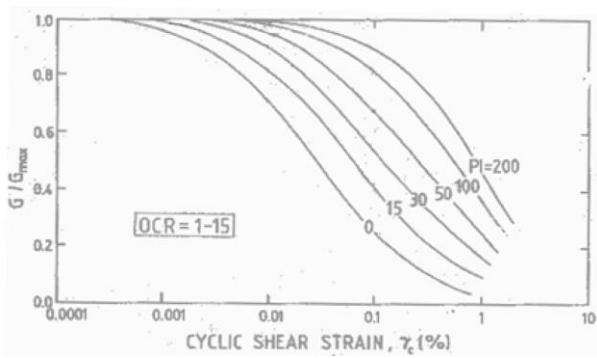
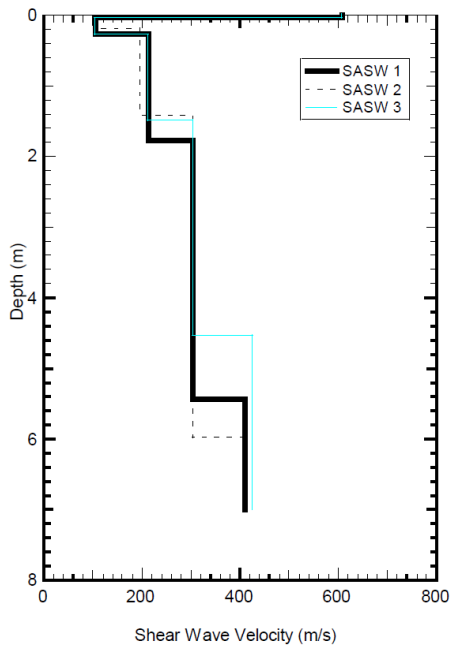


Figure 85 Shear-modulus reduction of various plasticity clays [%] (Vucetic and Dobry 1991)

Kayen et al. (2008) visited the dam site 15 days after the earthquake. They tested the shear wave velocity at three shallow locations at Aratozawa dam crest (Figure 86). Their findings were used for calibration of the small strain shear modulus at shallow depths for the later presented analysis.



**Figure 86 Shear-wave velocity measured at three locations of Aratozawa dam after Iwate – Miyagi earthquake (Kayen et al. 2008)**

#### 10.2.4 Dam behavior during Iwate – Miyagi earthquake

Aratozawa dam has shown little damage following the Iwate – Miyagi earthquake. Ohmachi and Tahara (2011) report a crest settlement of approximately 40cm, a permanent crest deformation of 4cm towards upstream and 6cm towards left side as well as minor cracks at right bank asphalt to concrete junction. The overall dam behavior was more than satisfactory with no large cracks or lateral us and ds spreading of the crest.

Ohmachi and Tahara furthermore published the pore water pressure development of pressure gauges within Aratozawa dam clay core and rockfill shoulders. Figure 87 shows the details. Prior the earthquake the reservoir water level was stable at 268.60masl with no signs of any excess pore water pressure from construction (project was completed in 1998, Figure 87 a). Seventeen minutes after the earthquake, the pore water pressure gauges show significant built up of excess pore water pressure (Figure 87 b) that tend to dissipate rapidly within the first day after the earthquake (more than 40%, Figure 87 c). The actual reservoir water level is plotted within every

read out. It can be seen that the reservoir water level rose 2.40m due to the landslide mass that slid into the reservoir, after that the reservoir water level was continuously lowered.

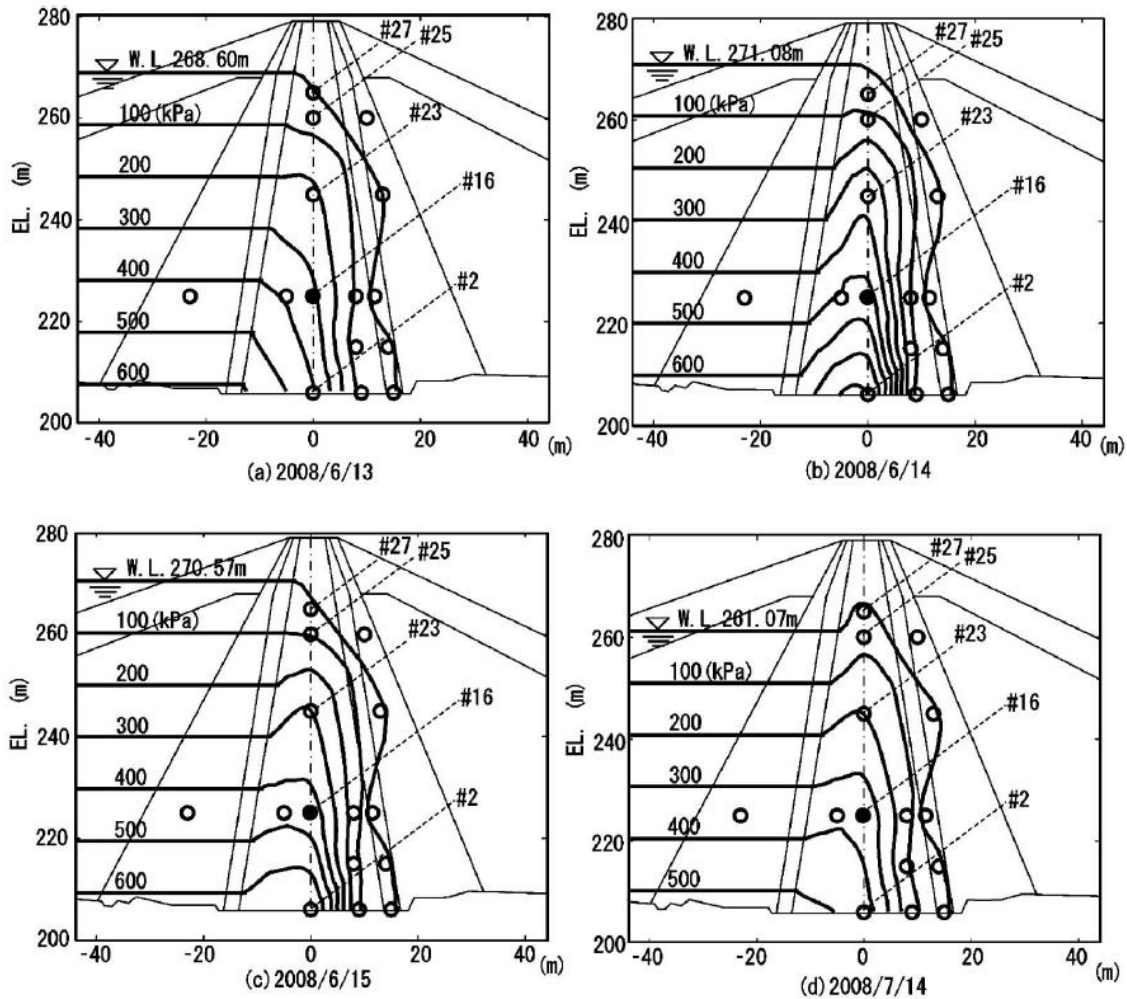


Figure 87 Pore water pressure development prior (a), immediately after (b) and past earthquake (Ohmachi and Tahara 2011)

Gauge Name	Gauge Elevation [masl]	Pore Water Pressure Prior Earthquake [kN/m <sup>2</sup> ]	Pore Water Pressure After Earthquake [kN/m <sup>2</sup> ]	Delta [kN/m <sup>2</sup> ]
#27	265	5	50	45
#25	260	47	112	65
#23	245	225	350	125
#16	225	315	530	215
#2	205	400	800	400

Table 15 Rise of pore water pressure within clay core material

## 10.3 Zipingpu Dam (CFRD)

### 10.3.1 Dam and site characterization

Zipingpu CFRD is a 156m high dam located in Sichuan Province, China. Total crest length sums up to 635m and total face slab area resulted in 117000m<sup>2</sup> (Guan 2009).

The resulting valley shape factor of Zipingpu dam is 4,81 indicating that deformation characteristics are not governed by cross valley arching. Therefore 2D analyses are sufficient for dynamic and static calculations.

The dam was built with quarry run limestone rockfill with 1.4 to 1 and 1,5 / 1,4 to 1 slope inclination at US and DS side respectively. The dam was designed for a pga of 0,26g by use of the pseudostatic approach(Guan 2009).

Figure 88 and Figure 89 show the layout and a typical cross section of Zipingpu dam.

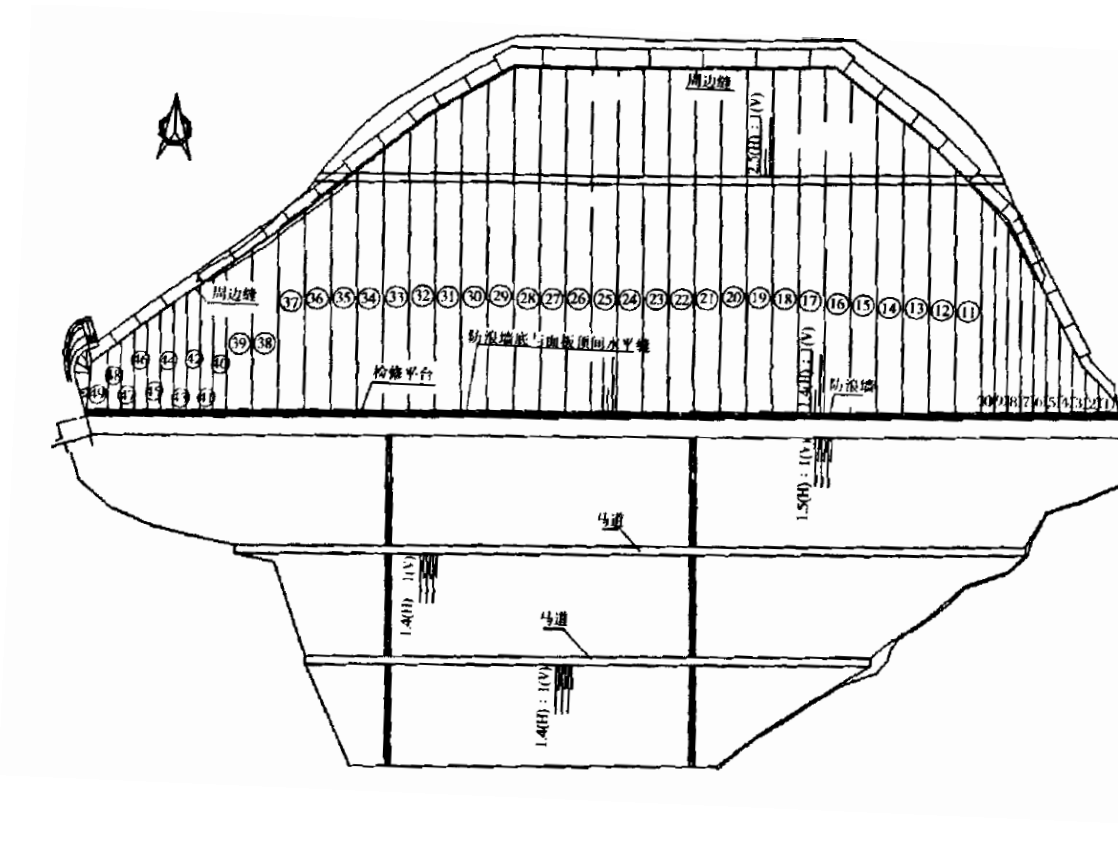


Figure 88 Layout of Zipingpu dam (Chen 2008)

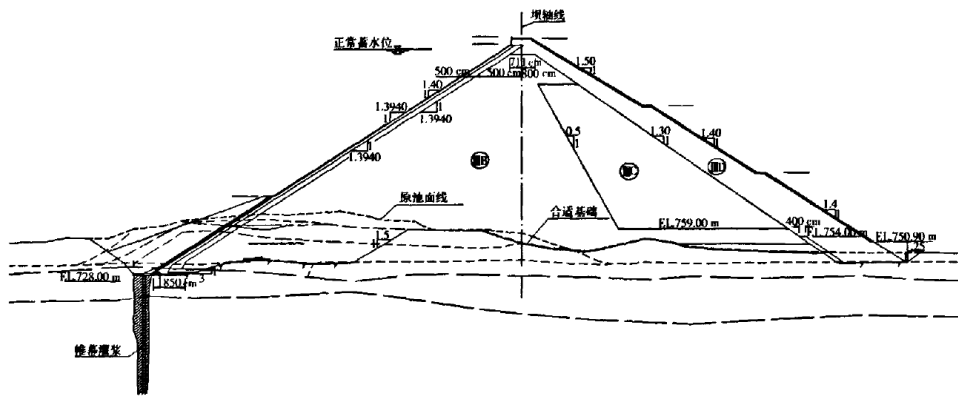


Figure 89 Typical section of Zipingpu dam (Chen 2008)

### 10.3.2 Causative earthquake

Zipingpu CFRD was strongly shaken by the so called Wenchuan earthquake on May 12<sup>th</sup> in 2008. The earthquake reached a moment magnitude of 7,9. Zipingpu dam is located in a distance of 17km to the earthquake's epicenter. Dam axis and fault normal direction are approximately in line. In total seven aftershocks exceeding  $M_w=6,0$  were observed (Guan 2009).

Wenchuan earthquake has developed along Longmenshan thrust belt. Impounding of Zipingpu reservoir is suspected to be the main earthquake trigger (Xiao, 2012).

Zou et all. (2012) report that the hypocenter of Wenchuan earthquake was shallow (14km) and that the total rupture length was in the order of 240km.

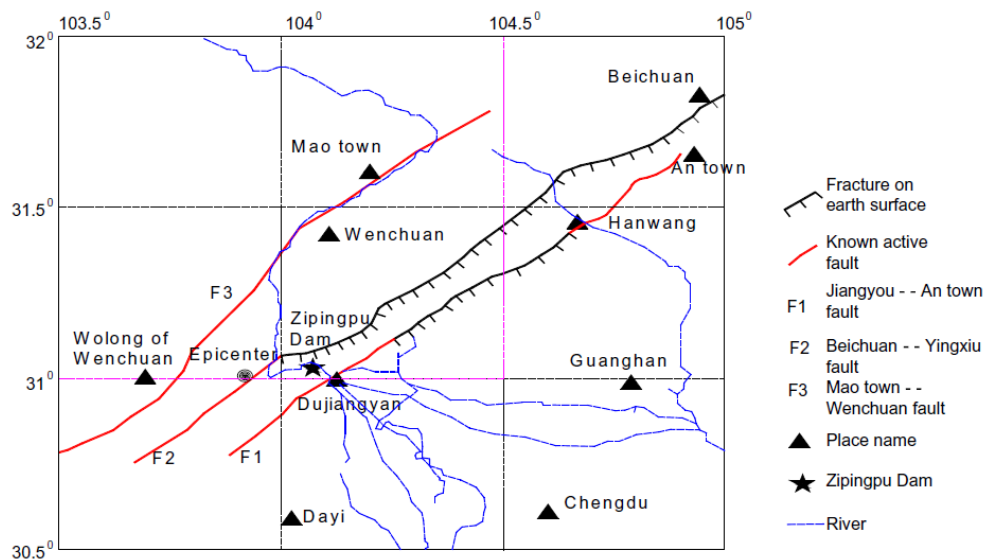


Figure 90 Location of Zipingpu dam, epicenter of Wenchuan earthquake and known fault systems (Zou 2012)

Zou (2012) reports that the well-equipped seismic observation system of the dam and reservoir area failed recording adequate data.

Unfortunately the only useful data was recorded by a single crest accelerograph. Furthermore, the recorded data needs to be cleared for local effects of fallen concrete bars that hit the instrument during the earthquake.

### 10.3.3 Dam behavior during Wenchuan earthquake

Guan (2009) provides detailed information on Zipingpu dam behavior. He reports massive spalling off of concrete edges at joint locations. These locations include the vertical parapet wall joints, the horizontal parapet to slab joints as well as the vertical slab joints mainly above but partly proceeding below reservoir water level. Furthermore he reports massive dislocation of individual concrete slabs from the supporting fill material. In case of third phase slabs, 55% of the slab area has shown dislocation from supporting fill material. Shear failure at cold joints and slip over of third phase slabs was observed. The concrete pavement at downstream crest edge nearly slid down the slope and loosening of the rip rap blocks could be observed at the dam's upper 5<sup>th</sup>. Figure 91 to Figure 96 shows pictures of Zipingpu damages.



**Figure 91 Rupture and spalling of parapet to slab joint (Guan 2009)**



**Figure 92 Dislocation of pavement at the crest's edge (Guan 2009)**



**Figure 93 Repair works at vertical slab joints (Guan 2009)**



**Figure 94 Massive spalling off of concrete edges at vertical slab joints (Chen 2008)**



**Figure 95 Repair works at cold joint slip over of 3<sup>rd</sup> phase slab after concrete removal (Guan 2009)**



**Figure 96 Cold joint failure and slip over of 3<sup>rd</sup> phase slab (Chen 2008)**

According to Guan (2009) the majority of all dam instruments remained functional after the earthquake and hence provide suitable information. Figure 97 shows the crest settlement due to the earthquake. The settlement readings were taken from the top of the parapet wall elements one day after the earthquake (May 13<sup>th</sup>) until July 22<sup>nd</sup>. It can be seen that the settlement immediately after the main shock resulted in a



maximum of 68cm. Within the following 2 months the maximum settlement increased up to 77cm. Guan furthermore states that a separation gap was found between the crest road concrete and the underlying rockfill and concludes that maximum rockfill settlements might be in the order of 90 to 100cm locally. Figure 98 shows the horizontal displacement after the earthquake again taken from top of parapet wall readings. The maximum applies to 21cm at July 22<sup>nd</sup>.

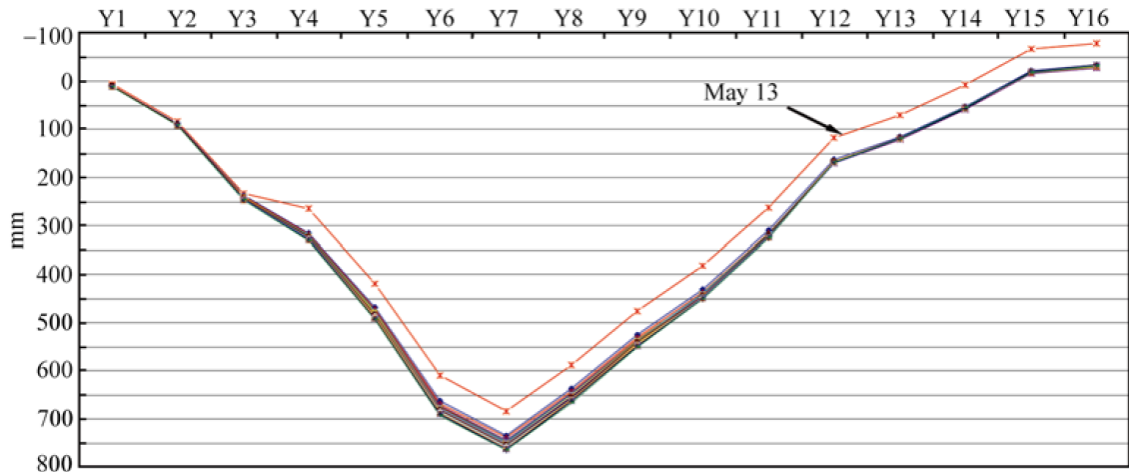


Figure 97 Vertical crest settlement taken from top of parapet wall readings (Guan 2009)

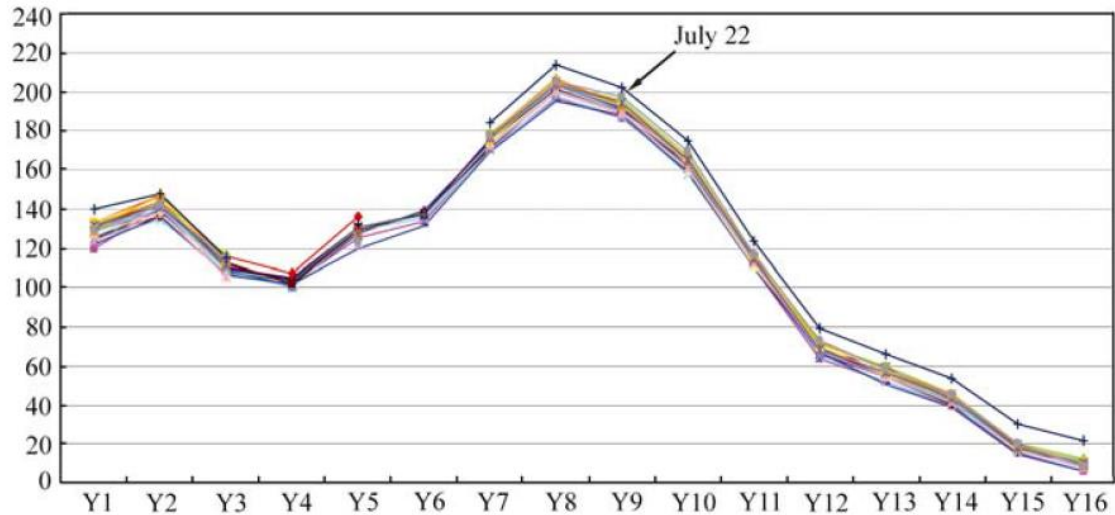


Figure 98 Horizontal displacement taken from top of parapet wall readings (+ = towards ds, Guan 2009)

Figure 99 shows the horizontal displacement vectors of ds shoulder and crest after the earthquake including deformations from aftershocks and stress redistribution creep. The deformation tends to be symmetric and gradually increase from the abutments to

the dam's mid. The horizontal deformation of surface monuments located at mid crest, mid berm EL 840 and mid berm EL 796 plot in the same range which is surprising if having in mind the results of state of the art deformation analysis. Following Newmark or Makdisi –Seed analysis the deformation (horizontal and vertical) should reduce gradually from crest to base. In case of Zipingpu dam this was clearly not the case.

Figure 100 shows the dam's inner vertical settlements as a result of the fill's dynamic densification. The settlements gradually decrease from crest to dam base elevation. Having in mind typical Newmark or Makdisi – Seed results, the settlements at the upper third would be highest whilst settlements within the lower two thirds would be very low most likely zero. This is clear as the theoretical background relies on sliding masses and deep seated slip surfaces will always result in safety exceeding 1 (i.e. no deformation). Zipingpu dam in contrast clearly shows settlements that result from dynamic compaction. Largest values can be found in midsection, gradually reducing towards upstream or downstream surface and at same time all settlements accumulate from dam base to dam crest. At this state an analogy may be drawn from wetting settlements to dynamic compaction settlements (if the typical local loosening at the dam's shallow outer surface is neglected).

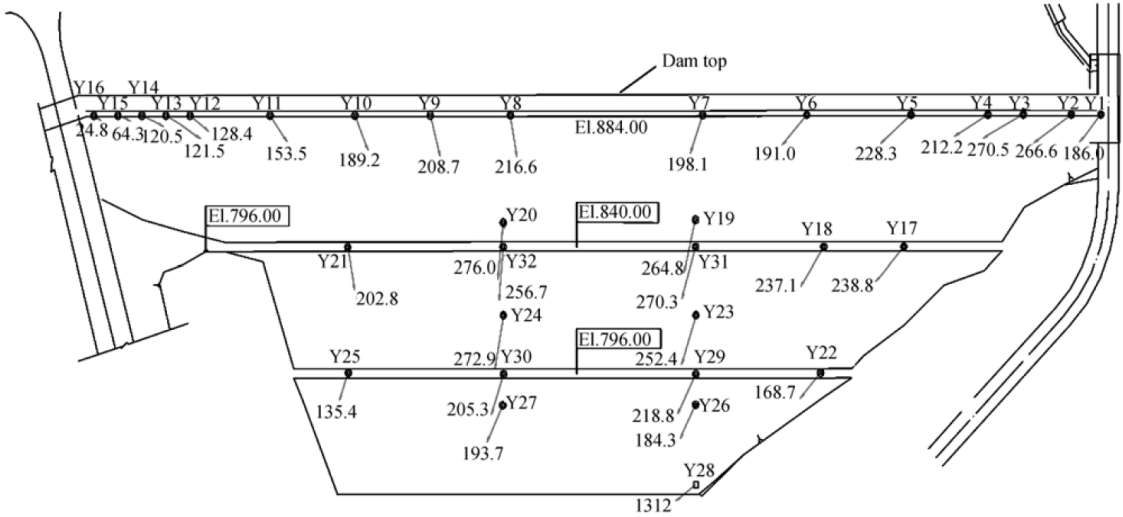


Figure 99 Horizontal displacement vectors of ds shoulder and crest surface monuments until July 20<sup>th</sup> (Guan 2009)

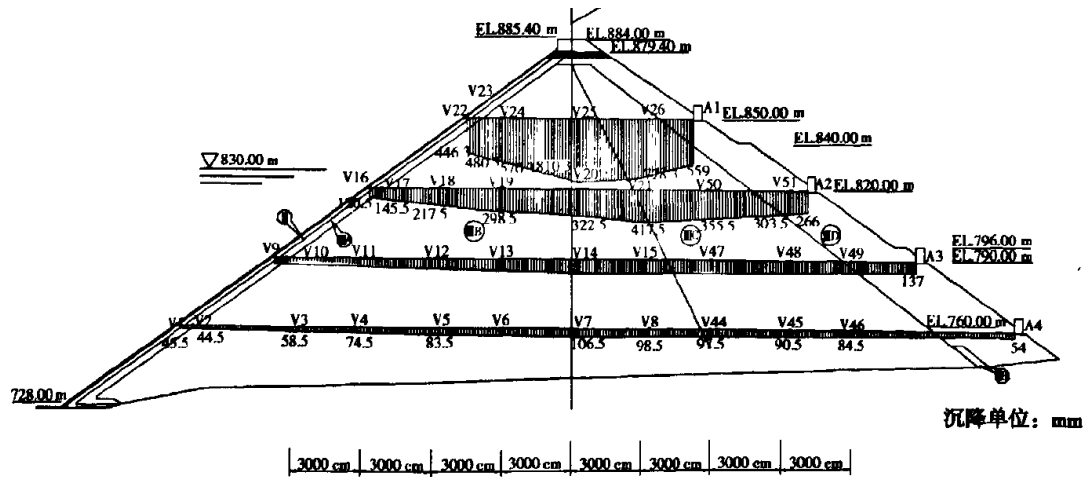


Figure 100 Internal fill settlement of Zipingpu CFRD (excluding settlements prior earthquake, Chen 2008)

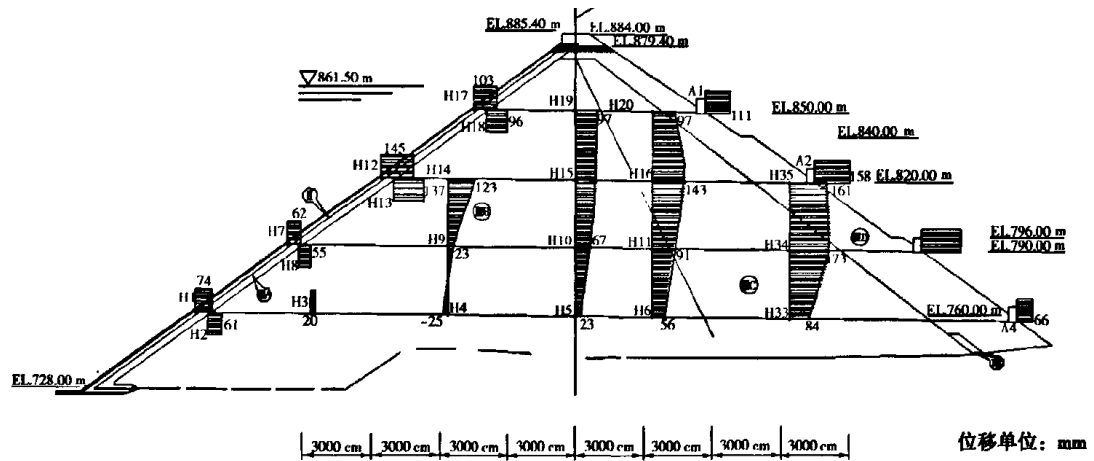


Figure 101 Internal fill displacement of Zipingpu CFRD (excluding deformations prior earthquake, Chen 2008)

During the earthquake the reservoir water level was located 48,3m below maximum reservoir level at elevation 828,7masl. After the earthquake the reservoir water level was kept below an elevation of 831masl. Leakage water is collected in a weir and total seepage increased from 10,4 l/sec before the earthquake to 19 l/sec after the earthquake. Figure 102 shows the measured seepage quantity and reservoir level development (Zeping 2009).

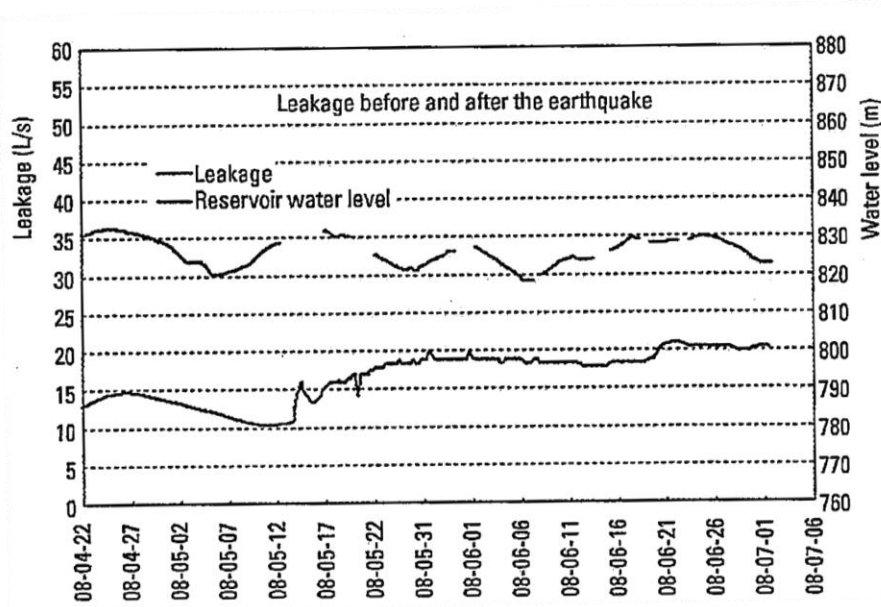


Figure 102 Leakage of Zipingpu dam before and after Wenchuan earthquake (Zeping, 2009)

Guan (2009) concludes on Zipingpu dam fill behavior: “ *The dam slopes contract inward, this is most obvious at the maximum profile. The contraction decreases with lowering of the dam elevation and almost no contraction has been observed below the first berm at El. 796.00m. After the strong earthquake, the resultant vector of the vertical seismic subsidence and horizontal displacement pointed to the inside of the dam body, which indicates a densification effect of rock fills. An aftershock measured 6.4 on the Richter scale had little effect on the dam deformation. No obvious variations were observed in deformation after two aftershocks with a magnitude of 6.1 occurring in the beginning of August.*”

## 10.4 Fujinuma Dam (Homogeneous)

### 10.4.1 Dam and site characterization

Fujinuma main dam is an 18.50m high earthfill dam located in Fukushima Prefecture, Japan. The dam failed during / after the Tohoku earthquake in March 11<sup>th</sup> 2011 (14:46 local time) causing the loss of 8 lives. Fujinuma dam construction was started in 1937. Construction were stopped during World War 2 and finalized in October 1949, serving as an irrigation reservoir. Figure 103 shows an aerial view of Fujinuma dams and irrigation reservoir prior failure. A typical cross section is shown in Figure 104. Upstream slope increases stepwise from 2.80 H : 1 V to 1.5 H : 1 V at crest elevation whilst downstream slope had an inclination of 2.50 H : 1 V. The dam crest had a width of 6m and length of 133m in longitudinal direction. The dam suffered significant leakage until the late 1970's and repair work were carried out from 1984 to 1992. In order to reduce the leakage, a grout curtain was successfully applied (JCOLD, 2012).

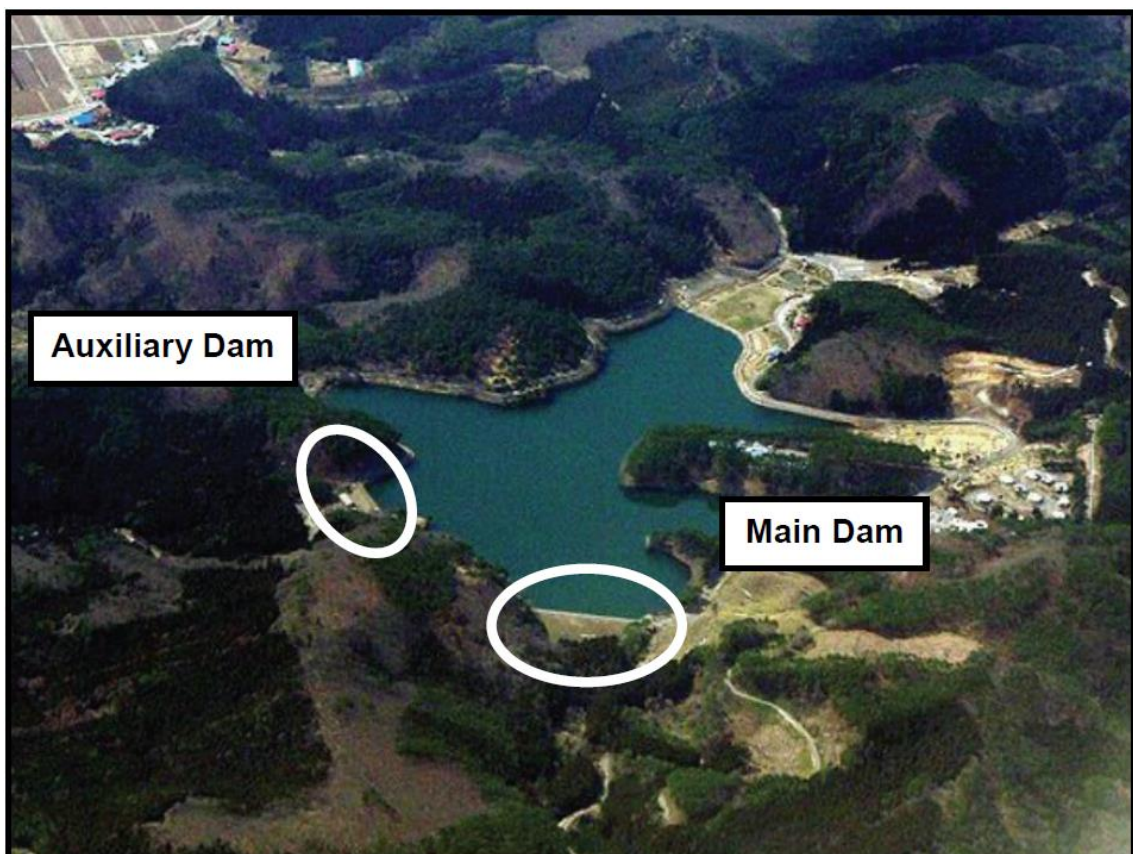


Figure 103 Aerial view of Fujinuma irrigation reservoir (Harder et al, 2011)

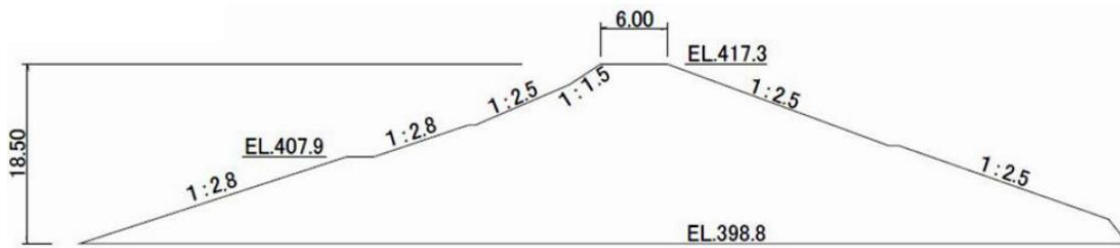


Figure 104 Typical cross section of main Fujinuma earthfill dam [m] (Matsumoto, N., Sasaki, T. and Ohmachi, T., 2001)

#### 10.4.2 Causative earthquake

Fujinuma dam failed due to the Tohoku earthquake in March 11<sup>th</sup> 2011. To date,  $M_w$  9.0 Tohoku earthquake ranks fourth in terms of the largest magnitude observed since 1900 (Table 4). The earthquake caused the loss of 15889 lives and 2601 persons still missing. The catastrophic effect mainly resulted from the destructive tsunami that hit the eastern coast of Honshu island. Fukushima Daiichi atomic power plant suffered severe damage from Tohoku earthquake and the resulting tsunami.

As reported by Matsumoto, Sasaki and Ohmachi (2001), overall damage to dams was generally low (excluding Fujinuma dam failure).

No acceleration records are available from Fujinuma dam site as no seismic monitoring equipment was installed. Figure 105 and Figure 106 show the accelerograms recorded in base rock of two accelerometers located in a distance of approximately 3km (FKSH08) and 23km (FKSH09) to Fujinuma dam site. From up to down, the records of each station represent the recordings in North-South, East-West and Up-Down accelerations. In general one can state that the peak ground acceleration of these two records do not exceed 0.19g. Within the later presented analysis, the records of FKSH08 are used as base input motion and are applied to the models lower boundary.

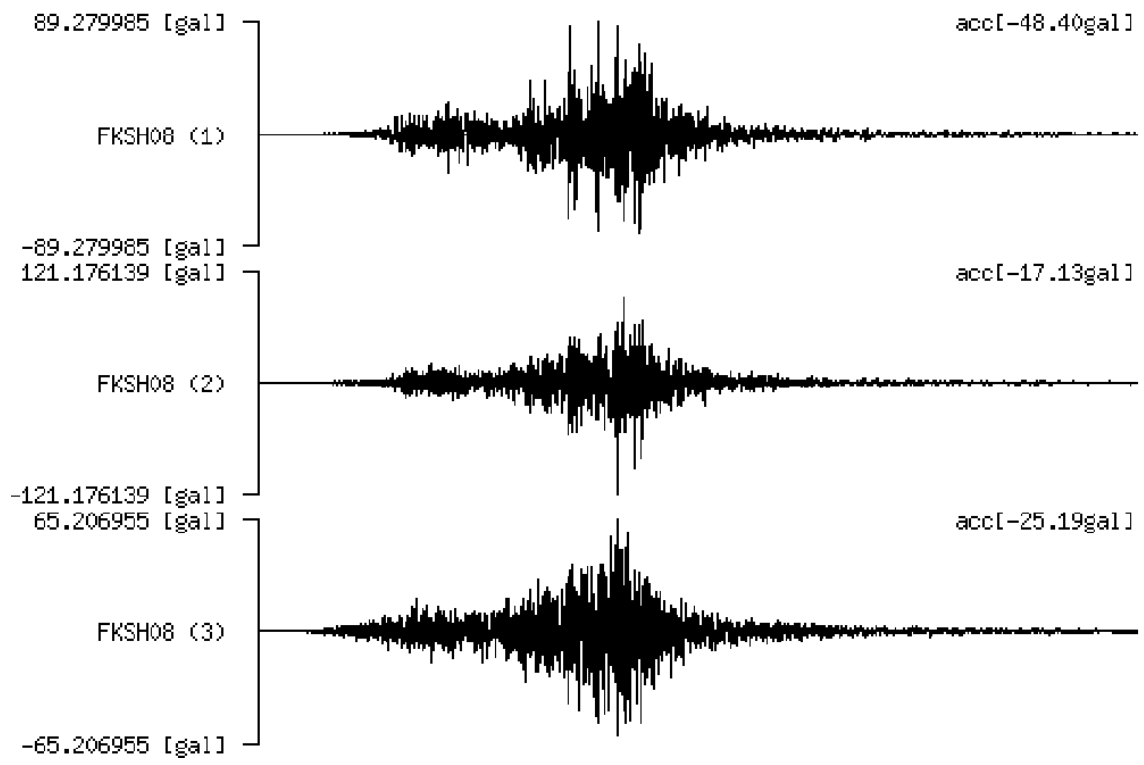


Figure 105 Accelerograms recorded by FKSH08 station situated in bedrock (courtesy NIED database)

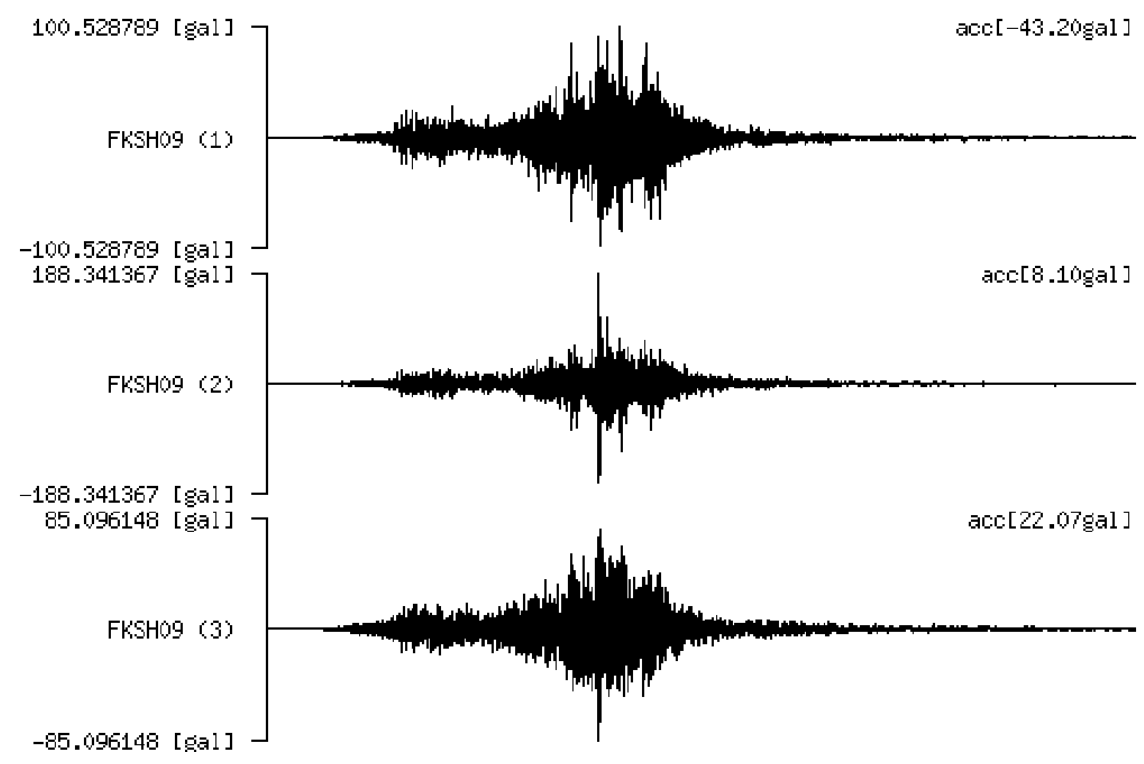


Figure 106 Accelerograms recorded by FKSH09 station situated in bedrock (courtesy NIED database)

### **10.4.3 Material parameters and construction details**

As previously mentioned the dam construction was stopped during World War 2 and finalized in 1949. Site investigations conducted by JCOLD (2012) revealed that the dam's middle and lower zones were constructed by 20 to 30cm thick compacted layers, whilst the upper zones consists of sand rich material that lack for compaction.

Harder et al (2011) visited the site on 23.04.2011 and photo documented their findings. Figure 107 shows the breached embankment in a view towards left abutment. They reported that the dam was built on black organic residual soil underlain by a layer of colluvial / alluvial origin. Underneath the colluvial / alluvial layer, tuff bed rock was seen on site. Locally tree stumps and roots where found in the black organic residual soil. Thus evidencing that clean up and preparation of the dam base was at least poor or simple not done. Within the dam footprint, a spring was observed draining water from bed rock to the former colluvial / alluvial layer. Black organic soil has also been used for embankment construction, as a 2m thick near horizontal layer was found at the scarf formed by the breach approximately 6m below former crest elevation. The black organic soil seemed to withstand the water flow better than the other fill material. Harder et al (2011) report that the embankment fill in general seemed to be cohesive material, however no evidence for filter material placed within dam cross section was found.

Charatpangoon et al (2014) visited the site after the failure and took samples for laboratory investigations. Within their article the authors describe that Fujinuma embankment mainly consisted of three types of material. Namely, the upper layer (6 to 8m, coarse light brown to grey sand), the middle layer (7 to 9m thick, brownish, cohesive soil) and the bottom layer (4 to 6m in thickness, black to dark grey, loamy clay to silty sand). In total 13 samples were taken at three locations representing the visually classified material types. These samples were tested for grain size distribution, permeability and triaxial shear strength (CU tests). Sampling method resulted in undisturbed samples, however Charatpangoon et al bear in mind that the samples were taken from a failed dam that was subject to strong ground motion. State of the art classification



resulted in the finding that bottom and middle embankment layer are not prone to liquefaction. The results of the triaxial tests are highlighted in Table 16.

Materials	Layer	$\gamma_{dry}$ (kN/m <sup>3</sup> )	$\gamma_{sat}$ (kN/m <sup>3</sup> )	$k_v \cong k_h / 4$ (m/s)	$E$ (MPa)	$K_w / n$ (GPa)	$\nu$	$c'$ (kPa)	$\phi'$ (deg)
Dam body	Bottom	16.0	18.00	$5.5E-7$	50.0	1.87	0.3	18.4	31
	Middle	14.0	16.00	$5.5E-7$	30.0	1.12	0.3	7.80	32
	Upper	16.0	18.00	$5.5E-7$	17.5	0.65	0.3	0.0	37
Foundation	-	30.0	-	-	300	-	0.2	-	-

**Table 16** Triaxial test results of samples taken at Fujinuma dam embankment after failure (Charatpangoon et al, 2014)



**Figure 107** View towards left abutment of breached Fujinuma dam (Harder et al., 2011)

One important question on Fujinuma dam material still remains open: Was the dam fill material susceptible to liquefaction or not.

At the time this thesis was written, no test on the seismic behavior of Fujinuma soils were available to the author. As described above, Charatpangoon (2014) has performed laboratory tests on Fujinuma dam fill materials and according to his findings he concludes that brown and greyfill do not fulfill the so called “Chinese criteria” and hence are not susceptible to liquefaction. However, he doubts this result himself and recommends further material testing as his judgement was based on grainsize analysis only.

Having in mind the tested unit weights of brownfill and sandfill it becomes clear that this material definitely lacks for compaction. The question is how to accurately judge if a material is liquefiable or not. There are clear standards for that. That’s not the point. In Engineering practice there is a technical solution. The point is that very often soils that in accordance to guidelines were classified non-liquefiable have liquefied in reality.

Very often the so called “Chinese criteria” is used for judgement whether a soil is susceptible to liquefaction or not. Seed and Idriss (1982) state that a clayey soil is subject to liquefaction only if all three points are fulfilled:

- Less than 15% particles smaller than 5µm
- Liquid limit < 35
- Water content to liquid limit > 0,9

Bray et al. (2004) point out that the so called “Chinese Criteria” shows deficiencies and according to their findings based on laboratory testing and site observations they conclude that the criterion needs to be adopted. Figure 108 shows the test results of Bray et al. (2004) plotted against the graphically illustrated “Chinese criteria”. It can be seen that numerous specimens that resulted in liquefaction or moderate liquefaction plot within the “Not Susceptible” area (circles = sample liquefied / square = sample showed moderate liquefaction / triangles = no liquefaction).

Figure 109 shows their recommended criteria for judgement whether a soil is susceptible to liquefaction or cyclic mobility.

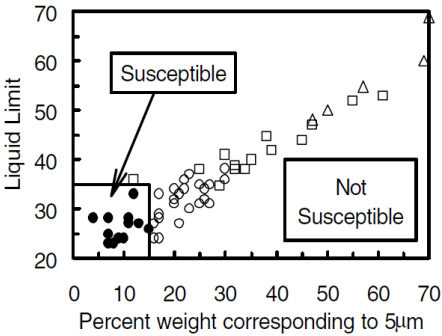


Figure 108 The “Chinese criteria” plotted against results of laboratory testing (Bray et al. 2004)

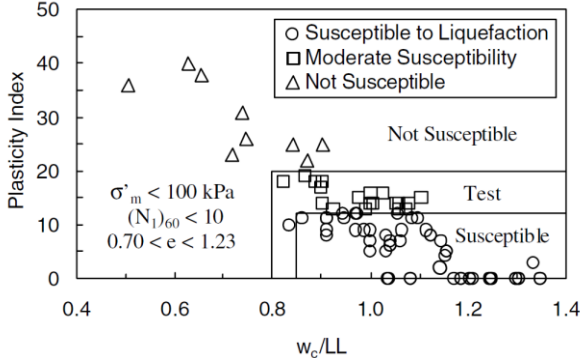


Figure 109 Criteria for judgement of liquefiable soils (Bray et al. 2004)

#### 10.4.4 Dam behavior during / after Tohoku earthquake

As reported by witnesses, the dam crest was overtopped 20 to 25min after the earthquake happened. The reservoir was near full supply level at that time (Matsumoto, Sasaki and Ohmachi, 2001).

Figure 110 shows a close up view of Fujinuma dam crest after the earthquake. The dam crest settled causing overtopping and breach of the dam.



Figure 110 Overtopped crest of Fujinuma dam (EERI, 2011)

JCOLD (2012) investigated the dam site after the failure and documented the findings thereof. Debris found downstream and upstream of the former dam axis was mapped to identify potential sliding mechanisms. As can be seen from Figure 111, numerous parts of concrete parapet beams could be found within the reservoir.

*They state: 'The dot colored blue is the parapet wall. The dot colored green is masonry riprap. The small square colored purple is the surface protection work. The rectangular colored yellow is concrete beam on the upper upstream slope. Most structural elements moved to upstream.'*

The spread of the dam debris indicates a slip failure towards upstream that triggered the crest overflow. However, JCOLD (2012) conclude that slides towards upstream and downstream must have occurred. They point out that the bracketed duration (acceleration exceeding 0.05g) lasted for more than 100 seconds, which has never been ob-

served before. Furthermore they stated that the peak acceleration at crest was estimated to be in the order of 0.44g.

The failure mode of the dam is quite controversially discussed in international dam society. If and where liquefaction occurred is one of the major questions. Ono et al. (2011) report that several sand boils were observed within Fujinuma dam reservoir whilst others state that there was no clear evidence for the presence of liquefaction (Charatpangoon et al, 2014).

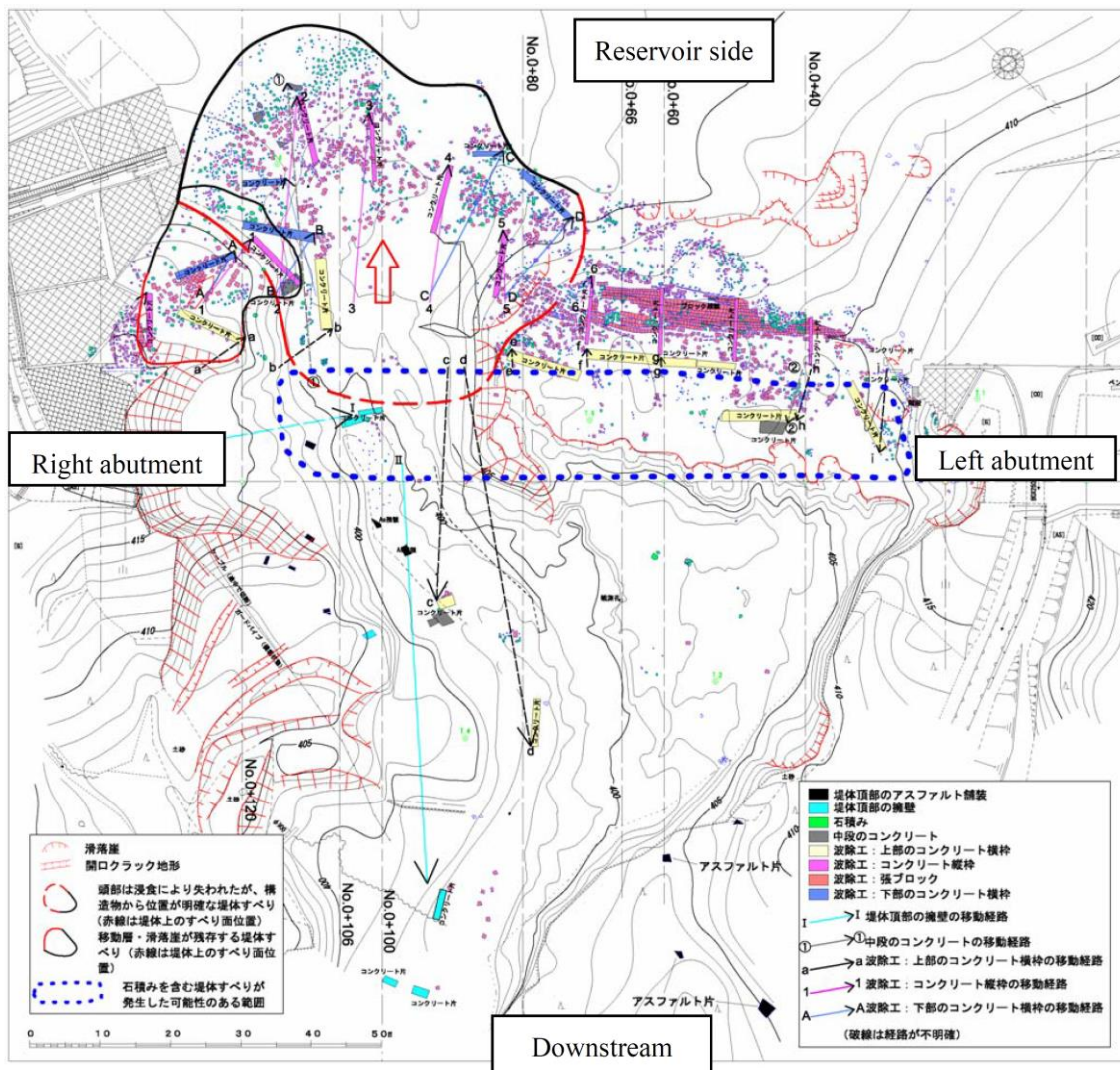


Figure 111 Mapping of rip rap and concrete blocks (JCOLD, 2012)

# 11 Modeling Procedure

## 11.1 Aratozawa Dam (ECRD)

### 11.1.1 Meshing

Figure 112 shows the numerical model of Aratozawa dam derived from software Geo-Studio 2012 at start of the dynamic calculation. The horizontal model size, it est the horizontal width of the base rock was selected 3 times the horizontal base width of the compressible fill materials. No rule has to be kept for selection of the base rock thickness. Comparatively these model dimensions seem to be too small especially if having in mind that Aratozawa dam was not built on high strength rock. In this case the selection was guided by the available seismic input data. Iwate / Miyagi earthquake was recorded by the dam's strong motion accelerograph at the dam's base gallery. This data is used as input for the dynamic model of Aratozawa dam. Hence the base rock was modeled only to evenly distribute the measured data within the dam footprint. The base rock therefore is modelled infinitely stiff. For this reason, the dimensions of the base rock were kept small to limit computation time.

Figure 113 plots the detailed section of Aratozawa dam model showing the overall geometry, material boundaries, the mesh and selected location of history points. History points depict the location of the strong motion accelerographs.

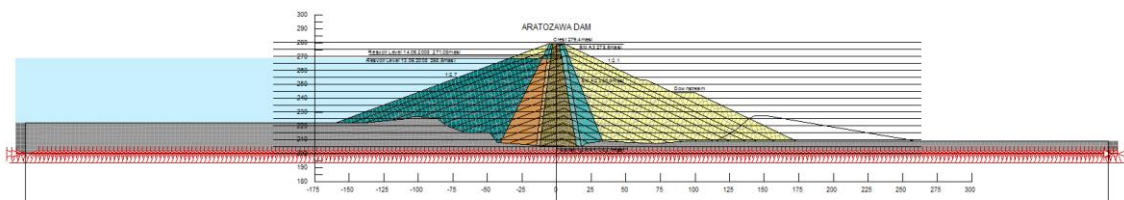


Figure 112 Aratozawa dam model after impounding, general view

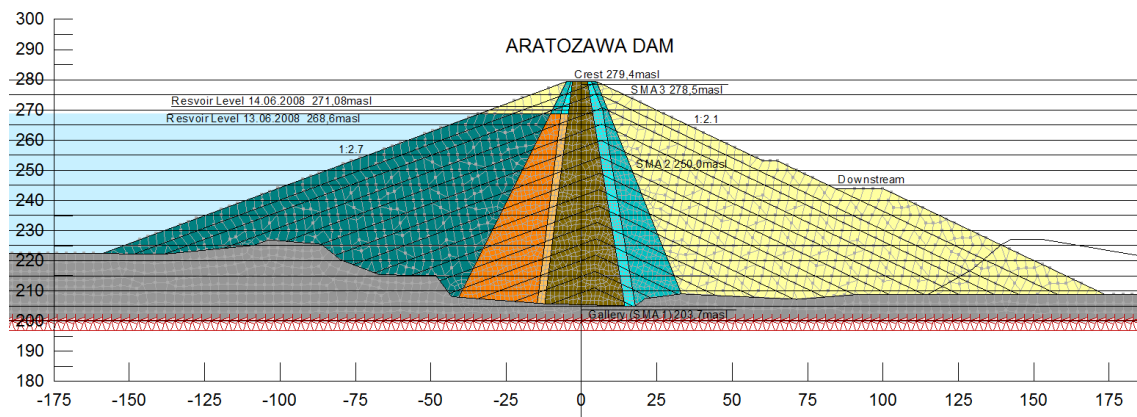
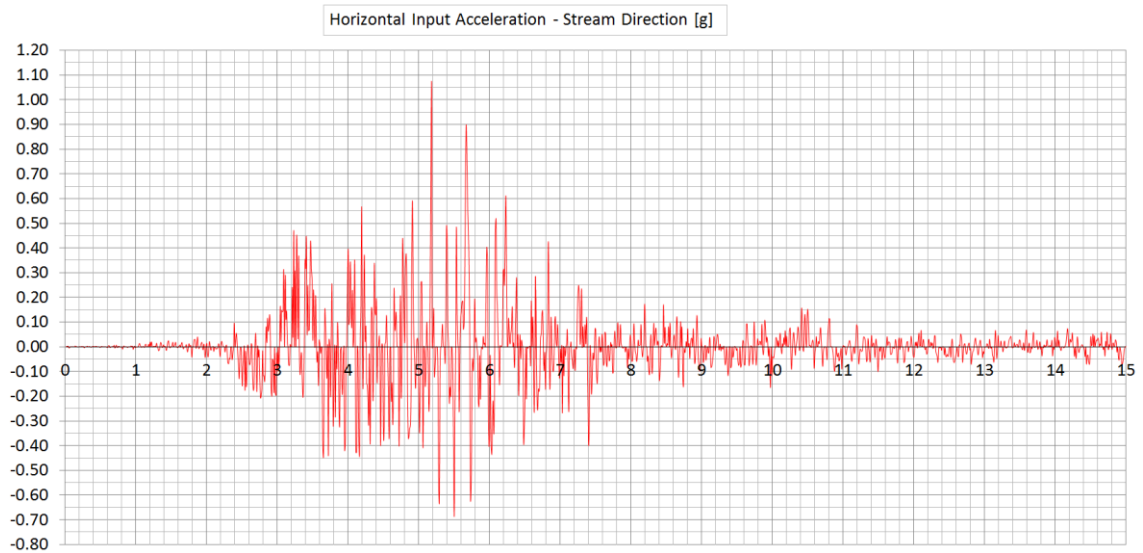


Figure 113 Aratozawa dam model after impounding, dam cross section

### 11.1.2 Seismic Input Motion

Due to the effort of JCOLD (2014), and with acceptance of the owner, the full set of seismic monitoring data of Aratozawa dam was published.

Seismic data is available in digital form of three strong motion accelerographs in three elevations within the dam core. SMA 1 is located within the dam base gallery at core to bed rock interface. SMA 2 is approximately located in the cores' upper third at elevation 250masl. SMA 3 is located approximately 1m below the crest at elevation 278,5masl. Seismic data is available for all three seismographs in all three directions up – down, upstream – downstream (orthogonal to dam axis) and in direction of the dam axis. Figure 114 and Figure 115 show the horizontal and vertical input acceleration applied to the lower base of Aratozawa dam model. Due to the high peak accelerations (horizontal near fault excitation = 1,04g in stream direction) Aratozawa dam forms an ideal case for the present thesis.



**Figure 114 Horizontal base acceleration Aratozawa dam model (adapted from JCOLD 2014)**

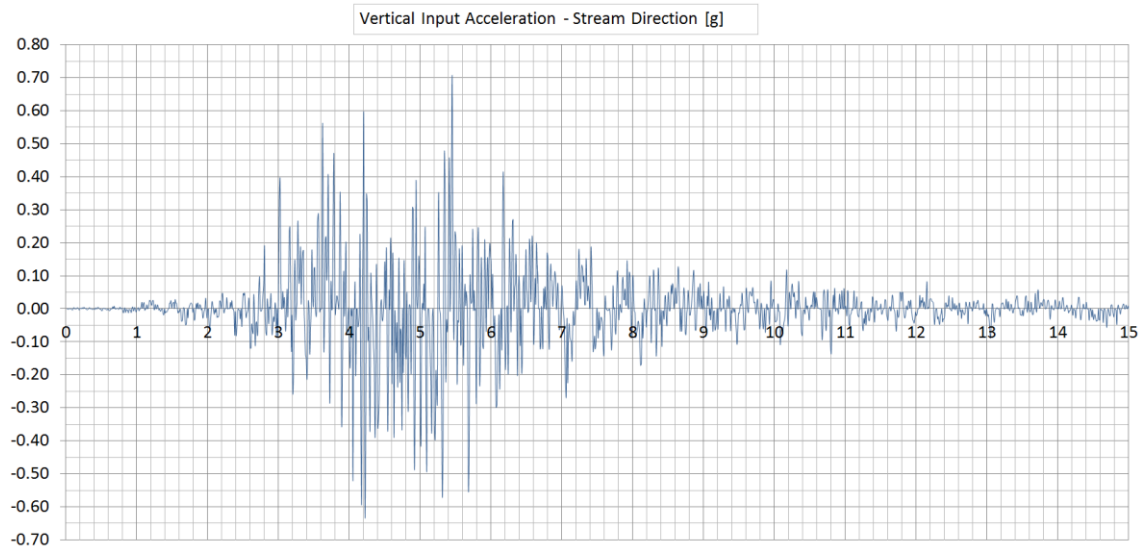


**Figure 115 Vertical base acceleration Aratozawa dam model (adapted from JCOLD 2014)**

### 11.1.3 Stepped Construction & Boundary Conditions

Within the model the dam was built in 15 steps (i.e. 5m thick layers) in order to accurately model the correct stress distribution within the zoned embankment. This procedure is of high importance for core type dams.

For calculation of initial stresses, construction steps and impounding, the boundary conditions at the model outer edges are the same. Vertical model boundaries shall be

fixed in horizontal and free in vertical direction whilst the horizontal base of the model was fixed in both directions. For accurate calculation of the phreatic surface and the pore water pressure distribution within the dam core, interface elements were added at downstream core to critical filter boundary. In order to gain the exact measured pore water pressure distribution within the dam core, the measured head was typed in as prescribed point value at the specific locations of #2, #16, #23, #25 and #27 pore water gauges.

For earthquake calculation the boundary conditions need to be changed. The horizontal model boundary (i.e. the base of the model) was fixed in both directions and the dynamic input accelerates this “fixed” base according to the time history data set. The left and right side vertical boundaries shall be able to deform freely in horizontal and vertical direction as two component (i.e. horizontal and vertical) time history sets were applied. Furthermore the vertical boundaries should not cause wave reflection as this might change the structure’s overall acceleration. Software Plaxis 2015 enables to do this by selection of a so called “Free Field” boundary. Within Geostudio the user may achieve comparable results if adding damping regions on left and right model edge. These damping elements basically are normal soil elements having the same material properties as their horizontal neighbor region but the user defines 99% along the full range of shear strain. Anyhow the overall model dimensions need to be selected in a range that ensures that the calculation results do not change significantly. This might call for an iterative procedure in some cases. In other words horizontal boundaries might also be fully fixed in both directions if the horizontal model dimension is wide enough. The application of free field boundaries is not a must but reduces the number of elements and hence reduces calculation time.

In case of Aratozawa dam soil liquefaction may be excluded for the outer shell materials due to its high coarseness. However the upstream critical filter might theoretically and the core definitely has built up significant pore water pressures. Ohmachi and Tahara (2011) back-calculated  $r_u$  – values resulting in  $r_u = 0,35$  at maximum assuming that the core materials full weight creates the minimum effective stresses. However, the



results of this study indicate that the core was close to and partly was subject to liquefaction at end of the earthquake. The calculated minor stresses within the core after impounding are based on estimated core modulus during construction and hence might be subject to discussions. Anyhow the calculation result is assumed not to be unrealistic as such behavior would better explain the rapid drainage of the excess pore water pressure as observed in the field.

Dynamic settlements of Aratozawa dam are mainly driven by dynamic compaction of the outer shoulders and to a limited extent to the result of consolidation settlements as the core shows time dependent drainage of the generated excess pore water pressures. In case of Aratozawa dam, the core rapidly drained the excess pore water pressures and hence observation data on crest settlement is only available as a combination of both settlement effects. The observed crest deformation resulted in a maximum settlement of 40cm.

No consolidation analysis was added within this study. Crest settlements are calculated by means of Newmark approach or by dynamic deformation analysis only.

Figure 116 to Figure 121 plot an extract of the model procedure.

Summing up, the selected calculation steps are as follows:

- Initial stresses
- Layered construction of embankment
- Impounding
- Prior earthquake stability analysis
- Earthquake analysis
- Post-earthquake deformation analysis
- Post-earthquake stability analysis

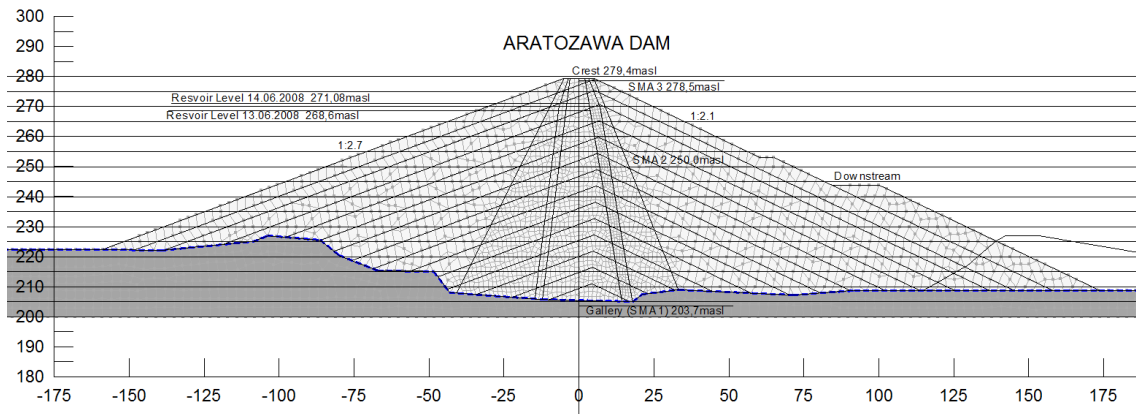


Figure 116 Aratozawa dam model – initial stresses

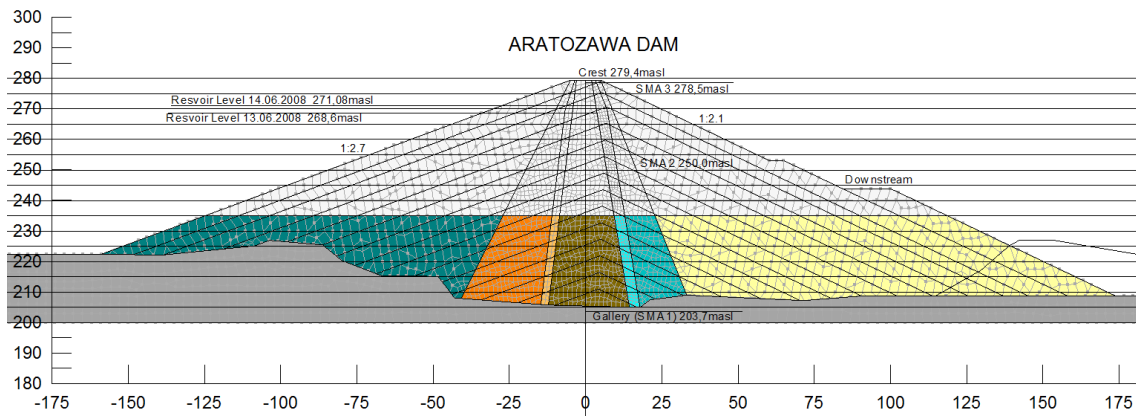


Figure 117 Aratozawa dam model – layered construction – placement of 6<sup>th</sup> layer

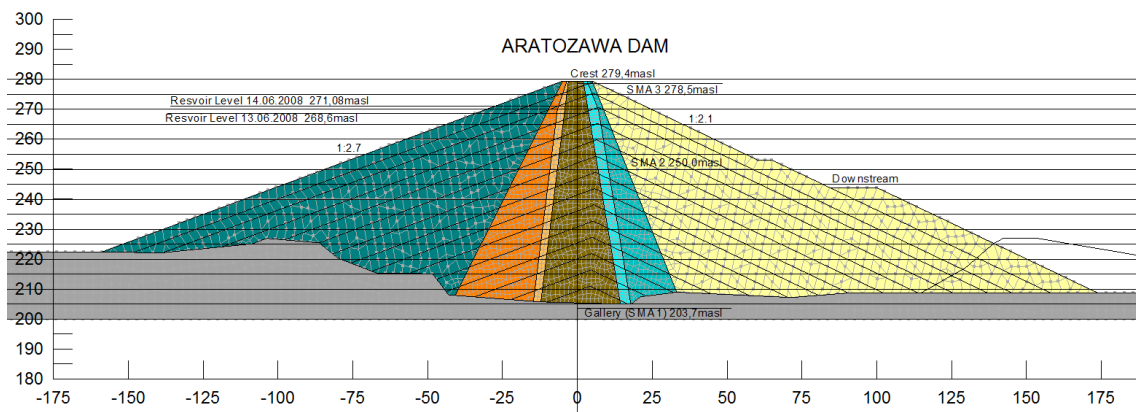


Figure 118 Aratozawa dam model – layered construction – last layer

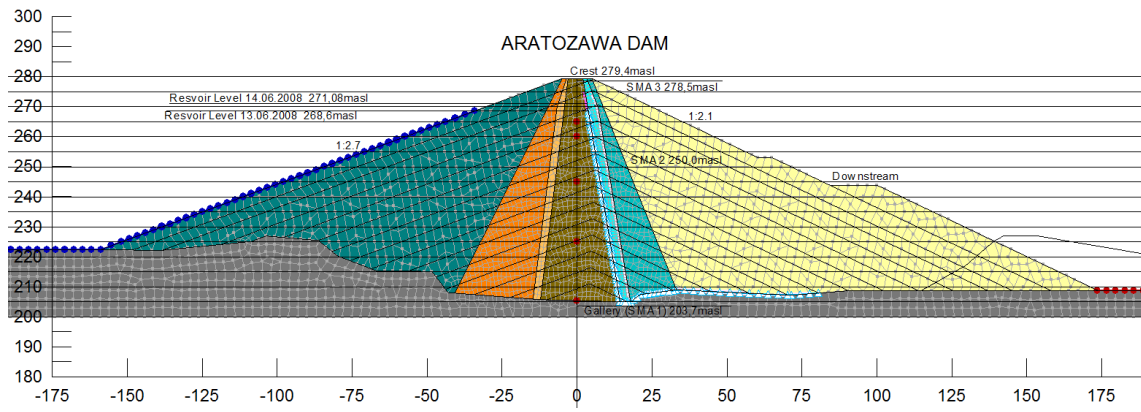


Figure 119 Aratozawa dam model – impounding

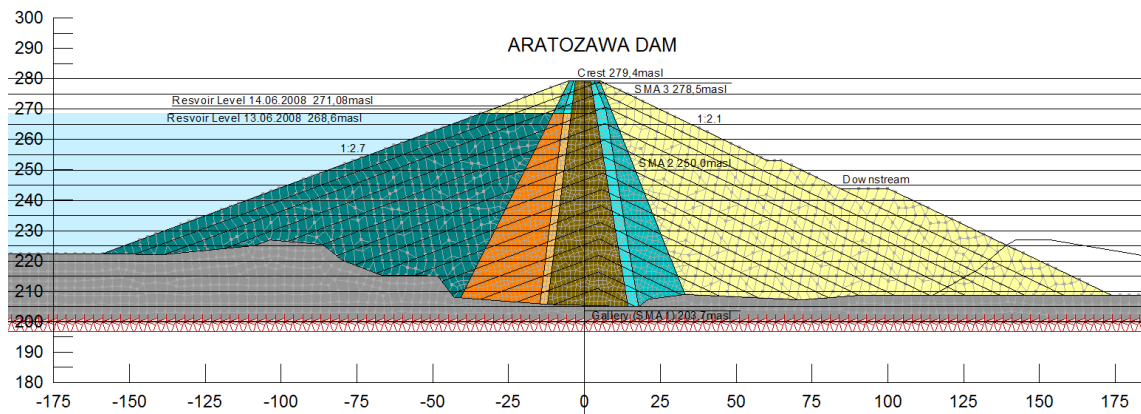


Figure 120 Aratozawa dam model – earthquake analysis

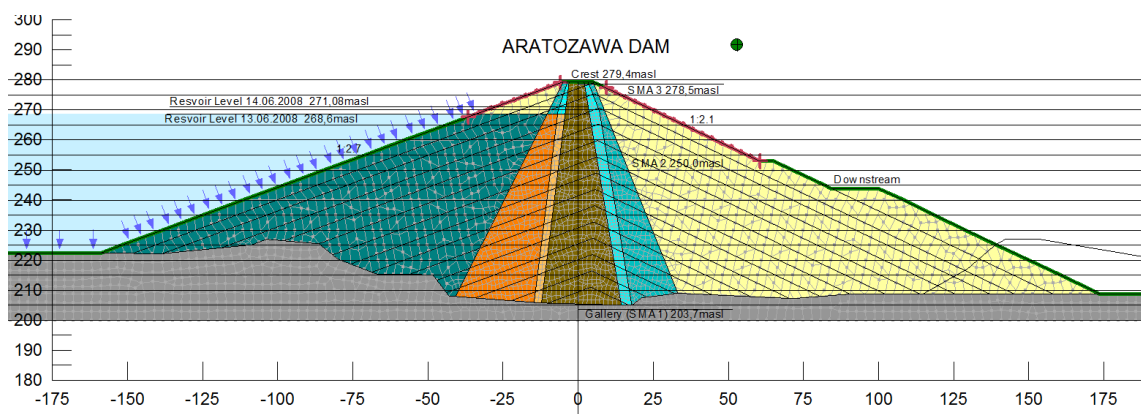


Figure 121 Aratozawa dam model – post-earthquake deformation - Newmark analysis

### 11.1.4 Equivalent number of Cycles vs. Rupture Distance

Calculating pore water pressure built up in GeoStudio Nonlinear analysis call for the definition of an equivalent number of stress cycles. Liu et al. (2001) presented a graph linking the equivalent number of stress cycles ( $N_{eq}$ ) to the moment magnitude ( $M_w$ ) and to the site's closest distance from the earthquakes' rupture plane ( $R$ ). Figure 122 plots this graph.

Input parameters for Aratozawa dam during <u>Iwate - Miyagi earthquake</u> are as follows:
$R = 0\text{km}$
$M_w = 6.9$
$\Rightarrow N_{eq} = 15$

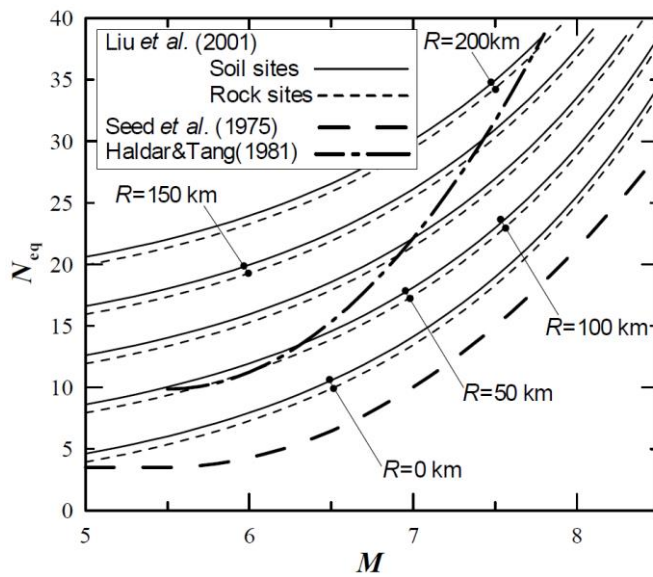


Figure 122 Empirical relationship of moment magnitude, equivalent number of cycles and rupture plane distance

### 11.1.5 Best Fit Input Parameter Sets

Table 17 sums up all material parameters applied to Aratozawa dam fill materials.

These parameters were applied to the Equivalent – Linear and Nonlinear analysis in software product (GeoStudio 2012). Where cells marked with a star resulted from observed behavior (i.e. material tests or back calculations, Ohmachi et al. 2011).

Material type	Clay Core	Critical Filter	Noncritical Filter	Rockfill	Bed Rock
Soil type acc. Unified Soil Classification System	GC-GM	-	-	-	-
Horizontal hydraulic conductivity $k_f$ [m/sec]	$1 \times 10^{-6}$ *	$1 \times 10^{-5}$ *	$1 \times 10^{-4}$ *	$1 \times 10^{-3}$ *	$1 \times 10^{-6}$
Colour in calculation upstream					
Colour in calculation downstream					
Weight above water table [kN/m <sup>3</sup> ]	20.9	21	21	22.5	-
Saturated Weight [kN/m <sup>3</sup> ]	20.9	23	24.5	25.5	23.5
Dilatation angle [°]	0	5	5	5	20
Poisson's ratio [-]	0.35	0.33	0.3	0.3	0.3
Young's Modulus E [kN/m <sup>2</sup> ]	15000	20000	25000	35000	2600000
Internal angle of friction [°]	6** / 25***	35	38	49	35
Cohesion [kN/m <sup>2</sup> ]	60** / 20***	0	0	0	250
Shear Modulus $G_{max}$ [kN/m <sup>2</sup> ]	see Fig. *	see Fig.	see Fig.	see Fig. *	$1 \times 10^{100}$
Damping Ratio [-] *	0.02	0.01	0.01	0.01	0.0001
Maximum Damping Ratio [-]*	0.24	0.24	0.19	0.19	0.0001

\* Applied to Nonlinear Analysis in Software GeoStudio only, values represent the lower and upper bound of damping vs. shear strain curves used in EL analysis

\*\*UU values applied during construction and impounding

\*\*\*CD values applied during shaking as plasticity develops stepwise in NL analysis / UU values applied in EL analysis

**Table 17 Material parameter sets applied to embankment fill material in GeoStudio EL and NL analysis**

Figure 123 and Figure 124 show the  $G_{max}$  reduction curve respectively the damping ratio vs. shear strain applied to Aratozawa dam for all Equivalent - Linear calculations. Curves as recommended by Vucetic and Dobry (1991) for PI = 30 were applied to the clay core. Curves applied to critical filter, noncritical filter and rockfill material result from large scale cyclic triaxial tests performed on Oroville and Venado dam materials by Seed, Wong, Idriss and Thomakin (1984).

Figure 126 plots the curve selected for pore water pressure built up within the clay core. When the pore water pressure ratio reaches 1 the soil is assumed to liquefy. The pore water pressure ratio is selected based on the ratio of the actual cyclic number divided by the number of equivalent stress cycles ( $N_L$ ). The curves are based on a for-

mula developed by DeAlba, Chan and Seed (1975). Figure 127 shows the shear stress ratio vs. actual number of cycles (N) based on large scale cyclic triaxial tests on clay core material from Sathoo (2011).

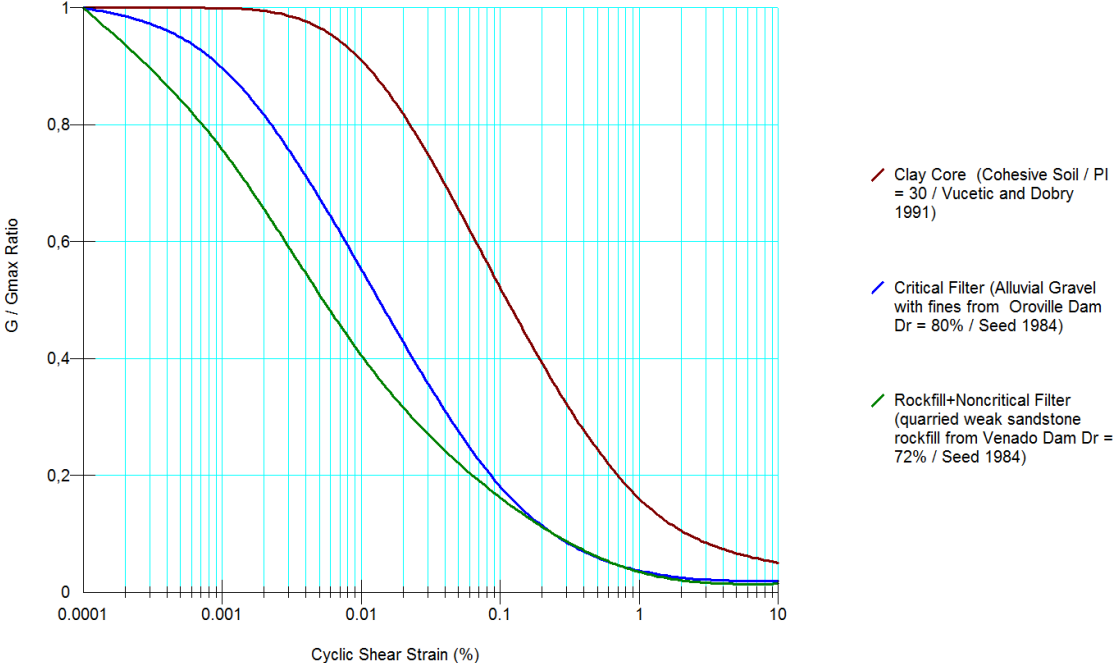


Figure 123 Shear modulus reduction vs. shear strain applied to embankment fill material in GeoStudio EL analysis

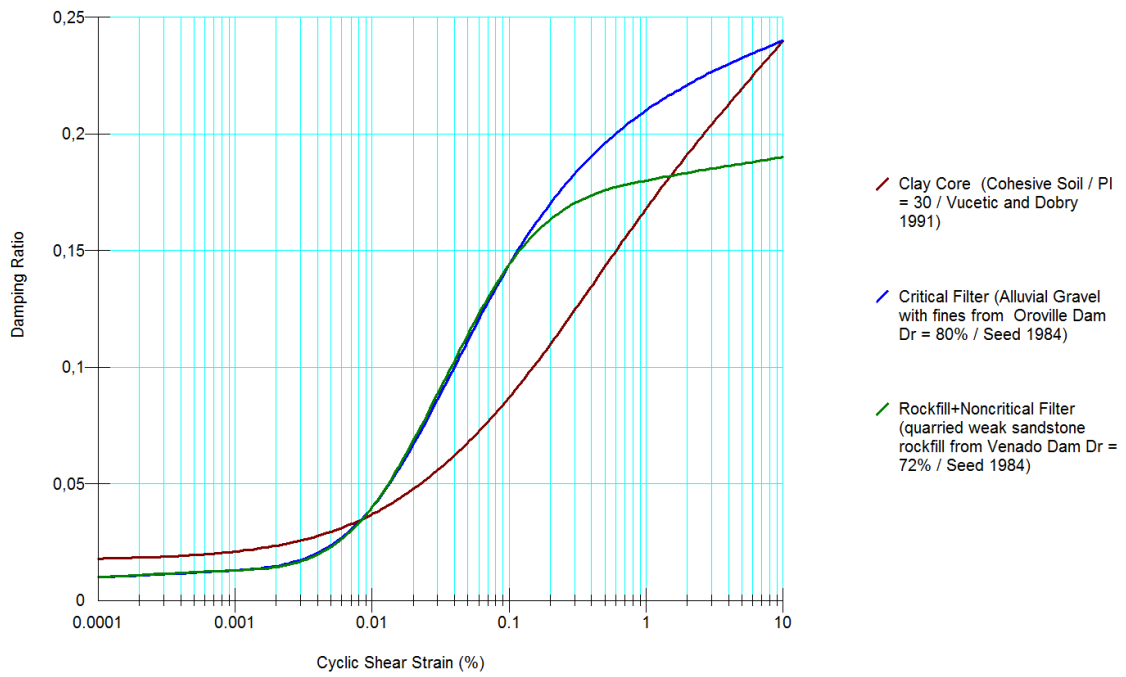


Figure 124 Damping ratio vs. shear strain applied to embankment fill material in GeoStudio EL analysis

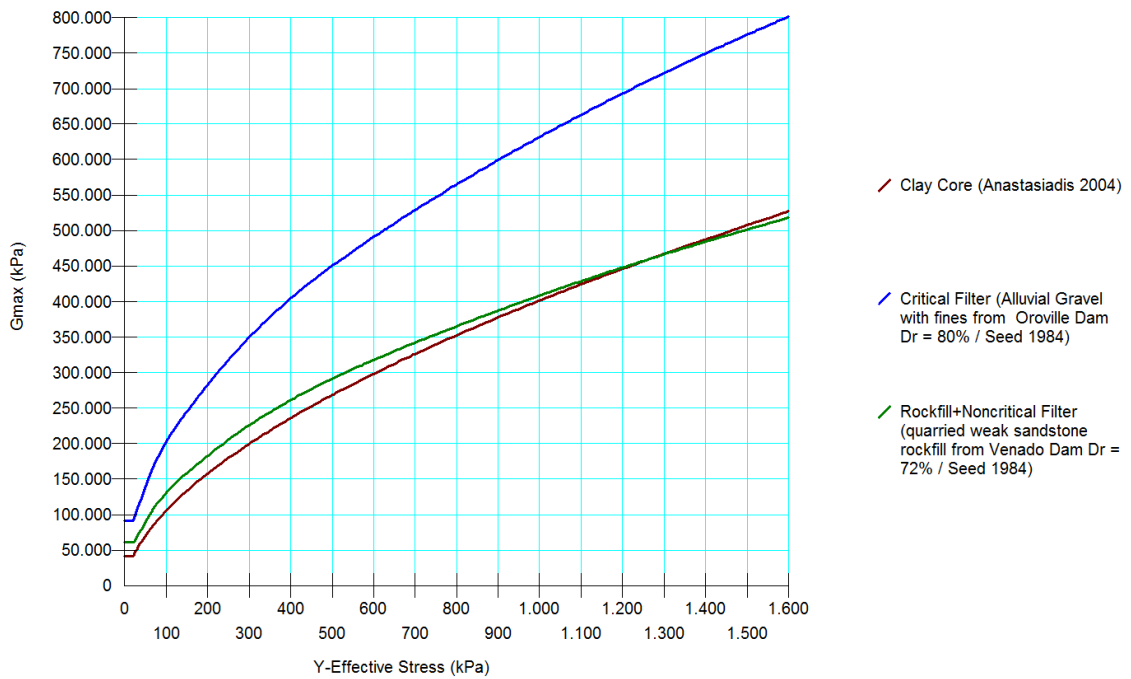
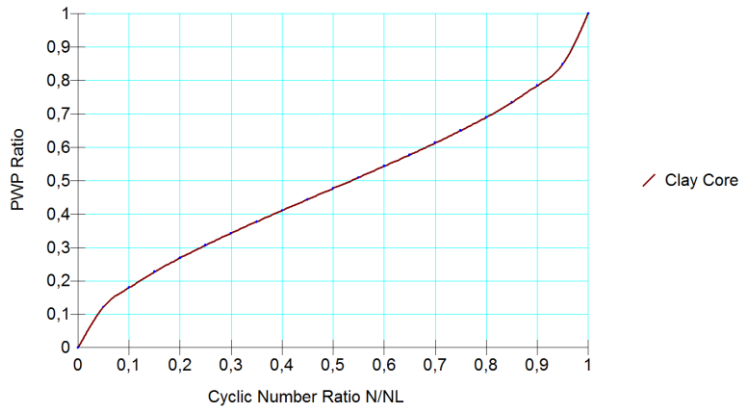
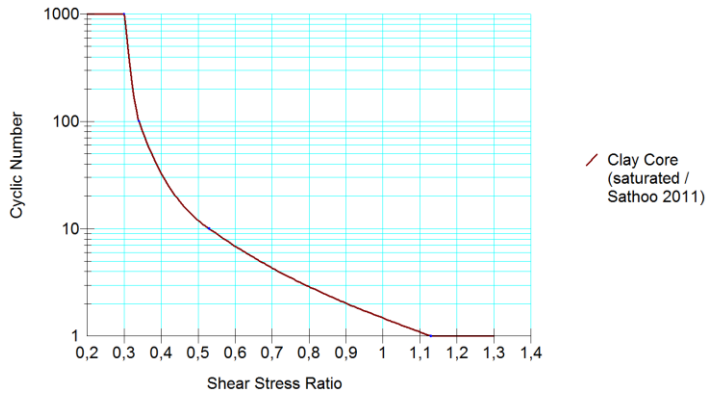


Figure 125 Shear modulus vs. vertical stress applied to embankment fill material in GeoStudio EL and NL analysis



**Figure 126 Pore water pressure built up vs. cyclic number ratio applied to the clay core in GeoStudio EL analysis**

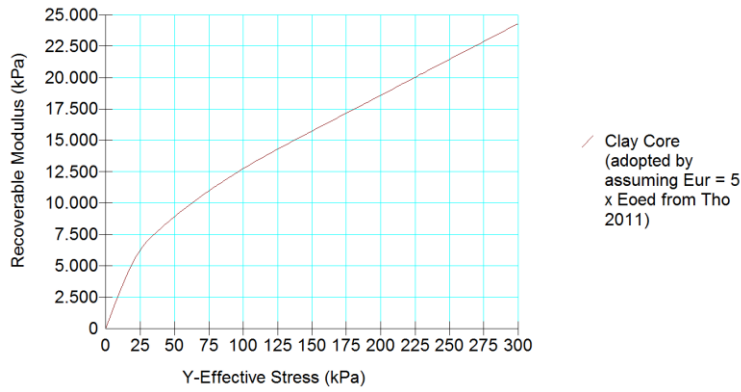


**Figure 127 Shear stress ratio vs. actual cyclic number applied to embankment fill material in GeoStudio EL analysis**

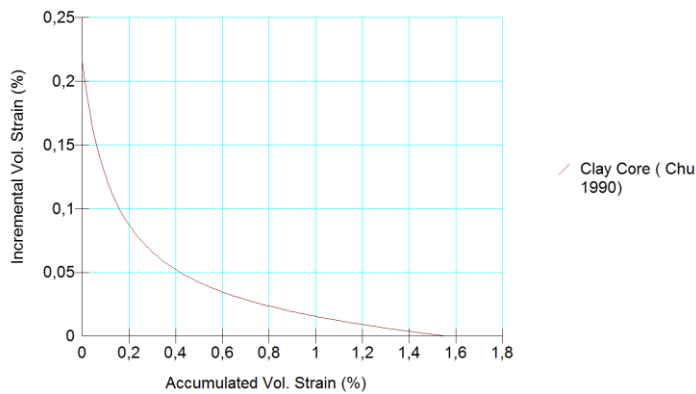
GeoStudio 2012 software uses the Martin – Finn – Seed pore water pressure generation within its Nonlinear dynamic analysis. GeoStudio calculates the MFS parameters from a set of two input curves (Figure 128 and Figure 129).

Figure 128 plots the recoverable modulus curves applied to the clay core material of Aratozawa dam. Figure 129 shows the accumulated vs. incremental volumetric strain curves again applied to the core material only.





**Figure 128 Recoverable modulus vs. vertical effective stress applied to embankment fill material in GeoStudio NL analysis**



**Figure 129 Accumulated vs. incremental volumetric strain functions applied to embankment fill material in GeoStudio NL analysis**

Table 18 sums up all parameters applied to the materials of Aratozawa dam in Plaxis Software product. Where cells marked with a star resulted from observed behavior (i.e. material tests or back calculations, Ohmachi et al. 2011). Within Plaxis, three types of material models were used for all calculation phases. Linear Elastic model was applied to base rock for all calculation phases from initial, to layered construction, dynamic calculation and post-earthquake deformations. Hardening Soil Small strain (HSS) model was used for all compressible materials for initial and layered construction. UBC2D model was applied to clay core material for the dynamic analyses whereas all other fill materials (rockfill, critical- and noncritical filters) use the Generalized Hardening Soil Small Strain (GHS) model. Damping ratios and the related frequency of each

material was selected in an iterative procedure. Depending on the calculated shear strain, damping ratios in detail were selected as shown in Figure 124 (i.e. the GeoStudio input data to achieve maximum comparability of both software packages).

Material type	Clay Core	Critical Filter	Noncritical Filter	Rockfill	Bed Rock
Soil type acc. Unified Soil Classification System	GC-GM	-	-	-	-
Horizontal hydraulic conductivity $k_f$ [m/sec]	$1 \times 10^{-6}$ ★	$1 \times 10^{-5}$ ★	$1 \times 10^{-4}$ ★	$1 \times 10^{-3}$ ★	$1 \times 10^{-6}$
Colour in calculation upstream					
Colour in calculation downstream					
Weight above water table [kN/m <sup>3</sup> ]	20.9	21	21	22.5	-
Saturated Weight [kN/m <sup>3</sup> ]	20.9	23	24.5	25.5	23.5
Dilatation angle [°]	0	5	5	5	5
Poisson's ratio [-]	0.35	0.33	0.3	0.3	0.3
Reference pressure $p_{ref}$ [kN/m <sup>2</sup> ]	100	100	100	100	-
$E_{50}^{ref}$ [kN/m <sup>2</sup> ]	20000	30000	35000	60000	-
$E_{oed}^{ref}$ [kN/m <sup>2</sup> ]	15000	20000	25000	35000	-
$E_{ur}^{ref}$ [kN/m <sup>2</sup> ]	40000	120000	70000	12000	-
Power $m$ [-]	0.25	0.7	0.75	0.85	-
Elastic shear modulus $k_G^e$	2100	-	-	-	-
Plastic shear modulus $k_G^p$	1960	-	-	-	-
Elastic bulk modulus $k_b^e$	1470	-	-	-	-
Power elastic shear module $n_e$	0.4	-	-	-	-
Power plastic shear modulus $n_p$	0.3	-	-	-	-
Power elastic bulk modulus $m_e$	0.4	-	-	-	-
Failure ratio [-]	0.75	0.7	0.8	0.85	-
Internal angle of friction [°]	6** / 25***	35	38	49	45
Internal angle of friction at constant volume [°]	23***	-	-	-	-
Cohesion [kN/m <sup>2</sup> ]	60** / 20***	0	0	0	250
Shear Modulus / $G_o^{ref}$ [kN/m <sup>2</sup> ]	-	202000	130000	130000	★ $6 \times 10^7$
Damping Rayleigh $\alpha$ [-]	0.246	0.105	0.326	0.2646	$4.19 \times 10^{-3}$
Damping Rayleigh $\beta$ [-]	$0.125 \times 10^{-3}$	$1.16 \times 10^{-3}$	$0.357 \times 10^{-3}$	$0.234 \times 10^{-3}$	$0.212 \times 10^{-3}$

\*\*UU values applied during construction and impounding

\*\*\*CD values applied during shaking as plasticity develops stepwise in NL analysis

**Table 18 Material parameter sets applied to embankment fill material in Plaxis NL analysis**

## 11.2 Zipingpu Dam (CFRD)

### 11.2.1 Meshing

Figure 130 shows the numerical model of Zipingpu dam derived from software Geo-Studio 2012 at the beginning of the dynamic calculation. The horizontal model size, it est the horizontal width of the base rock was selected 2 times the horizontal base width of the compressible fill materials as the dam is built on competent limestone rock foundation. No rule has to be kept for selection of the base rock thickness. Same as for Aratozawa dam, the input motion is supposed to be known and put at the model's lower base. The base rock therefore is modelled infinitely stiff. For this reason, the dimensions of the base rock were kept small to limit computation time.

Figure 131 plots the detailed section of Zipingpu dam model showing the overall geometry, material boundaries, the mesh and the selected locations of history points. One history point was placed at the location of the strong motion accelerograph (at crest downstream edge). The others were selected to obtain detailed output information at the specific location.

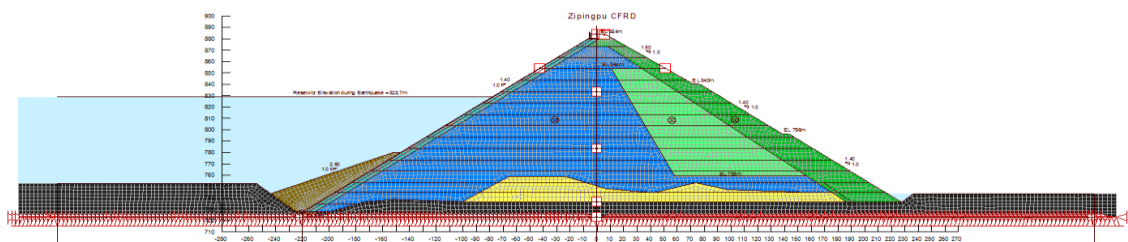


Figure 130 Zipingpu dam model after impounding, general view

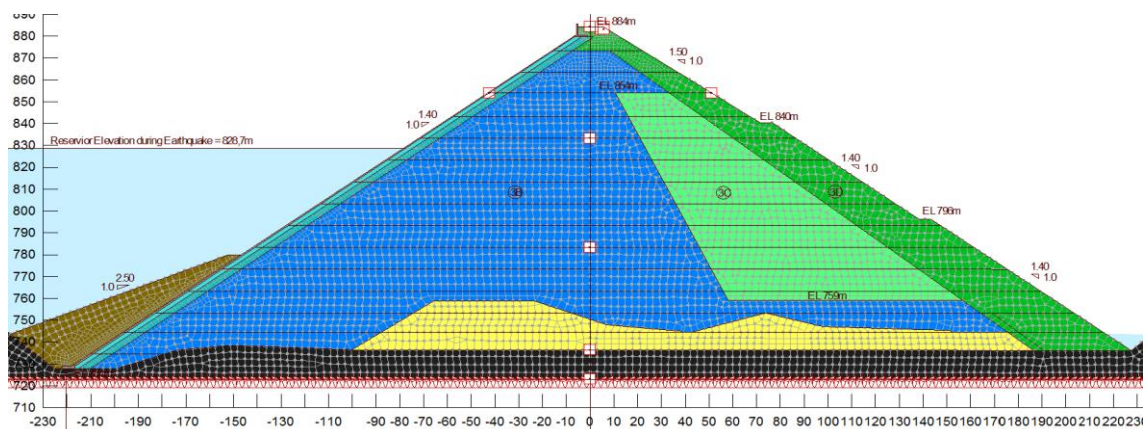


Figure 131 Zipingpu dam model after impounding, dam cross section

### 11.2.2 Seismic Input Motion

The only seismic data that might partly be useful for seismic analysis was recorded by the seismograph located at crest elevation (mid crest length, at downstream crest edge, Guan 2009). Figure 132 plots the recorded data.

First of all it can be seen that storage time was insufficient. Y-channel acceleration is still in an order of 0,15g when data recording stopped. The total recorded length sums up to approximately 50sec.

Figure 132 shows distinct single peaks between 20,5 sec and 21,5 seconds recording time. Figure 133 shows a close up picture of the only accelerograph that recorded seismic data. It can be seen that a piece of a concrete column is lying next to the accelerograph. This concrete column is a piece of an unreinforced passenger guiding "fence" that collapsed nearly for the entire length of the dam crest. Parts of it slid down the downstream shoulder other parts were found smashed on the pavement. The single peaks of the record are all located at the same time step in all three directions resulting in abnormal high accelerations exceeding 2g. Such a behavior is clearly abnormal and hence these peaks may simply be ignored as they do only represent the impact of the toppling guard "fence". Assuming that the acceleration peak that forced this "fence" to topple must have been before the concrete column's impact on ground, verifies that there is no "hidden" natural peak within this artificial peaks. Figure 132 furthermore shows a single peak in z-channel at 32sec recording time. If of natural source, such a high peak would normally be followed by slightly offset peaks in y or x channel but the recorded data does not show such peaks. Therefore, this peak is ignored and assumed to be of artificial origin (i.e. a result of movements of the concrete pieces or the fall down of the smaller piece from reduced height).

As a result it may be assumed that the recorded natural vertical and horizontal peak accelerations at dam crest are in the range of 0,8 to 0,9g.

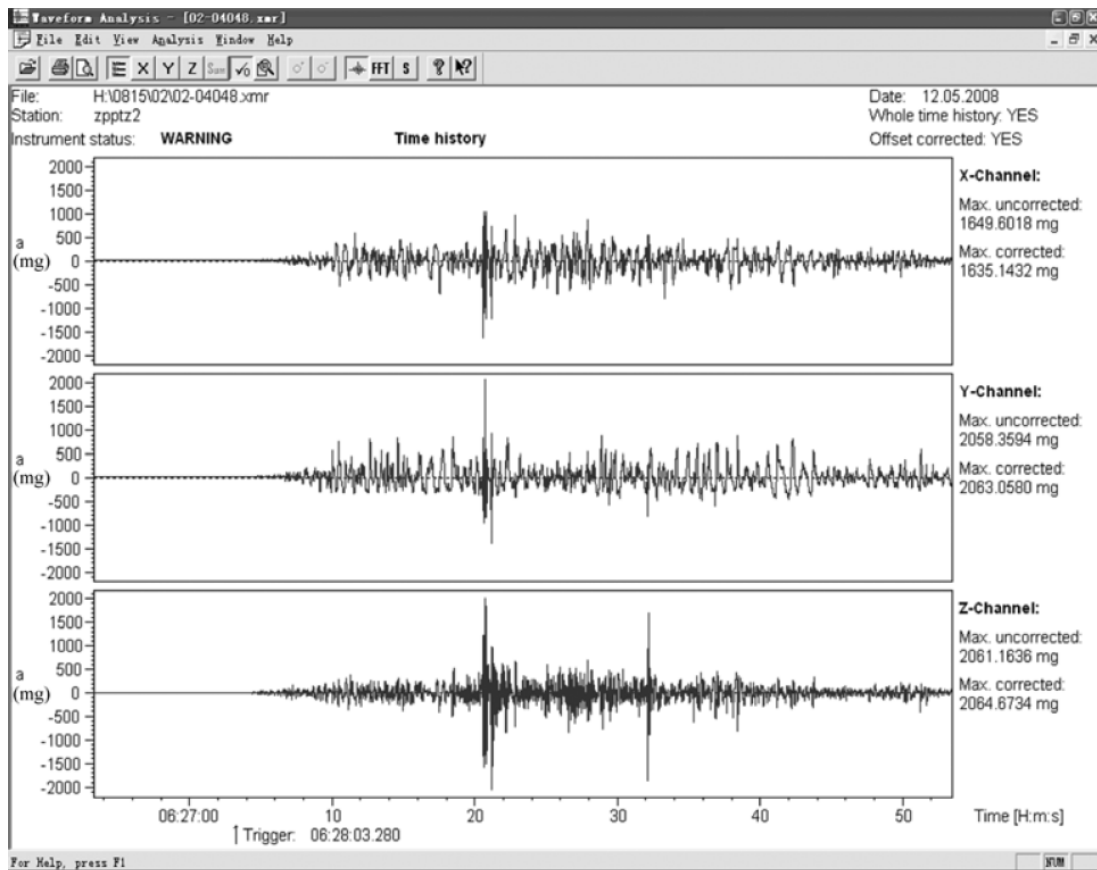


Figure 132 Accelerograph recordings at dam crest mid at the crest's downstream edge (Guan 2009)



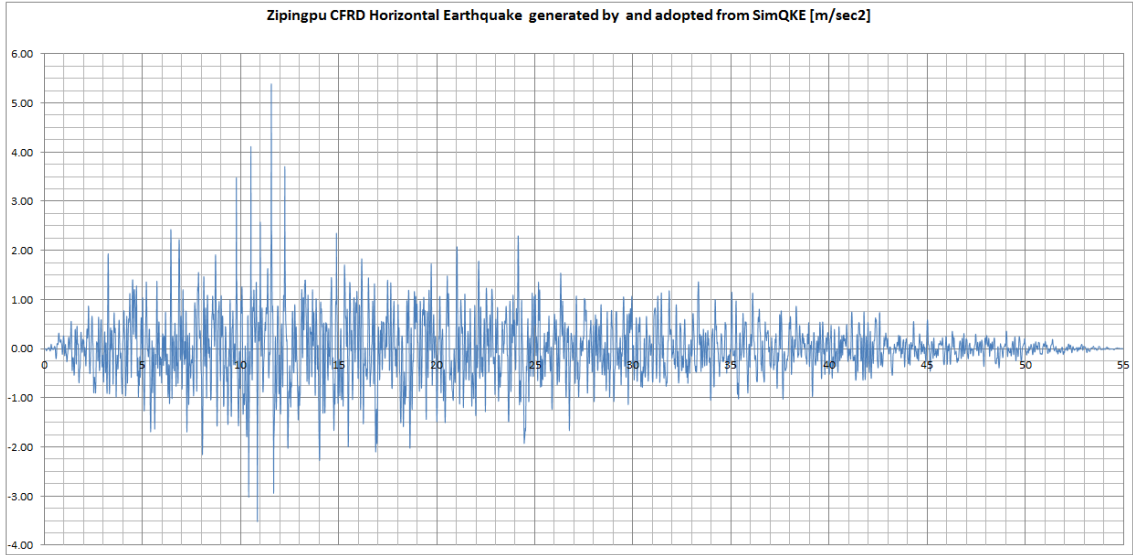
Figure 133 Crest accelerograph hit by destroyed unreinforced concrete guard elements (Zou 2012)

Kong et al. (2012) recommended the use of Diban station (Mao town) seismic records scaled to a pga of 0,55g for dynamic analysis of Zipingpu dam. However, Mao town is

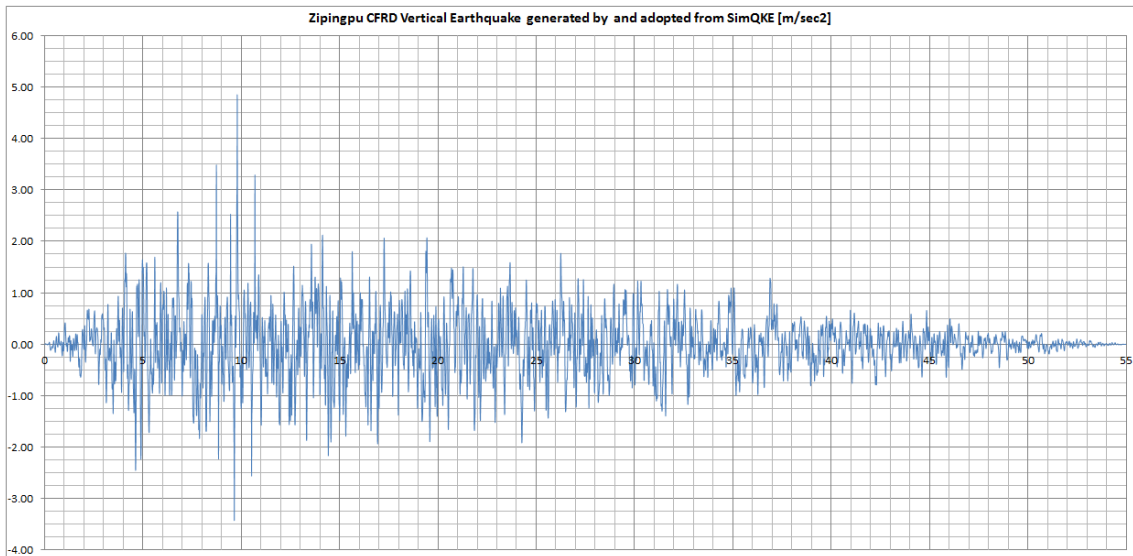
located in a distance of 70km to Zipingpu dam. Furthermore Mao town records lack for the typical near field single peaks, as a consequence Mao town records were not used as input excitation for this thesis. Instead of, the author decided to artificially generate an earthquake by use of SimQKE software (Gasparini and Vanmarcke, 1976). The pga (one single peak) was kept at 0,55g as recommended by Kong et all. (2012). A independently generated vertical earthquake was generated by the same procedure. In accordance to Eurocode 8, the vertical peak ground acceleration was set to 0,9 times the horizontal pga. Typically the vertical pga is selected 0,7 times the horizontal one, however near field observations have shown that the vertical pga often is in the same range or does also exceed the horizontal one. In accordance with recorded data from Aratozawa dam base gallery, near field typical single peaks were manually added to the generated earthquake sets (horizontal and vertical).

Figure 134 and Figure 135 show the horizontal and vertical input acceleration finally applied to the lower base of Zipingpu dam model.

Figure 136 plots the pseudo spectral acceleration of the generated input motions. Within this graph the red line plots the horizontal input motion whilst the blue line plots the vertical one.



**Figure 134 Horizontal base acceleration Zipingpu dam model**



**Figure 135 Vertical base acceleration Zipingpu dam model**

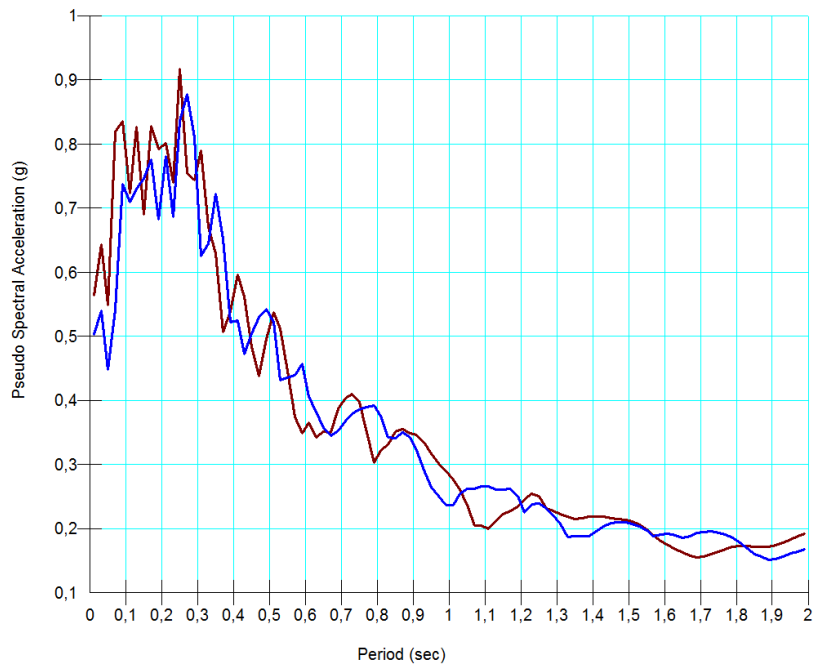


**Figure 136 Spectral response of generated input acceleration Zipingpu CFRD**

Despite the above mentioned deficiencies of missing acceleration records, Zipingpu CFRD was selected to be an ideal case study for this thesis as it is the only high and modern CFRD that was ever shaken by a severe earthquake. Besides that, Zipingpu dam is a well monitored dam that delivered valuable and detailed information on the dam's inner and outer deformation behavior. The knowledge international dam society gained from this case study is huge.

### 11.2.3 Stepped Construction & Boundary Conditions

Within the model the dam was built in 18 steps (i.e. 5m thick layers) in order to accurately model the correct stress distribution within the zoned embankment. As the Young's moduli of all fill material does not vary too much, this procedure is of lower importance in case of Zipingpu dam.

As for Aratozawa dam, the boundary conditions are the same for calculation of initial stresses, construction steps and impounding. Vertical model boundaries are fixed in horizontal and free in vertical direction whilst the base of the model was fixed in both directions. For earthquake analysis the boundary conditions were changed in the same way as described previously for Aratozawa dam analysis.

In case of Zipingpu dam soil liquefaction may be excluded for all materials due to its high coarseness or due to the high compaction work. Dynamic settlement of Zipingpu dam is driven by dynamic compaction of the outer shoulders only.

Figure 137 to Figure 144 plot an extract of the model procedure.

Summing up, the selected calculation steps are as follows:

- Initial stresses
- Layered construction of embankment
- Placement of the concrete slab and parapet wall
- Placement of 1A material and last embankment layer at crest elevation
- Impounding
- Prior earthquake stability analysis
- Earthquake analysis
- Post-earthquake deformation analysis
- Post-earthquake stability analysis



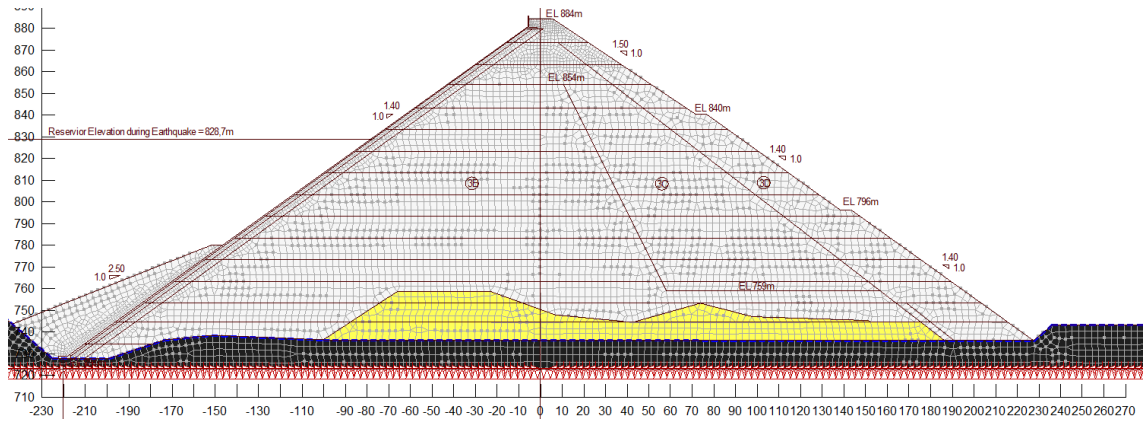


Figure 137 Zipingpu dam model – initial stresses

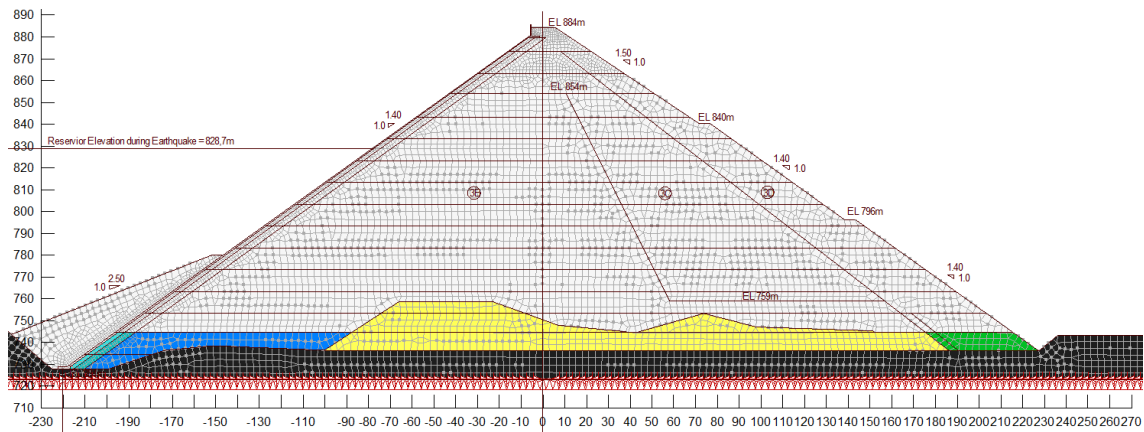


Figure 138 Zipingpu dam model – layered construction – placement of 2<sup>nd</sup> layer

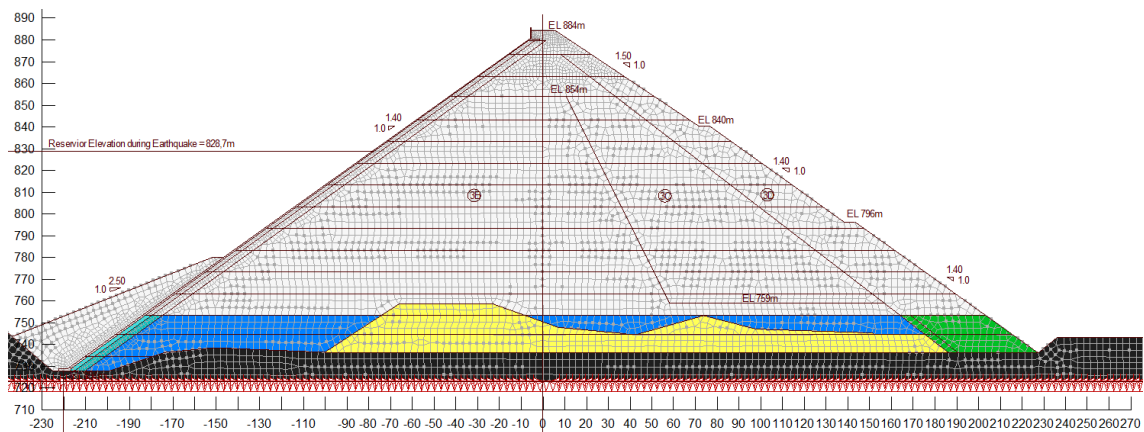


Figure 139 Zipingpu dam model – layered construction – placement of 3<sup>rd</sup> layer

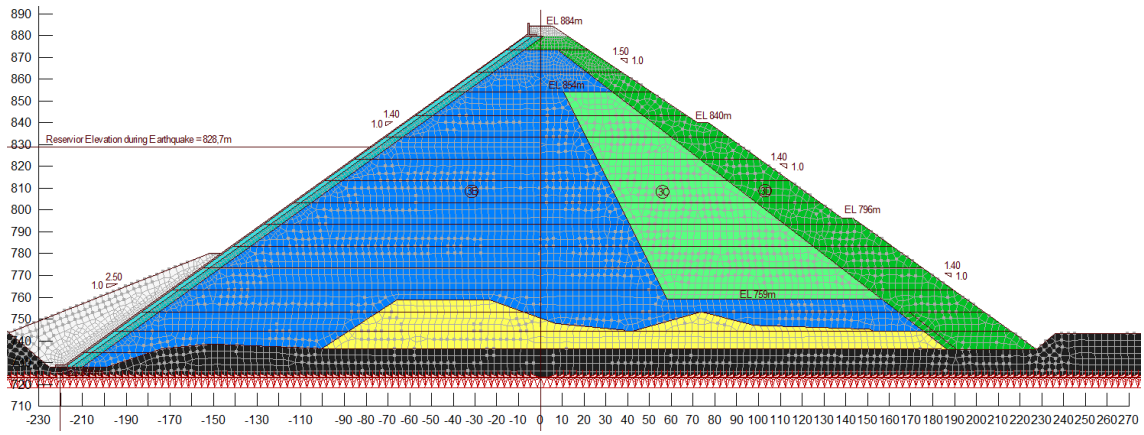


Figure 140 Zipingpu dam model – layered construction – placement of concrete slab and parapet wall

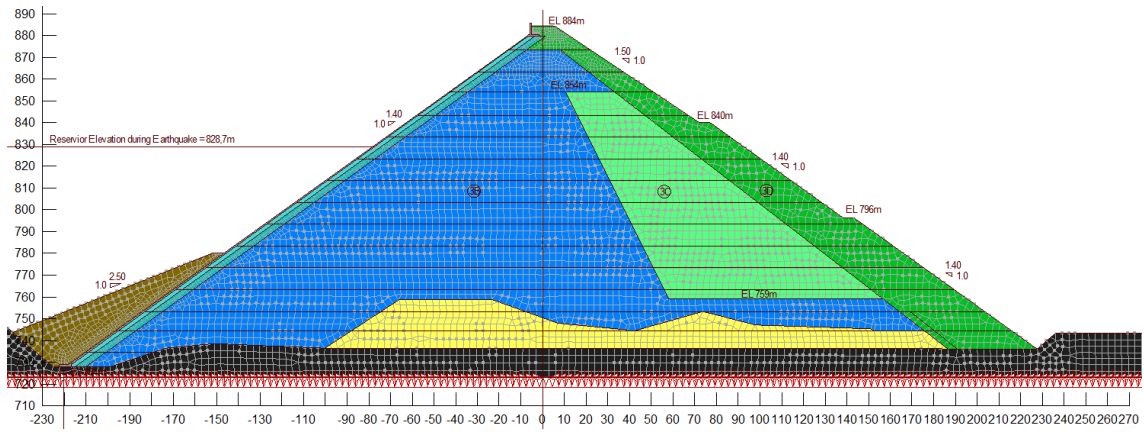


Figure 141 Zipingpu dam model – layered construction – last layer + 1A material placement

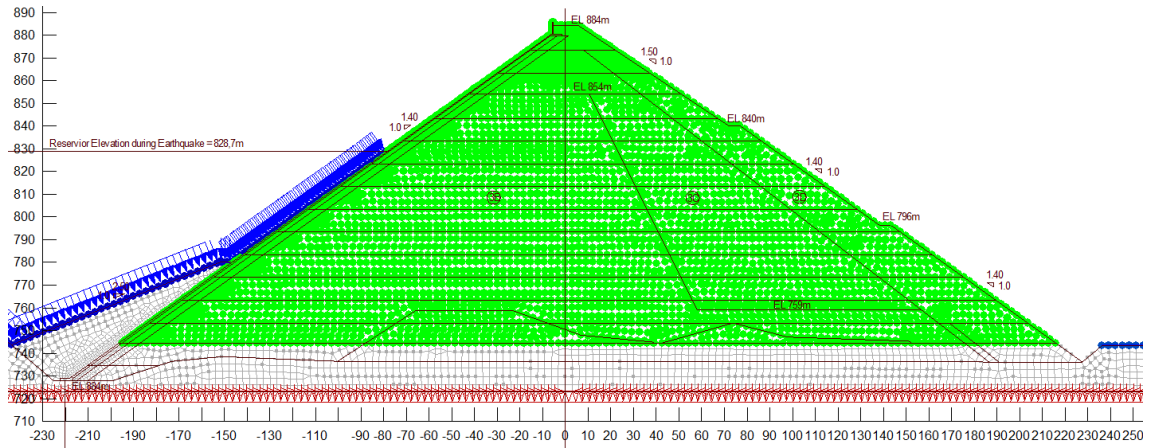


Figure 142 Zipingpu dam model – impounding – boundary conditions

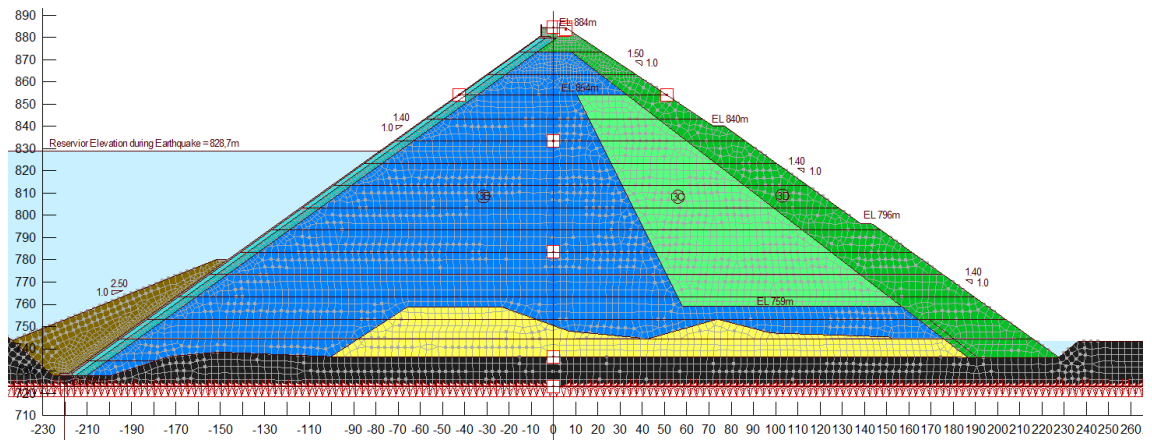


Figure 143 Zipingpu dam model – earthquake analysis

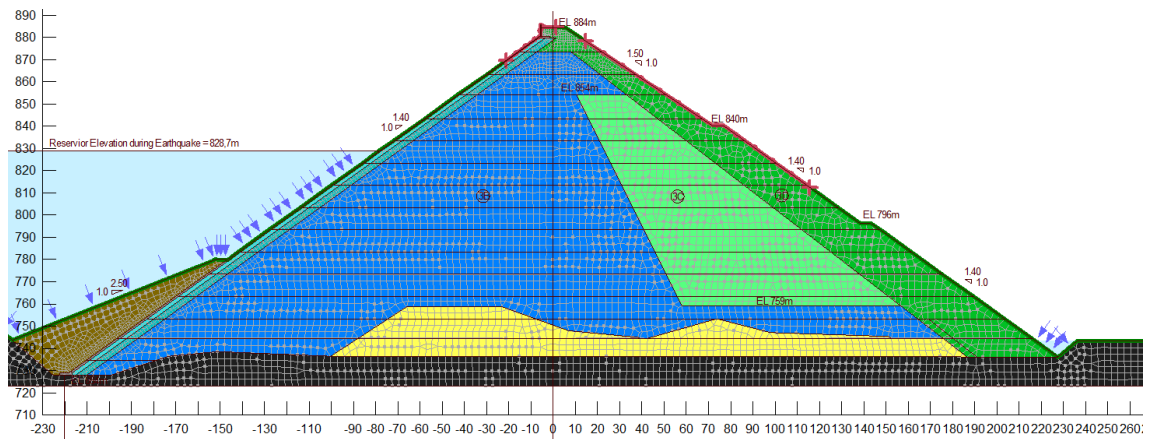


Figure 144 Zipingpu dam model – post-earthquake deformation - Newmark analysis

### 11.2.4 Equivalent number of Cycles vs. Rupture Distance

The number of equivalent stress cycles was estimated by use of Figure 122.

Input parameters for Zipingpu dam during <u>Wenchuan earthquake</u> are as follows:
R = 0km
$M_w = 7.9$
$\Rightarrow N_{eq} = 24$

### 11.2.5 Best Fit Input Parameter Sets

Table 19 sums up all material parameters applied to Zipingpu dam fill materials. Cells marked with a star resulted from observed behavior (i.e. material tests or back calculations). Other parameters were selected in accordance to test results on comparable material (reference given within the plots) or simply estimated by the author within the materials typical ranges. These parameters were applied to the Equivalent – Linear and Nonlinear analysis in software product GeoStudio 2012.

Material type	1A Material	Alluvium	2B Material	3A Material	3B Material	3C Material	3D Material	Concrete	Bed Rock
Horizontal hydraulic conductivity $k_f$ [m/sec]	$1 \times 10^{-6}$	$1 \times 10^{-3}$	$1 \times 10^{-5}$	$1 \times 10^{-3}$	$1 \times 10^{-3}$	$1 \times 10^{-3}$	$1 \times 10^{-3}$	$1 \times 10^{-9}$	$1 \times 10^{-6}$
Colour in calculation									
Unit Weigth [kN/m <sup>3</sup> ]	20.9	21	21	21	22.5	22	21	24.5	23.5
Dilatation angle [°]	0	8	8	8	5	5	5	15	20
Poisson's ratio [-]	0.35	0.3	0.33	0.3	0.3	0.3	0.3	0.2	0.3
Young's Modulus E [kN/m <sup>2</sup> ]	30000	60000	80000	75000	70000	55000	60000	2000000	2600000
Internal angle of friction [°]	30	38	45	49	49	49	49	45	35
Cohesion [kN/m <sup>2</sup> ]	15	0	0	0	0	0	0	500	250
Shear Modulus $G_{max}$ [kN/m <sup>2</sup> ]	see Fig.	see Fig.	see Fig.	see Fig.	see Fig.	see Fig.	see Fig.	3500000	$1 \times 10^{100}$
Damping Ratio [-] *	0.02	0.01	0.01	0.01	0.01	0.01	0.005	0.01	0.01
Maximum Damping Ratio [-]*	0.255	0.24	0.24	0.24	0.24	0.19	0.2	0.02	0.02

\* Applied to Nonlinear Analysis in Software GeoStudio only, values represent the lower and upper bound of damping vs. shear strain curves used in EL analysis

**Table 19 Material parameter sets applied to embankment fill material in GeoStudio EL and NL analysis**

Figure 145 and Figure 146 show the  $G_{max}$  reduction curve respectively the damping ratio vs. shear strain applied to Zipingpu dam for all Equivalent - Linear and Nonlinear analyses in software GeoStudio 2012. 1A Material was estimated to have a PI = 15. Curves as published by Vucetic and Dobry (1991) were applied. The curves applied to

all other granular fill material resulted from large scale cyclic triaxial tests performed on Orroville, Pyramid and Venado dam materials performed by Seed, Wong, Idriss and Thomakin (1984).

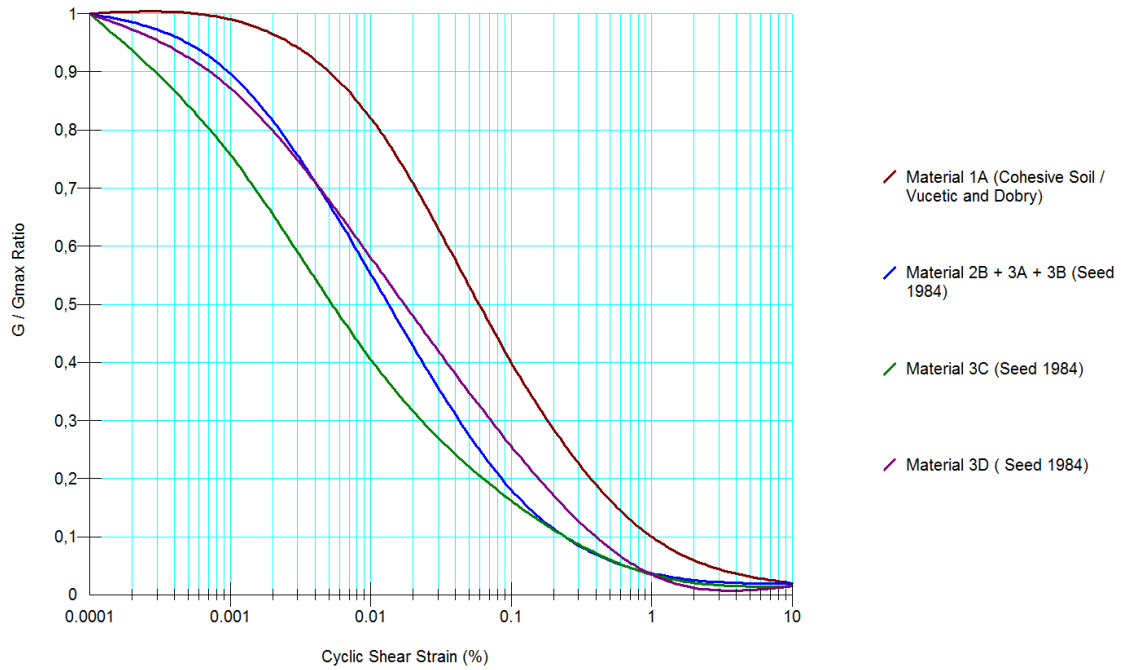


Figure 145 Shear modulus reduction vs. shear strain applied to embankment fill material in GeoStudio EL analysis

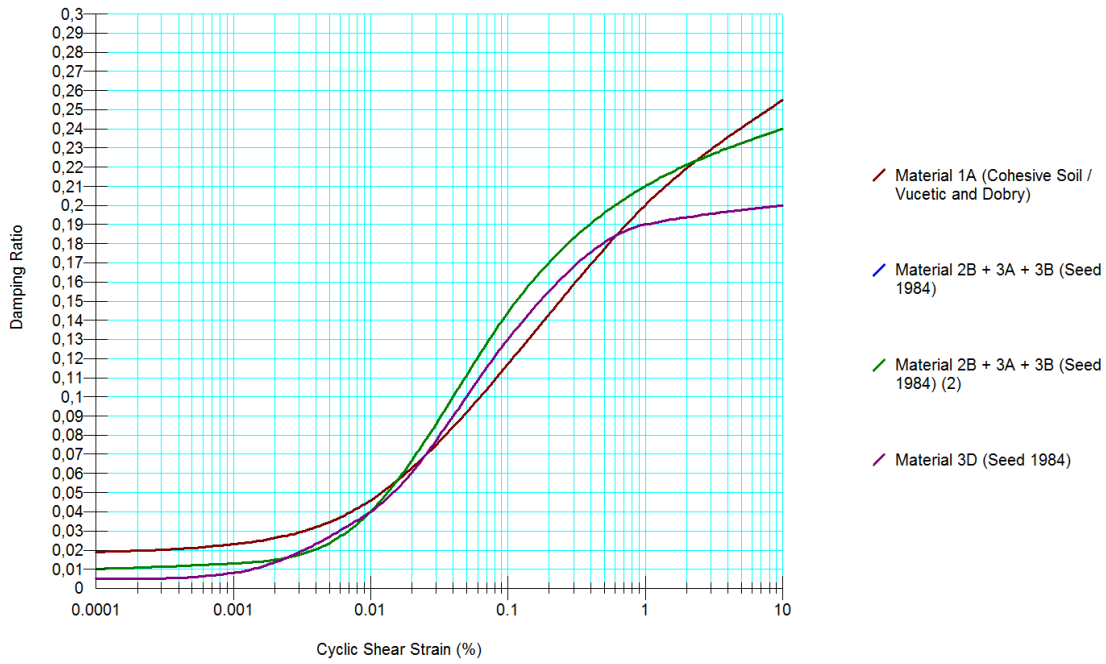


Figure 146 Damping ratio vs. shear strain applied to embankment fill material in GeoStudio EL analysis

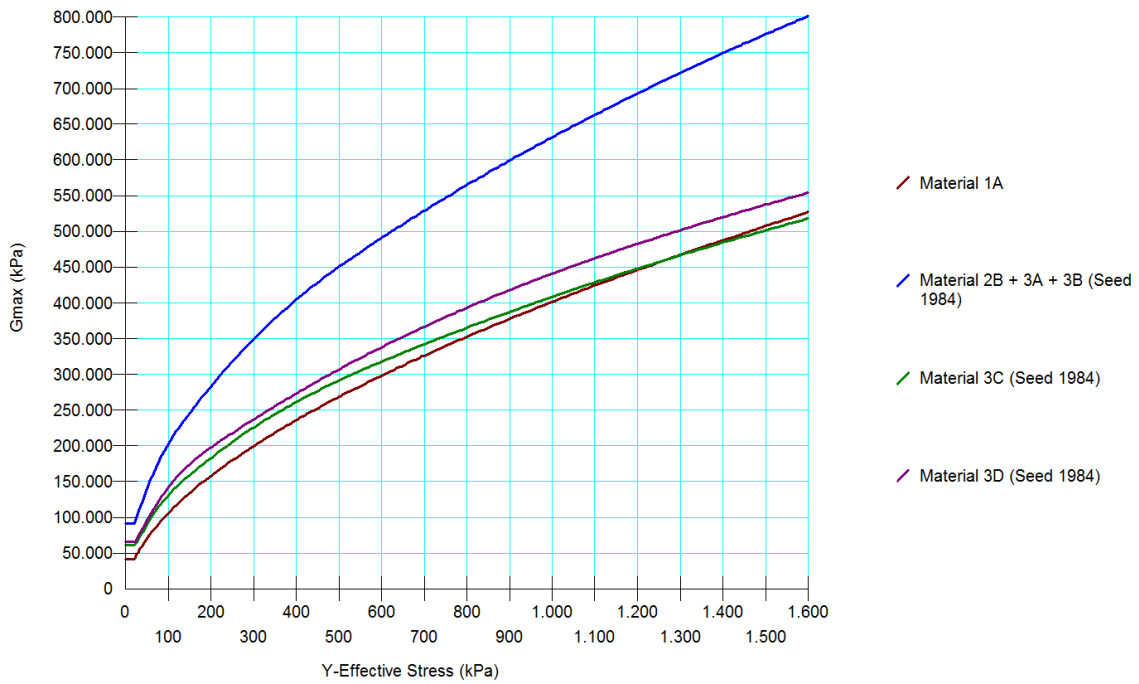


Figure 147 Shear modulus vs. vertical stress applied to embankment fill material in GeoStudio EL and NL analysis

Table 20 sums up all parameters applied to the materials of Zipingpu dam in Plaxis Software product. Cells marked with a star resulted from observed behavior (i.e. material tests or back calculations). Other parameters were estimated by the author within the materials typical ranges. Within Plaxis, three types of material models were used for all calculation phases. Again Linear Elastic model was applied to the base rock for all calculation phases from initial, to layered construction, dynamic calculation and post-earthquake deformations. Hardening Soil Small strain (HSS) model was used for all compressible materials for initial and layered construction. As recommended by Plaxis, damping ratios were selected in accordance to the materials natural frequency for each material in an iterative procedure. Depending on the calculated shear strain, damping ratios in detail were selected as shown in Figure 147 (i.e. the GeoStudio input data to achieve maximum comparability of both software packages).

Material type	1A Material	Alluvium	2B Material	3A Material	3B Material	3C Material	3D Material	Concrete	Bed Rock
Horizontal hydraulic conductivity $k_f$ [m/sec]	$1 \times 10^{-6}$	$1 \times 10^{-3}$	$1 \times 10^{-5}$	$1 \times 10^{-3}$	$1 \times 10^{-3}$	$1 \times 10^{-3}$	$1 \times 10^{-3}$	$1 \times 10^{-9}$	$1 \times 10^{-6}$
Colour in calculation									
Unit Weigth dry [kN/m <sup>3</sup> ]	18	21	21	21	22.5	22	21	24.5	23.5
Unit Weigth saturated [kN/m <sup>3</sup> ]	20.9	-	-	-	-	-	-	24.5	23.5
Dilatation angle [°]	0	8	8	8	5	5	5	15	20
Poission's ratio [-]	0.35	0.3	0.33	0.3	0.3	0.3	0.3	0.2	0.3
Reference pressure $p_{ref}$ [kN/m <sup>2</sup> ]	100	100	100	100	100	100	100	-	-
$E_{50}^{ref}$ [kN/m <sup>2</sup> ]	10000	73000	120000	105000	90000	70000	75000	-	-
$E_{oed}^{ref}$ [kN/m <sup>2</sup> ]	8000	55000	80000	75000	70000	55000	55000	-	-
$E_{ur}^{ref}$ [kN/m <sup>2</sup> ]	20000	151000	240000	210000	180000	140000	150000	-	-
Power m [-]	0.5	0.35	0.42	0.47	0.35	0.3	0.4	-	-
Failure ratio [-]	0.9	0.85	0.87	0.8	0.85	0.75	0.8	-	-
Young's Modulus E [kN/m <sup>2</sup> ]	-	-	-	-	-	-	-	2000000	2600000
Internal angle of friction [°]	30	38	45	49	49	49	49	45	35
Cohesion [kN/m <sup>2</sup> ]	15	0	0	0	0	0	0	500	250
Shear Modulus / $G_0^{ref}$ [kN/m <sup>2</sup> ]	11520	238000	202000	202000	202000	130000	140000	3500000	$1 \times 10^{100}$
Damping Rayleigh $\alpha$ [-]	0.5585	0.123	1.49	0.244	0.115	0.175	0.255	$4.19 \times 10^{-3}$	$4.19 \times 10^{-3}$
Damping Rayleigh $\beta$ [-]	$0.707 \times 10^{-3}$	$0.0624 \times 10^{-3}$	$3.77 \times 10^{-3}$	$0.525 \times 10^{-3}$	$0.263 \times 10^{-3}$	$0.486 \times 10^{-3}$	$0.453 \times 10^{-3}$	$0.212 \times 10^{-3}$	$0.212 \times 10^{-3}$

**Table 20 Material parameter sets applied to embankment fill material in Plaxis NL analysis**

## 11.3 Fujinuma Dam (Homogeneous)

### 11.3.1 Meshing

Figure 148 shows the numerical model of Fujinuma dam derived from software GeoStudio 2012. The horizontal model size was selected following a simple rule of thumb. Horizontal width = 7 times the horizontal base width of the compressible materials within the dam footprint. The vertical width in this case was guided by FKSH08 observation station resulting in 40m thick bedrock.

FKSH08 seismic observation station is part of Japan's seismic observation network KiK-Net. Further information about KiK-Net and FKSH08 station may be found in chapter: 9.1 Japan's seismic observation networks KiK-Net & K-Net and in chapter: 9.2.1 Seismic Observation Station FSKH08.

The thickness of the Tuff base rock in Fujinuma dam model was selected the same as in FKSH08 station as the lower accelerograph of FSKH08 is situated 40m deep in rock.

Figure 149 plots the detailed section of Fujinuma dam model showing the overall geometry, material boundaries, the mesh and selected location of history points. Figure 150 shows a close up of special interest. The orange colored upper fill is supposed to be cohesion-less sand whilst the lower brown material is cohesive silty sand. It can be seen that the upstream boundary between these two materials needed very fine meshing and interface elements. This was done to exclude any tensile stresses that would transmit otherwise from brownfill to sandfill. The reason for this is: within Non-linear analysis in GeoStudio 2012, cohesionless soils under limited tensile stress would completely liquefy due to a numerical discontinuity in pore water pressure generation. Further details on this are presented in chapter: 0





## Results and Comparison.

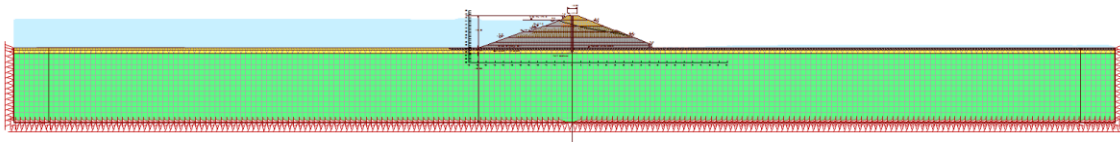


Figure 148 Fujinuma dam model after impounding, general view

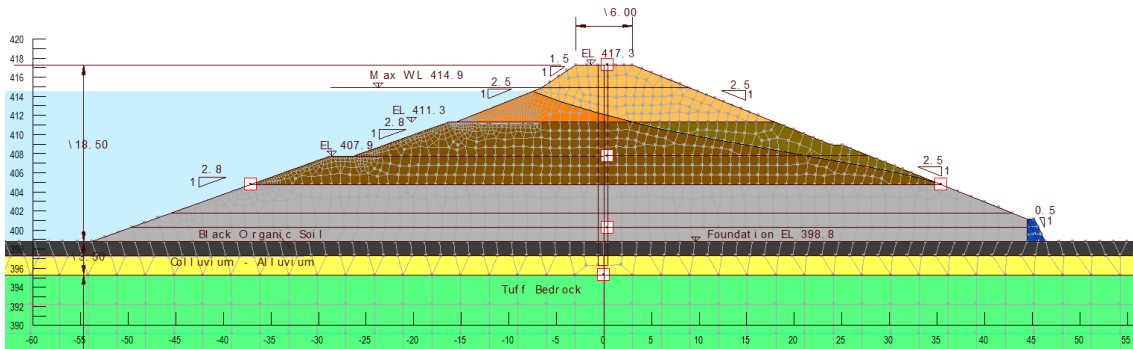


Figure 149 Fujinuma dam model after impounding, dam cross section

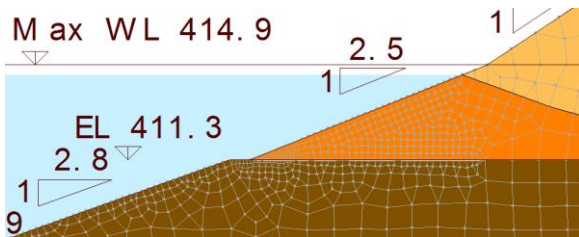


Figure 150 Fujinuma dam model close up view cohesive to non-cohesive materials

### 11.3.2 Seismic Input Motion

As no seismic observation stations were installed at Fujinuma dam, there is no information on the base acceleration. However, Japan spent enormous effort on a comparably dense observation network. Due to this effort, the seismic observation station FSKH08 monitored the acceleration of Tohoku earthquake in a depth of 48m in stable rock. FSKH08 station is composed of a pair of seismographs. One is located at ground surface whilst the other is placed within a borehole in stable rock. FKSH08 station is located in a distance of 3,2km from Fujinuma dam site. Distance, geological and topographical situation indicate that FKSH08 provides the best input data for back analysis of Fujinuma dam. Within chapter: 9.2.1 a FE model was developed in order to back

calculate the dynamic material properties of FKSH08 subsoil and base rock. The calibrated material set of FKSH08 base rock was then used for Fujinuma dam seismic analysis.

Data observed in FSKH08 borehole seismograph is available in North – South, East – West and Up – Down direction. In order to act as input for Fujinuma dam analysis, the two horizontal components were rotated to result in input that is orthogonal to Fujinuma dam axis.

Figure 151 and Figure 152 show the horizontal and vertical input acceleration applied to the base of Fujinuma dam model. It can be seen that the ground motion did not result in extraordinary high peak acceleration (note the recording was taken in a depth of 48m below ground) but it was of extra ordinary long duration.

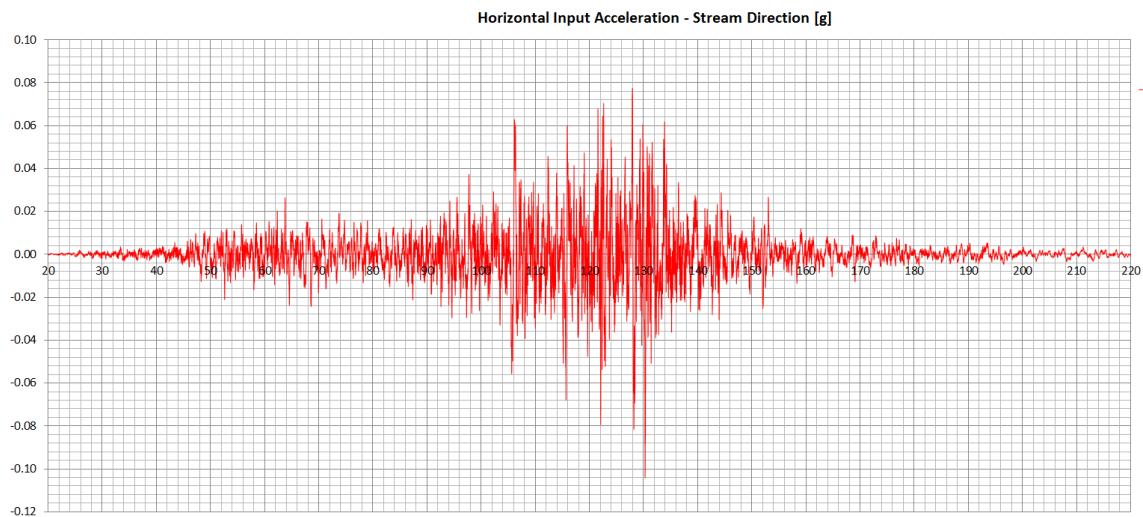


**Figure 151 Horizontal base acceleration Fujinuma dam model**

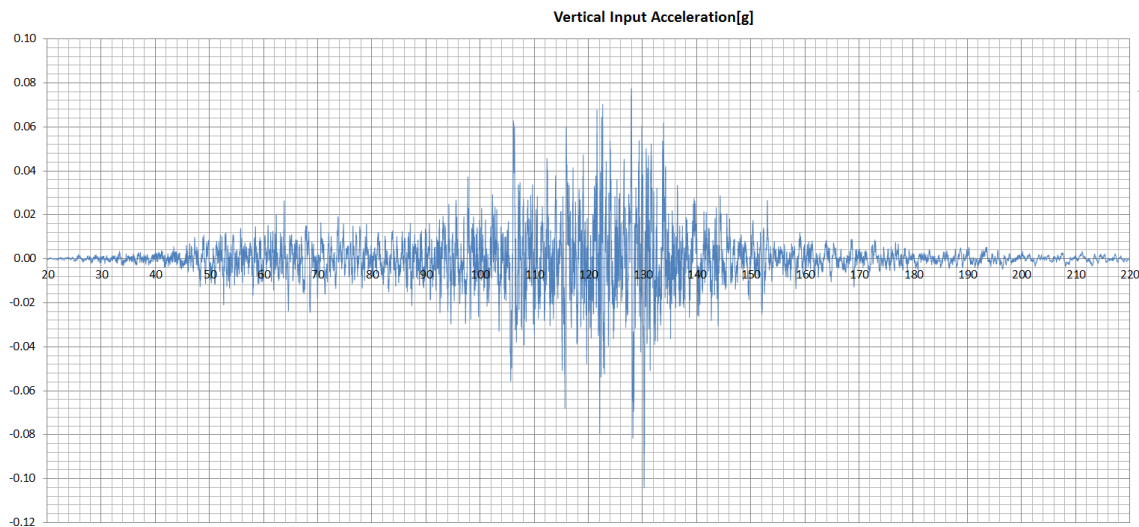


**Figure 152 Vertical base acceleration Fujinuma dam model**

The dam model was further calibrated against an earlier control earthquake where no damage of the dam occurred. Hence the second strongest earthquake ever recorded by station FKSH08 was selected and the input acceleration thereof was processed as described above to gain adequate input data for Fujinuma dam check analysis. This procedure was done to ensure that the selected material sets come as close to reality as possible.

One might bear in mind: Liquefaction of hardened concrete is quite easy in Finite Element analysis.

### **11.3.3 Stepped Construction & Boundary Conditions**

Within the model the dam was built in 6 steps in order gain the correct stress distribution of the embankment. While this procedure is of highest importance for embankments with zones of varying stiffness (especially core type dams) it is of minor importance for Fujinuma dam. Never the less stepped construction was applied for this model too.

For calculation of initial stresses, construction steps and impounding the boundary conditions are the same. Vertical model boundaries shall be fixed in horizontal and free in vertical direction whilst the horizontal base of the model was fixed in both directions. During earthquake calculation the boundary conditions need to be changed.

The model base boundary was fixed in both directions and the dynamic input accelerates this “fixed” base following the time history data set. The vertical boundary was selected to deform freely in horizontal and vertical direction. Furthermore “Free Field” boundaries were applied in Plaxis software and damping regions were added in GoeStudio software to the left and right side edges.

The deformation of embankments after an earthquake is of special interest to judge if the dam behaves in a safe manner. Extreme deformations may induce a dam’s failure with catastrophic consequences.

In case of Fujinuma dam soil liquefaction seems to play an important role for the dam’s failure. In order to calculate the embankment’s deformation it is important to define two cases. Firstly deformations that directly result from and during the earthquake and secondly deformations that result from gravity driven (i.e. static) forces due to the loss of shear strength of liquefied material zones. Hence in case of Fujinuma seismic analyses, a second “Stress- Redistribution” analysis was added just after the earthquake calculation. The boundary conditions of this stress – redistribution calculation are the same as discussed for initial stress, stepped construction and impounding steps.

Furthermore, global (and local) stability calculations were performed prior and after the earthquake, on upstream and downstream slopes. GeoStudio 2012 enables the user to perform such stability calculations in a wide range of international standards. Plaxis 2015 relies on a single “global” factor of safety derived from FE stability calculations only (i.e. stress - deformation analysis in a wider sense).

Figure 153 to Figure 157 plot an extract of the model procedure (only those steps where changes can be seen graphically)

Summing up, the selected calculation steps are as follows:

- Initial stresses
- Layered construction of embankment
- Impounding
- Prior earthquake stability analysis

- Earthquake analysis
- Post-earthquake deformation analysis
- Post-earthquake stability analysis

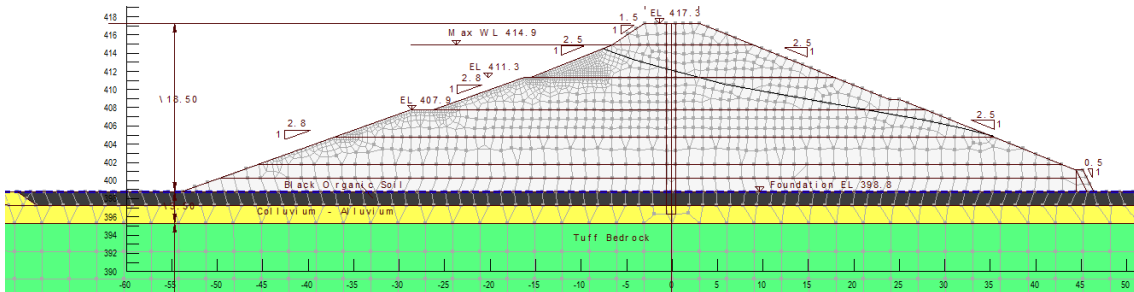


Figure 153 Fujinuma dam model – initial stresses

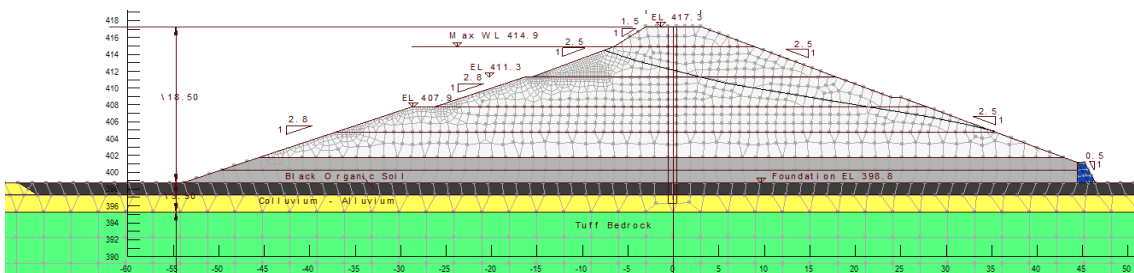


Figure 154 Fujinuma dam model – layered construction – first layer

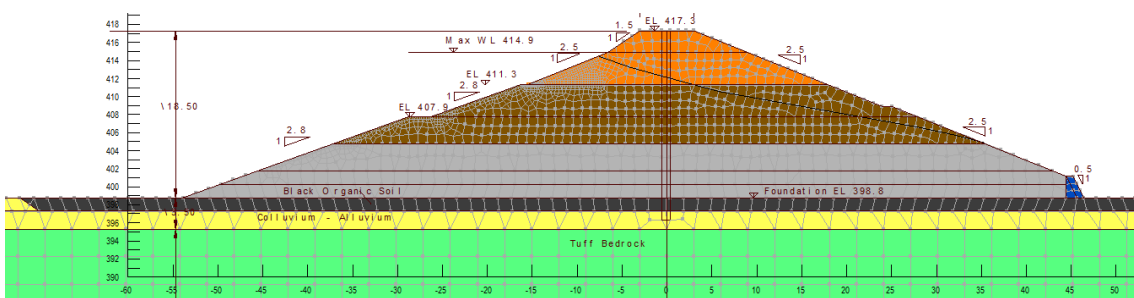


Figure 155 Fujinuma dam model – layered construction – last layer

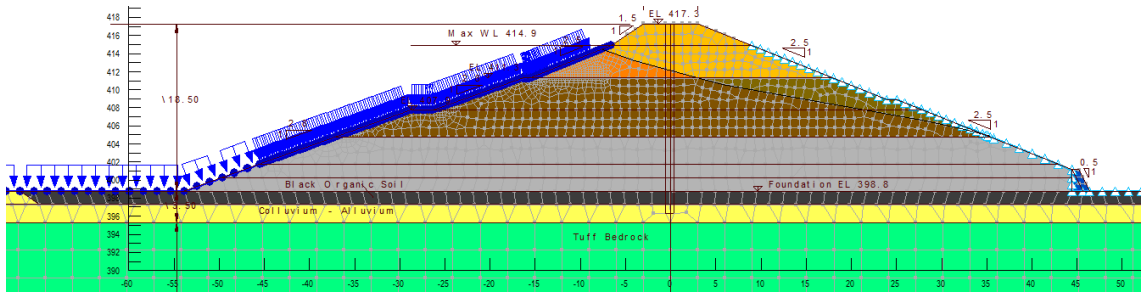


Figure 156 Fujinuma dam model – impinging

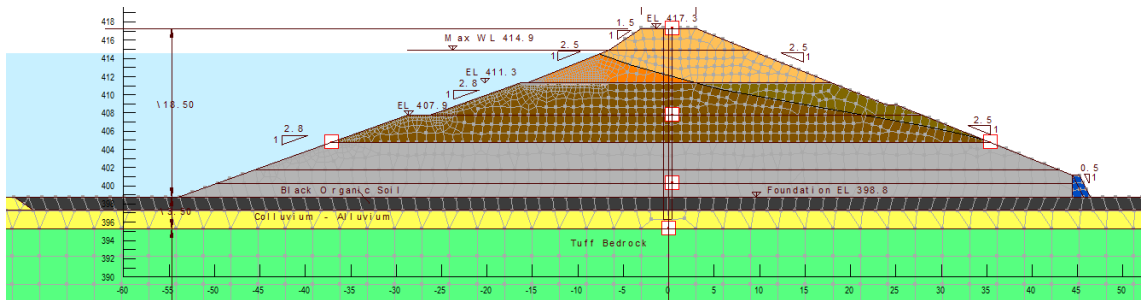


Figure 157 Fujinuma dam model – earthquake analysis

### 11.3.4 Equivalent number of Cycles vs. Rupture Distance

The number of equivalent stress cycles was estimated by use of Figure 122. Due to the low number of  $M_w = 9.0$  earthquakes and the corresponding lack of data, Figure 122 logically lacks for information in the  $M_w = 9.0$  range. However, the result may still be estimated graphically.

Input parameters for Fujinuma dam during <u>Tohoku earthquake</u> are as follows:	Input parameters for Fujinuma dam during <u>Check earthquake</u> are as follows:
$R = 100\text{km}$	$R = 10\text{km}$ (assuming $10 \times 10 \text{ km}$ fault dimensions)
$M_w = 9.0$	$M_w = 5.7$
$\Rightarrow N_{eq} = 68$	$\Rightarrow N_{eq} = 7$

### 11.3.5 Best Fit Input Parameter Sets

Table 21 sums up all material parameters applied to Fujinuma dam fill materials. These parameters were applied to the Equivalent – Linear and Nonlinear analysis in software product GeoStudio 2012. Cells marked \*\* resulted from laboratory tests on undisturbed Fujinuma dam fill samples acc. to Charatpangoon 2014.

Material type		Sandfill	Brownfill	Greyfill	Black Organic Soil	Alluvium - Colluvium	Tuff Rock
Soil type acc. Unified Soil Classification System		SW - SM	SC or CL	SM	-	-	-
Shear wave velocity [m/sec]		100	80*	180*	180*	200	360*
$G_{max}$ [kN/m <sup>2</sup> ]		18000	11520	55080	55080	76000	650000
Horizontal hydraulic conductivity $k_{f,x}$ [m/sec]		$5.5 \times 10^{-7}$ **	$5.5 \times 10^{-7}$ **	$5.5 \times 10^{-7}$ **	$3.6 \times 10^{-8}$	$6 \times 10^{-6}$	$1 \times 10^{-7}$
Vertical hydraulic conductivity $k_{f,y}$ [m/sec]		$1.4 \times 10^{-7}$	$1.4 \times 10^{-7}$	$1.4 \times 10^{-7}$	$1.8 \times 10^{-8}$	$1.5 \times 10^{-6}$	$1 \times 10^{-7}$
Colour in calculation							
Weight above water table [kN/m <sup>3</sup> ]		16**	14**	16**	-	-	-
Saturated Weight [kN/m <sup>3</sup> ]		18**	16**	18**	20	19	13
Dilatation angle [°]		0	0	0	0	0	5
Poission's ratio [-]		0.3**	0.3**	0.3**	0.45	0.25	0.13
Young's Modulus E [kN/m <sup>2</sup> ]		17500**	30000**	50000**	20000	20000	300000
Internal angle of friction [°]		37**	32**	31**	23	37	40
Cohesion [kN/m <sup>2</sup> ]		0**	8**	18**	20	2	500
Steady state shear strength when liquefied [kN/m <sup>2</sup> ]	Steady state strength [kN/m <sup>2</sup> ]	4	6	7	4	3	-
	Collapse surface angle [°]	25.3	22.1	21.4	3	25.3	-
Damping Ratio [-] ***		0.02	0.0195	0.02	0.02	0.02	0.0045
Maximum Damping Ratio [-]***		0.27	0.262	0.27	0.27	0.27	0.37

\* Shear wave profile according to Harder et al. 2011

\*\*Parameter based on laboratory tests on undisturbed Fujinuma dam fill samples acc. to Charatpangoon 2014

\*\*\* Applied to Nonlinear Analysis in Software GeoStudio only, values represent the lower and upper bound of damping vs. shear strain curves used in EL analysis

**Table 21 Material parameter sets applied to embankment fill material in GeoStudio EL and NL analysis**

Figure 158 and Figure 159 show the  $G_{max}$  reduction curve respectively the damping ratio vs. shear strain applied to Fujinuma dam for all Equivalent - Linear calculations.  $PI = 0$  was applied to materials without significant cohesion i.e. the sandfill and alluvial layers.  $PI = 10$  was applied to cohesive materials i.e. brownfill, greyfill and the black organic subsoil. Both curves were directly taken or estimated from Vucetic and Dobry (1991). Damping of Tuff rock was taken from the intensive research of Jeon (2008) on Tuff specimens. These material parameters remain unchanged for calculation of both earthquakes: Tohoku and check earthquake.



Figure 160 plots the curves selected for pore water pressure built up. When the pore water pressure ratio reaches 1 the soil is assumed to liquefy. The pore water pressure ratio is selected based on the ratio of actual cyclic number divided by the number of equivalent stress cycles (NL). The curves are based on a formula developed by DeAlba, Chan and Seed (1975). Figure 161 shows the shear stress ratio vs. actual number of cycles (N). Again these curves remain unchanged for calculation of both earthquakes: Tohoku and check earthquake.

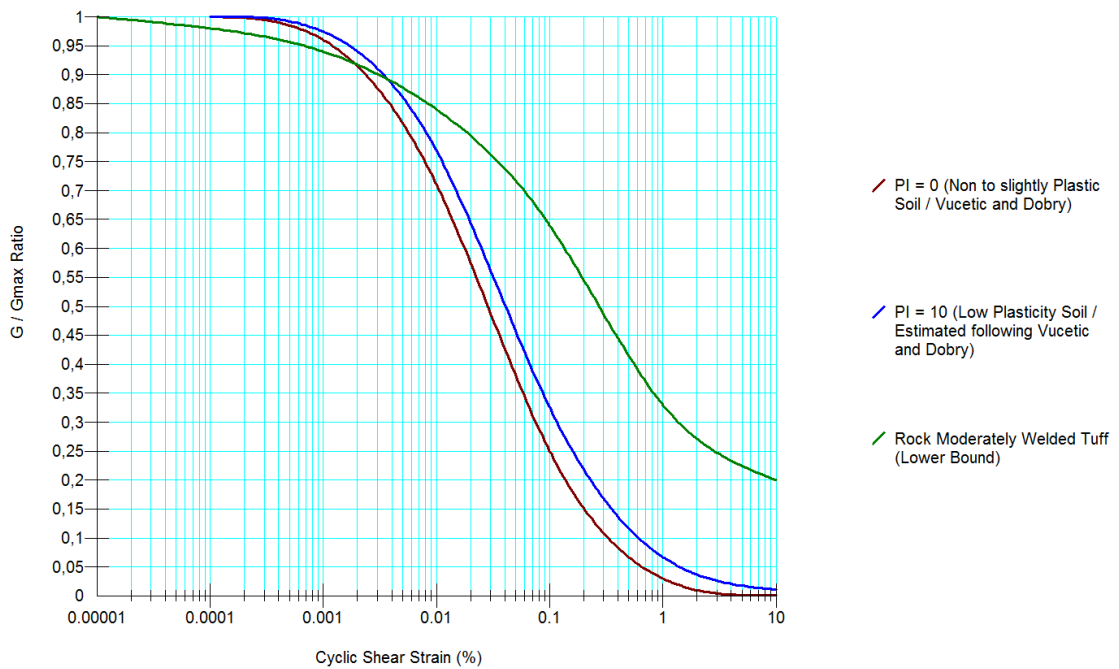


Figure 158 Shear modulus reduction vs. shear strain applied to embankment fill material in GeoStudio EL analysis

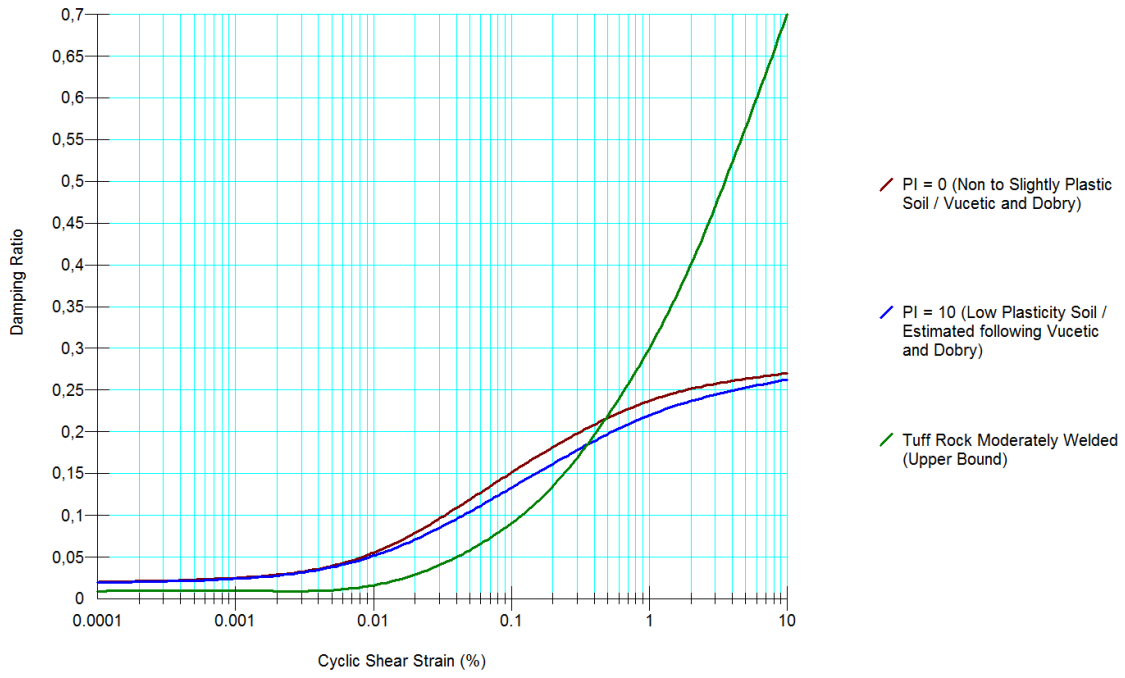


Figure 159 Damping ratio vs. shear strain applied to embankment fill material in GeoStudio EL analysis

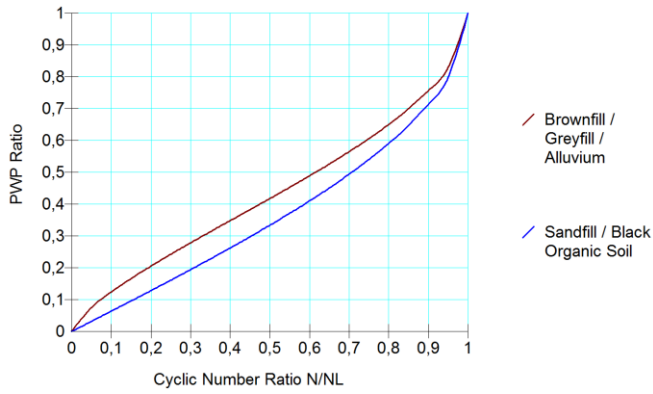
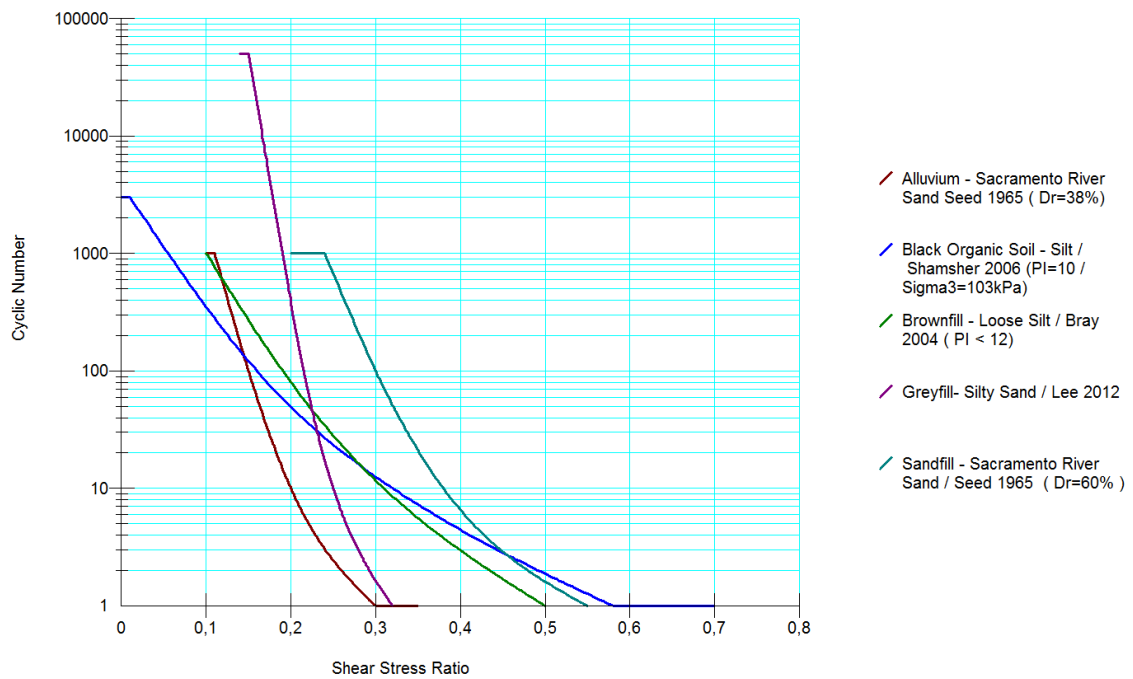


Figure 160 Pore water pressure built up vs. cyclic number ratio applied to embankment fill material in GeoStudio EL analysis



**Figure 161 Shear stress ratio vs. actual cyclic number applied to embankment fill material in GeoStudio EL analysis**

GeoStudio 2012 software uses the Martin – Finn – Seed pore water pressure generation within its Nonlinear dynamic analysis. Compared to the Equivalent – Linear analysis, nonlinear analyses provide the important benefit of pore water pressure generation during calculation for each time step. Thus, the effects of liquefaction on the dynamic behavior as substantially increased damping and  $G_{max}$  reduction can be simulated. GeoStudio calculates the MFS parameters from a set of two input curves (Figure 162 and Figure 163).

Martin Finn Seed procedure is an important development in numerical description of the liquefaction process. The Procedure has lots of benefits and only a few drawbacks. Unfortunately Martin Finn Seed procedure is not a widely spread model and hence input parameters are rare in international literature as they are usually not part of standard soil investigations. Furthermore it has to be pointed out that the selected parameter set shall on the one hand ideally fit the soil type and on the other hand it needs to be selected in accordance with the soils shear strain during the earthquake. This combination is only found in literature if the soil testing program has been done

explicitly to determine the MFS parameters. It is not possible to derive a consistent set of values from a standard site investigation program.

Figure 162 plots all recoverable modulus curves applied to the material of Fujinuma dam. These curves remain unchanged for calculation of both earthquakes: Tohoku and check earthquake. Figure 163 shows the accumulated vs. incremental volumetric strain curves applied to Fujinuma dam material. The procedure how MFS procedure is incorporated in GeoStudio 2012 indirectly assumes that the material that might liquefy has negligible or no cohesion. If cohesive material is investigated, material in tensile minimum stress area in the range from 0.5 to 0 kPa will always liquefy no matter the size of the dynamic loading is. Figure 164 plots this discontinuity in case of brownfill applied to the check earthquake. It is impossible to avoid this local discontinuity due to the mathematical formulation of the curve. It will create a small band of liquefaction as a result but if the user is aware of it, it will not cause any further abnormalities. However, the reader has to bear that in mind when checking the later presented results of the check earthquake.

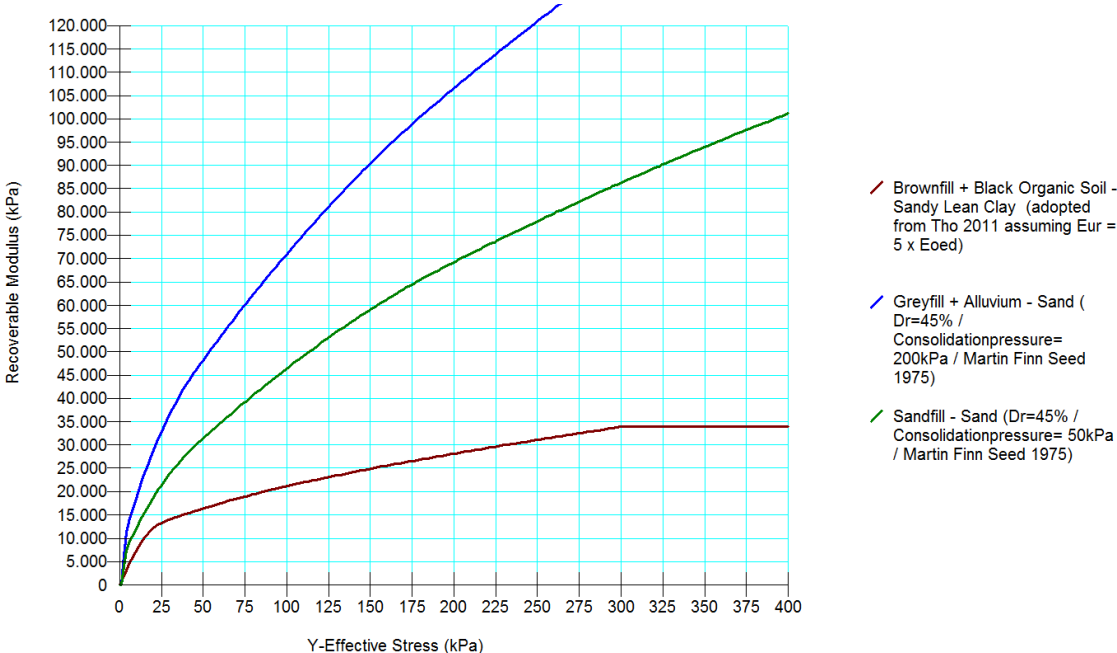
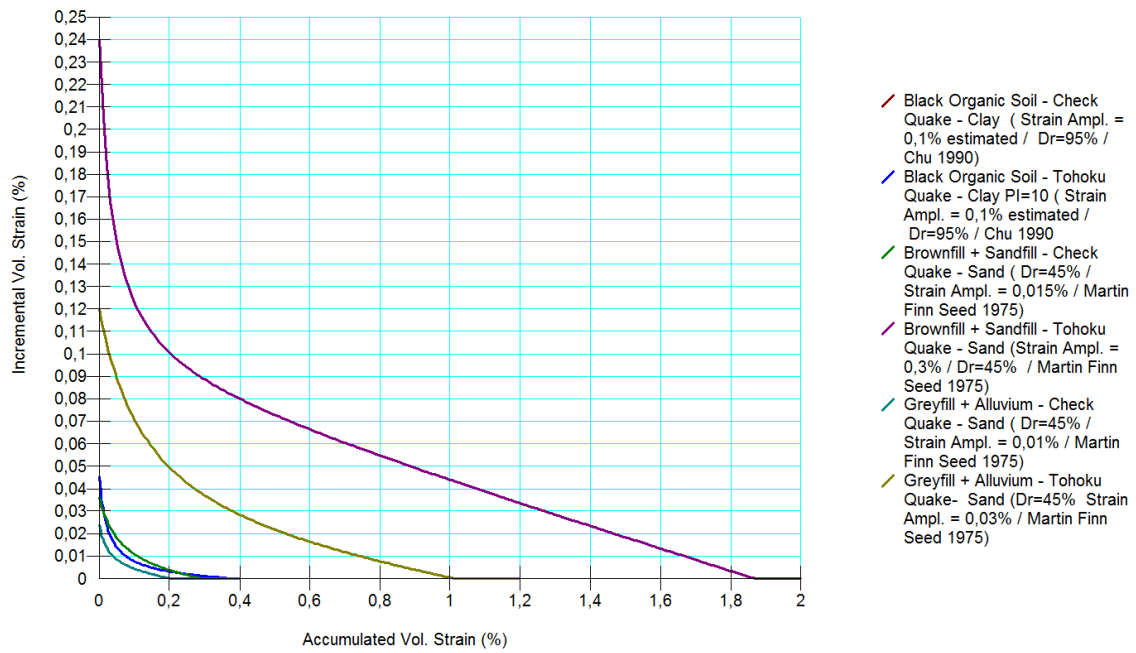
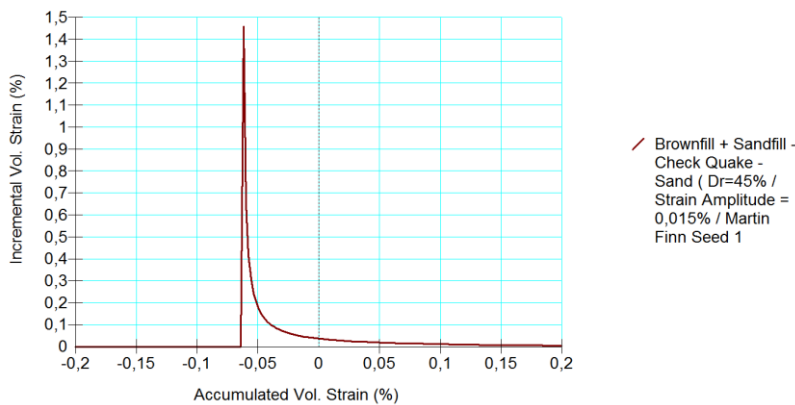


Figure 162 Recoverable modulus vs. vertical effective stress applied to embankment fill material in GeoStudio EL analysis



**Figure 163 Accumulated vs. incremental volumetric strain functions applied to embankment fill material in Geo-Studio NL analysis**



**Figure 164 Discontinuity of accumulated vs. incremental volumetric strain**

Table 22 sums up all parameters applied to the materials of Fujinuma dam in Plaxis Software product. Cells marked \*\* resulted from laboratory tests on undisturbed Fujinuma dam fill samples acc. to Charatpangoon 2014. Within Plaxis, three types of material models were used for all calculation phases. Linear Elastic model was applied to

base rock for all calculation phases from initial, to layered construction, dynamic calculation and post-earthquake deformations. Hardening soil small strain (HSS) model was used for all compressible materials for initial, layered construction and post-earthquake deformations. HSS model was applied to black organic soil during dynamic analysis too. UBC2D model was applied to all liquefiable materials for the dynamic analyses. Again the model of Fujinuma dam was calculated for the Tohoku earthquake which led to the dam's failure and for physical reliability, for the Check earthquake too. As the pore water pressure built up in Plaxis is a fully closed formulation mainly depending on the unloading- / reloading-modulus, the same parameter set can be used for calculation of Tohoku and Check earthquake. The Martin – Finn – Seed pore water pressure model as used in GeoStudio, calls for an iterative adaptation of the MFS-function to the resulting shear strains in each zone.

Damping ratios and related frequencies of each material were selected in an iterative procedure. Depending on the calculated shear strain, damping ratios in detail were selected as shown in Figure 159 (i.e. the GeoStudio input data to achieve maximum

comparability of both software packages).

Material type		Sandfill	Brownfill	Greyfill	Black Organic Soil	Alluvium - Colluvium	Tuff Rock
Soil type acc. Unified Soil Classification System		SW - SM	SC or CL	SM	-	-	-
Shear wave velocity [m/sec]		-	-	-	-	-	900
Compressionla wave velocity [m/sec]		-	-	-	-	-	2150
Poissions ratio [-]		-	-	-	-	-	0.39
Horizontal hydraulic conductivity $k_{f,x}$ [m/sec]		$5.5 \times 10^{-7}$ **	$5.5 \times 10^{-7}$ **	$5.5 \times 10^{-7}$ **	$3.6 \times 10^{-8}$	$6 \times 10^{-6}$	$1 \times 10^{-7}$
Vertical hydraulic conductivity $k_{f,y}$ [m/sec]		$1.4 \times 10^{-7}$	$1.4 \times 10^{-7}$	$1.4 \times 10^{-7}$	$1.8 \times 10^{-8}$	$1.5 \times 10^{-6}$	$1 \times 10^{-7}$
Colour in calculation							
Weigth above water table [kN/m <sup>3</sup> ]		16**	14**	16**	-	-	-
Saturated Weigth [kN/m <sup>3</sup> ]		18**	16**	18**	20	19	13
Reference pressure $p_{ref}$ [kN/m <sup>2</sup> ]		100	100	100	100	100	
Dilatation angle [°]		0	0	0	0	0	5
$E_{50}^{ref}$ [kN/m <sup>2</sup> ]		15000	10000	12000	12000	13000	-
$E_{oed}^{ref}$ [kN/m <sup>2</sup> ]		12000	8000	9600	9600	10400	-
$E_{ur}^{ref}$ [kN/m <sup>2</sup> ]		30000	20000	36000	36000	39000	-
Elastic shear modulus $k_G^e$		180	115.2	551	-	760	-
Plastic shear modulus $k_G^p$		67	38.4	204	-	281	-
Elastic bulk modulus $k_G^e$		126	80.6	386	-	532	-
Power elastic shear module $n_e$		0.5	0.5	0.5	-	0.5	-
Power plastic shear modulus $n_p$		0.4	0.4	0.4	-	0.4	-
Power elastic bulk modulus $m_e$		0.5	0.5	0.5	-	0.5	-
Failure ratio [-]		0.8	0.8	0.8	0.9	0.8	
Young's Modulus E [kN/m <sup>2</sup> ]		-	-	-	-	-	300000
Internal angle of friction [°]		37**	32**	31**	23	37	40
Internal angle of friction at constant volume [°]		35	30	29	-	35	-
Cohesion [kN/m <sup>2</sup> ]		0**	8**	18**	20	2	500
Damping Rayleigh $\alpha$ [-]		2.32	2.32	1.595	2.9	3.045	
Damping Rayleigh $\beta$ [-]		$1.96 \times 10^{-3}$	$1.96 \times 10^{-3}$	$1.35 \times 10^{-3}$	$0.612 \times 10^{-3}$	$2.57 \times 10^{-3}$	$1.96 \times 10^{-3}$

\* Shear wave profile according to Harder et all. 2011

\*\*Parameter based on laboratory tests on undisturbed Fujinuma dam fill samples acc. to Charatpangoon 2014

**Table 22 Material parameter sets applied to embankment fill material in Plaxis NL analysis**





## 12 Results and Comparison

### 12.1 Aratozawa Dam (ECDR)

Figure 165 shows the pore water pressure resulting from seepage analysis. For further reference, Figure 168 shows the minimum effective stresses within core region after impounding. The minimum effective stress exceeds zero in the clay core at every point.

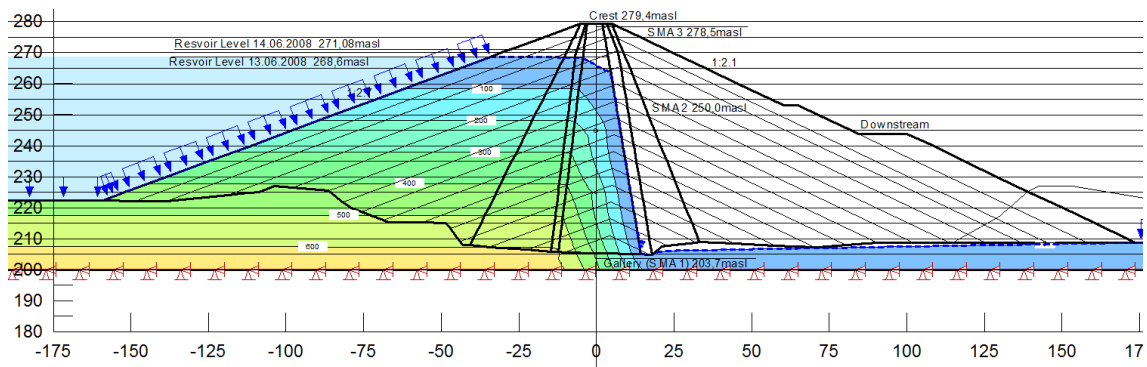


Figure 165 Pore water pressure distribution after impounding (prior earthquake) of Aratozawa dam

It shall be explained how input parameters are connected to stress plots to better understand the stepwise calculation. Figure 166 shows the effective vertical stresses of Aratozawa dam shortly prior the earthquake analysis. Software product GeoStudio links all input parameters to the effective vertical stress whilst software Plaxis links it to the major principal stress ( $\sigma_1$ ). Figure 123 to Figure 125 show the selected material parameters for the earthquake analysis. These material parameters are represented by curves in a graph plotted against the effective vertical stress. For example, point A (see Figure 166) plots in the dam's downstream shoulder at an effective vertical stress range of  $800 \text{ kN/m}^2$ . The shear modulus that is applied to the finite element within the first iteration would then be calculated from  $G_{\max}$  and  $G_{\max}$  reduction. According to Figure 125,  $G_{\max}$  would result in  $370000 \text{ kN/m}^2$ .  $G_{\max}$  would then be multiplied by a factor that varies from the calculated shear strain at that element ( $G_{\max}$  Reduction, see Figure 123). Here the difference between Equivalent Linear and Nonlinear analysis pops up. The  $G_{\max}$  reduction value and the damping values are calculated referring to the resulting (cyclic) shear strain. The shear strain in Nonlinear analysis is calculated in

each time step during the earthquake. The shear strain in Equivalent Linear Analysis is adjusted at the end of the earthquake analysis again for each iteration. Figure 167 shows a close up view of the calculated cyclic shear strain at time step 4,82 sec during the Nonlinear earthquake analysis. At point A the cyclic shear strain would result in 0,0005%, hence the shear modulus would result in  $370000 \times 0,82 = 303000 \text{ kN/m}^2$ . The damping applied to the finite element would result in  $0,01 = 1\%$  (Figure 124).

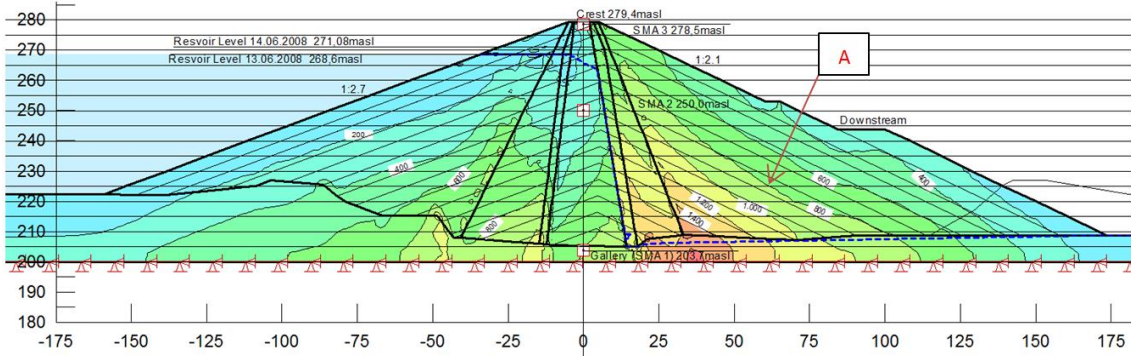


Figure 166 Effective vertical stresses after impounding and prior earthquake of Aratozawa dam [kN/m<sup>2</sup>]

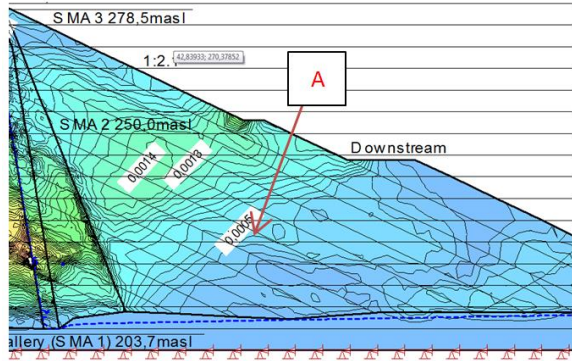


Figure 167 Cyclic shear strain at 4,82 sec during the earthquake analysis of Aratozawa dam [-]

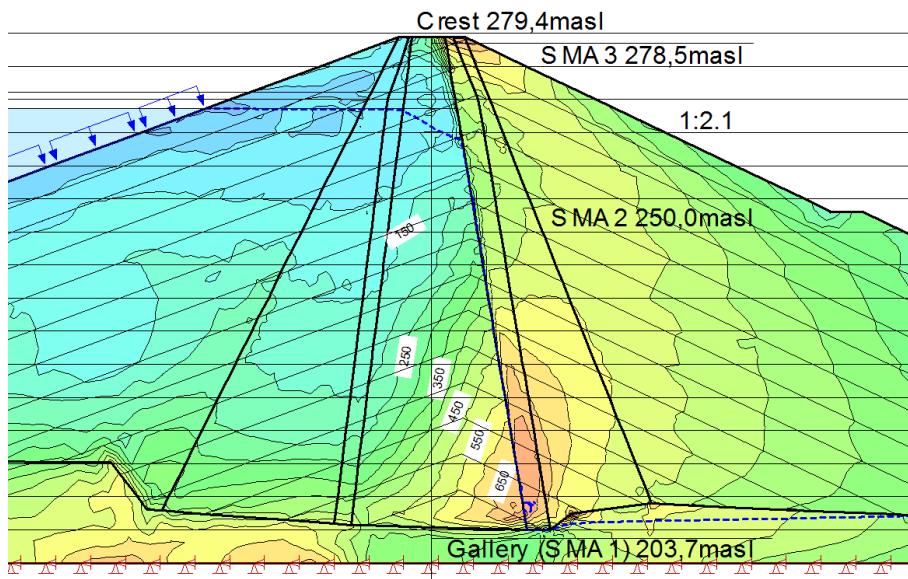


Figure 168 Effective minimum stresses within the clay core after impounding of Aratozawa dam [kN/m<sup>2</sup>]

### 12.1.1.1 Linear Equivalent Code – GeoStudio 2012

Figure 169 and Figure 170 plot the horizontal respectively the vertical peak acceleration due to Iwate / Miyagi earthquake. The spotted view is typical for near fault excitation as the impulse is typically strong (single peaks) but short in duration, lacking for a bundle of frequencies mainly in the lower frequency region. But, this keeps true for earthquakes resulting from single shear planes only. Mega earthquakes often result from the time delayed connection of several single previously separated shear planes.

Figure 171 and Figure 172 show the horizontal and vertical crest accelerograph calculated at SMA 3 location. The resulting peak acceleration is 0,57g in horizontal direction and 0,64g in vertical direction. Compared to the observed peak accelerations (i.e. 0,54g horizontal / 0,63g vertical) the calculated results perfectly fit the measured ones. The result in a first view surprises.

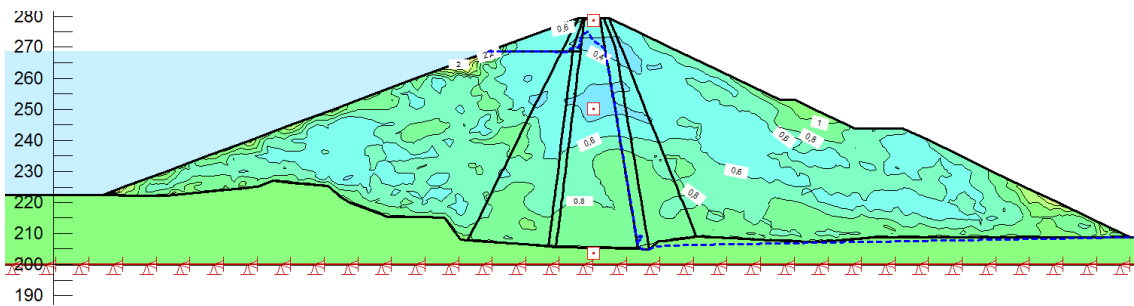


Figure 169 Horizontal peak acceleration due to Iwate / Miyagi earthquake [g] (EL GeoStudio)

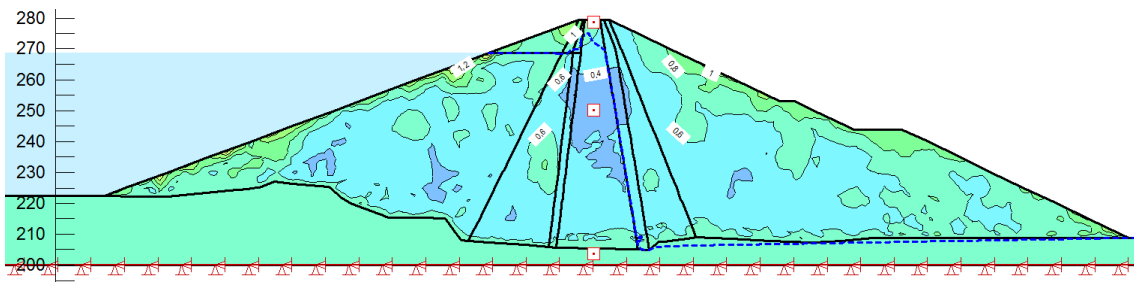


Figure 170 Vertical peak acceleration due to Iwate / Miyagi earthquake [g] (EL GeoStudio)

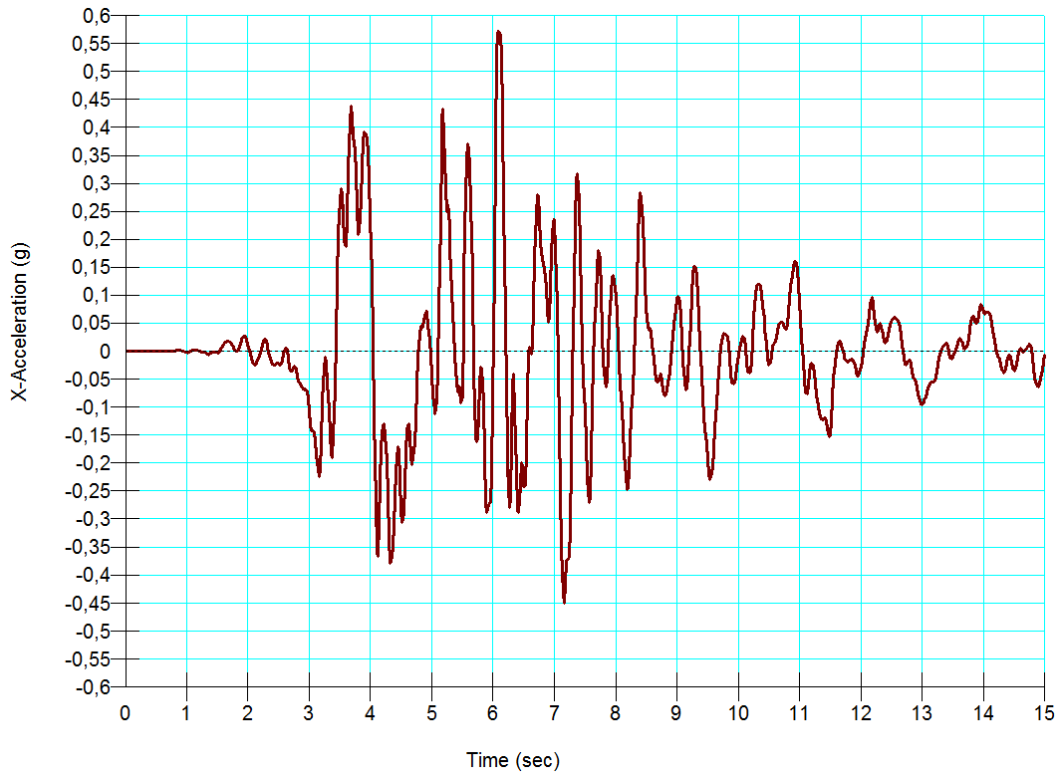


Figure 171 Horizontal crest acceleration calculated from Iwate / Miyagi earthquake – SMA 3 [g] (EL GeoStudio)

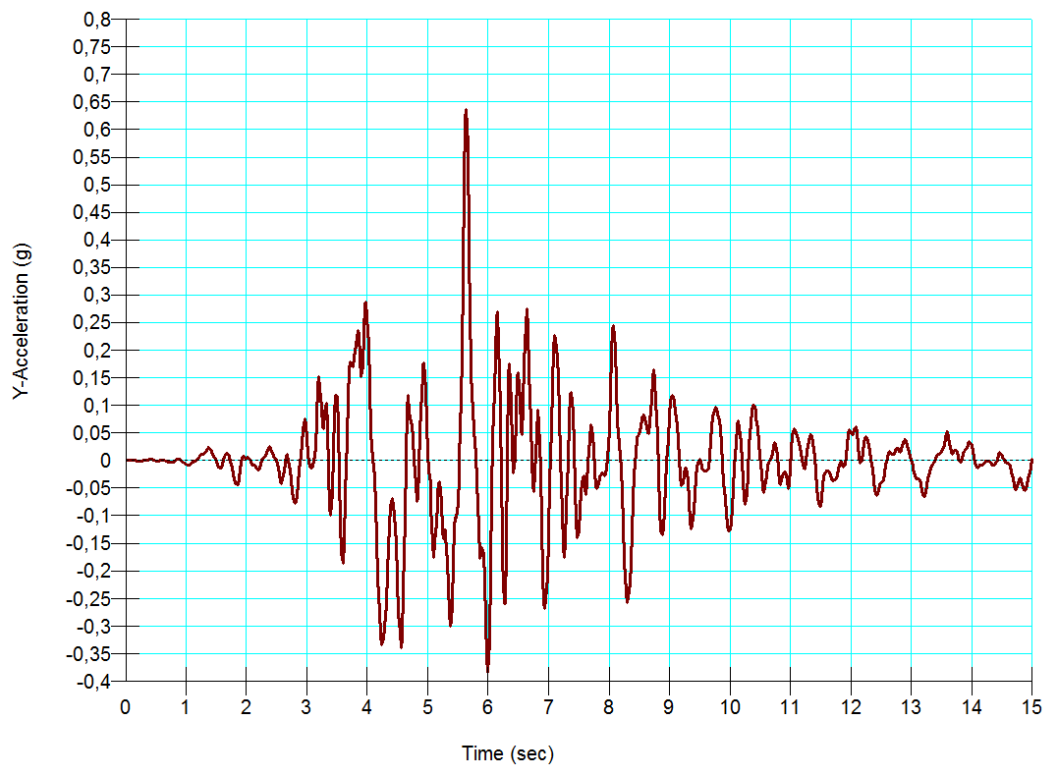


Figure 172 vertical crest acceleration calculated from Iwate / Miyagi earthquake – SMA 3 [g] (EL GeoStudio)

Figure 173 shows the calculated pore water pressure distribution after Iwate / Miyagi earthquake. It can be seen that the pore water pressure rose significantly within the core region. Figure 174 plots the pore water pressure development in detail. Comparing the calculated increase (Figure 175) with the measured increase in pore pressure (Table 15) indicates that the result is in acceptable agreement with monitoring data. Clearly the pore water pressure does not fit accurately for all 5 gauge locations but having in mind the rough formulations / assumptions of the constitutive model the result surprises. In addition, Figure 175 plots the effective minimum stresses within core region as a result to the risen pore pressures after the earthquake. The plotted range starts from  $5\text{kN/m}^2$ . Hence white plotted areas show locations that are close to liquefaction or that have liquefied. At higher elevations, this is to some extent due to the overestimated pore water pressure development.

Figure 176 shows one drawback of the Equivalent – Linear analysis. By nature EL analysis cannot simulate plastic deformations of the fill zone. This becomes clear in Figure 176 as the crest “settlement” directly follows the prescribed displacement of the earthquake input data. Figure 177 plots the calculated settlement resulting from so called stress – redistribution analysis. A stress redistribution analysis, in this case does not include consolidation settlement. It simply redistributed stresses from single elements that are not in equilibrium at end of the dynamic analysis. The crest settlement from stress – redistribution analysis result in a total settlement of 3cm. It may be stated that stress – redistribution analysis are better applied to homogeneous dams or in cases where fill materials show significant decrease in shear strength. In case of earth core rockfill dams the high strength outer shell material hinders the horizontal deformation of the core material.

Judging earthquake deformations in rockfill material therefore needs to be based on other calculations. As long as liquefaction is not the governing reason for earthquake induced deformations, this can be done by state of the art approaches as Newmark’s double integration or Makdisi – Seed method.

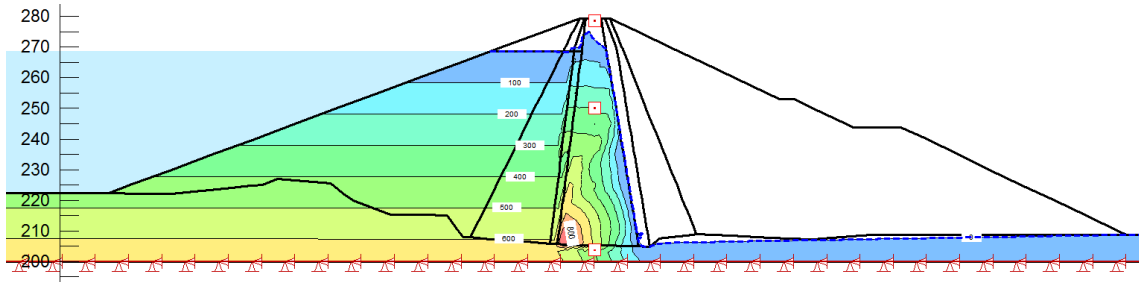


Figure 173 Pore water pressure distribution after Iwate / Miyagi earthquake [ $\text{kN/m}^2$ ] (EL GeoStudio)

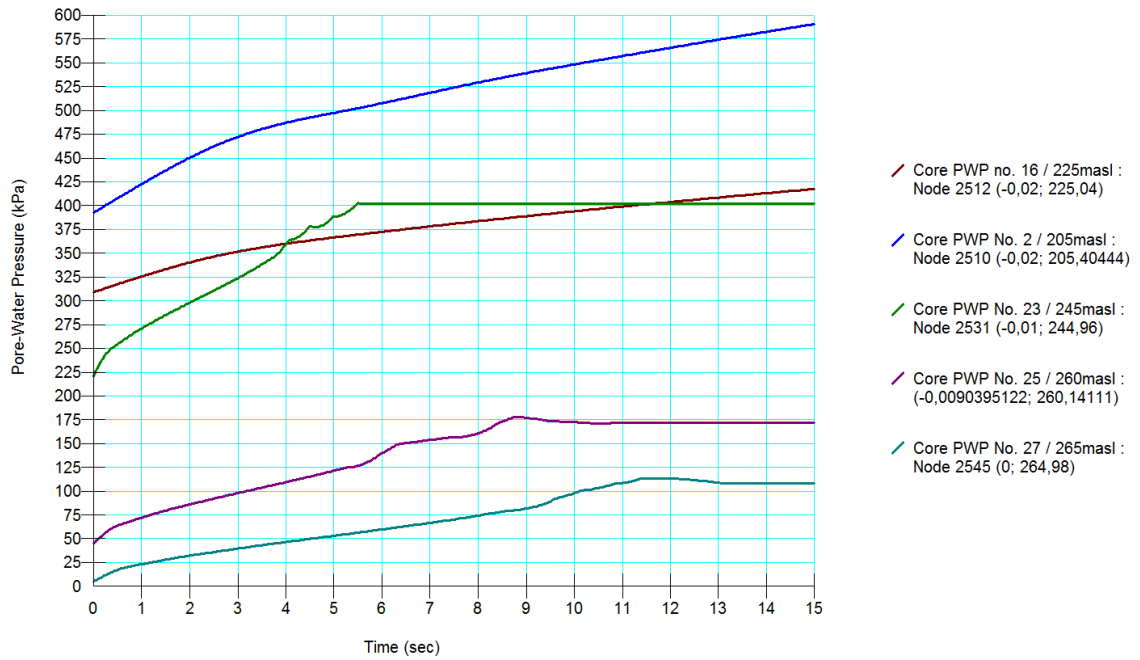


Figure 174 Pore water pressure development during Iwate / Miyagi earthquake [ $\text{kN/m}^2$ ] (EL GeoStudio)

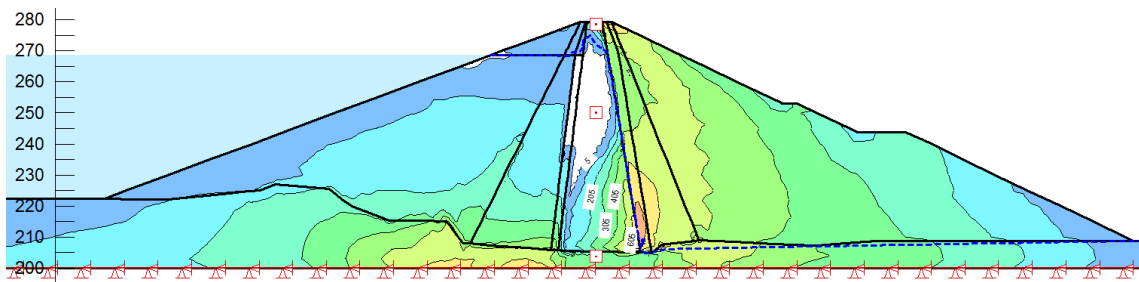


Figure 175 Distribution of effective minimum stresses after Iwate / Miyagi earthquake [ $\text{kN/m}^2$ ] (EL GeoStudio)

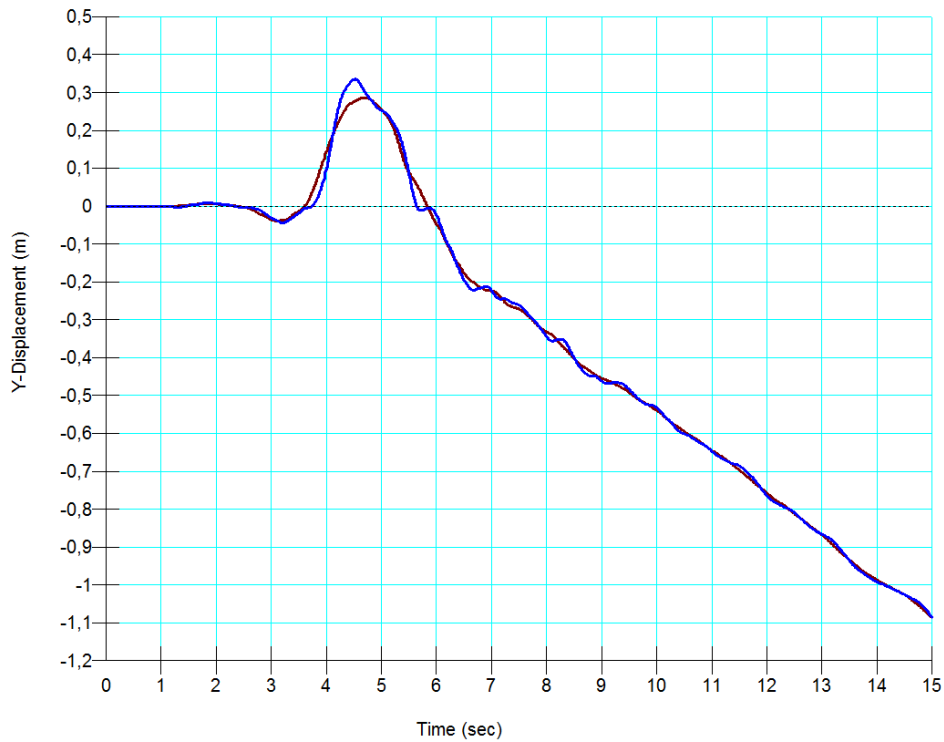


Figure 176 Vertical crest vs. base displacement [m] (EL GeoStudio)

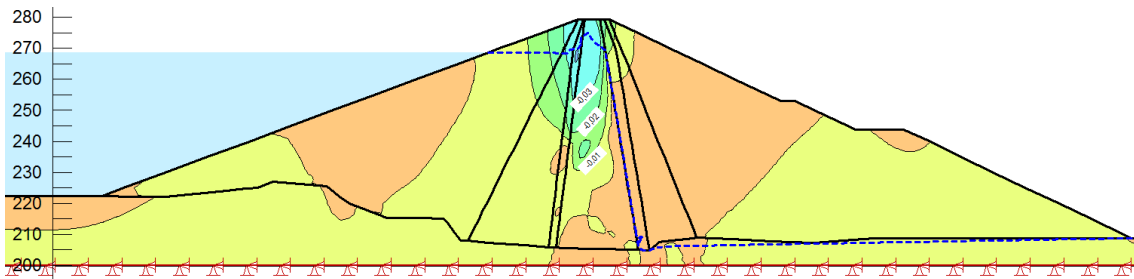


Figure 177 Vertical crest settlement from post-earthquake stress – redistribution analysis[m] (EL GeoStudio)

Figure 178 to Figure 184 plot the results from Newmark's double integration. Newmark's double integration is incorporated into GeoStudio 2012 and may be added as a further calculation step to estimate the dam's permanent deformations. The calculated acceleration of every specified slip surface in every **stored** time step is compared against the yield acceleration. If the calculated average acceleration of a specific sliding mass exceeds the yield acceleration, deformation will occur. The final deformation of



the sliding mass is calculated by double integrating the model base input acceleration for all time steps where slippage occurs in the predefined direction (no backwards movement). The final deformation of a sliding mass in crest region hence is based on the deformation of a rigid mass, sliding on a horizontal plane whereas the rigid mass is accelerated by the model base input acceleration, which 100m below crest region (Newmark, 1976).

This method still is the recommended state of the art procedure for judging a dam's deformation after an earthquake. In case of high embankment dams it may be stated: the "sliding" mass is nor a rigid structure, nor is the sliding plane horizontal nor is its deformation equal to the double integrated base excitation. However, still there is no other type of analysis that would realistically describe the inner densification and outer loosening in granular fill dams that were subject to earthquake shaking (at the time this thesis is written, the author is at least not aware of it).

Figure 178 shows the Newmark type deformation of a slip circle moving towards downstream. The slip surface is approximately planar with an inclination of  $16^\circ$  towards horizontal. The calculated deformation resulted in 38cm, it est 10cm settlement (= vertical deformation). Figure 182 shows the highest deformation of a sliding mass resulting from analysis on upstream movements. The surface is slightly curved having an average inclination of  $23^\circ$  towards horizontal. The calculated maximum deformation is 15cm resulting in 6cm settlement. Following Newmark approach, the settlements of upstream and downstream movements need to be summed up in order to gain the maximum total crest settlement. Which is 16cm in this case.

This result might easily be increased or decreased by changing the shear strength of the materials in the small stress range. Hence achieving the observed 40cm would be an easy job. It may be noted that minor changes at a rockfill material's small stress range shear resistance are easy to communicate and to defend as this range varies strongly within laboratory testing.

The previously stated shall not be seen as a guide on how to manipulate the results of such analysis. It shall be seen as an open discussion on benefits and drawbacks of design methods compared to real dam behavior.

Figure 179 plots the results of another slip circle towards downstream. If comparing the shape and total mass with the slip circle plotted in Figure 178 it appears very similar, however the calculated result of this sliding mass is 11,6m. The result is unrealistic and would indicate a complete destruction of the crest road whilst the core at reservoir elevation remains intact. Besides physical reality, it may be pointed out that this result is still in line with international design practice as no uncontrolled release of stored water would be the consequence. In case of an SEE earthquake, repair works are acceptable.

If a design Engineer wants to avoid any discussion about this unattractive 11,6m deformation, it might be helpful to increase the specified minimum depth of slip circles by some cm. In this case the 11,6m deformation would not show up again.

Figure 180 plots a slip surface approximately twice as deep. The deformation results in 6cm. Obviously the deformations decrease rapidly with increasing depth of the slip surfaces. Figure 181 and Figure 184 plot slip circles showing approximately zero deformation. Following these results the dam is only subject to dynamic settlements in its upper third. This is in clear contrast to observed dam behavior (Figure 100).

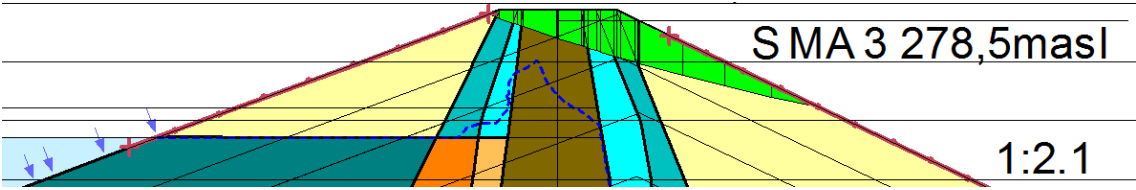


Figure 178 Downstream slip circle resulting in a deformation of 0,38m (EL GeoStudio)

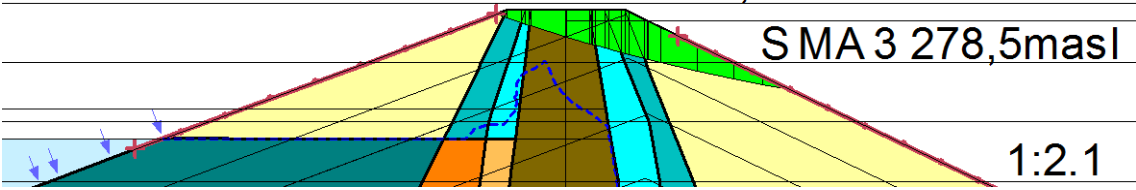


Figure 179 Downstream slip circle resulting in the highest deformation of 11,6m (EL GeoStudio)

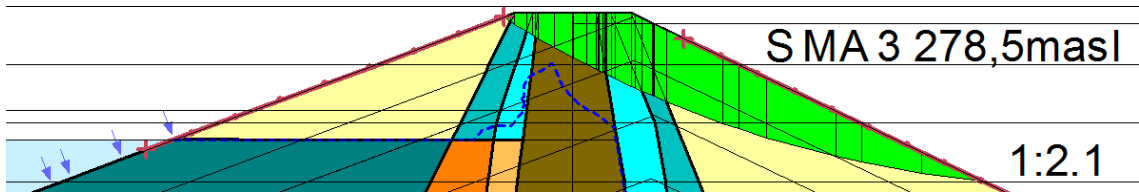


Figure 180 Downstream slip circle resulting in a deformation of 0,061m (EL GeoStudio)

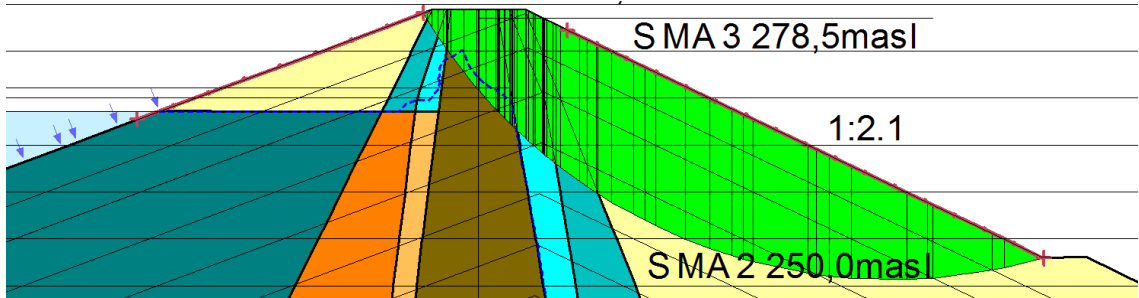


Figure 181 Downstream deep seated slip circle resulting in a deformation of 0,00m (EL GeoStudio)

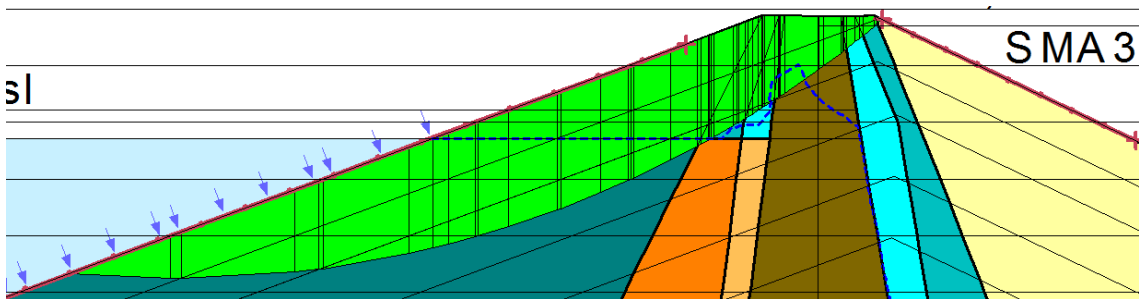


Figure 182 Upstream slip circle resulting in highest deformation of 0,15m (EL GeoStudio)

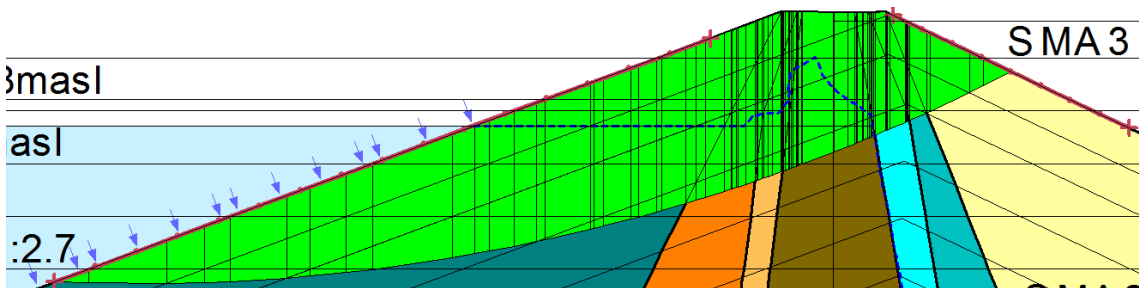


Figure 183 Upstream deep seated slip circle resulting in a deformation of 0,04m (EL GeoStudio)

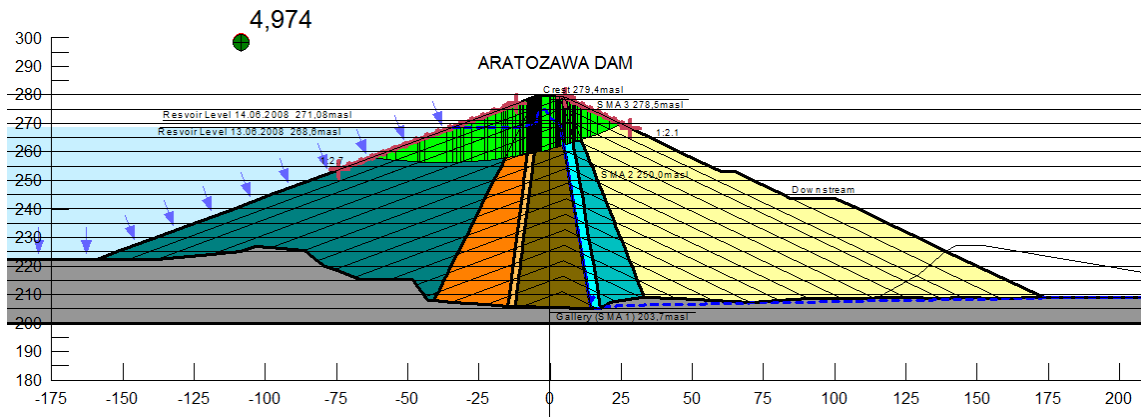


Figure 184 General view of slip surface resulting in approximately 0,00m of deformation (EL GeoStudio)

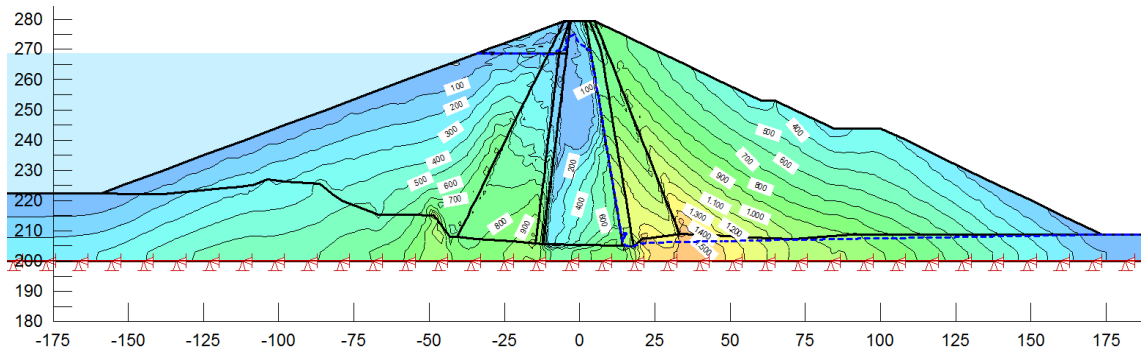


Figure 185 Effective vertical stresses after Iwate / Miyagi earthquake [ $\text{kN/m}^2$ ] (EL GeoStudio)

### 12.1.1.2 Non Linear Codes – GeoStudio 2012

Unfortunately the post processing of Nonlinear analysis does not allow plotting the distribution of vertical and horizontal peak acceleration within the embankment during shaking. Hence peak accelerations have to be judged on the output of previously set history (i.e. observation) points. Figure 186 and Figure 187 show the horizontal and vertical crest acceleration calculated at location of SMA 3. The resulting peak accelerations are 1,80g in horizontal direction and 1,6g in vertical direction. Compared to the observed peak accelerations (i.e. 0,54g horizontal / 0,63g vertical) the calculated results are far above the observed ones. Referring to knowledge gained during the later presented calibration of Plaxis NL model, the wide spread is assumed to result from the linear formulation of damping in GeoStudio NL analysis. Within GeoStudio 2012 NL analysis the damping linearly increases with decreasing  $G/G_{max}$  value.

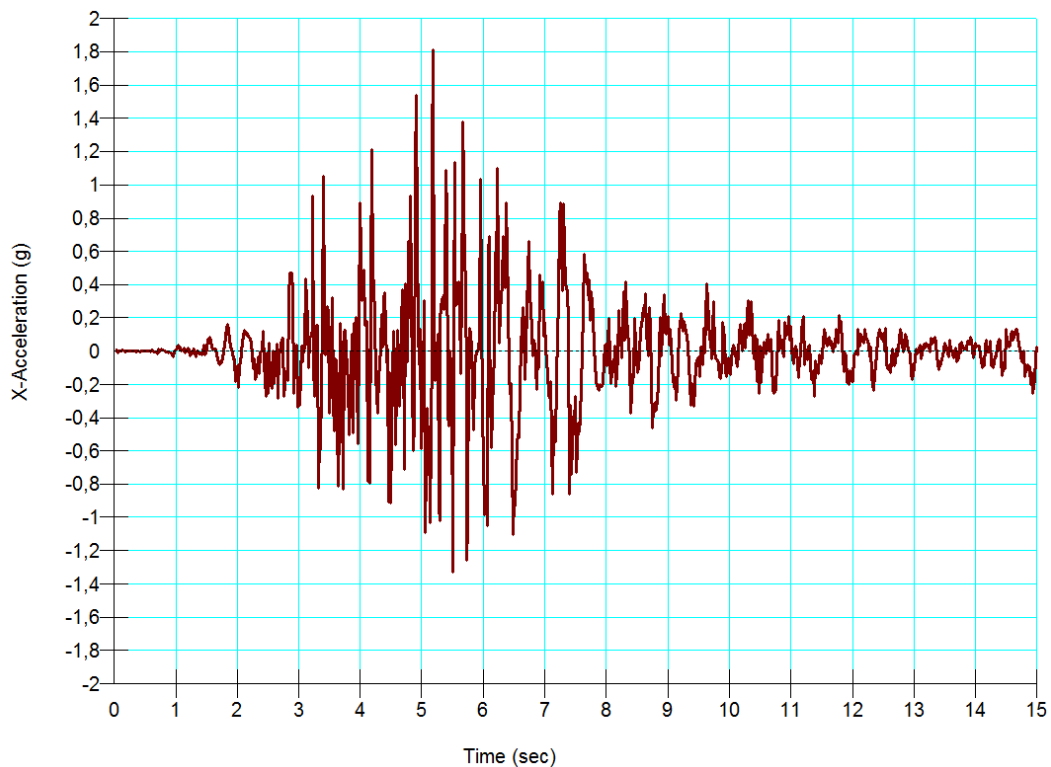
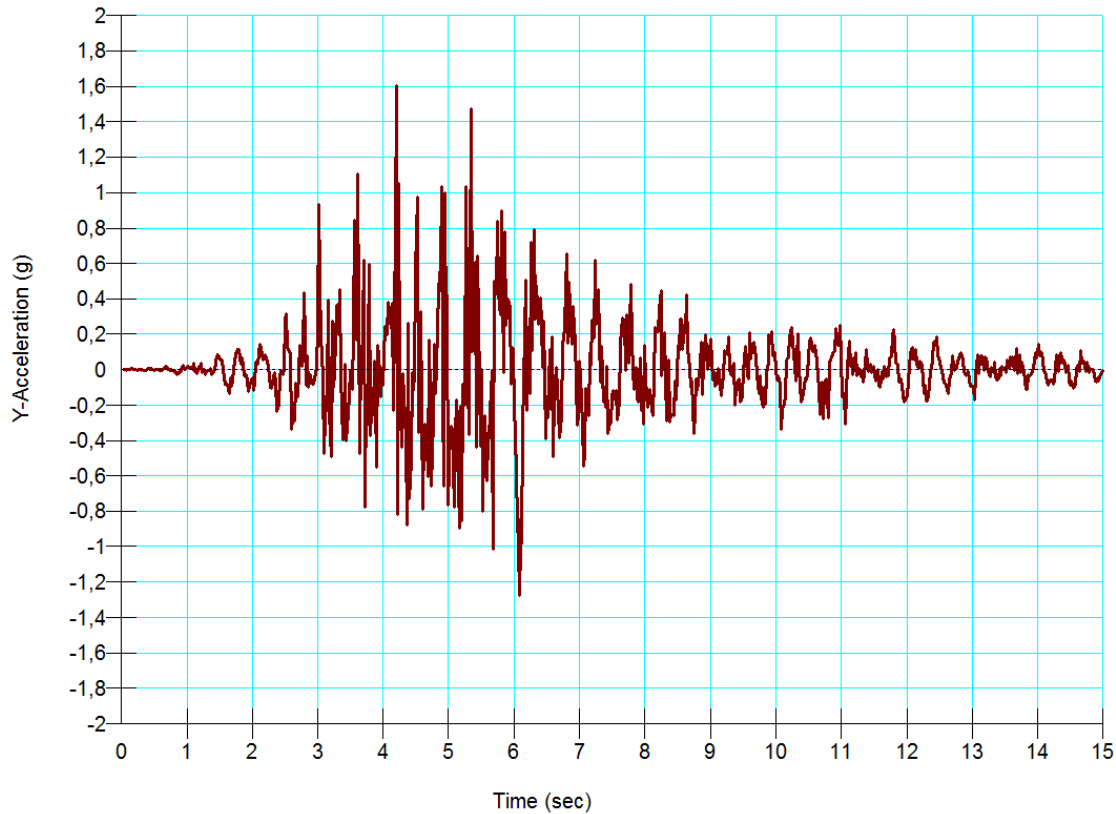


Figure 186 Horizontal crest acceleration calculated from Iwate / Miyagi earthquake – SMA 3 [g] (NL GeoStudio)



**Figure 187 Vertical crest acceleration calculated from Iwate / Miyagi earthquake – SMA 3 [g] (NL GeoStudio)**

Figure 188 shows the calculated pore water pressure distribution after Iwate / Miyagi earthquake. It can be seen that the pore water pressure rose locally but did not distribute within the core region. Figure 189 plots the pore water pressure development in details. Comparing the calculated increase (Figure 189) with the measured increase in pore pressure (Table 15) indicates that the result is far from monitoring data. Single locations as Pore water pressure gauge No. 16 (245masl) resulted in good agreement. However other gauges as No. 27, No. 25 and No. 23 overestimate the pore water pressure development. In contrast, gauge No. 2 completely fails in predicting the observed data and results in data far beyond the monitored ones.

Figure 190 plots the effective minimum stresses within core region as a result to the risen pore pressures during the earthquake. The plotted range starts from  $5\text{kN/m}^2$ . Hence areas plotting in white color show locations that are close to liquefaction or that have liquefied.

Figure 191 shows a benefit of the Nonlinear method. During the stepwise calculation of the earthquake, plastic points occur resulting in permanent deformation of the crest (i.e. 7cm).

In a next step further plastic deformations may be calculated from stress – redistribution analysis (16cm, Figure 193). As a consequence, the calculated permanent crest settlement sums up to 23cm. Further crest settlement might result from consolidation analysis as the excess pore water pressure would have to drain causing limited settlements. Still this is not in the range of the observed maximum crest settlement (i.e. 40cm locally) but the deformation patterns as shown in Figure 192 and Figure 193 are at least in general accordance with observed deformation patterns.

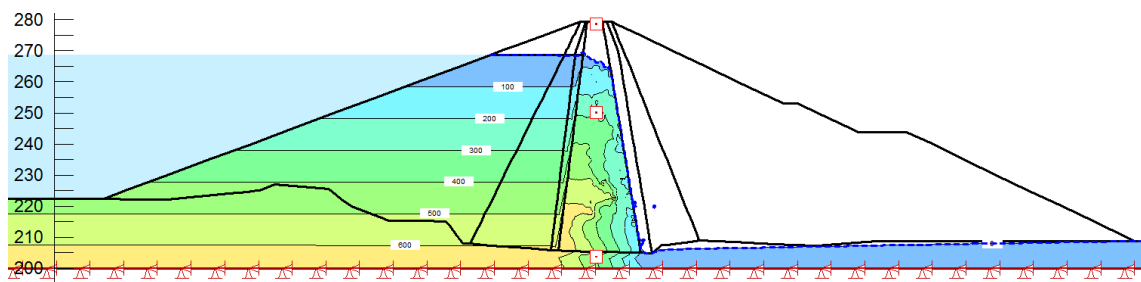


Figure 188 Pore water pressure distribution after Iwate / Miyagi earthquake [ $\text{kN/m}^2$ ] (NL GeoStudio)

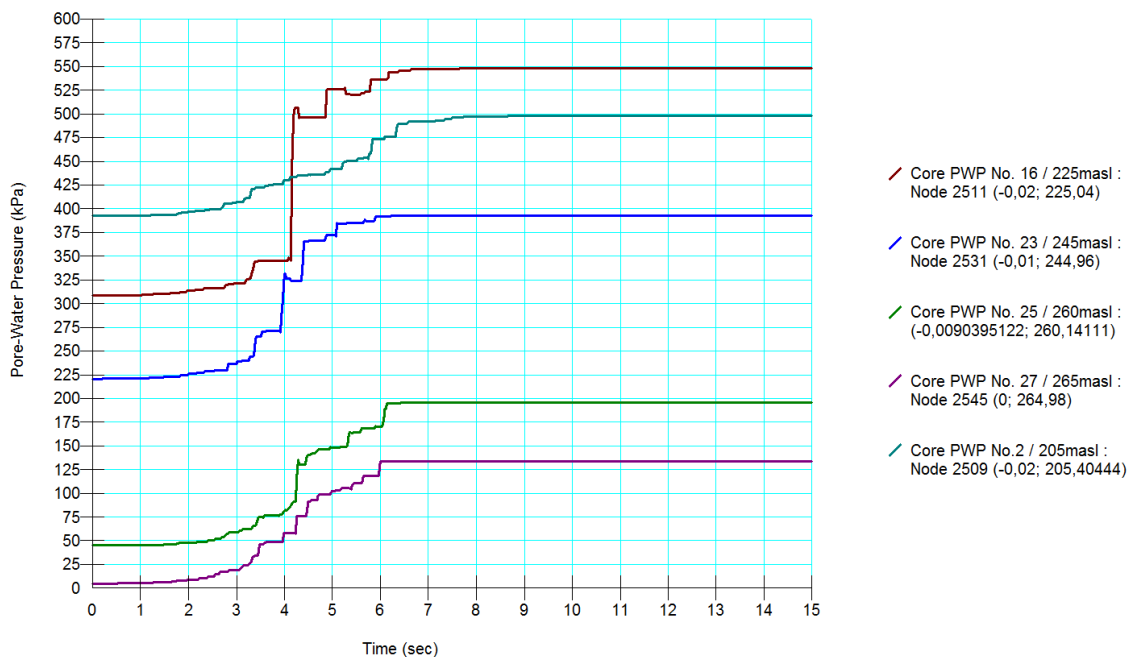


Figure 189 Pore water pressure development during Iwate / Miyagi earthquake [kN/m<sup>2</sup>] (NL GeoStudio)

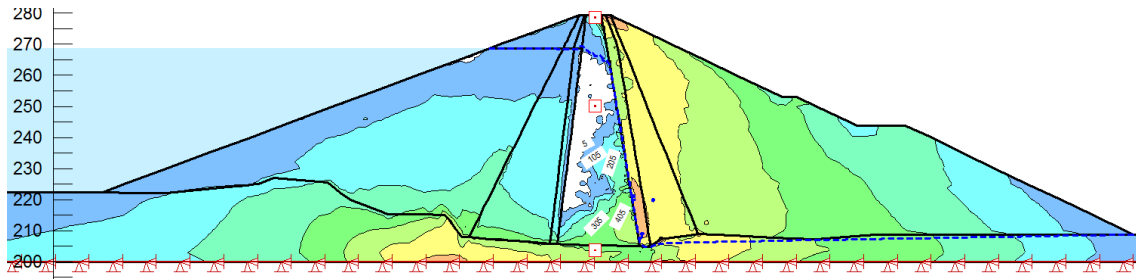


Figure 190 Distribution of effective minimum stresses after Iwate / Miyagi earthquake [kN/m<sup>2</sup>] (NL GeoStudio)

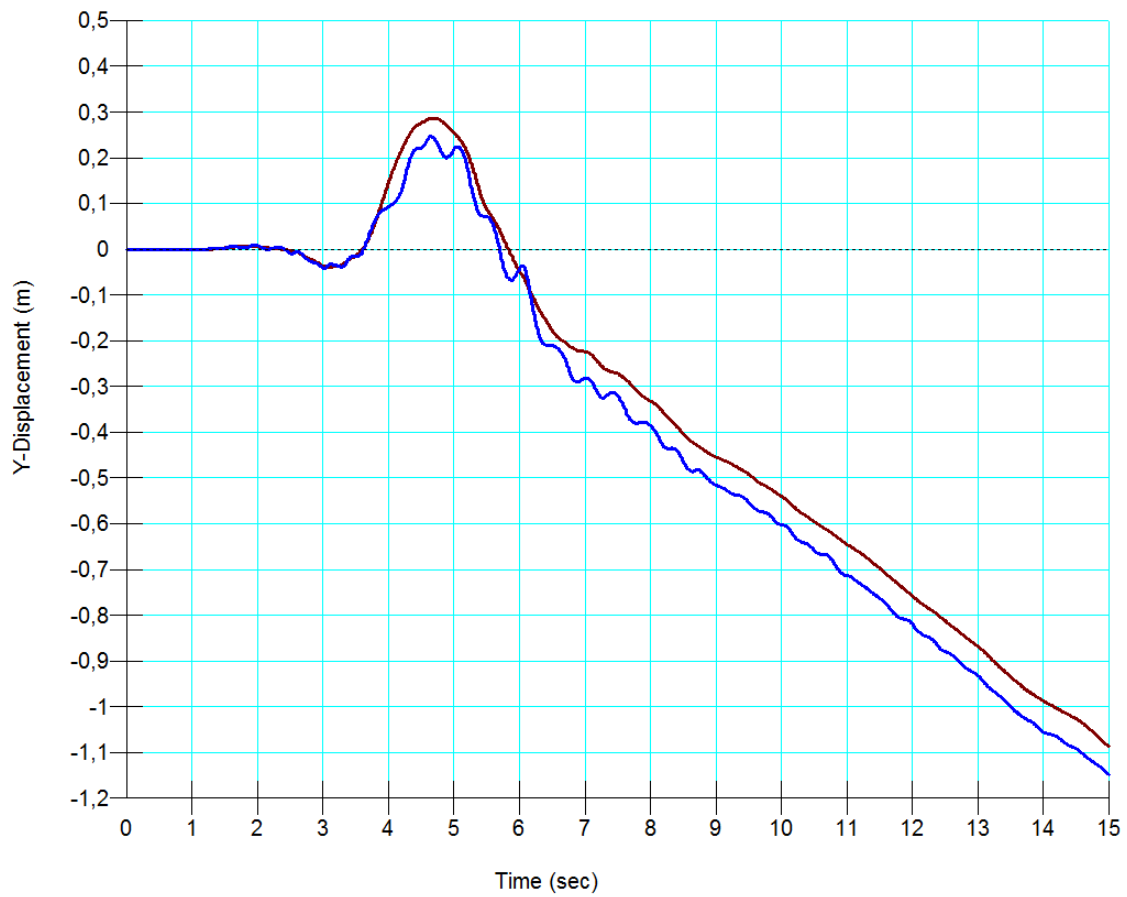


Figure 191 Vertical crest vs. base displacement [m] (NL GeoStudio)



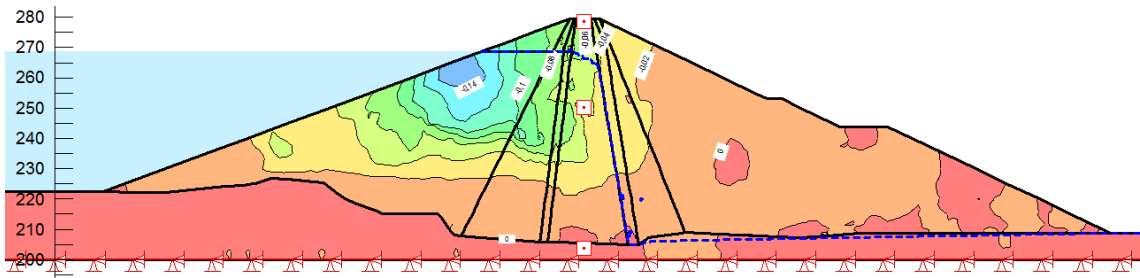


Figure 192 Vertical crest settlement, permanent deformation as a result of dynamic analysis [m] (NL GeoStudio)

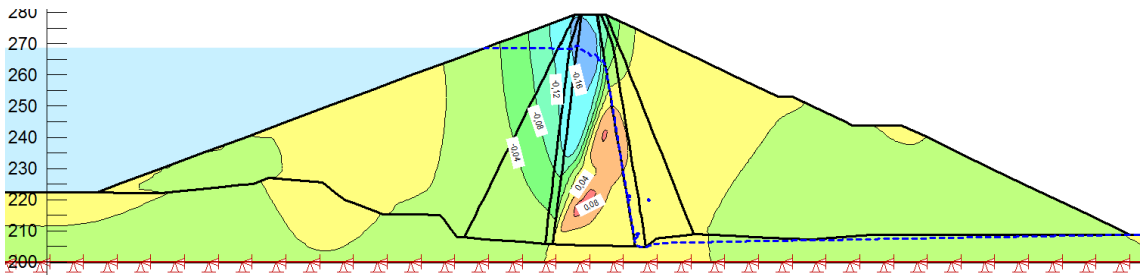


Figure 193 Vertical crest settlement, permanent deformation as a result of post-earthquake stress redistribution analysis [m] (NL GeoStudio)

Figure 194 to Figure 199 plot the results from Newmark's double integration. The results shall be shown for further comparison to EL analysis only. It becomes clear that Newmark's method cannot realistically simulate the dynamic behavior of large dams.

Figure 194 shows the Newmark type deformation of a slip circle moving towards downstream. The slip surface is approximately planar with an inclination of  $14^\circ$  towards horizontal. The calculated deformation resulted in 145cm, which is 35cm vertical deformation. Figure 198 shows the highest deformation of a sliding mass resulting from slip surfaces towards upstream. The surface is slightly curved having an average inclination of  $22^\circ$  towards horizontal. The calculated maximum deformation is 0,02cm resulting in approximately 1cm settlement. Summing up settlements that result from movements towards upstream and towards downstream, the crest would settle 36cm. The result plots very close to the observed 40cm of crest settlement. Even if the result seems to be promising, once again it shall be pointed out that this result might easily be increased or decreased by changing the shear strength of the material in the small stress range. Furthermore it has to be kept in mind that the "good" deformation result

of the Nonlinear method in this case is based on an 3,4 times overestimation of the horizontal crest acceleration.

Figure 195 plots the results of another slip circle towards downstream. If comparing the shape and total mass with the slip circle plotted in Figure 194 it appears very similar, however the calculated result of this sliding mass is 54m.

Summing up, former comments remain unchanged as stated above on Newmark's results following Equivalent - Linear analysis. The same comments hold true if Newmark's approach follows a Nonlinear analysis.

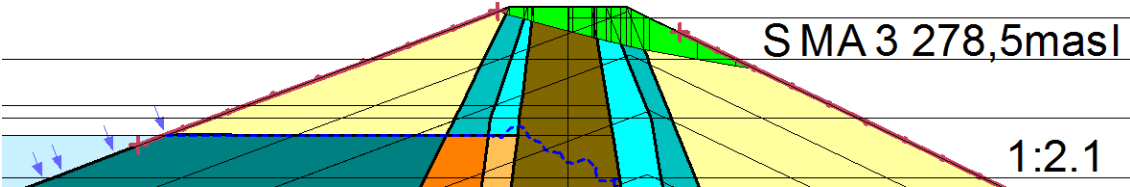


Figure 194 Downstream slip circle resulting in a deformation of 1,45m (NL GeoStudio)

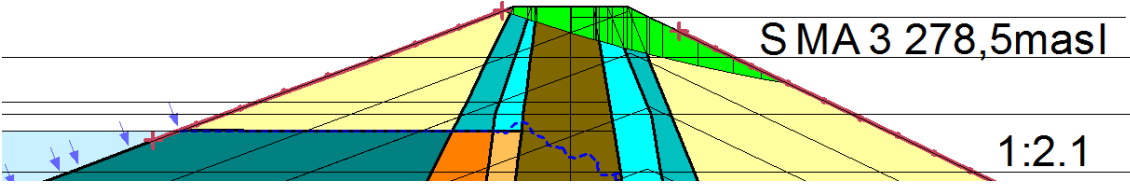


Figure 195 Downstream slip circle resulting in the highest deformation of 54m (NL GeoStudio)

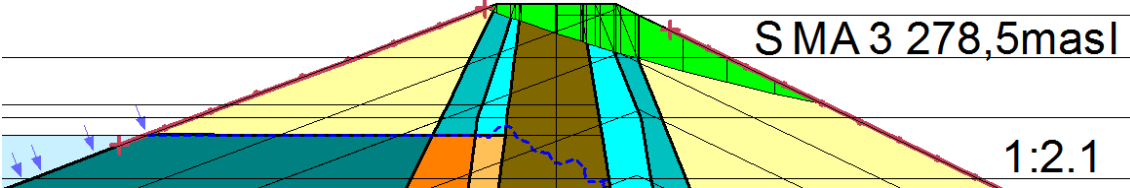


Figure 196 Downstream slip circle resulting in a deformation of 0,10m (NL GeoStudio)

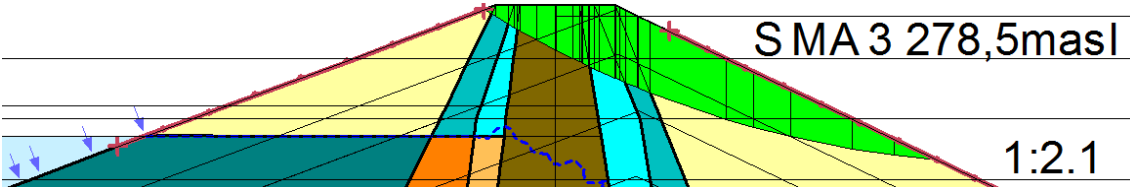


Figure 197 Downstream deep seated slip circle resulting in a deformation of 0,00m (NL GeoStudio)

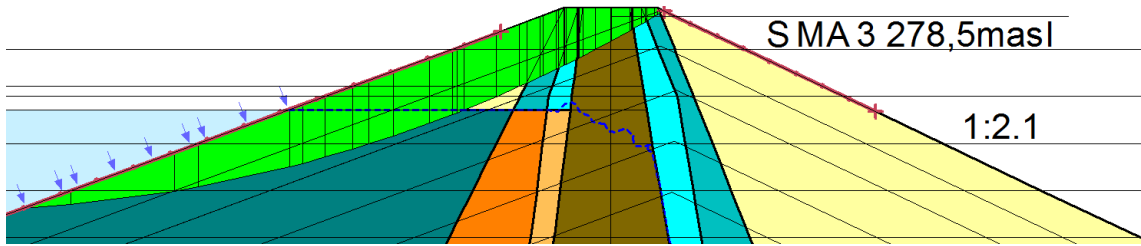


Figure 198 Upstream slip circle resulting in highest deformation of 0,02m (NL GeoStudio)

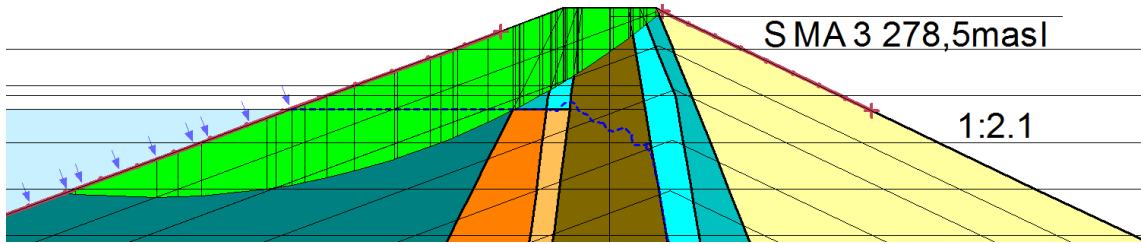


Figure 199 Upstream deep seated slip circle resulting in a deformation of 0,00m (NL GeoStudio)

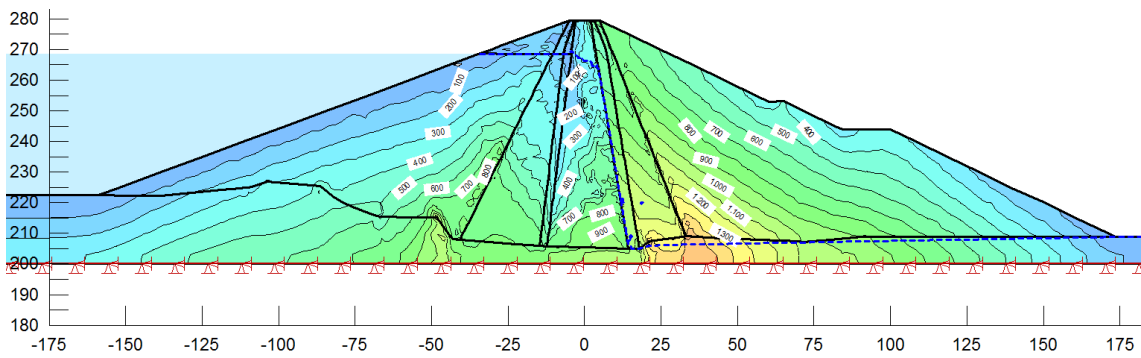


Figure 200 Effective vertical stresses after Iwate / Miyagi earthquake [ $\text{kN/m}^2$ ] (NL GeoStudio)

### 12.1.1.3 Non Linear Codes – Plaxis 2015

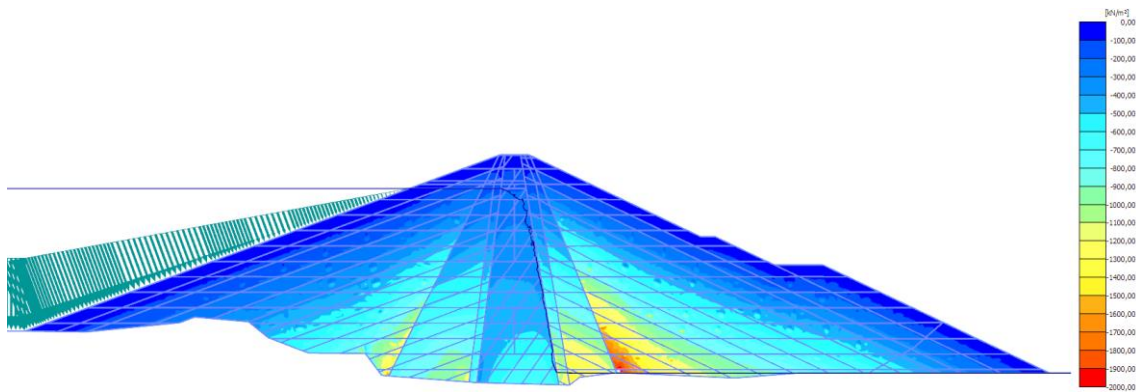


Figure 201 Effective vertical stresses prior earthquake analysis of Aratozawa dam [kN/m<sup>2</sup>] (NL Plaxis)

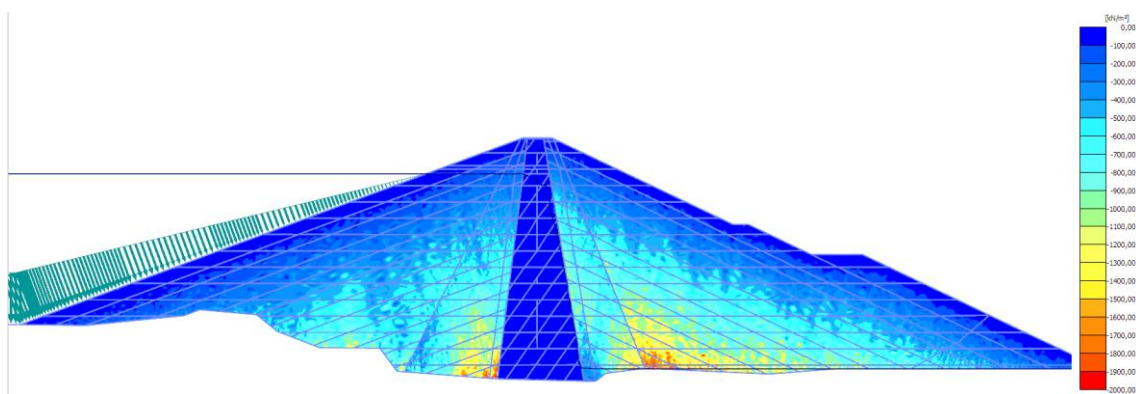
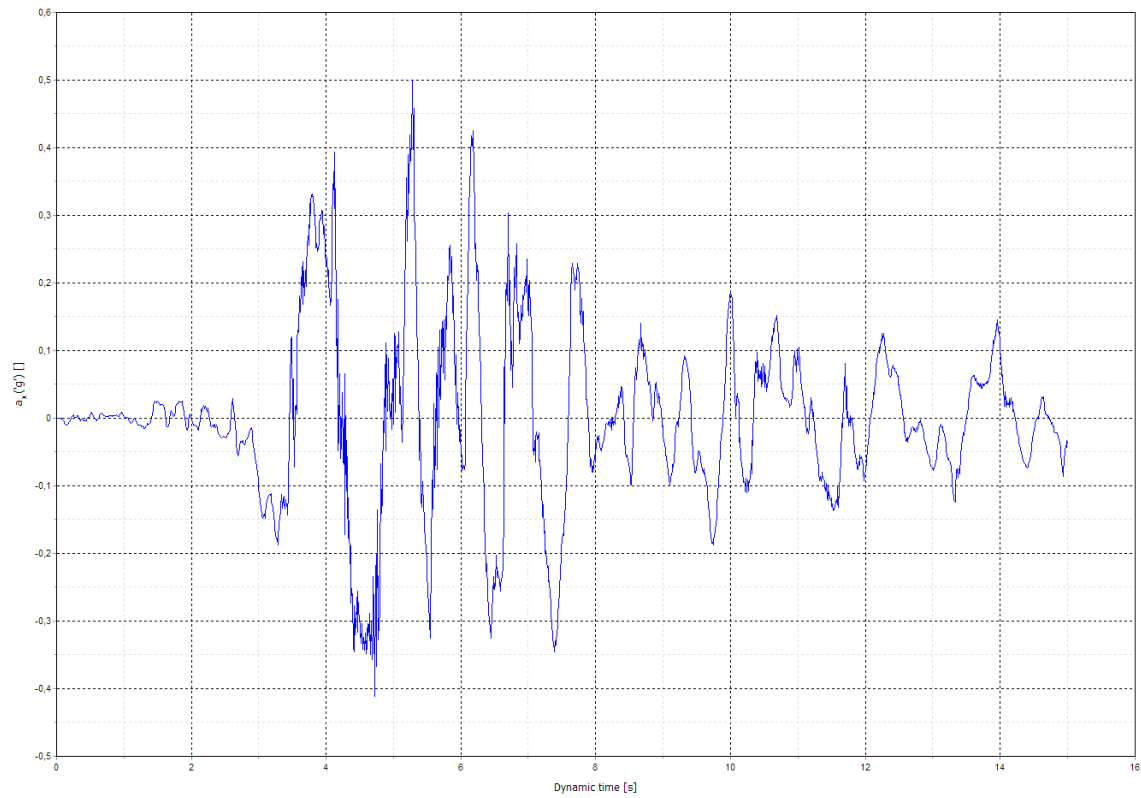


Figure 202 Effective vertical stress distribution after earthquake analysis [kN/m<sup>2</sup>] (NL Plaxis)

Post processing of Plaxis 2015 Nonlinear analysis does not allow plotting the normalized distribution of vertical and horizontal peak acceleration within a single plot. Hence peak accelerations will be judged on the output of previously set history (i.e. observation) points. Figure 203 and Figure 204 show the horizontal and vertical crest acceleration calculated at location of SMA 3. The resulting peak accelerations are 0,50g in horizontal direction and 0,37g in vertical direction. Compared to the observed peak accelerations (i.e. 0,54g horizontal / 0,63g vertical) the calculated results are in good agreement in case of the horizontal data. The vertical crest acceleration is significantly underestimated. SMA 3 is located within the dam core material. From later presented graphs (Figure 207) it can be seen that significant parts of the dam core reached the

$\sigma_3 = 0$  criterion, i.e. liquefaction in other words. Comparing the calculated horizontal crest acceleration (Figure 203) with records made on top of liquefied soils during Niigata earthquake (Figure 34) it may be seen that Plaxis 2015 is able to simulate the behavior of soil liquefaction realistically.



**Figure 203 Horizontal crest acceleration calculated from Iwate / Miyagi earthquake – SMA 3 [g] (NL Plaxis)**

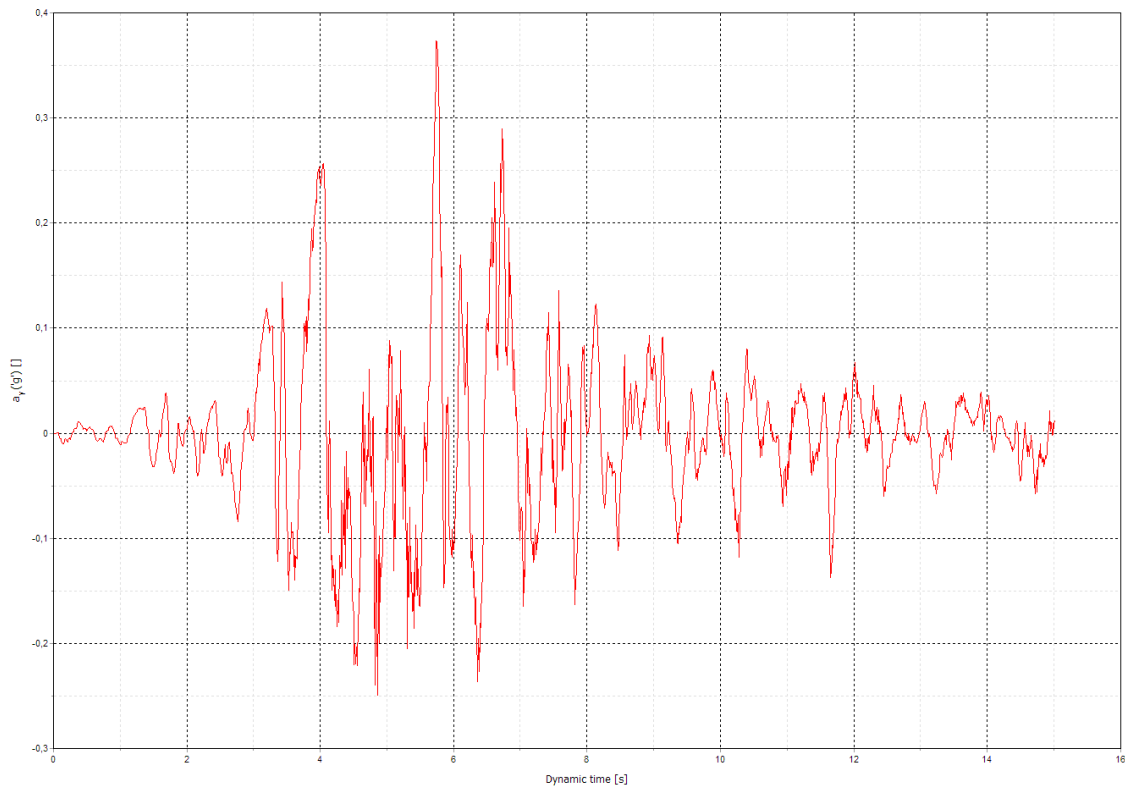


**Figure 204 Vertical crest acceleration calculated from Iwate / Miyagi earthquake – SMA 3 [g] (NL Plaxis)**

Figure 205 shows the calculated pore water pressure distribution after Iwate / Miyagi earthquake. The pore water pressure rose significantly within the core region. Figure 206 plots the detailed pore water pressure development. Comparing the calculated increase (Figure 206) with the measured increase in pore pressure (Table 15) indicates that the majority of all pore water pressure gauges overestimate the monitoring data. It may be stated that all monitored excess pore water pressures have disappeared within 3 days after the earthquake with the largest decrease (-40%) within the first day. Readings were taken 17 minutes after the earthquake; hence the analysis result is not unrealistic as it reproduces data immediately at end of the dynamic shaking. Pore pressure gauge No. 2 (205masl) is in very good agreement with observed data, whilst pore pressure gauge No. 16 (245masl) significantly exceeded the monitored data. Other gauges as No. 27, No. 25 and No. 23 overestimate the pore water pressure development in a realistic way.

Figure 207 plots the development of effective minimum stresses within core region at specified pore water pressure gauges. From this plot it can be seen that all gauges lo-

cated in elevations above 225masl indicate that the core has liquefied. It shall be pointed out that the distribution of effective minimum stresses within core region is in close relation with estimations that had to be made on core stiffness during construction period.

Figure 208 shows again a benefit of the Nonlinear method, resulting from earthquake excitation permanent crest deformation can directly be calculated from this analysis method (Figure 209). As these deformations do only partly cover the mechanism that lead to the dam's total dynamic deformations, further plastic deformations need to be calculated from stress – redistribution analysis in a further step (Figure 210). Hence the calculated permanent crest settlement sums up to 36cm (Figure 209 + Figure 210). As stated previously in EL results discussion, further crest settlement might result from consolidation analysis as the excess pore water pressure would have to drain resulting again in (limited) crest settlement. Referring to the 40cm observed maximum crest settlement, the result positively surprises.

This result shall be discussed in contrast to state of the art procedures as Newmark sliding block or Makdisi- Seed analysis. Even if this result seems to be in very good agreement none of the stated analysis can cover the real deformation of rockfill material in seismic loading. From Figure 209 one might assume that the overall deformation pattern of Aratozawa is dominated by plastic deformations within the clay core. However, it is the rockfill settlements that force the core to compress and not vice versa.

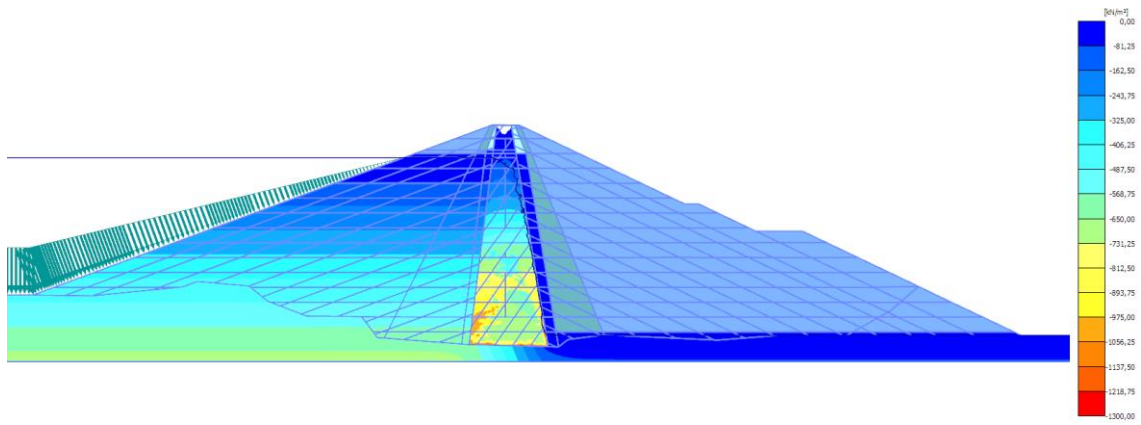
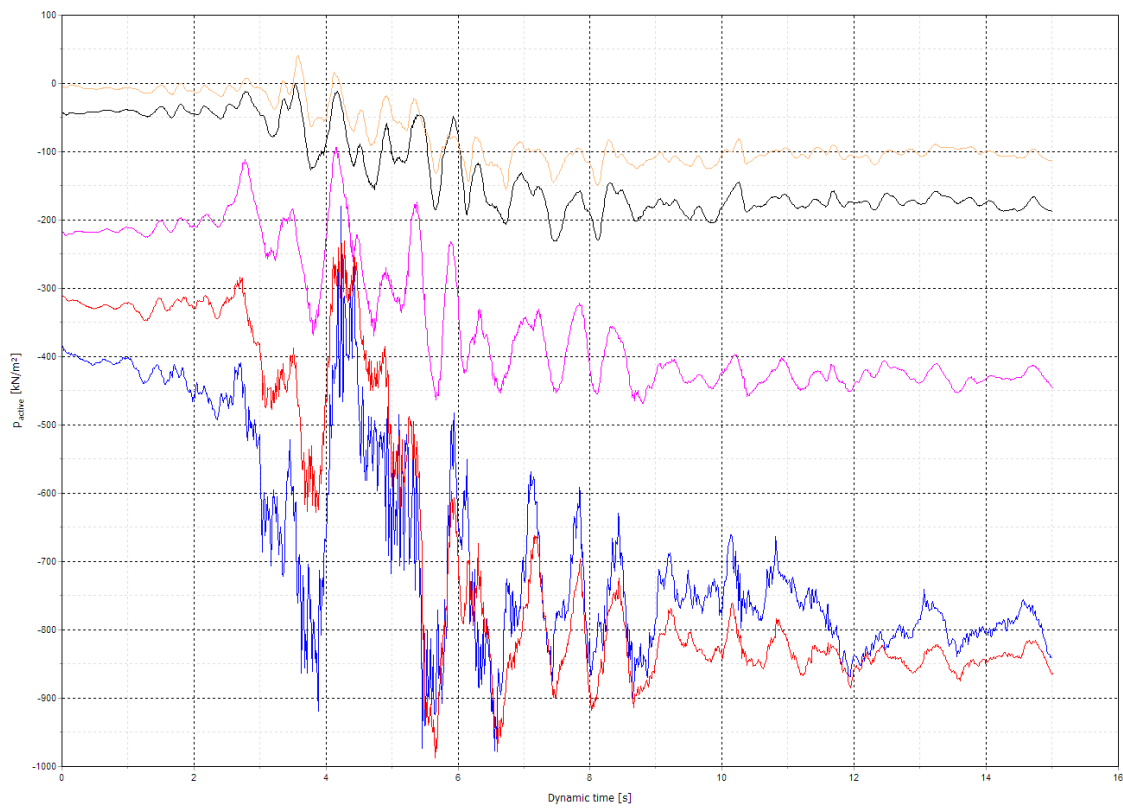


Figure 205 Pore water pressure distribution after Iwate / Miyagi earthquake [ $\text{kN/m}^2$ ] (NL Plaxis)



Aratozawa Dam Pore Water pressure Development Core

- Core PwP 205masl
- Core PwP 225masl
- Core PwP 245masl
- Core PwP 260masl
- Core PwP 265masl

Figure 206 Pore water pressure development during Iwate / Miyagi earthquake [ $\text{kN/m}^2$ ] (NL Plaxis)



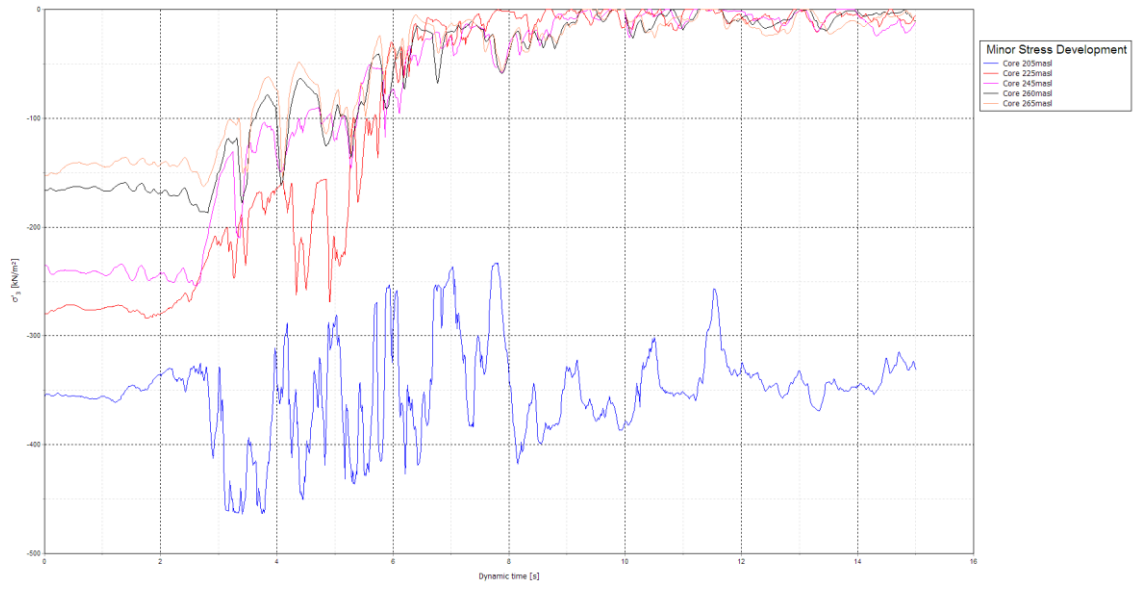


Figure 207 Development of effective minimum stresses during Iwate / Miyagi earthquake [ $\text{kN/m}^2$ ] (NL Plaxis)

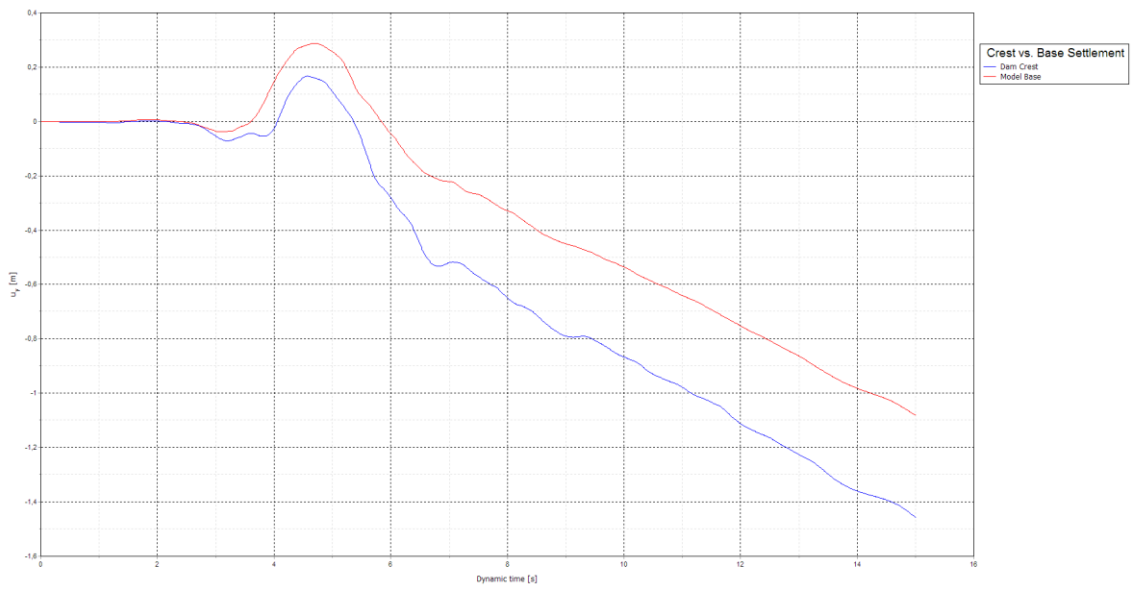
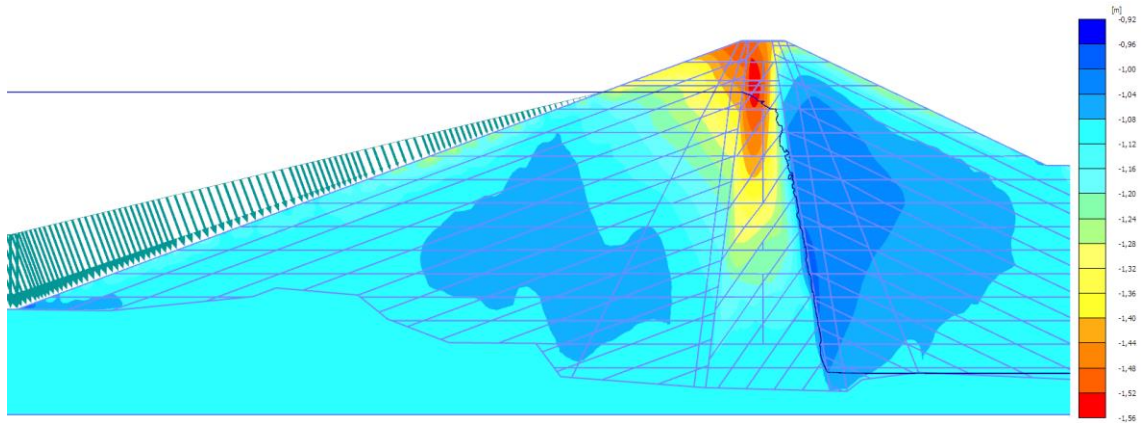
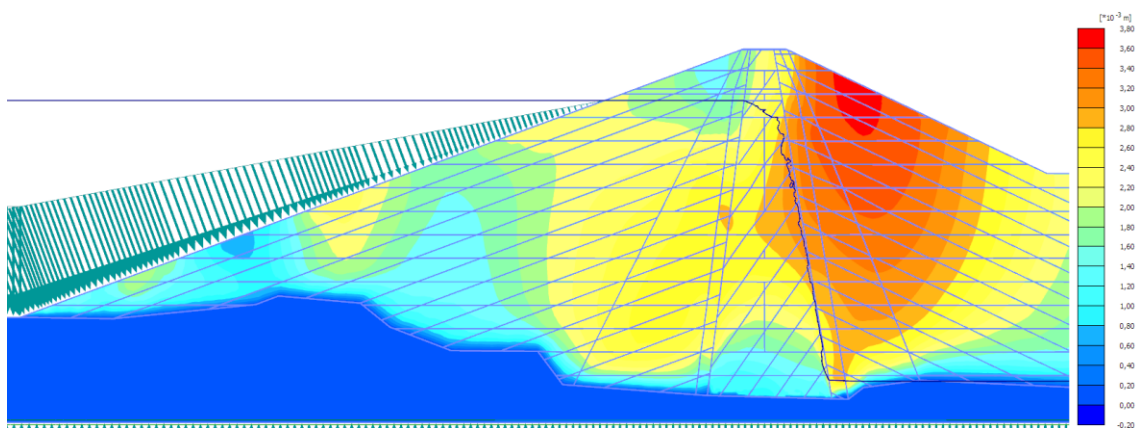


Figure 208 Vertical crest vs. base displacement [m] (NL Plaxis)



**Figure 209 Vertical crest settlement, permanent deformation as a result of dynamic analysis [m] (NL Plaxis)**



**Figure 210 Vertical crest settlement, permanent deformation as a result of post-earthquake stress redistribution analysis [m] (NL Plaxis)**

Figure 211 plots all points where the failure criterion was reached at least once during the dynamic shaking. It shall be pointed out that an element may reach the point of failure and deforms for a short time span of one or two or more time steps, but is in equilibrium for all other time steps and especially at end of the shaking. Figure 211 sums up all these points and plots them all together even though they did never occur at same time. It can be seen that nearly all elements went through the state of yielding during the strong shaking of Iwate – Miyagi earthquake.

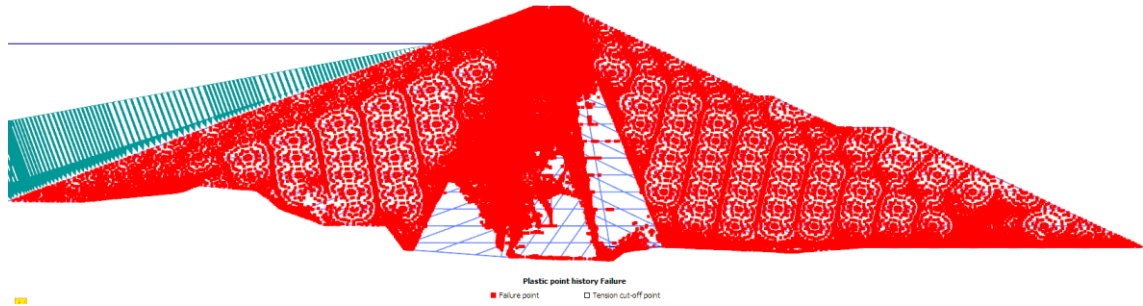


**Figure 211 Failure points (red dots) where the yield criterion was reached during or at end of the dynamic calculation of Iwate / Miyagi earthquake (NL code, Plaxis)**



## 12.2 Zipingpu Dam (CFRD)

Figure 212 shows the result of Zipingpu dam seepage analysis.

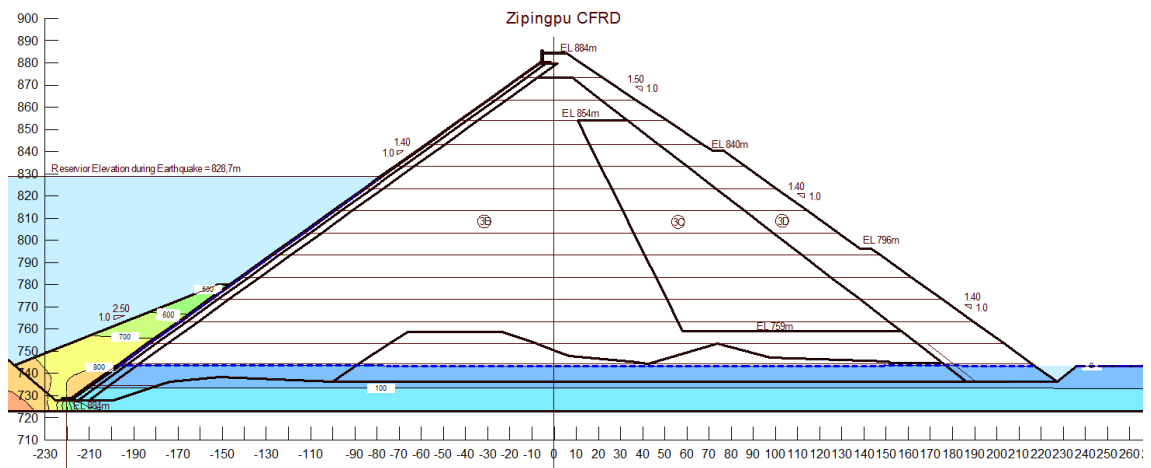


Figure 212 Pore water pressure distribution after impounding (prior earthquake) of Zipingpu dam

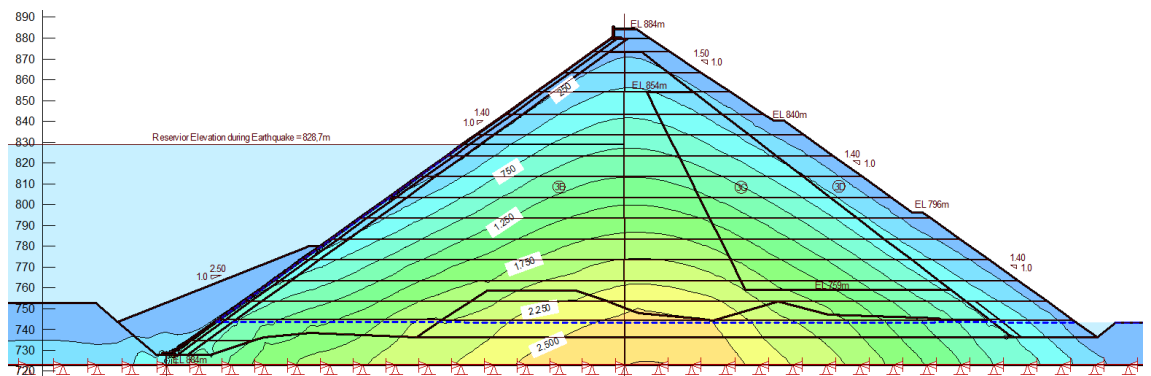


Figure 213 Effective vertical stress distribution after impounding and shortly prior earthquake of Zipingpu dam

### 12.2.1.1 Linear Equivalent Code – GeoStudio 2012

Figure 214 and Figure 216 plot the calculated horizontal respectively the vertical peak acceleration at location of the crest seismograph due to the artificially generated input of Wenchuan earthquake. Zipingpu dam was located very close to the (first) epicenter, hence the input needed to account for the typical single peaks in near field excitation too. But In contrast to results of Aratozawa dam it can be seen that the peak accelera-

tions are much better distributed (less spotted). This is mainly a result from two reasons.

Firstly Wenchuan earthquake was a mega earthquake where several single shear planes ruptured stepwise (time delayed). Thus the excitation is rich in all frequencies and long in duration.

And secondly, the dam type itself with stiff material in all fill zones results in an evenly distributed acceleration pattern within the embankment. It may be stated that the second reason is the main cause why a Clay Core Rockfill dam better performs in seismic loading conditions compared to Surface Lined Rockfill dams. Evenly distributed peak accelerations do also mean that in each single time step the actual acceleration is widely spread within the embankment. In other words, a potential “sliding” mass would get a much higher average acceleration as most areas within this sliding mass have accelerations of same size and especially of same direction. In Rockfill dams with central core (especially true for Clay Core Rockfill dams) the average acceleration within such a “sliding” mass would be significantly smaller as most areas within this “sliding” mass would have accelerations that vary largely in size and direction.

Figure 215 and Figure 217 show another detail that is of highest importance in dynamic modelling. Stiff crest road layers need to be modeled accurately. Asphalt layers or in case of Zipingpu dam concrete slabs distribute the acceleration in crest region locally. Hence if the strong motion accelerometer is located in the closer vicinity of stiff road layers they need to be foreseen in the analysis.

Figure 218 and Figure 219 show the horizontal and vertical crest acceleration calculated at the location of the strong motion instrumentation. The resulting peak acceleration is 0,73g in horizontal and 0,85g in vertical direction. As previously discussed in chapter 11.2.2 Zipingpu dam Seismic Input Motion, monitored peak crest accelerations had to be adopted for fallen concrete bars. The peak crest acceleration was estimated resulting in 0,8 to 0,9g in horizontal and vertical direction. Hence it may be stated that the calculated result is in good agreement with observed data.

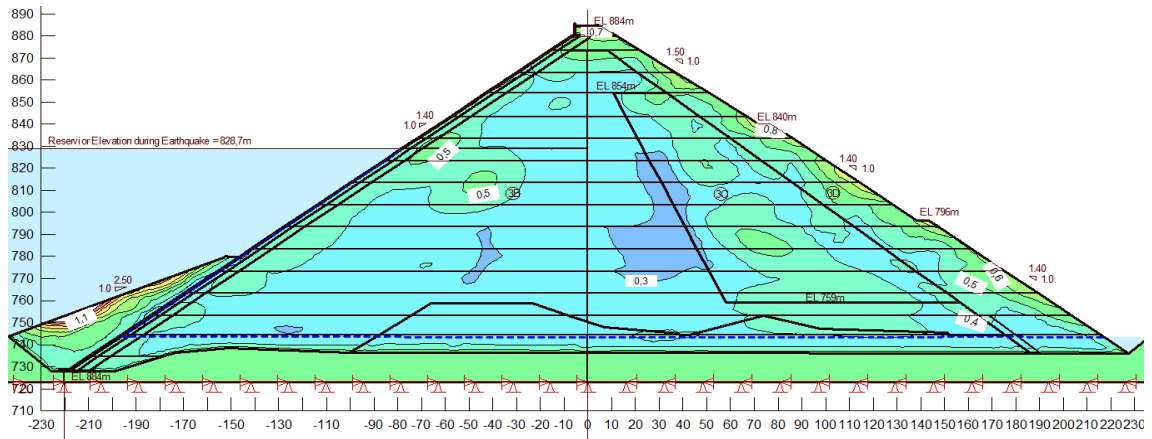


Figure 214 Horizontal peak acceleration due to Wenchuan earthquake [g] (EL GeoStudio)

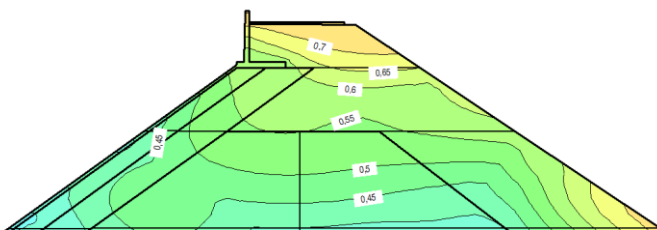


Figure 215 Horizontal peak acceleration in crest region [g] (EL GeoStudio)

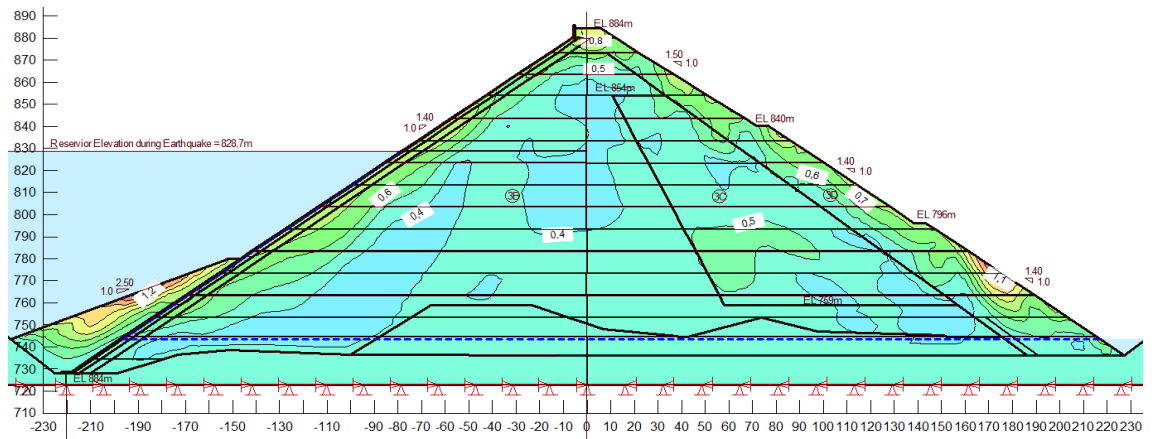


Figure 216 Vertical peak acceleration due to Wenchuan earthquake [g] (EL GeoStudio)

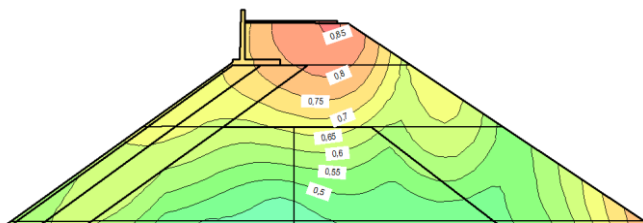
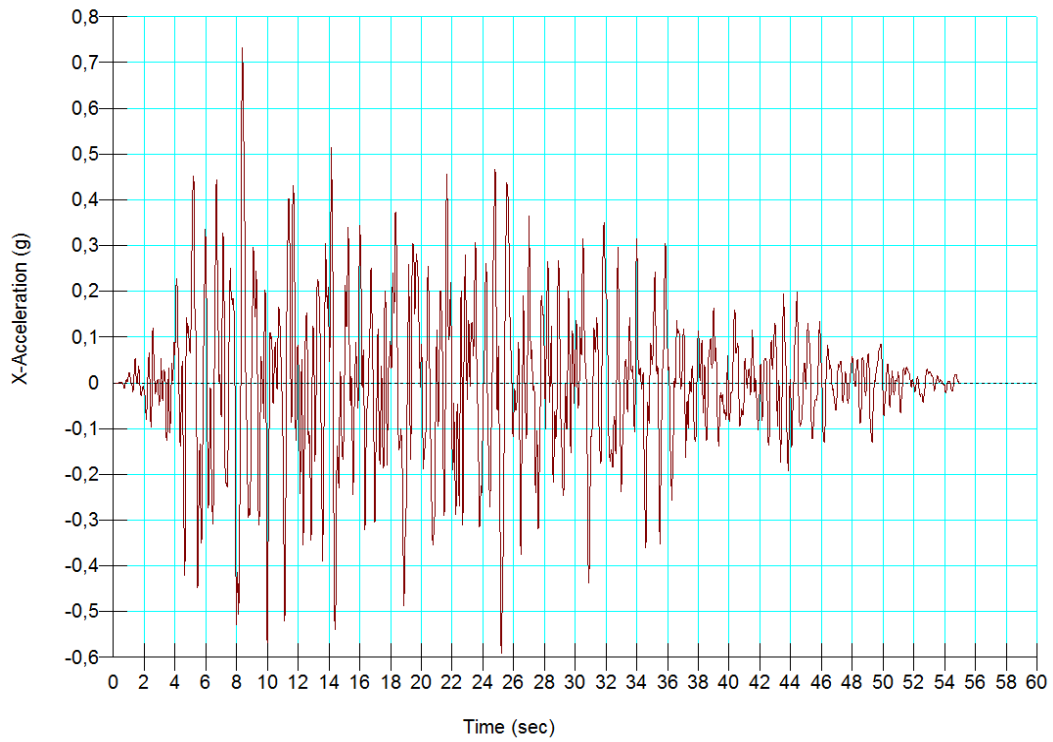
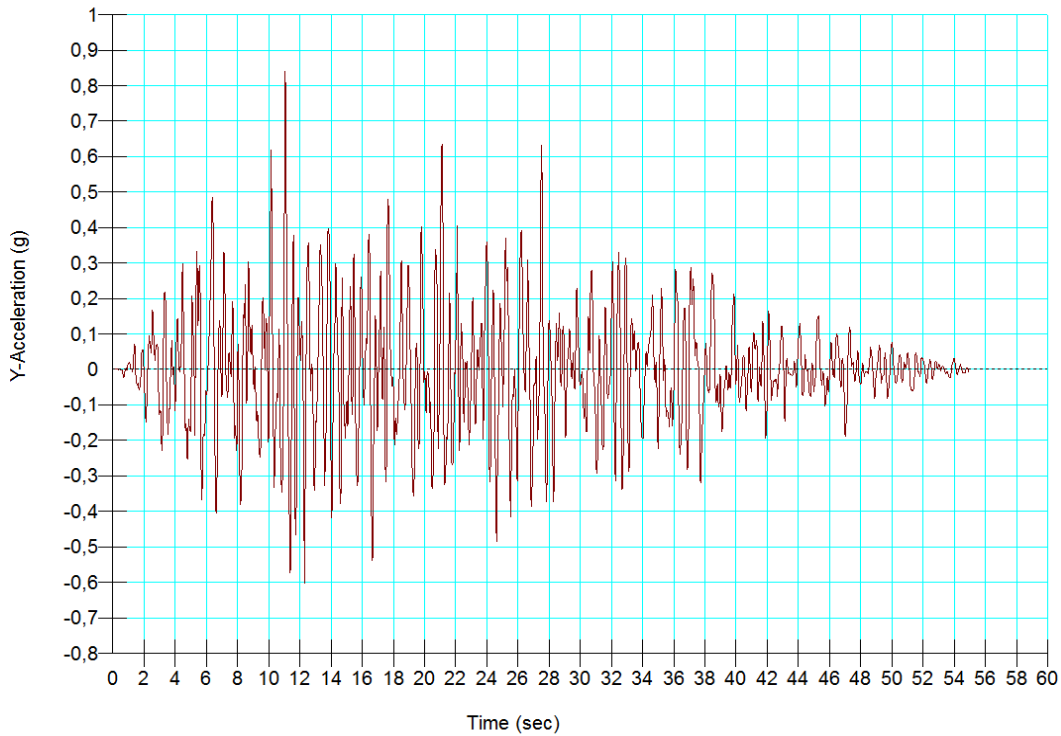


Figure 217 Vertical peak acceleration in crest region [g] (EL GeoStudio)



**Figure 218 Horizontal crest acceleration calculated from Wenchuan earthquake [g] (EL GeoStudio)**



**Figure 219 Vertical crest acceleration calculated from Wenchuan earthquake [g] (EL GeoStudio)**



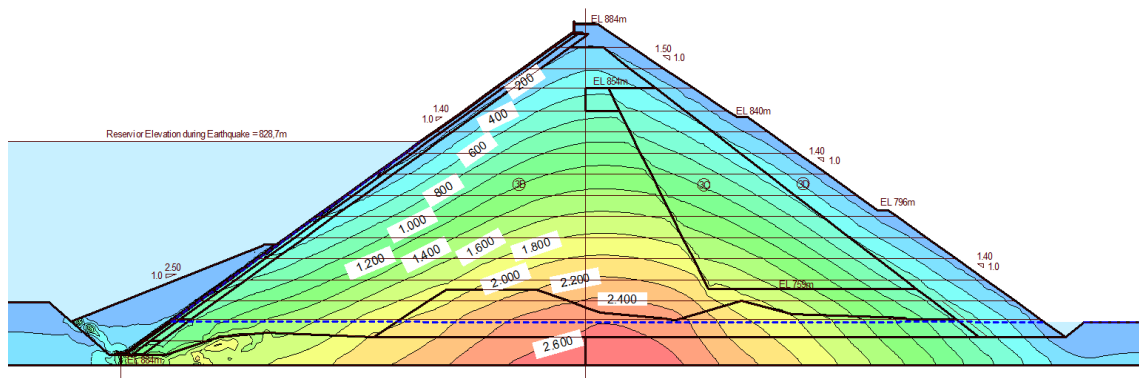


**Figure 220 Effective vertical stresses after Wenchuan earthquake [ $\text{kN/m}^2$ ] (EL GeoStudio)**

Figure 221 shows the settlement of the crest vs. the settlement of the model base. As previously stated for several times, the EL model is not able to directly compute plastic deformations from each time step. Figure 222 shows the result of additional post-earthquake stress-redistribution analysis. Summing up the crest settlement from Figure 221 and Figure 222 the permanent crest settlement results in 0cm. As this result is not in accordance with observed dam behavior, earthquake deformations are calculated by Newmark's double integration in a further step.

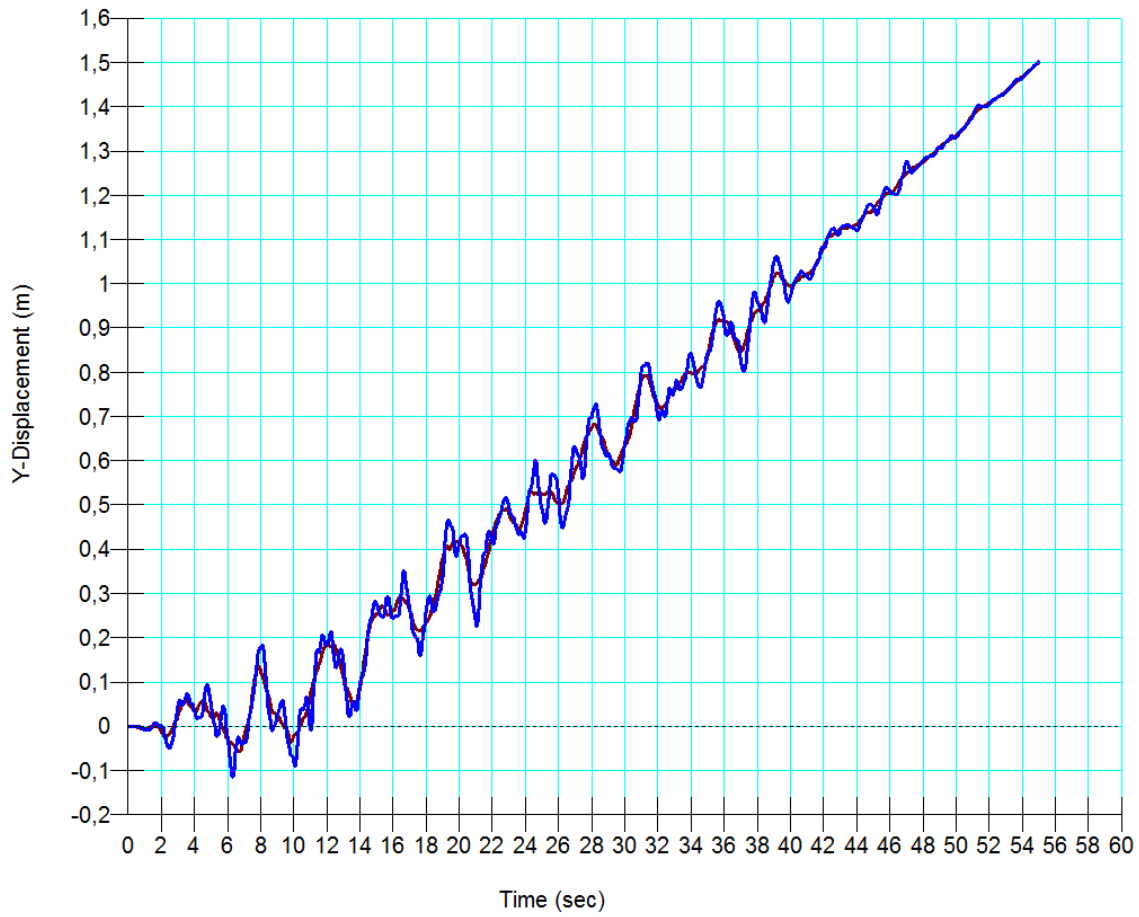


Figure 221 Vertical crest vs. base displacement [m] (EL GeoStudio)

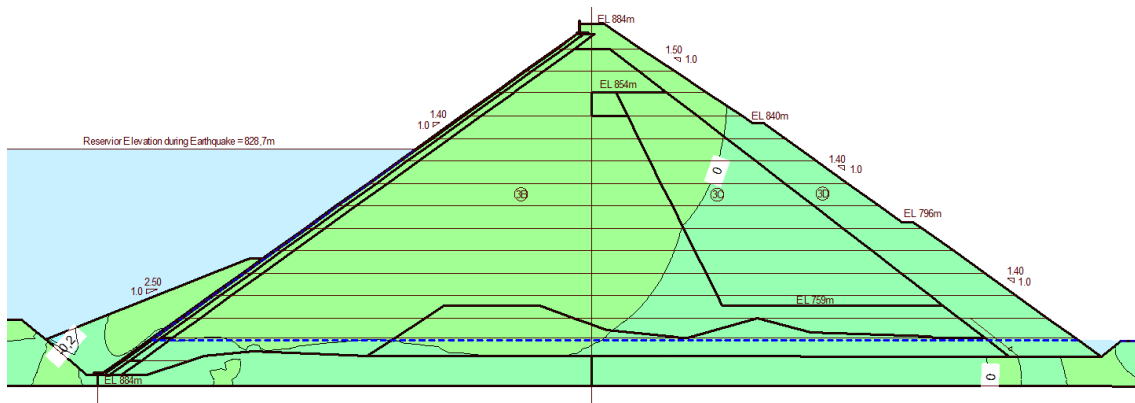


Figure 222 Vertical crest settlement, permanent deformation as a result of post-earthquake stress-redistribution analysis [m] (EL GeoStudio)

Figure 223 to Figure 228 plot the results from Newmark's double integration analysis. Figure 223 shows the Newmark type deformation of a slip circle moving towards

downstream. The slip surface is approximately planar with an inclination of  $32^\circ$  towards horizontal. The calculated deformation resulted in 119cm, which is equal to 63cm settlement. Figure 226 shows the largest deformation of a sliding mass resulting from analysis on upstream movements. The surface is planar having an average inclination of  $28^\circ$  towards horizontal. The calculated maximum deformation is 26cm resulting in 12cm settlement. Thus the total crest settlement sums up to  $63 + 12 = 75$ cm in this case. This result is in very good agreement with data observed after the first major earthquake. Guan (2009) reports immediate settlements of 68cm after the main shock but points out that a 20cm wide gap was found below the crest road concrete slab when repair works were started.

As stated previously, this result can vary largely with selected rockfill shear strength. This result might easily be increased or decreased by changing the shear strength of the materials in the small stress range.

Figure 224 plots the first slip surface that includes the whole crest wall. The calculated deformation resulted in 6cm. As previously observed from Aratozawa dam results, the deformations decrease rapidly with increasing depth of the slip surfaces. Figure 225 and Figure 228 plot slip circles showing approximately zero deformation. These results indicated that the dam is subject to dynamic settlements in its upper third only. Following the results of Newmark's double integration, material located within the lower two thirds would show zero deformation. This is in clear contrast to observed dam behavior (Figure 100). Zipingpu dam has shown a continuous decrease of settlement from crest level down to the dam base. The highest settlement was located at the dam crest decreased stepwise along whole dam height. The crest settlements did not concentrate to its upper third. Please refer to chapter 10.3.3 Dam behavior during Wenchuan earthquake for further details on observed behavior of Zipingpu CFRD. Figure 228 is of special interest as it plots a slip circle that approximately exits the dam body a location where the concrete slab was sheared off. The slip surface plotted in Figure 228 resulted in 0 displacements.

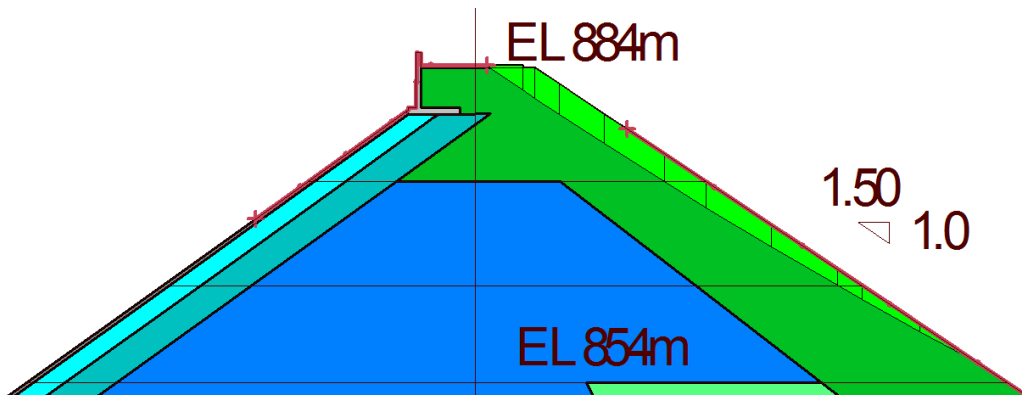


Figure 223 Downstream slip circle resulting in the largest deformation of 1,19m (EL GeoStudio)

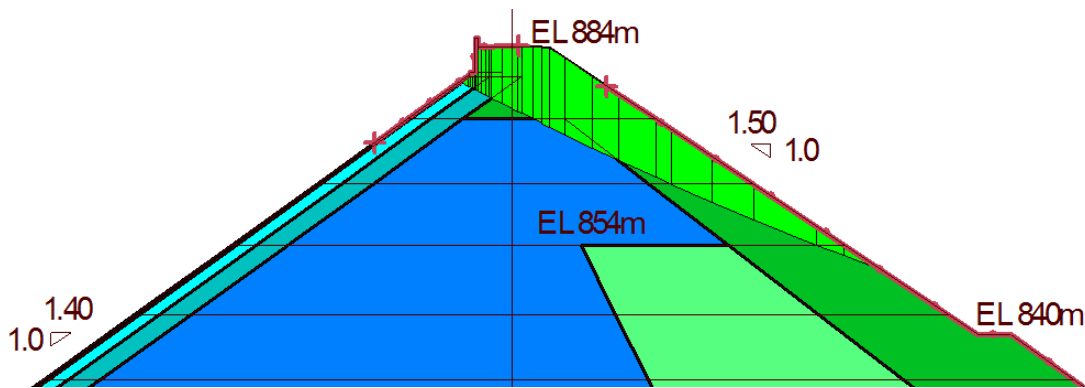


Figure 224 Downstream slip circle resulting in a deformation of 0,06m (EL GeoStudio)

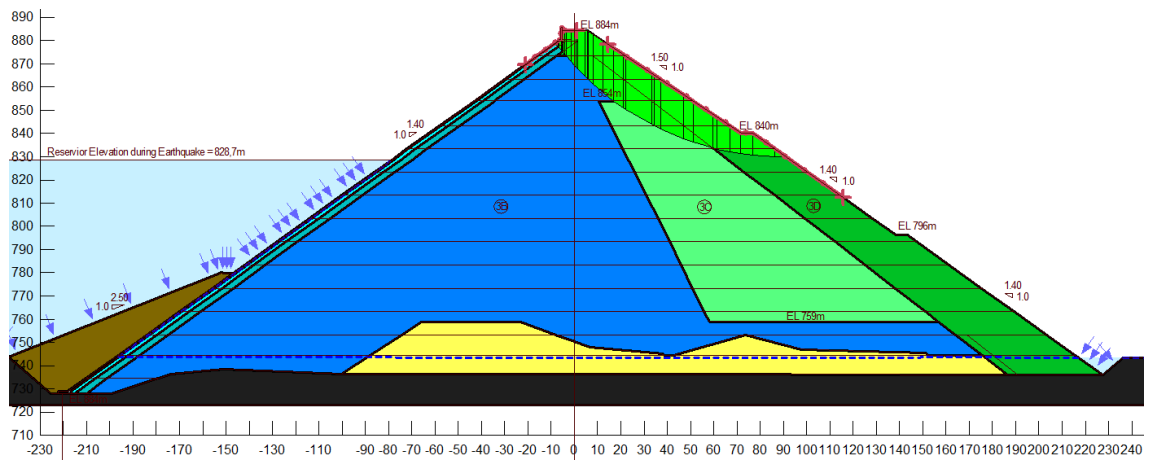


Figure 225 General view of slip surface resulting in approximately 0,00m deformation (EL GeoStudio)

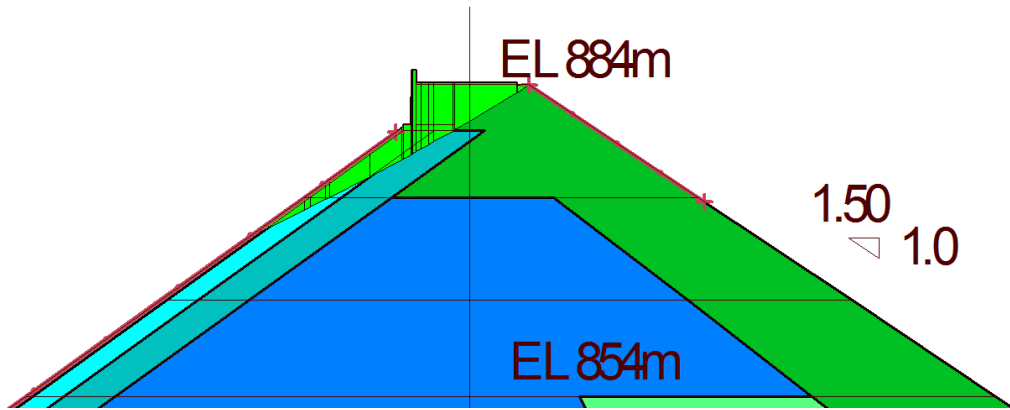


Figure 226 Upstream slip circle resulting in highest deformation of 0,26m (EL GeoStudio)

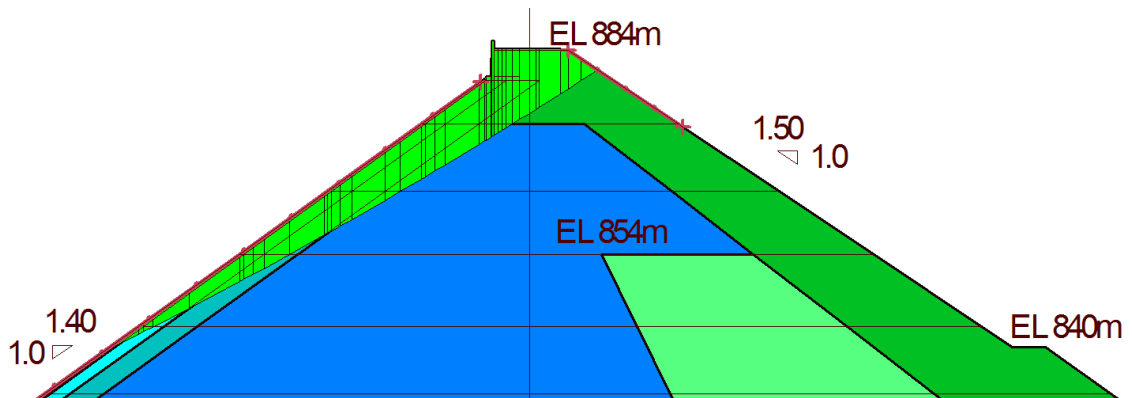


Figure 227 Upstream "deep" seated slip circle resulting in a deformation of 0,02m (EL GeoStudio)

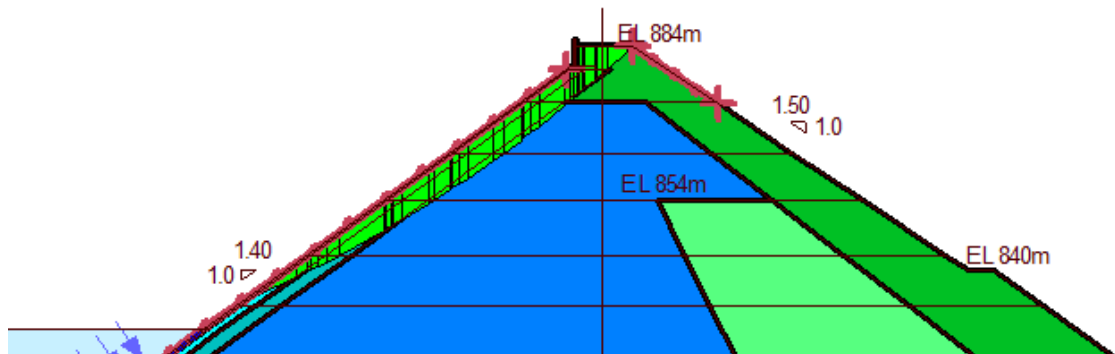


Figure 228 Upstream slip surface resulting in approximately 0,00m of deformation (EL GeoStudio)

### 12.2.1.2 Non Linear Codes – GeoStudio 2012

Figure 229 and Figure 230 show the horizontal and vertical crest acceleration calculated at location of the strong motion instrument. The resulting peak accelerations are 1,3g in horizontal direction and 1,3g in vertical direction. Hence it may be stated that the calculated result is above estimated / observed peak values. Again the Nonlinear analysis in GeoStudio overestimates the observed peak accelerations. The same result was observed for all cases studies. Most likely this is due to the linear formulation of the decrease in damping. Please note, due to the significant increase of computer performance in Nonlinear analysis, the last 25 seconds of the input acceleration had to be calculated within a separated analysis. Therefore the presented read out data had to be merged.

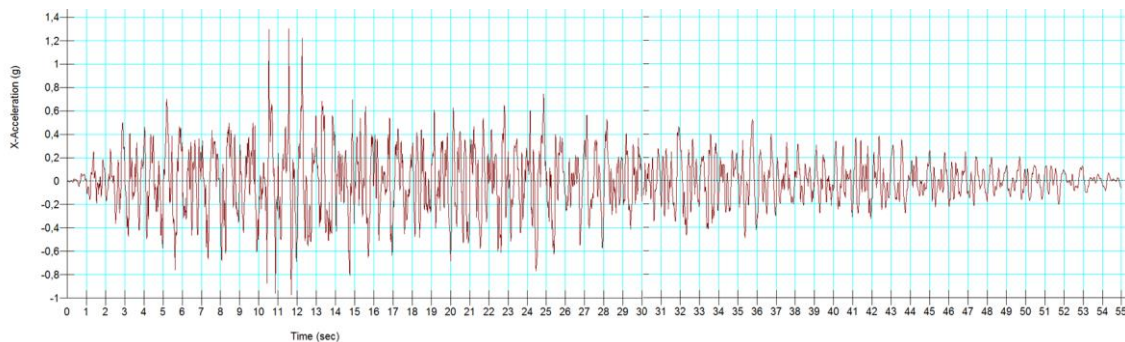


Figure 229 Horizontal crest acceleration calculated from Wenchuan earthquake [g] (NL GeoStudio)

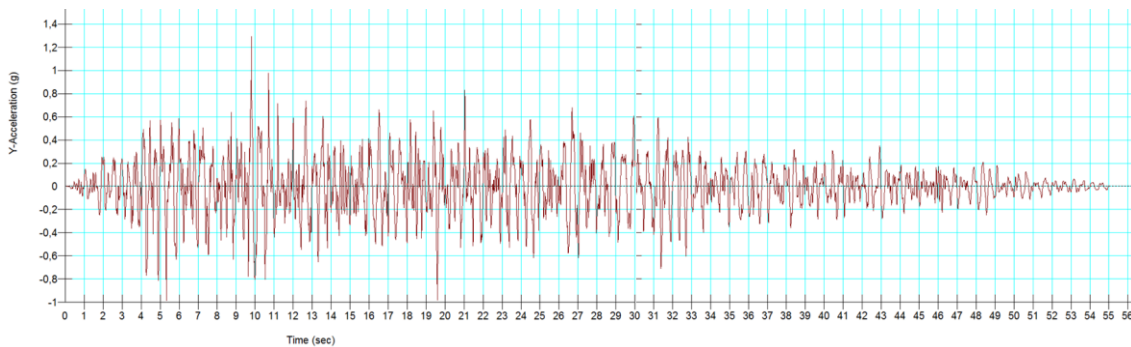


Figure 230 vertical crest acceleration calculated from Wenchuan earthquake [g] (NL GeoStudio)

Figure 231 shows the calculated delta settlement of Zipingpu dam at end of the non-linear dynamic analysis. The total crest settlement resulted in 4cm settlement. It may

be stated that this method significantly underestimates the dynamic deformation of rockfill material.

Figure 232 shows the result of additionally performed post-earthquake stress-redistribution analysis. As no liquefiable material is present within Zipingpu dam, post – earthquake stress – redistribution analysis should result in zero displacement.

In a next step earthquake induced permanent deformation is calculated by Newmark’s double integration.

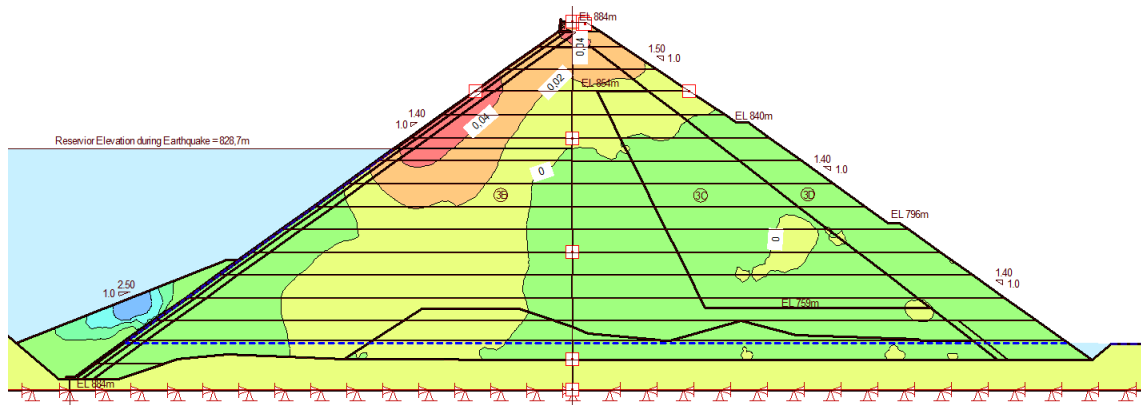


Figure 231 Vertical delta crest settlement as a result of plasticity conditions reached during shaking [m]. (NL GeoStudio)

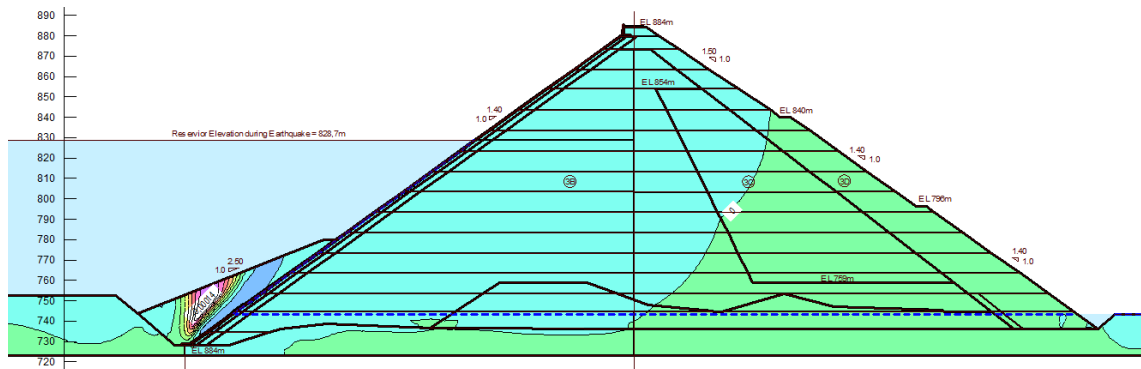


Figure 232 Vertical crest settlement, permanent deformation as a result of post-earthquake stress-redistribution analysis [m] (NL GeoStudio)

Figure 233 to Figure 238 plot the results from Newmark’s double integration analysis to calculate the dam’s dynamic deformation.

Figure 233 shows the Newmark type deformation of a slip circle moving towards downstream. The slip surface is close to planar with an average inclination of 30° towards horizontal. The calculated deformation resulted in 69cm, i.e. 35cm vertical deformation. Figure 236 shows the largest deformation of a sliding mass resulting from movements towards upstream direction. The surface is close to planar having an average inclination of 28° towards horizontal. The calculated maximum deformation is 137cm resulting in 64cm settlement. Thus the total crest settlement sums up to 35 + 64 = 99cm in this case. This result slightly overestimates the data observed after the first major earthquake. Guan (2009) reports immediate settlements of 68cm after main shock but points out that a 20cm wide gap was found below a crest road concrete slab when repair works were started.

Again, this result might easily be varied with selected rockfill shear strength.

Figure 234 plots the first slip surface that includes the whole crest wall. The calculated deformation resulted in 4cm. As observed from Aratozawa dam and previously presented results of Zigingpu EL analysis, the calculated deformations decrease rapidly with increasing depth of the slip surfaces. Figure 235 and Figure 238 plot slip circles showing approximately zero deformation. As observed previously, Newmark’s method indicated that dynamic deformations would only take place at the dam’s upper third, whilst the rest of the dam would not show any deformations. This is in clear contrast to observed dam behavior (Figure 100).

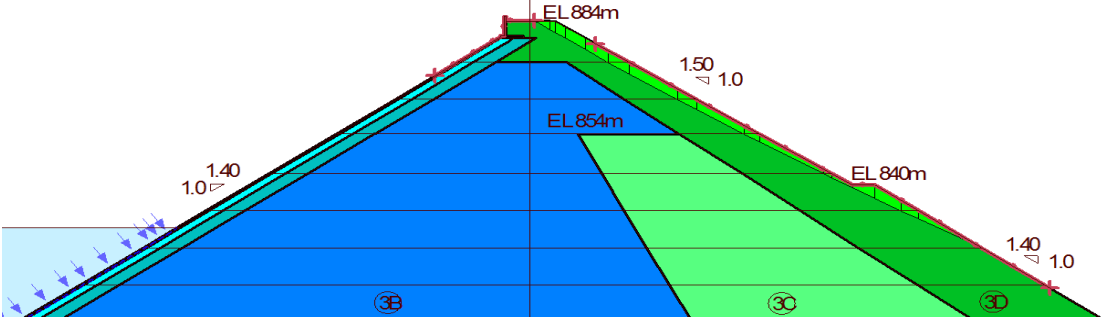


Figure 233 Downstream slip circle resulting in the largest deformation of 0,69m (NL GeoStudio)



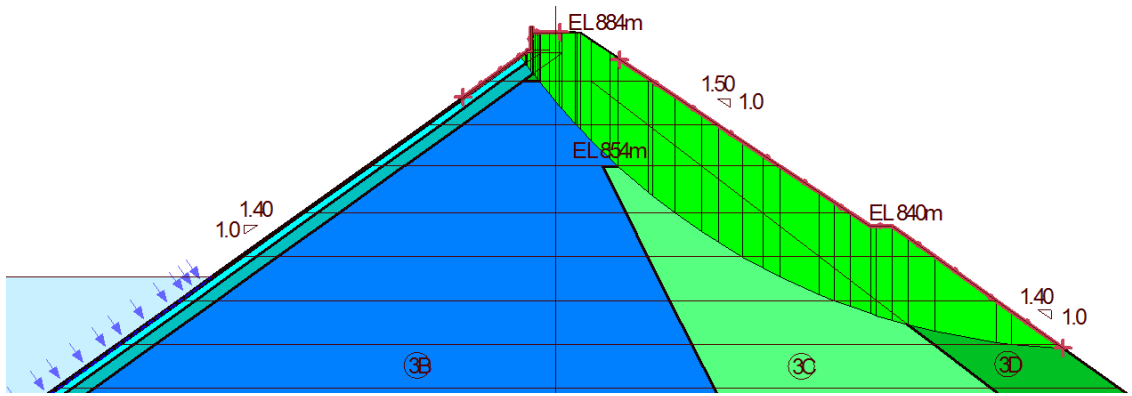


Figure 234 Downstream slip circle first one including the whole crest and resulting in a deformation of 0,04m (NL GeoStudio)

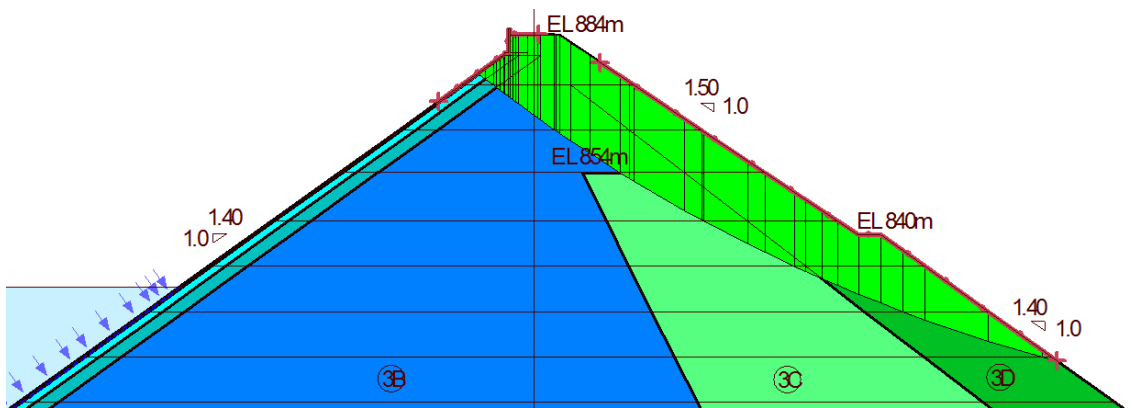


Figure 235 Downstream slip surface resulting in approximately 0,00m deformation (NL GeoStudio)

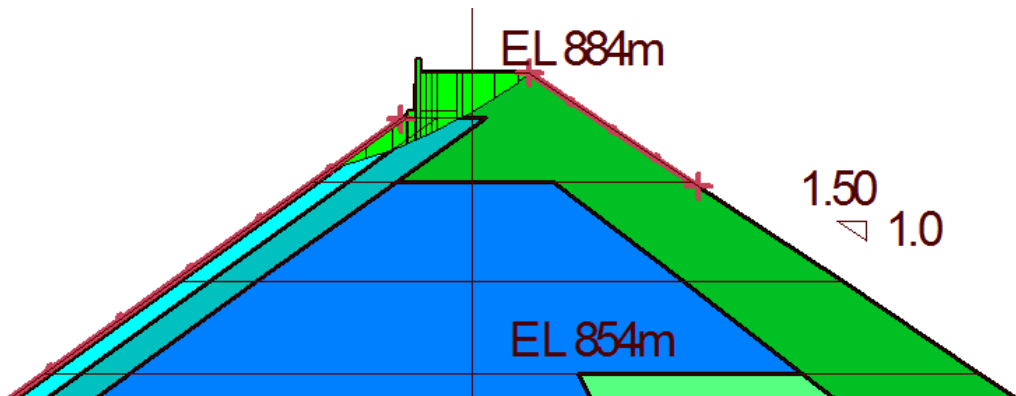


Figure 236 Upstream slip circle resulting in highest deformation of 1,37m (NL GeoStudio)

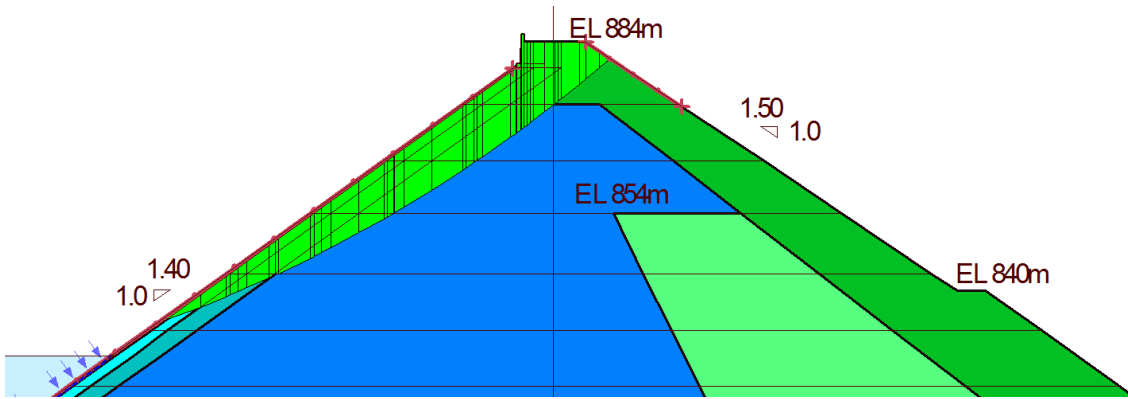


Figure 237 Upstream “deep” seated slip circle resulting in a deformation of 0,025m (NL GeoStudio)

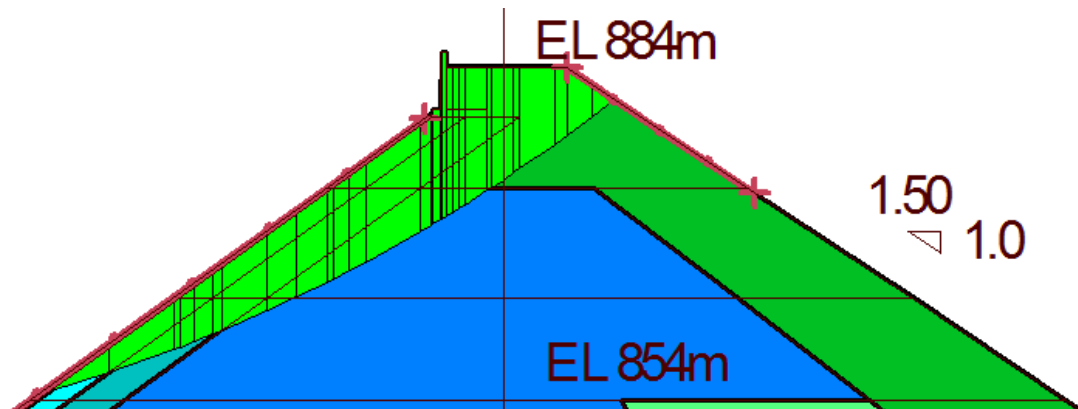


Figure 238 Upstream slip surface resulting in approximately 0,00m of deformation (NL GeoStudio)

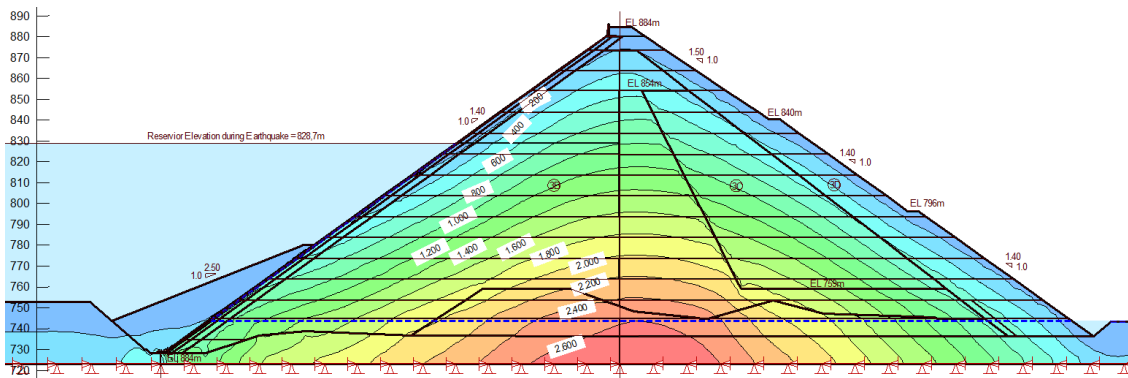


Figure 239 Effective vertical stresses after Wenchuan earthquake [kN/m<sup>2</sup>] (NL GeoStudio)

### 12.2.1.3 Non Linear Codes – Plaxis 2015

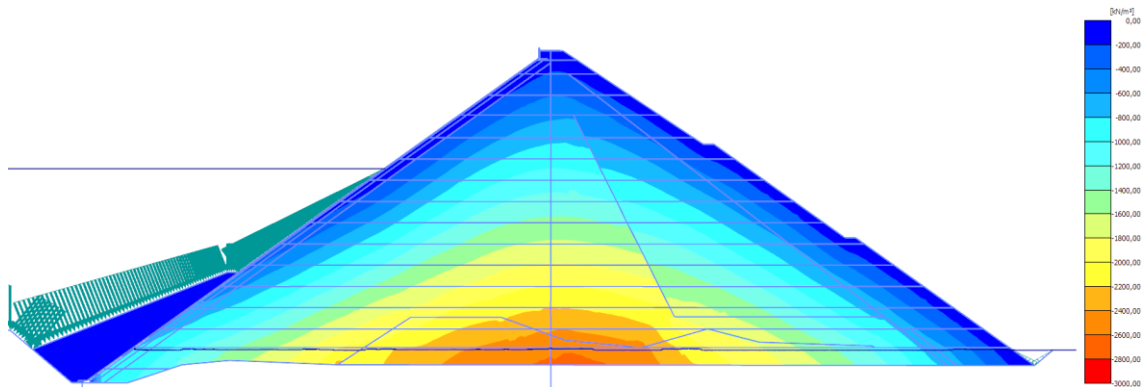


Figure 240 Effective vertical stress distribution prior earthquake analysis [kN/m<sup>2</sup>] (NL Plaxis)

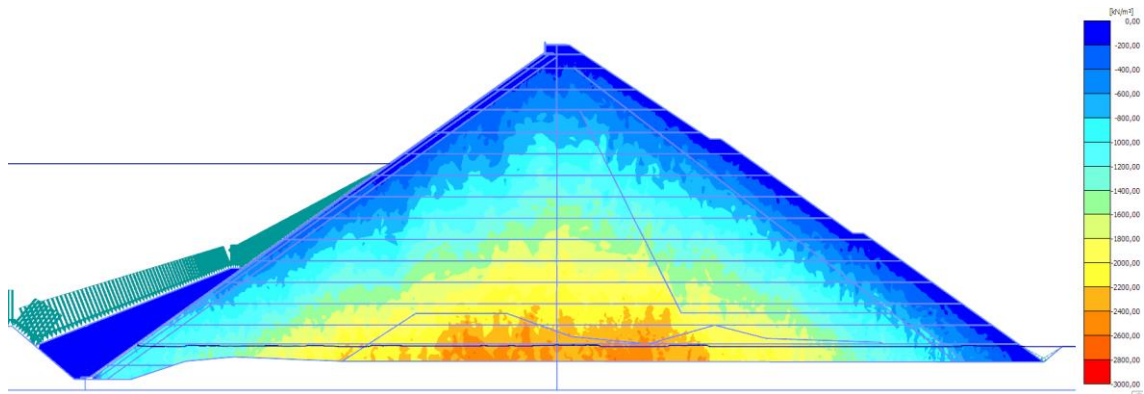


Figure 241 Effective vertical stress distribution after earthquake analysis [kN/m<sup>2</sup>] (NL Plaxis)

As for the other case studies too, peak acceleration plots separated in horizontal and vertical direction can't be provided.

Figure 242 and Figure 243 show the horizontal and vertical crest acceleration calculated at the location of the strong motion instrumentation. The resulting peak acceleration is 0,76g in horizontal and 1,08g in vertical direction. In contrast to the monitored acceleration (0,8 to 0,9g in horizontal and vertical direction), the calculated result is in acceptable agreement.

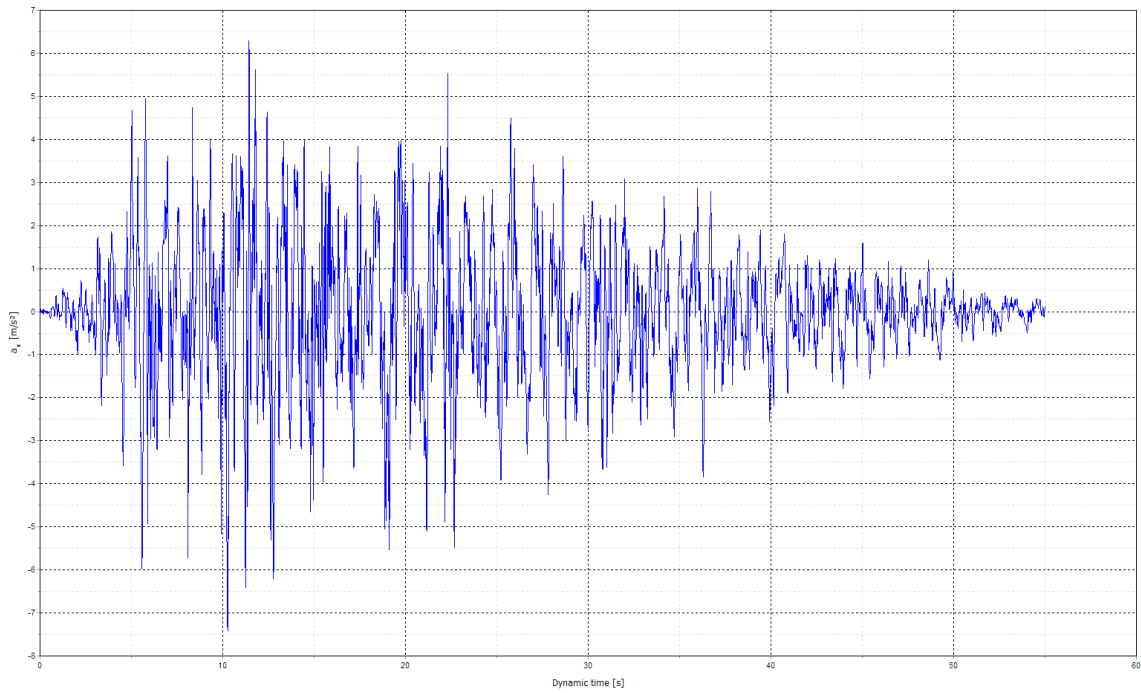


Figure 242 Horizontal crest acceleration calculated from Wenchuan earthquake [m/sec<sup>2</sup>] (NL Plaxis)

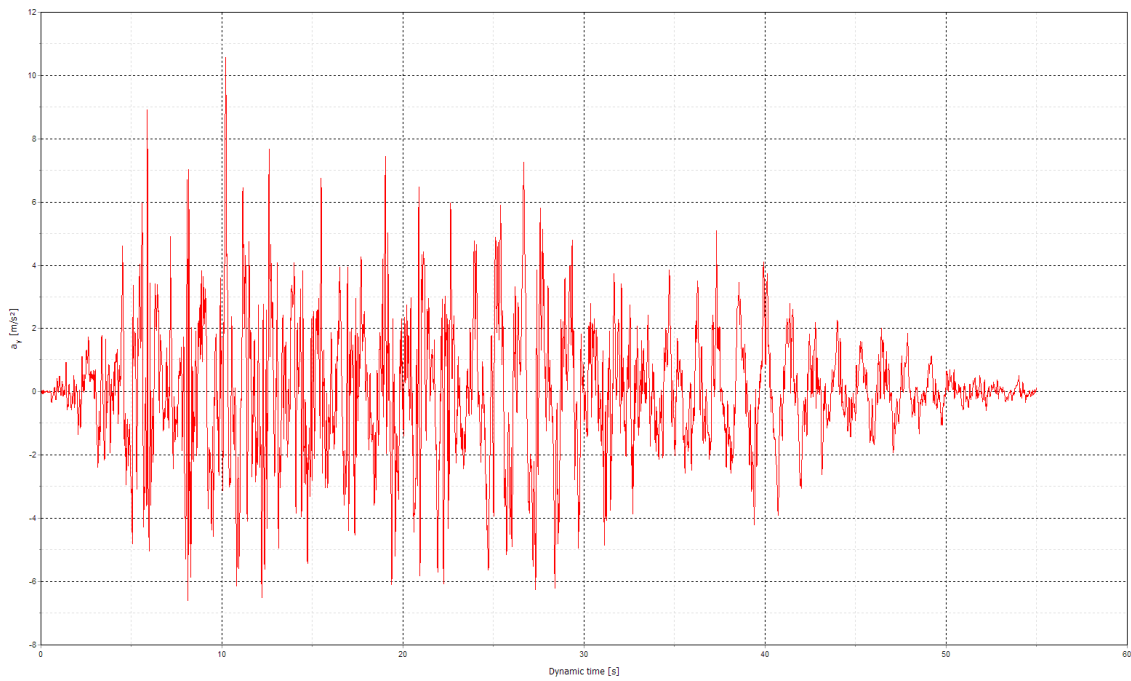


Figure 243 vertical crest acceleration calculated from Wenchuan earthquake [m/sec<sup>2</sup>] (NL Plaxis)

Figure 244 shows the settlement of the crest vs. the settlement of the model base. The delta deformation may be termed the permanent deformation at the end of the earthquake. The calculated permanent crest settlement resulted in 32cm at end of Wenchuan earthquake. The permanent horizontal displacement of the crest resulted in 25cm towards downstream.

Figure 245 and Figure 246 show the result of additional post-earthquake stress-redistribution analysis. If correct the calculated settlements should result in a negligible order. The crest settlement resulted in 0,2cm and the horizontal crest displacement in 0,3cm displacement towards downstream.

As a result the permanent crest settlement (from Figure 244) results in 32cm. This result significantly underestimates the observed dynamic settlements. The permanent horizontal crest displacements (from Figure 244) resulted in a permanent displacement of 25cm towards downstream. Comparing this result to real dam behavior (Figure 98) it may be stated that the result shows acceptable agreement in direction and size. Real crest deformation resulted in 20cm towards downstream. If judging the calculated horizontal crest displacement it shall be noted that the calculated crest settlement at same time resulted in one third of the observed deformations. In general it may be concluded that the dynamic deformations cannot be reproduced accurately.

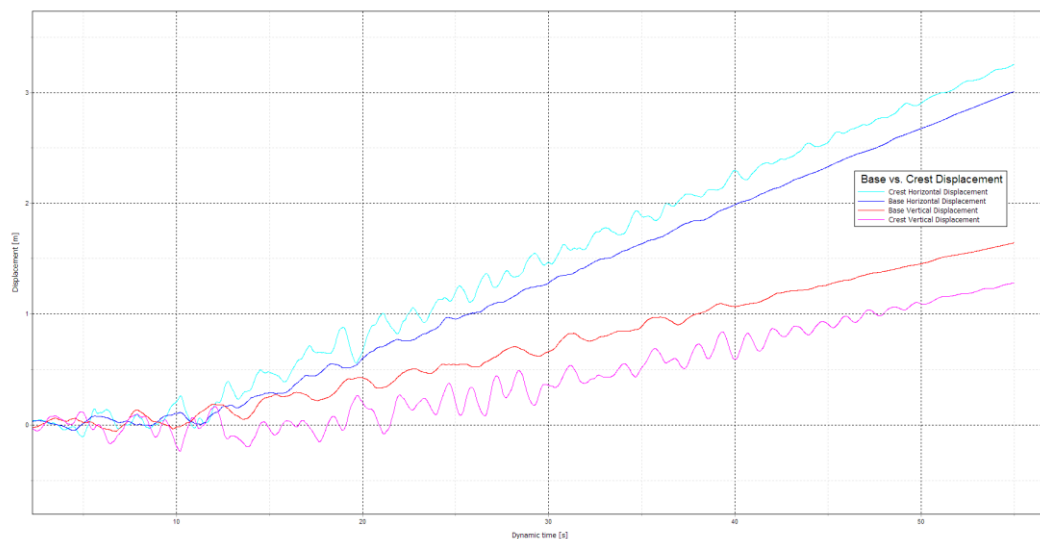
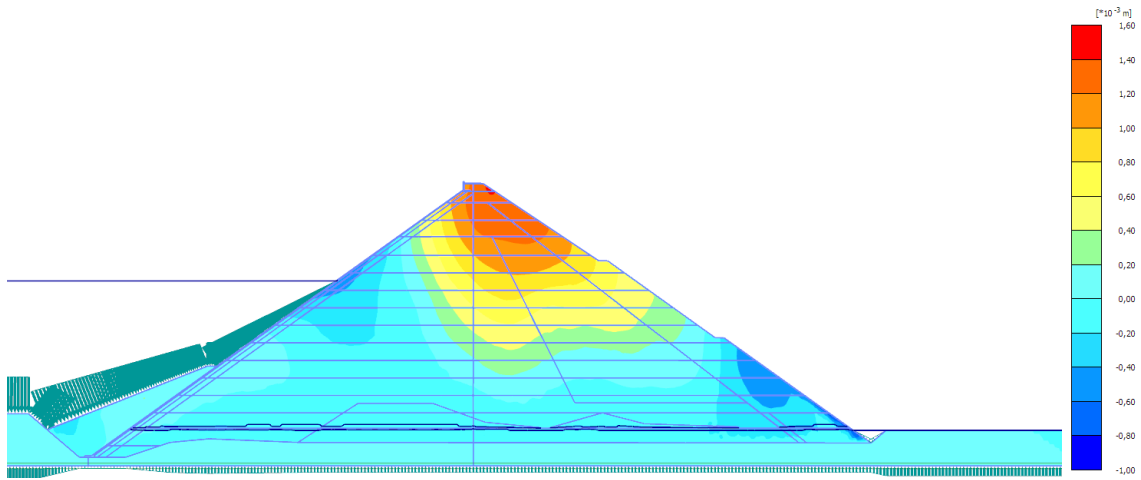
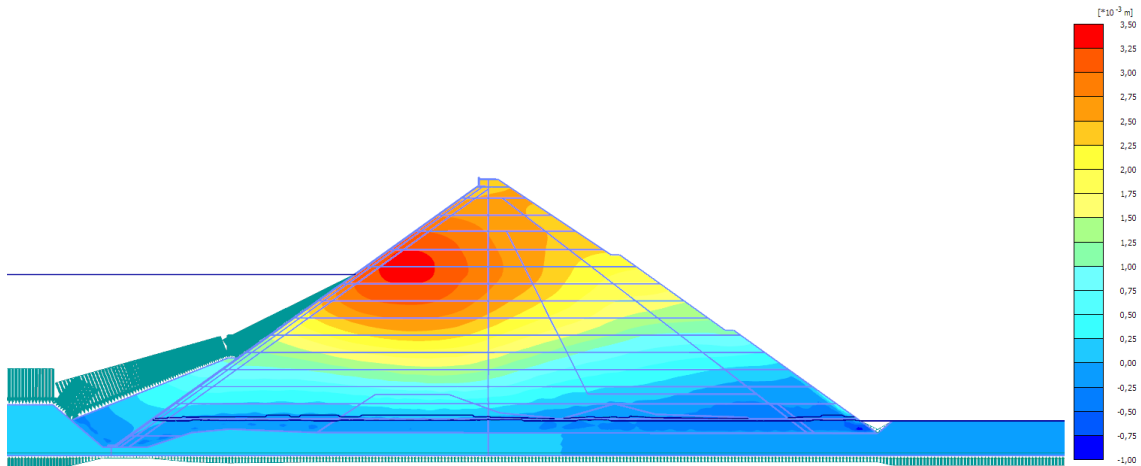


Figure 244 Vertical crest vs. base displacement [m] (NL Plaxis)



**Figure 245 Vertical crest settlement, permanent deformation as a result of post-earthquake stress-redistribution analysis [m] (NL Plaxis)**



**Figure 246 Horizontal crest displacement, permanent deformation as a result of post-earthquake stress-redistribution analysis [m] (NL Plaxis)**

Figure 247 plots all points where the failure criterion was reached at least once during the dynamic shaking. It can be seen that nearly all elements in the downstream shoulder and those located significantly above the reservoir water level went through the state of yielding during the strong shaking of Wenchuan earthquake. A red dot is plotted for each element; hence denser dots do only represent a finer mesh at that location.

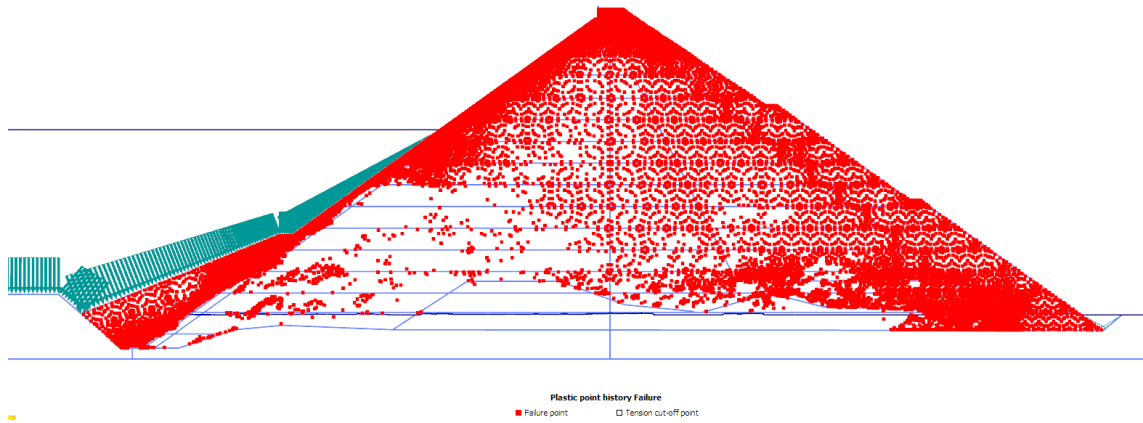


Figure 247 Failure points (red dots) where the yield criterion was reached during or at end of the dynamic calculation of Wenchuan earthquake (NL code, Plaxis)





### 12.3 Homogeneous Embankment

Figure 248 and Figure 249 show the global factor of safety of both slopes prior earthquake. The factor of safety for the upstream slope is well above and in case of downstream slope it is roughly in the range of what international guidelines accept as the minimum for steady state conditions. One thing might attract the Engineer's attention. The phreatic surface within the dam body at downstream slope is comparatively high. Even if Fujinuma dam was built without an internal drainage system and the phreatic surface is mainly based on laboratory test results (Charathpangoon, 2014). The phreatic surface is to the opinion of the author better interpreted as the line of fully saturated pore volume due to matrix suction. Anyway, it has to be pointed out that the final results are not sensible to the exact location of the phreatic surface (if it varies in a realistic range).

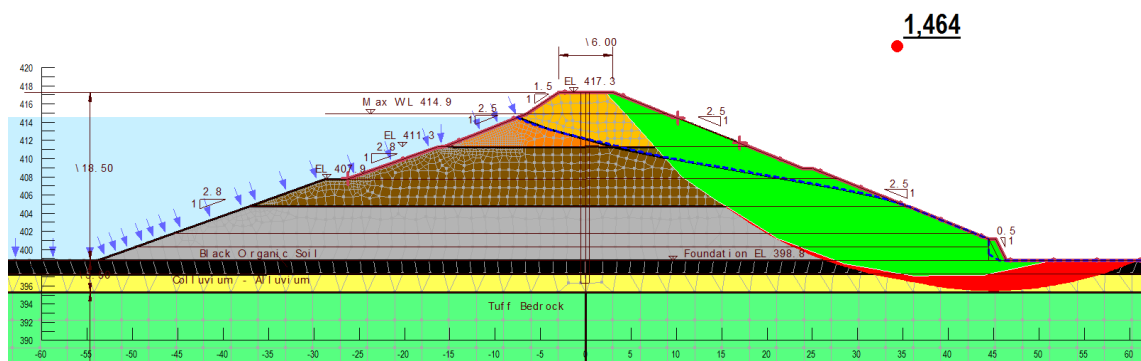


Figure 248 DS global factor of safety, prior earthquake static conditions

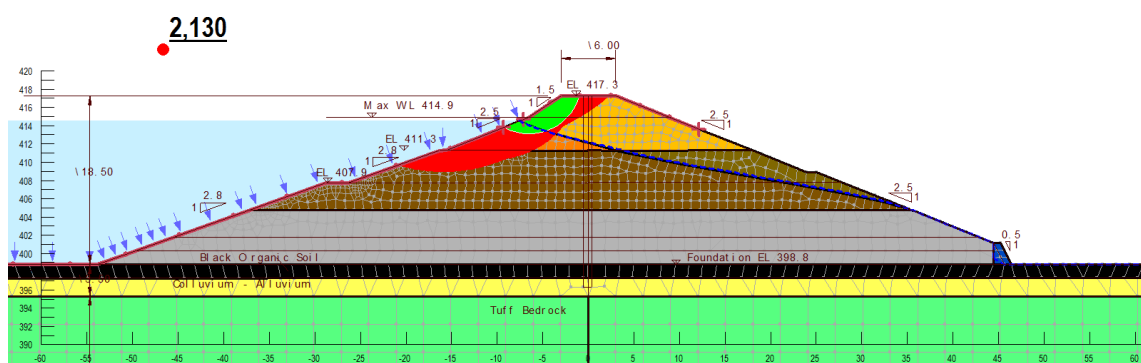
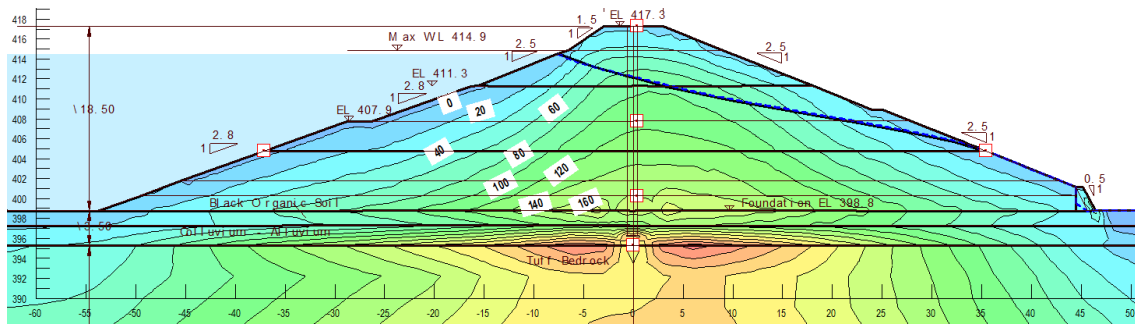


Figure 249 US global factor of safety, prior earthquake static conditions



**Figure 250 Effective vertical stress distribution after impounding shortly prior earthquake analysis of Fujinuma dam**

### **12.3.1.1 Linear Equivalent Code – GeoStudio 2012**

#### 12.3.1.1.1 Check Earthquake

Figure 251 to Figure 255 plot the results of stability calculations after the dam was subject to check earthquake excitation. It can be seen that all factors of safety plot above 1.00 (despite the fact that a severely cracked embankment was assumed within the stability calculations, see slope near areas with black hatches).

The assumption of cracks has to be seen in close connection to the later presented results of Tohoku earthquake. For sure cracks have not developed within Fujinuma embankment due to the check earthquake. Cracks were assumed in post-earthquake stability calculations only to demonstrate that it is not the sole assumption of cracks that will later cause factors of safety below 1.00 after Tohoko earthquake.

If no cracks are assumed in case of check earthquake, the dam's global factor of safety remains unchanged prior and after check earthquake (Figure 248 and Figure 249).

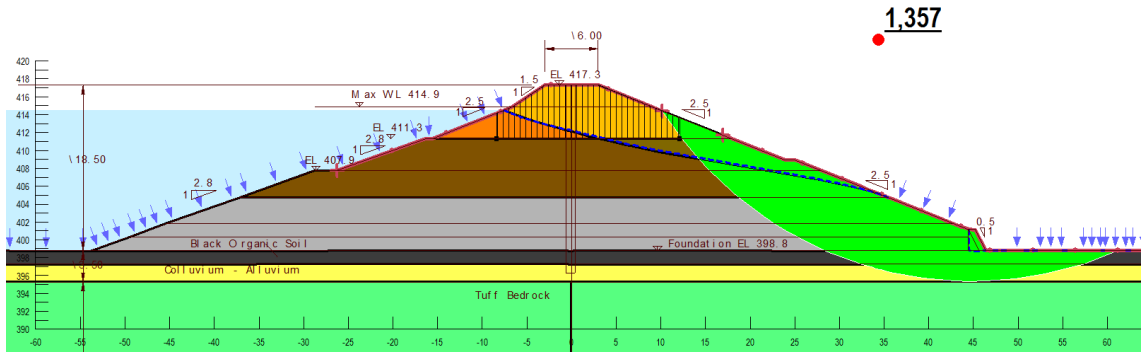


Figure 251 DS global factor of safety after check earthquake (slope stability based on EL analysis, GeoStudio)

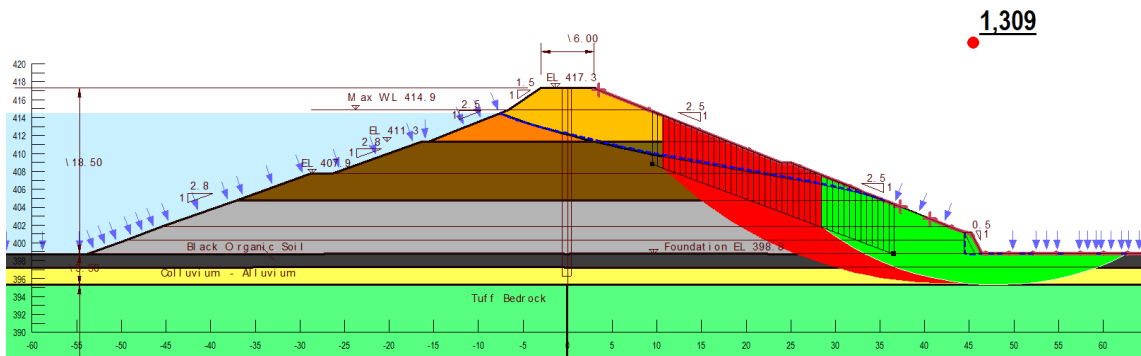


Figure 252 DS local factor of safety after check earthquake (slope stability based on EL analysis, GeoStudio)

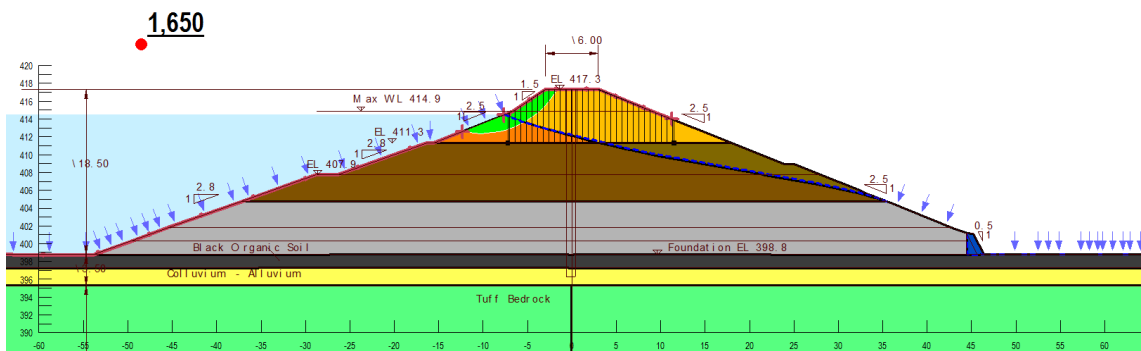


Figure 253 US local factor of safety after check earthquake (slope stability based on EL analysis, GeoStudio)

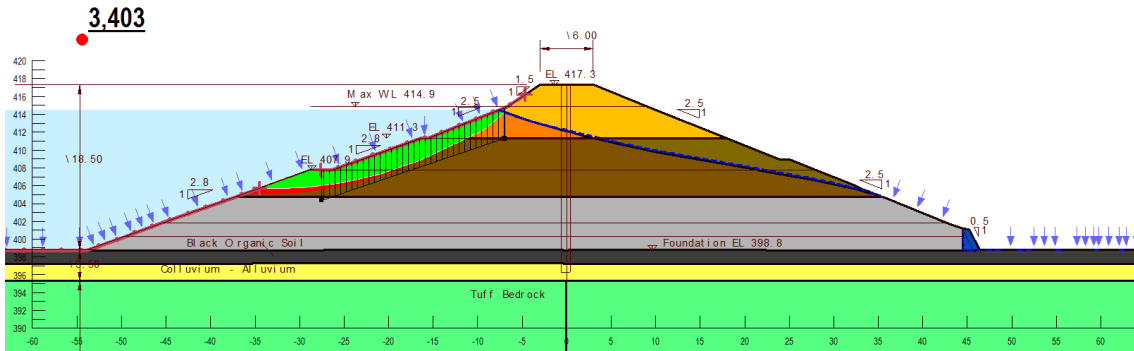


Figure 254 US local factor of safety after check earthquake (slope stability based on EL analysis, GeoStudio)

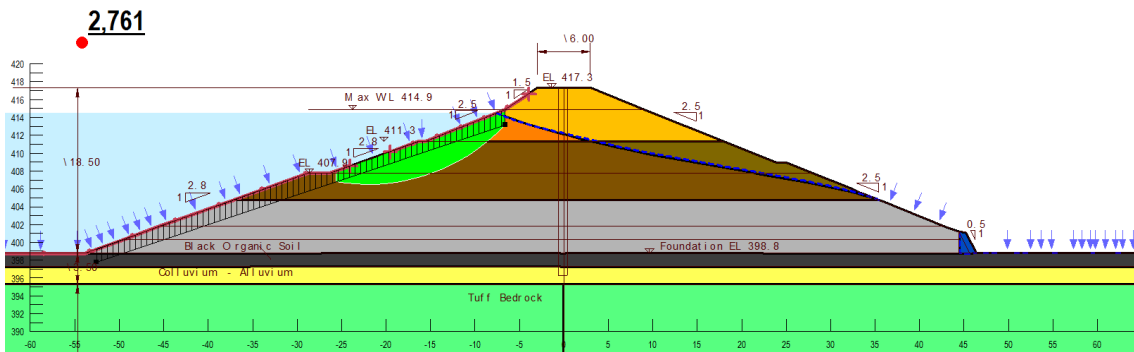


Figure 255 US local factor of safety after check earthquake (slope stability based on EL analysis, GeoStudio)

Figure 256 and Figure 257 show the performance of Fujinuma dam as a result of the check earthquake (EL analysis). Figure 256 proves that no liquefaction has developed at all. Figure 257 plots Fujinuma dam's post-earthquake deformations after check earthquake. The resulting deformation is essentially zero.

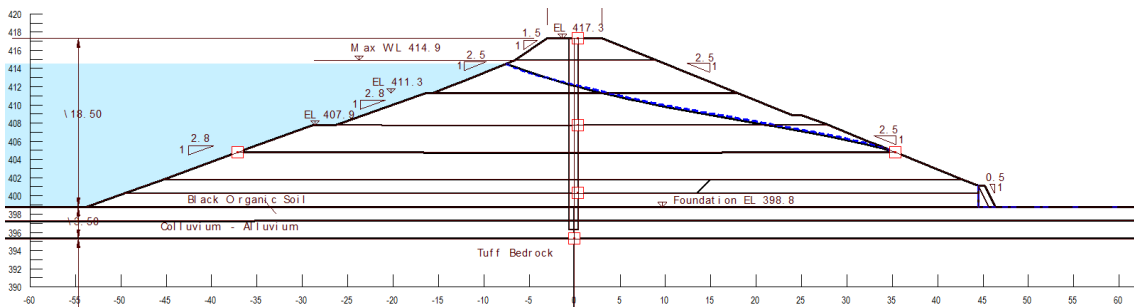


Figure 256 Liquefaction plot after check earthquake (liquefied material would be marked in yellow color, EL analysis, GeoStudio)

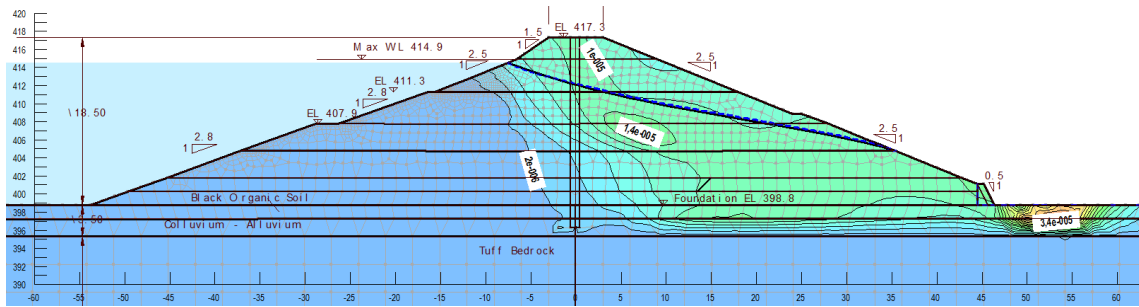


Figure 257 Post-earthquake deformations after check earthquake [m] (EL analysis, GeoStudio)

### 12.3.1.1.2 Tohoku Earthquake

Tohoku earthquake induced large dynamic shear strains in Fujinuma dam's embankment. Figure 258 to Figure 264 show the results of stability calculations after the earthquake. In accordance to large strains, local cracks were assumed at different locations. It can be seen that none of the calculated slip surfaces plots above 1.00. All results indicate a slope failure. Of special interest are the sliding masses towards upstream direction as they explain the upstream movement of concrete elements as mapped in the field after dam failure (Figure 111).

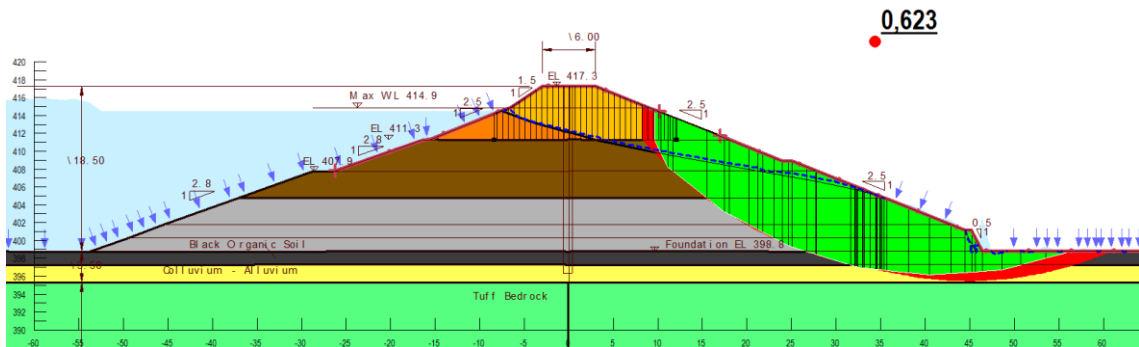


Figure 258 DS local stability after Tohoku earthquake (slope stability based on EL analysis, GeoStudio)

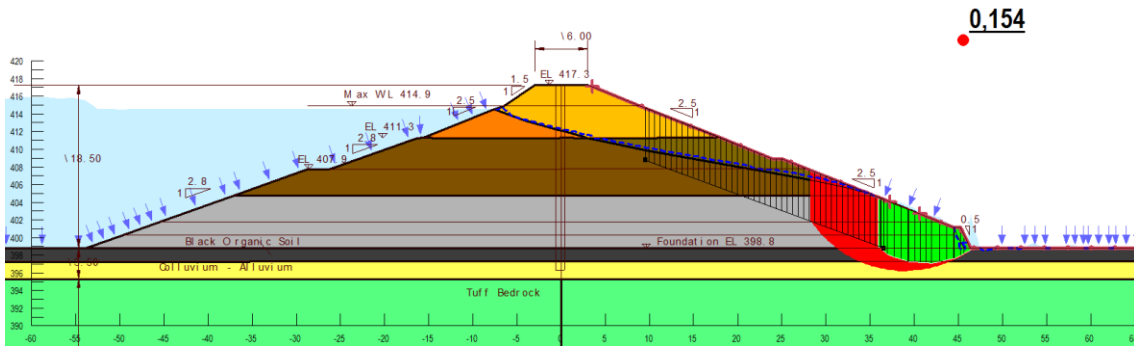


Figure 259 DS local stability after Tohoku earthquake (slope stability based on EL analysis, GeoStudio)

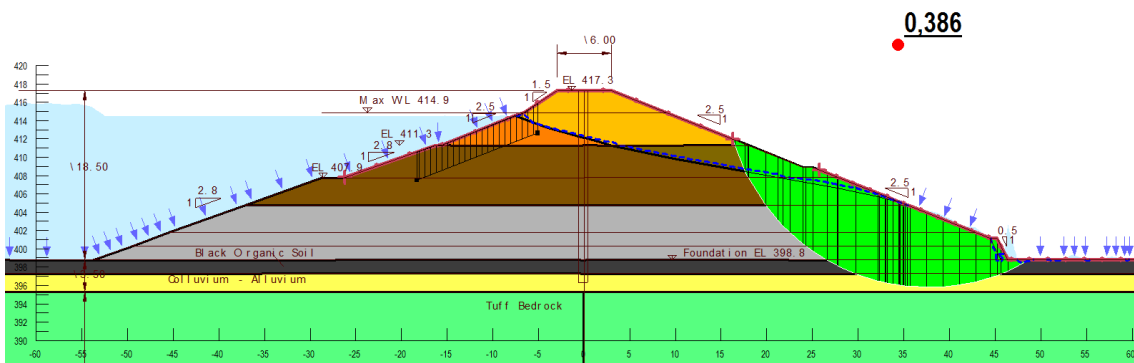


Figure 260 DS local stability after Tohoku earthquake (slope stability based on EL analysis, GeoStudio)

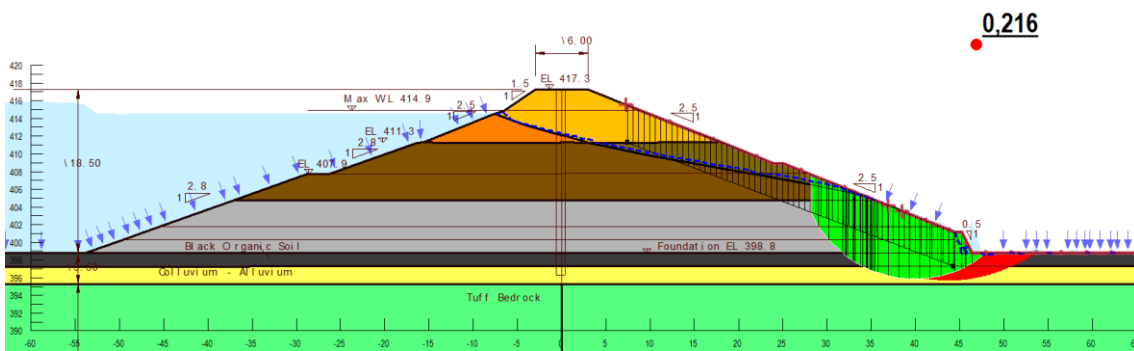


Figure 261 DS local stability after Tohoku earthquake (slope stability based on EL analysis, GeoStudio)

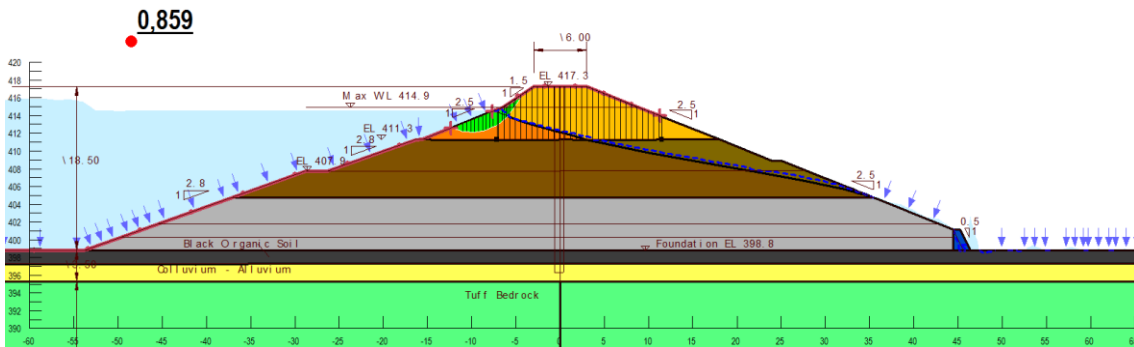


Figure 262 US local stability after Tohoku earthquake (slope stability based on EL analysis, GeoStudio)

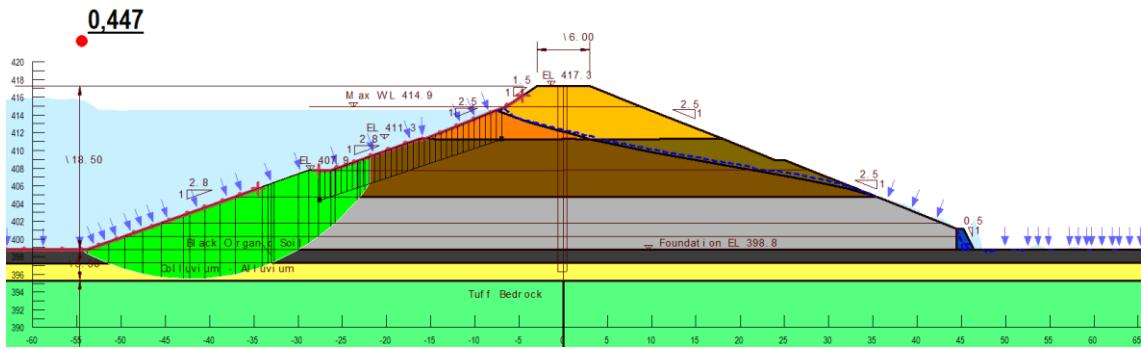


Figure 263 US local stability after Tohoku earthquake (slope stability based on EL analysis, GeoStudio)

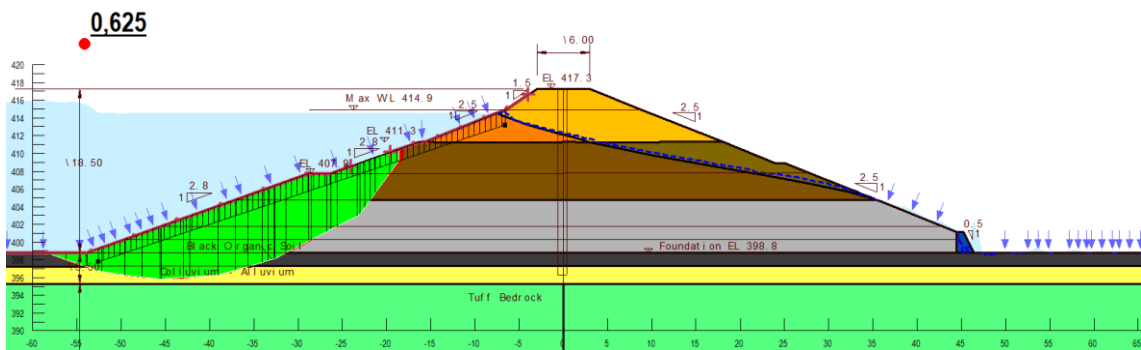


Figure 264 US local stability after Tohoku earthquake (slope stability based on EL analysis, GeoStudio)

Figure 265 plots zones that have liquefied at end of Tohoku earthquake based on Equivalent – Linear analysis.

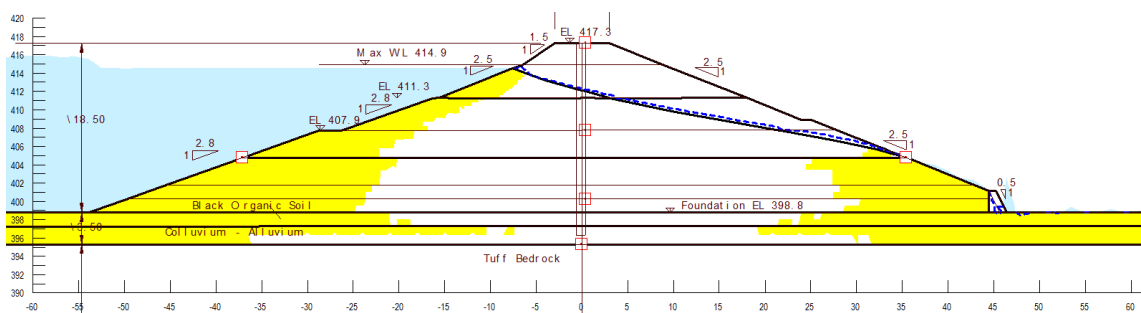


Figure 265 Liquefied zones within Fujinuma embankment after Tohoku earthquake (EL analysis, GeoStudio)

Figure 266 and Figure 267 plot the calculated post-earthquake deformation. All plots result from static stress-redistribution analyses. GeoStudio realistically reduces the shear strength to the specified residual strength for all finite elements that were

marked liquefied in prior calculation steps. Figure 267 shows the settlement of Fujinuma dam crest. The local maximum in crest region results in 25cm, far away from causing over flow. The governing factor guiding the final crest settlement is the Young's modulus of the fill materials.

As long as liquefied finite element's stress state plots below the collapse "line" it behaves plastic and all the load will be transferred to those elements that did not liquefy. Hence those elements are loaded and their Young's modulus would have to be changed to the specific load increase to achieve more realistic deformations. Lacking for detailed stress strain plots from Fujinuma dam material, the Young's modulus was kept constant. Anyway it would be impossible to select a constant Young's modulus that would fit all stress ranges within the area of stress redistribution. Such a value would always have to be a (best) guess.

This demonstrates that the Engineer shall not rely on the output of such calculations. As long as liquefaction may occur, it is hard to impossible to state that crest deformations are in an acceptable range. In a wider sense the Engineer would also have to judge crack depths in accordance with calculated deformation results to judge the dam stability. It can be seen in later presented results that more sophisticated approaches result in more realistic deformations, but still their results need to be based on extensive laboratory investigations. And then again, accurate judgement of deformations will be limited to a view cases only. The majority of all cases will still remain "un-judgable" if a dam failure would result in significant loss of property or life.

Figure 268 plots the vertical crest settlement vs. the vertical displacement at model base. It can be seen that both graphs are the same. Again this needs to be kept in mind when judging the output. An Equivalent – Linear model cannot capture permanent deformations that might develop during the earthquake. If these deformations are deemed to be of significant size, such deformations might be estimated by adding a Newmark double integration method. The total settlement then will result in the sum of the Newmark double integration and the stress – redistribution analyses.



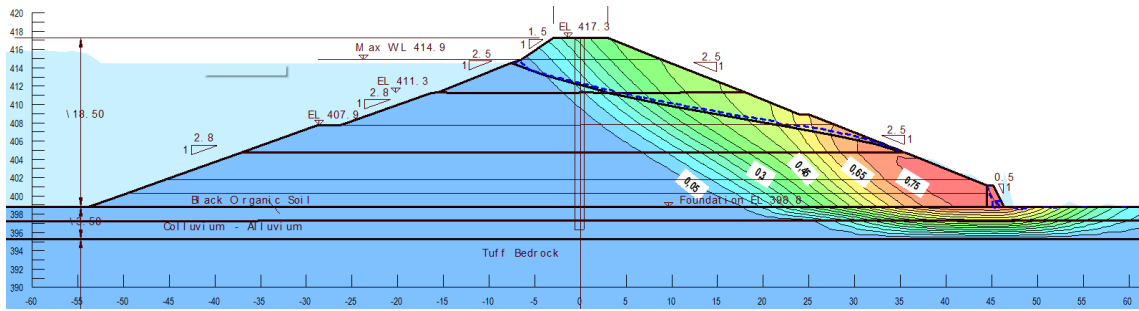


Figure 266 Post-earthquake xy - displacements after Tohoku earthquake (EL analysis, GeoStudio)

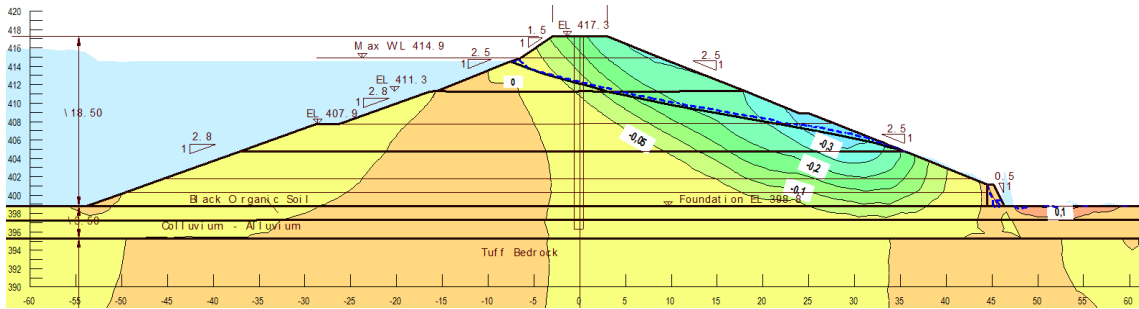


Figure 267 Post-earthquake settlement after Tohoku earthquake (EL analysis, GeoStudio)

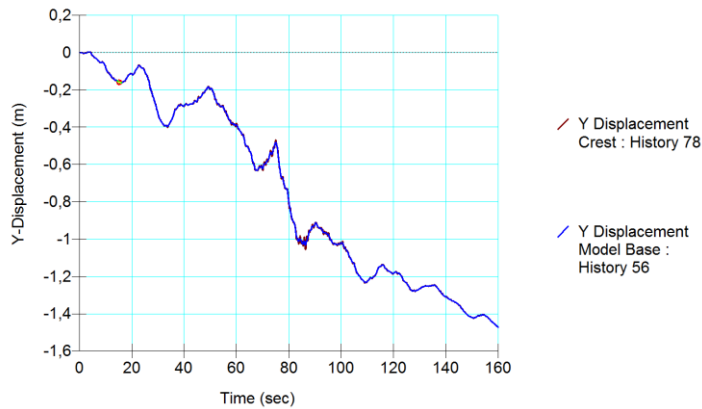
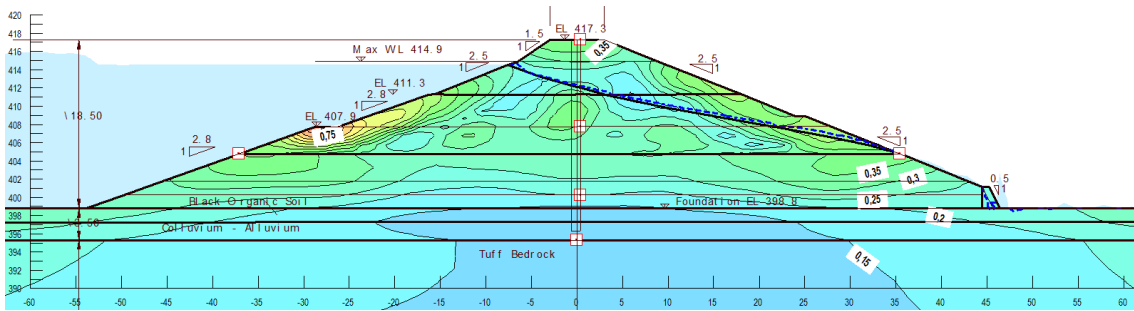
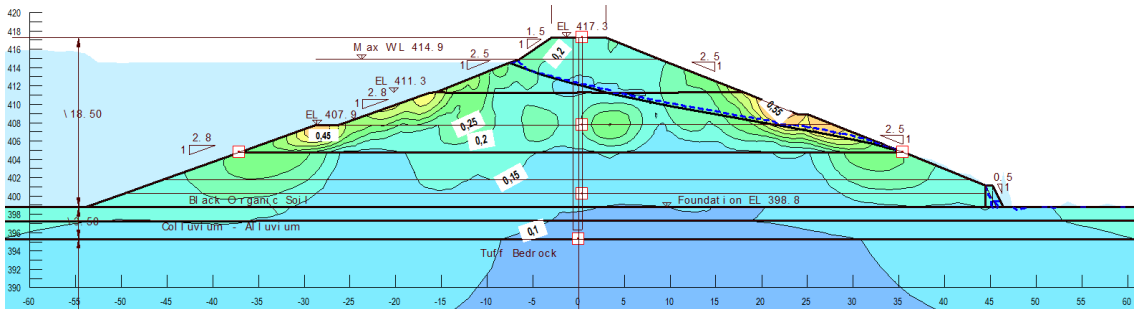


Figure 268 Vertical crest settlement vs. vertical model base settlement at end of dynamic calculation [m] (EL analysis, GeoStudio)

Figure 269 and Figure 270 plot the peak accelerations in horizontal respectively in vertical direction. The horizontal peak crest acceleration results in 0,35g whilst the vertical results in 0,2g.



**Figure 269 Peak horizontal crest acceleration during Tohoku earthquake [g] (EL analysis, GeoStudio)**



**Figure 270 Peak vertical crest acceleration during Tohoku earthquake [g] (EL analysis, GeoStudio)**

Figure 271 plots the pore water pressure built up during the dynamic event. In EL analysis, pore water pressure is calculated in the end of the earthquake. Hence when the dynamic excitation is over, the model compares the peak shear stress with the applied material sets and then calculates the pore water pressure for each stored time step. Above plotted peak crest accelerations need to be judged in that respect. The Equivalent – Linear model is not able to calculate the effects of pore water pressure in detail. Especially in case of limited liquefaction a Nonlinear model needs to be used to capture significant effects as damping that come with soil liquefaction.

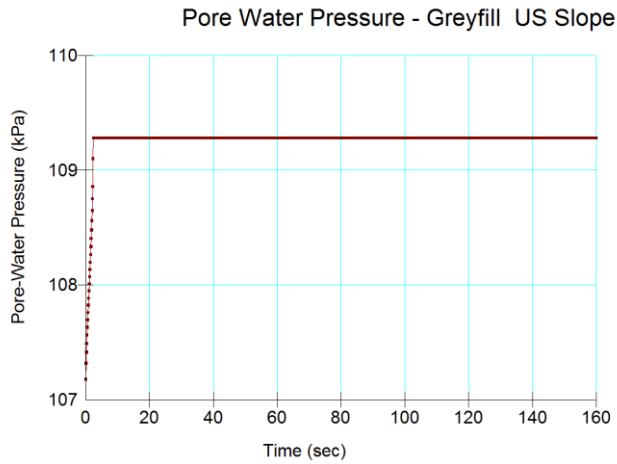


Figure 271 Pore water pressure development vs. dynamic time (EL analysis, GeoStudio)

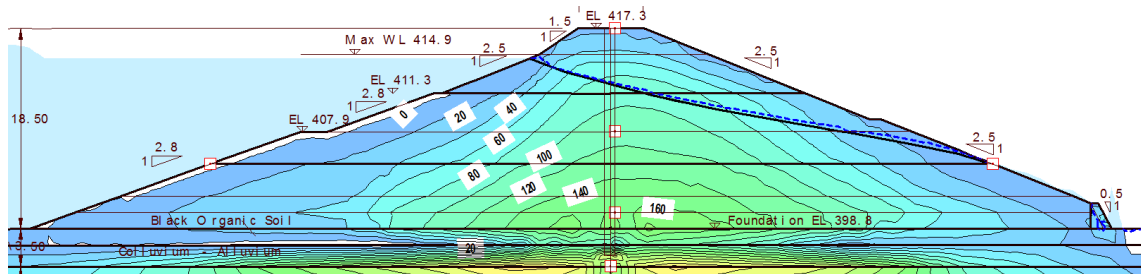


Figure 272 Effective vertical stresses after Tohoku earthquake (EL analysis, GeoStudio)

### 12.3.1.2 Non Linear Codes – GeoStudio 2012

#### 12.3.1.2.1 Check Earthquake

Figure 273 to Figure 277 plot the results of stability calculations after the dam was subject to check earthquake excitation (Nonlinear analyses). It can be seen that all factors of safety plot above 1.00. Again a cracked embankment was assumed within the stability calculations (as it has been done in Equivalent – Linear analyses results).

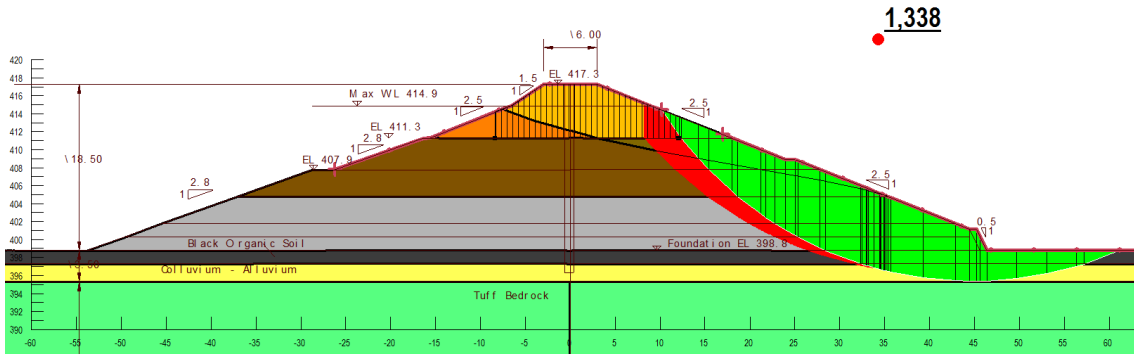


Figure 273 DS global factor of safety after check earthquake (slope stability based on NL analysis, GeoStudio)

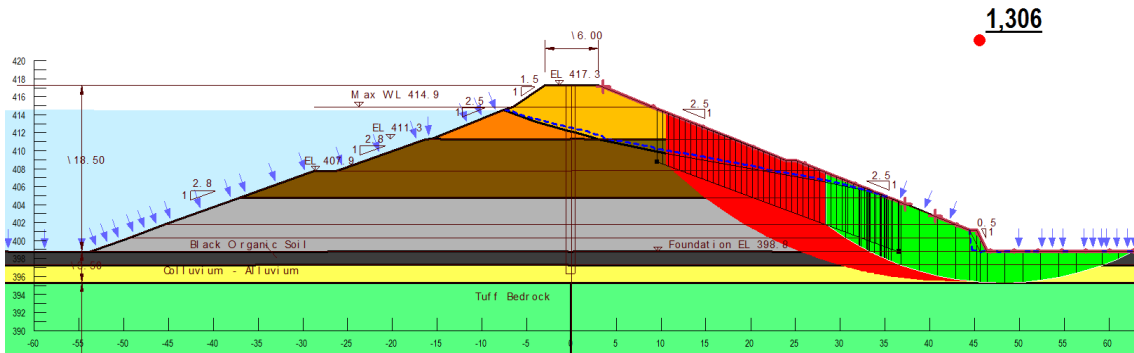


Figure 274 DS local factor of safety after check earthquake (slope stability based on NL analysis, GeoStudio)

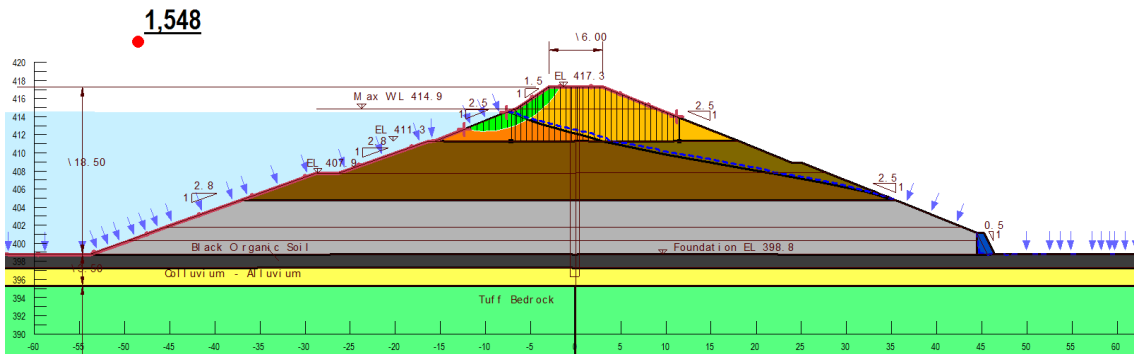


Figure 275 US local of safety after check earthquake (slope stability based on NL analysis, GeoStudio)

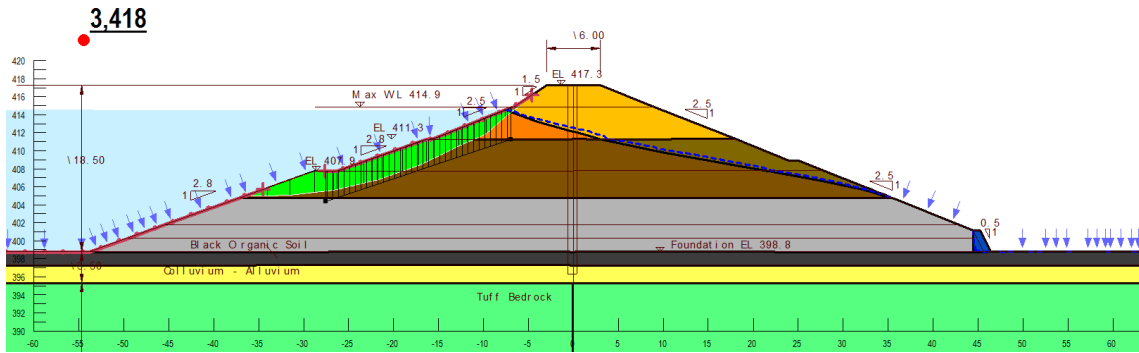


Figure 276 US local of safety after check earthquake (slope stability based on NL analysis, GeoStudio)

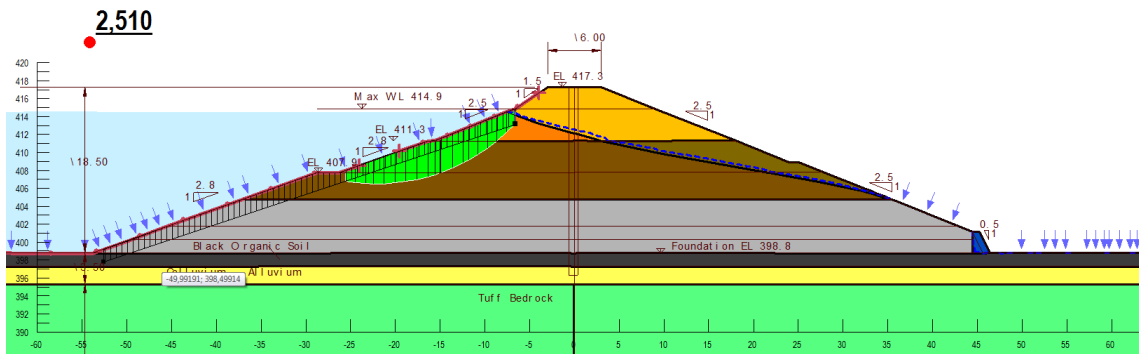


Figure 277 local of safety after check earthquake (slope stability based on NL analysis, GeoStudio)

Figure 278 and Figure 279 show Fujinuma dam behavior after the occurrence of check earthquake. Figure 278 shows all elements that have liquefied during the check earthquake marked in yellow color. A small band indicating local liquefaction may be seen within this figure. As discussed in chapter 11.3.5, this liquefaction is due to a numerical discontinuity and is not related to real liquefaction. It is a consequence in the software's approach on how to calculate the Martin – Finn - Seed input parameters in the tensile stress range. Figure 279 shows Fujinuma dam's post-earthquake deformations after the check earthquake has shaken the dam. It can be seen that the calculated deformations are essentially zero.

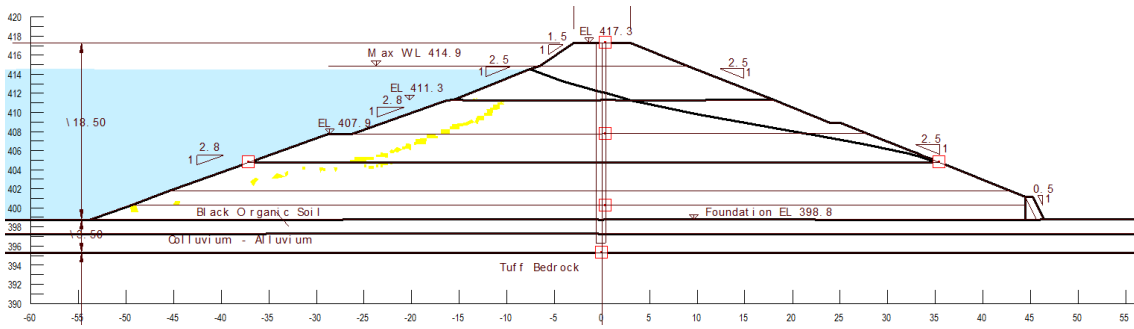


Figure 278 Liquefaction plot after check earthquake (liquefied material would be marked in yellow color, NL code, GeoStudio)

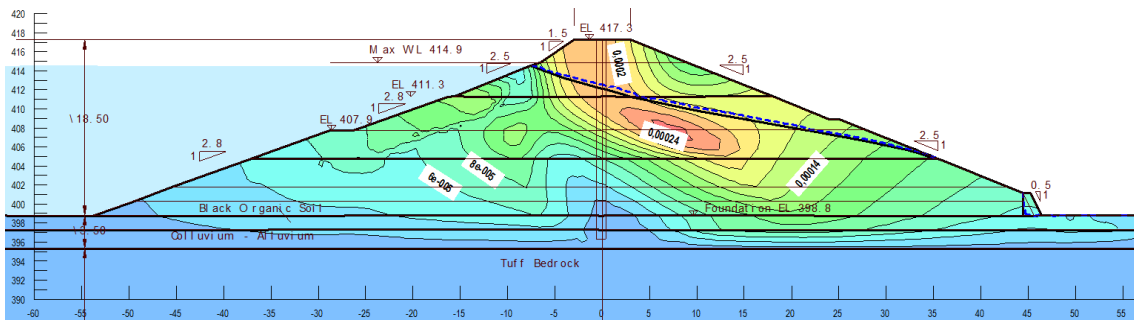


Figure 279 Post-earthquake deformations after check earthquake [m] (NL code, GeoStudio)

### 12.3.1.2.2 Tohoku Earthquake

Figure 280 to Figure 286 show the results of post-earthquake stability calculations following a Nonlinear analysis of Tohoku earthquake. Again, local cracks were assumed at the same locations as done in previous analyses. The result remains unchanged regardless which type of dynamic analysis was used. None of the calculated slip surfaces plots above 1.00. All results indicate a slope failure.

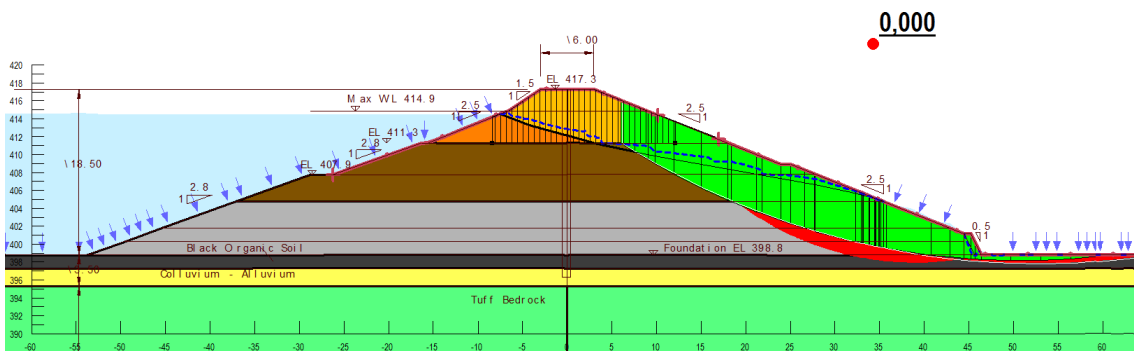


Figure 280 DS local stability after Tohoku earthquake (slope stability based on NL analysis, GeoStudio)

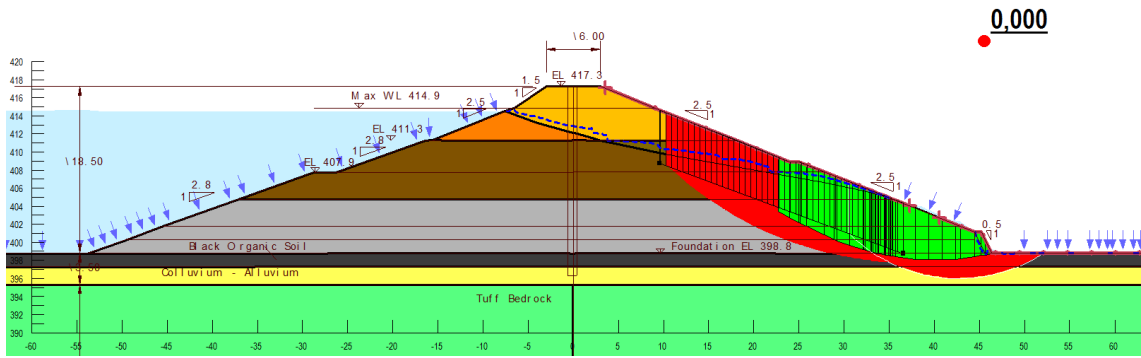


Figure 281 DS local stability after Tohoku earthquake (slope stability based on NL analysis, GeoStudio)

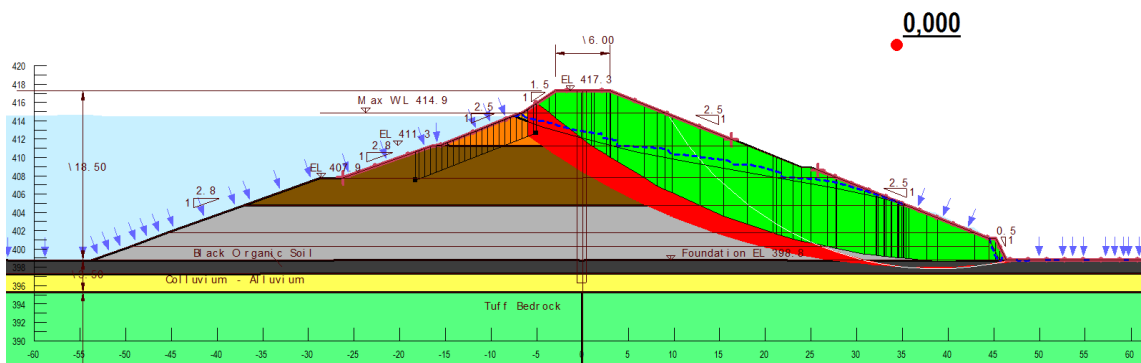


Figure 282 DS local stability after Tohoku earthquake (slope stability based on NL analysis, GeoStudio)

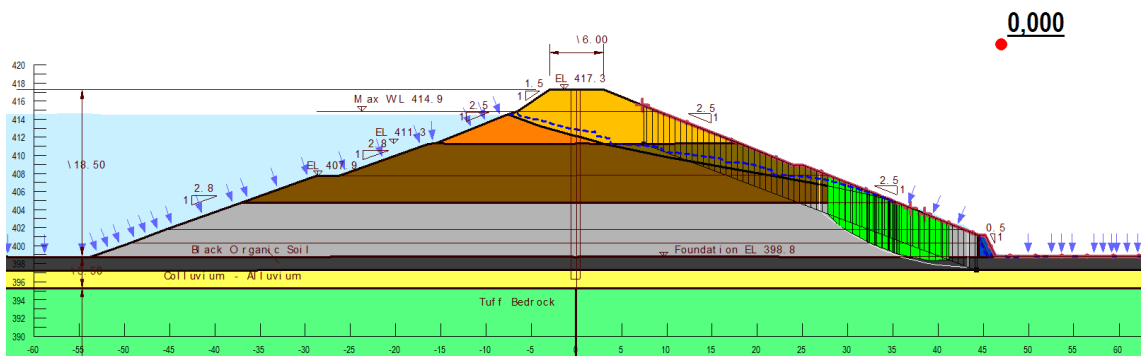


Figure 283 DS local stability after Tohoku earthquake (slope stability based on NL analysis, GeoStudio)

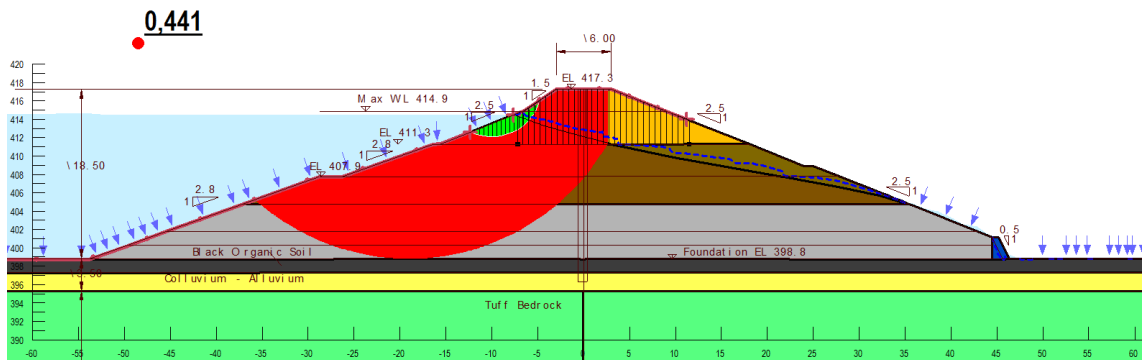


Figure 284 US local stability after Tohoku earthquake (slope stability based on NL analysis, GeoStudio)

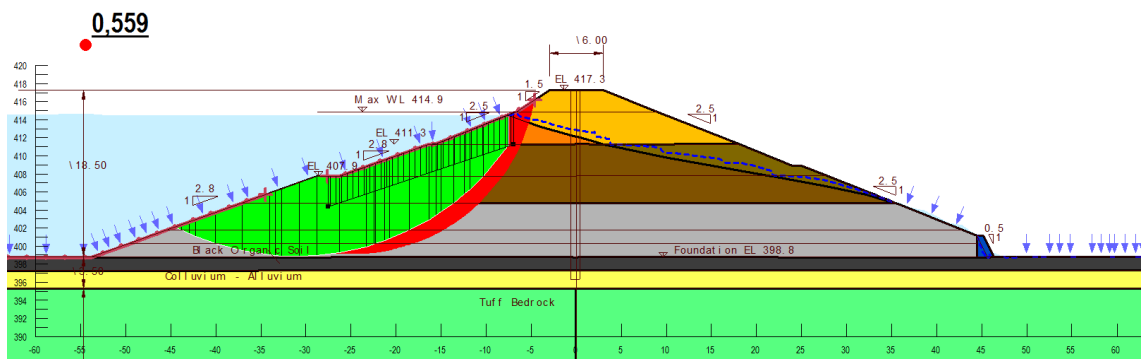


Figure 285 US local stability after Tohoku earthquake (slope stability based on NL analysis, GeoStudio)

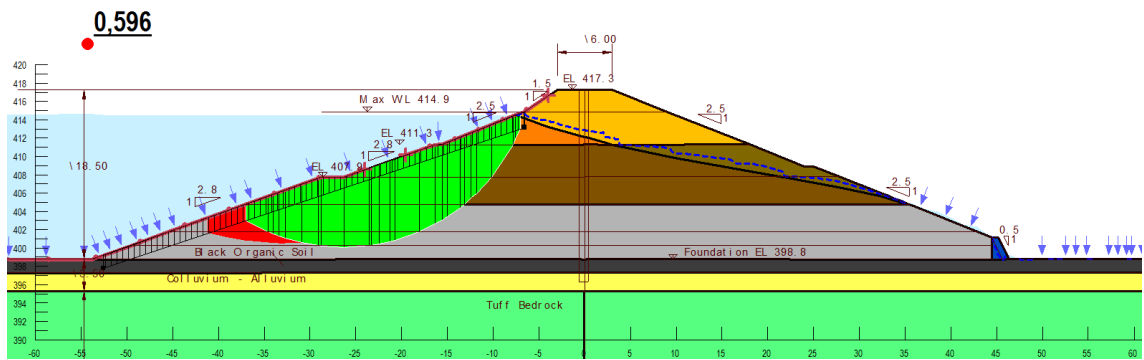
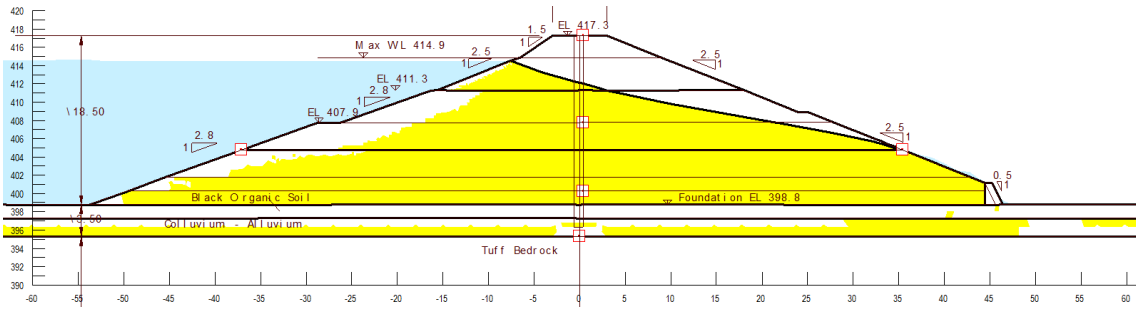


Figure 286 US local stability after Tohoku earthquake (slope stability based on NL analysis, GeoStudio)

Figure 287 shows those zones that have liquefied at end of Tohoku earthquake resulting from Nonlinear analyses. Compared to the results of the EL calculation, the plot shows significantly more liquefaction. It has to be pointed out that due to the different pore water pressure models and the related varying input parameters it is impossible to compare these two liquefaction plots with sufficient accuracy.





**Figure 287 Liquefied zones within Fujinuma embankment after Tohoku earthquake (NL code, GeoStudio)**

Figure 266 to Figure 290 plot the calculated post-earthquake deformations. These plots result from static stress-redistribution analysis. GeoStudio reduces the shear strength for all finite elements that were marked liquefied for Nonlinear analysis too. Figure 289 shows the crest settlement of Fujinuma dam. The local maximum in crest region results in 390cm, clearly causing over flow and failure of the dam. Even though this result is highly realistic (refer to Figure 110) it has to be pointed out that it is more a stroke of luck as to the author's opinion, the available data was not detailed enough to rely on such deformation analysis. Again, the Engineer shall not rely on the output of deformation calculations in case of liquefiable soils.

Figure 291 plots the vertical crest settlement vs. the vertical displacement at model base. It can be seen that there is little differential settlement evidencing the benefit of the Nonlinear model. In contrast to the EL method, NL analysis enables plastic deformations during the earthquake.

Figure 290 plots the post-earthquake settlements in 1:1 scale. It becomes clear that such deformations would clearly induce the dam's failure.

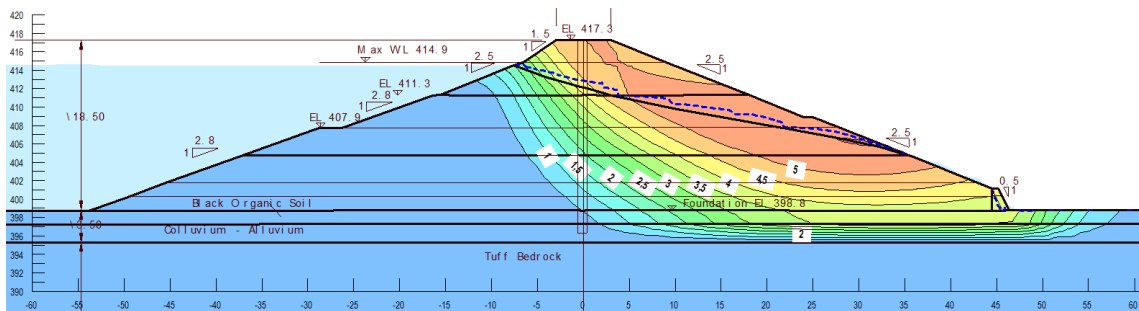


**Figure 288 Post-earthquake xy - displacements after Tohoku earthquake (NL code, GeoStudio)**

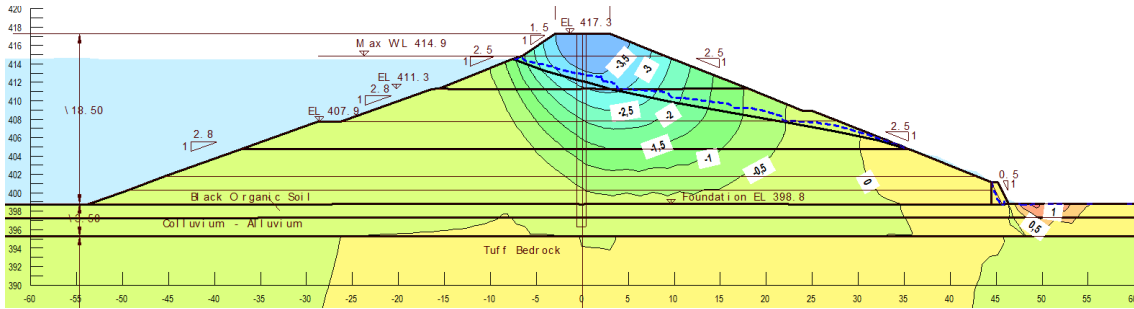


Figure 289 Post-earthquake settlement after Tohoku earthquake (NL code, GeoStudio)

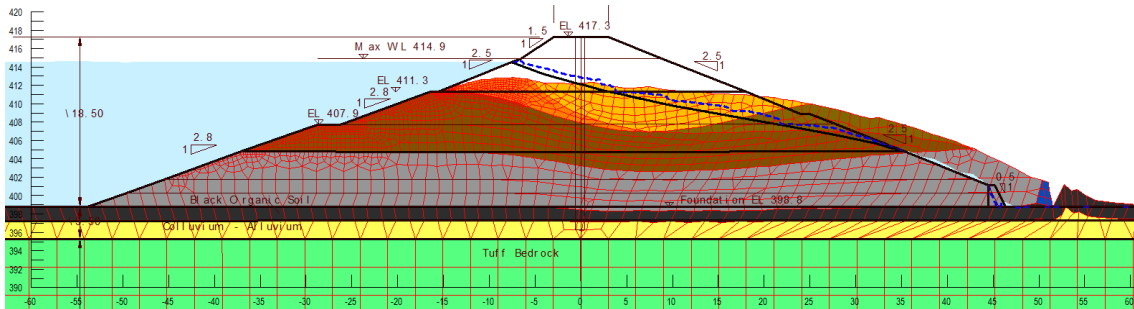


Figure 290 Post-earthquake settlement after Tohoku earthquake, deformed mesh 1:1 (NL code, GeoStudio)

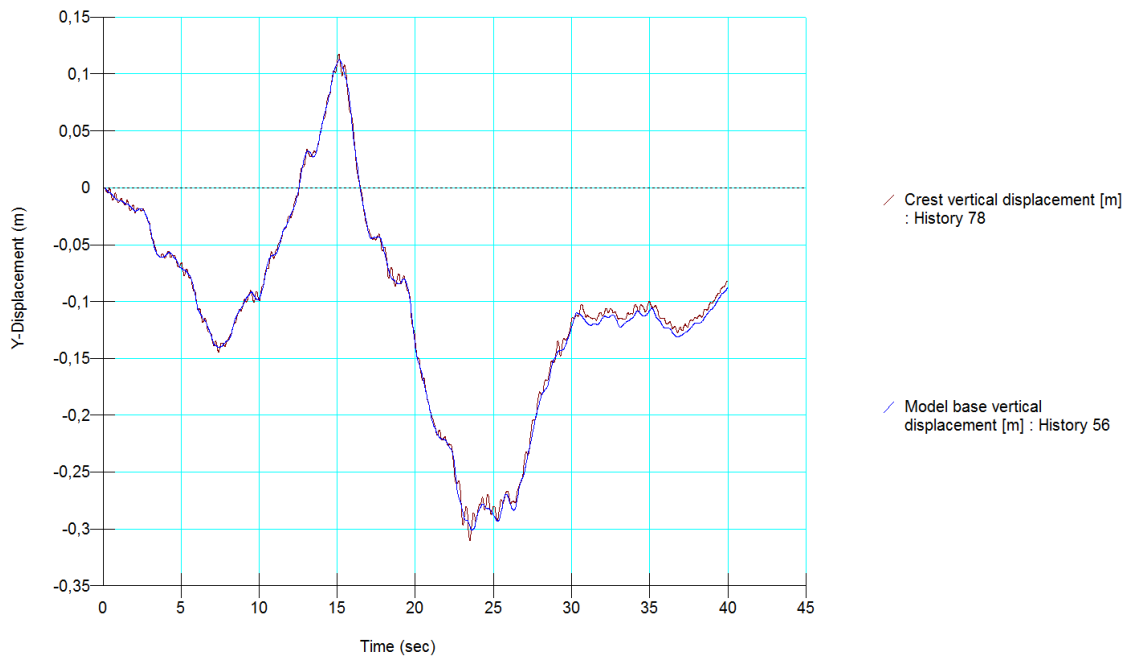
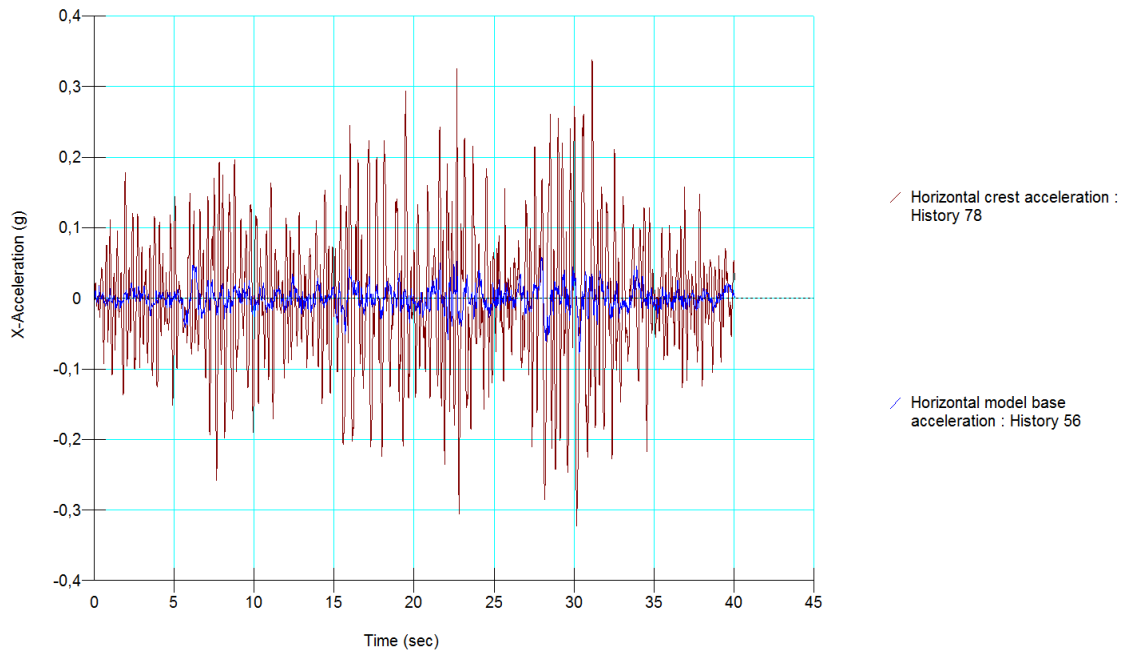


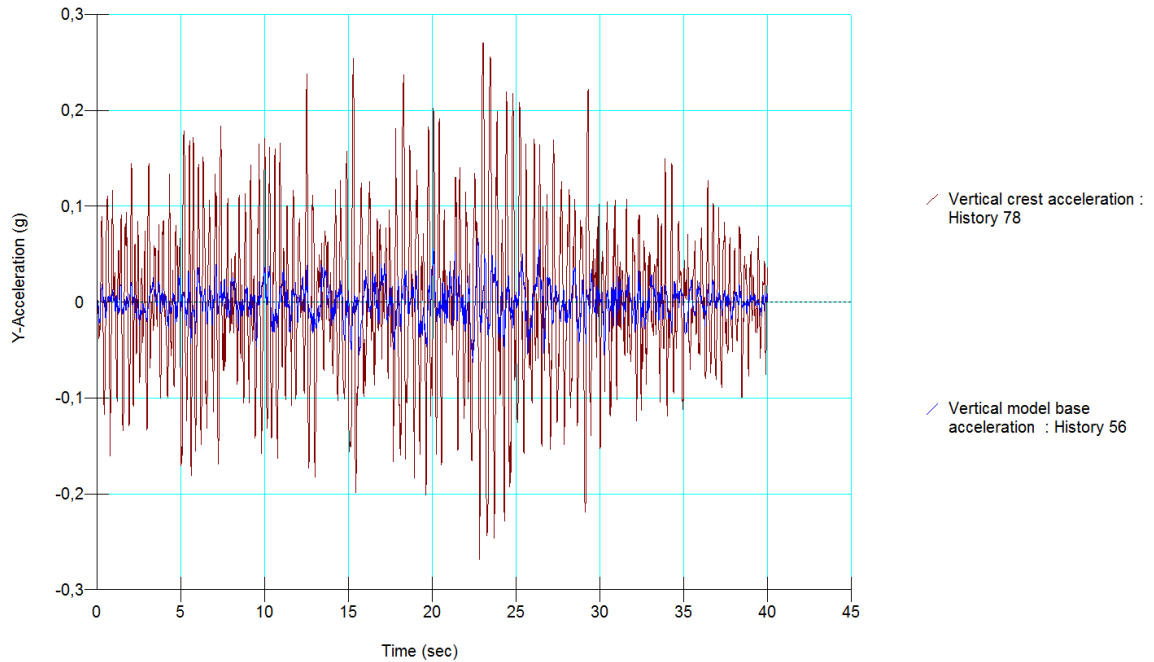
Figure 291 Vertical crest settlement vs. vertical model base settlement at end of dynamic calculation [m] (NL code, GeoStudio)

Figure 292 and Figure 293 plot the peak accelerations in horizontal respectively in vertical direction. The horizontal peak crest acceleration resulted in 0,34g whilst the verti-

cal result is 0,27g. Referring to the results of EL analysis, both analysis provide comparable crest accelerations.



**Figure 292 Horizontal crest acceleration vs. horizontal model base acceleration during Tohoku earthquake [g] (NL code, GeoStudio)**



**Figure 293 Vertical crest acceleration vs. vertical model base acceleration during Tohoku earthquake [g] (NL code, GeoStudio)**

Figure 294 plots the pore water pressure built up during the dynamic event. It can be seen that the pore water pressure rises until the minimum stress (i.e.  $\sigma_3$ ) is reached. This is the point when the element liquefied.

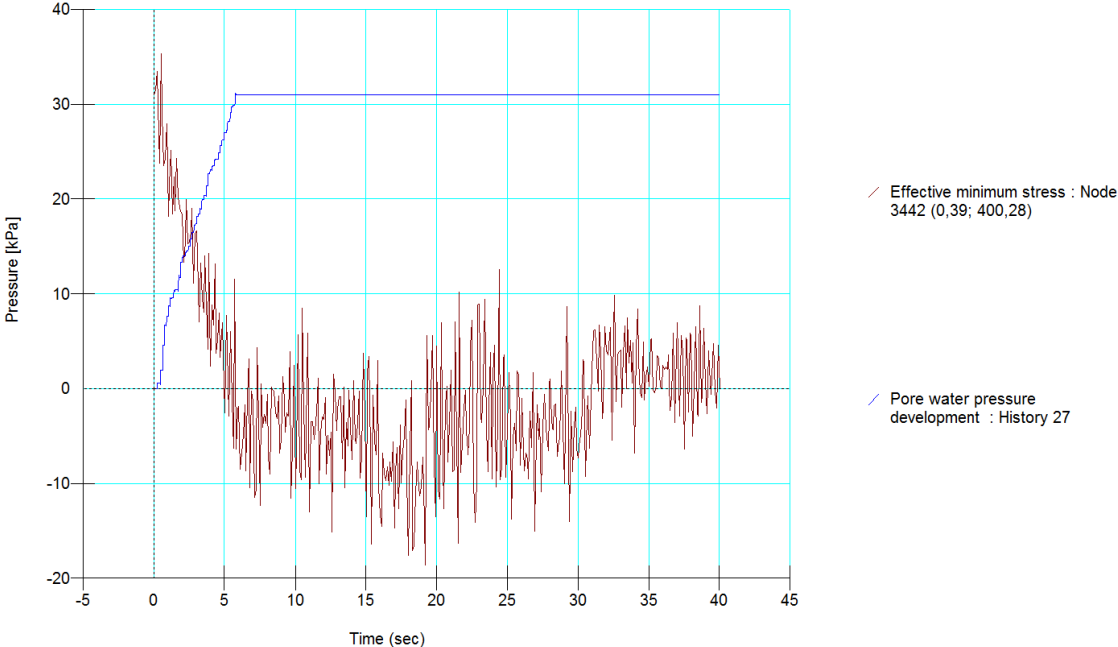


Figure 294 Pore water pressure development vs. dynamic time (NL code, GeoStudio)

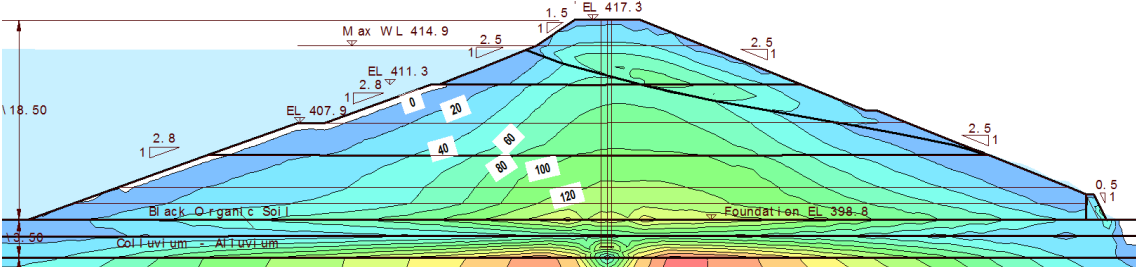


Figure 295 Effective vertical stresses after Tohoku earthquake (NL code, GeoStudio)

### 12.3.1.3 Non Linear Codes – Plaxis 2015

Figure 296 shows the result of a pre-earthquake stability analysis. In a FE – global stability analysis all material parameters are stepwise reduced until a clear failure mechanism develops. Hence Figure 296 shows a maximum deformation of 54cm but this is only due to the reduction of the material parameters. The dam itself is stable and the minimum (local) factor of safety results in 1.53.

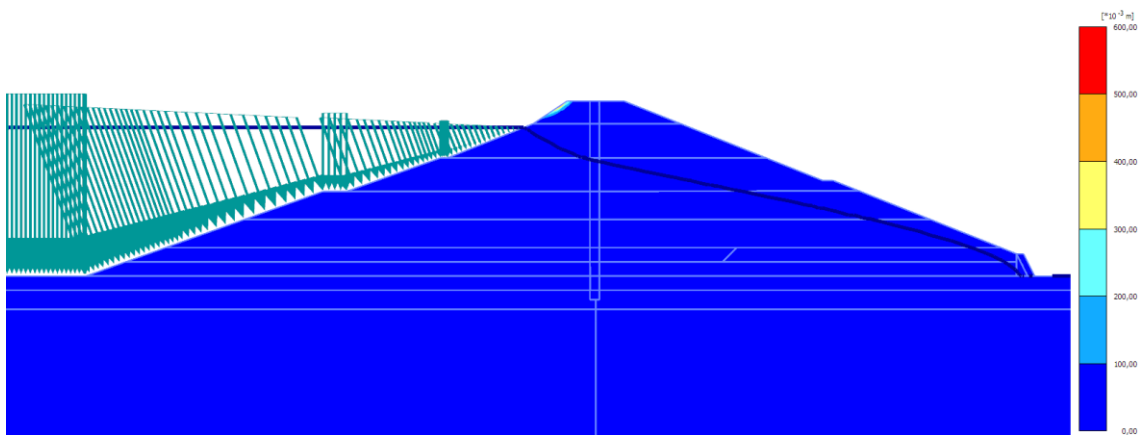


Figure 296 Pre-earthquake stability analysis (Plaxis)

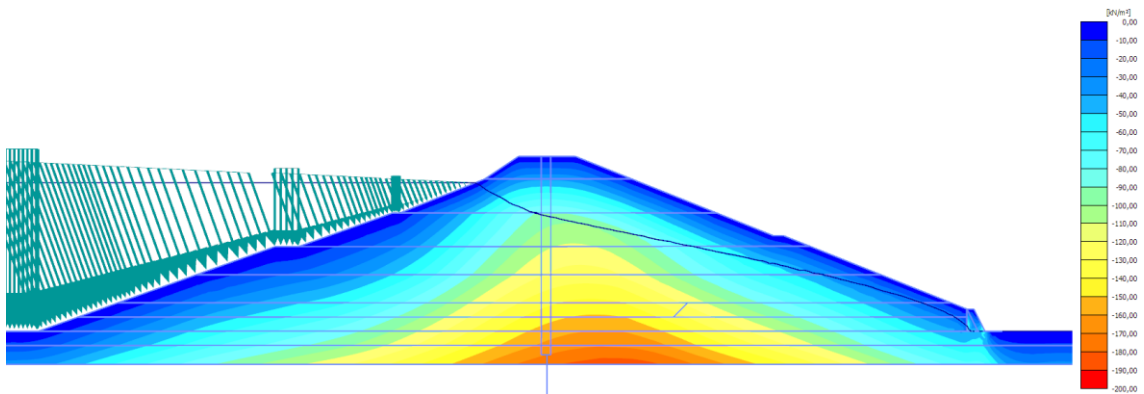


Figure 297 Effective vertical stresses prior earthquake analysis (Plaxis)

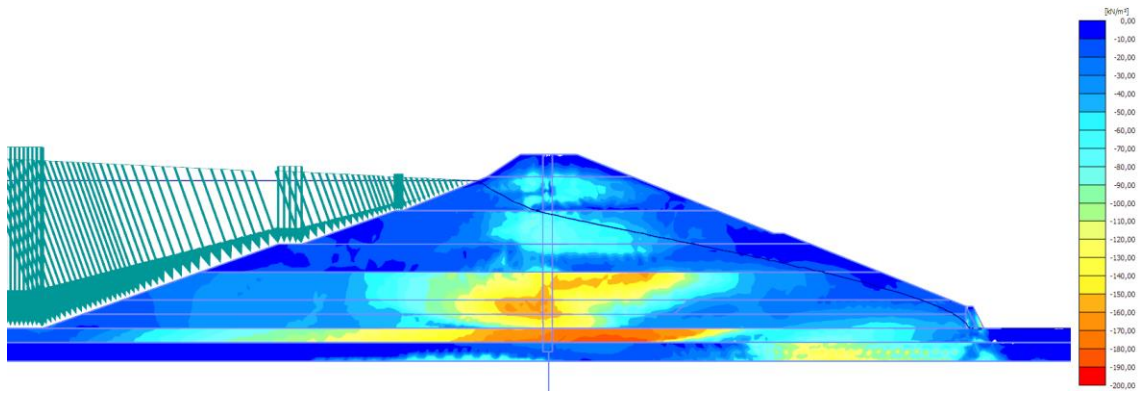


Figure 298 Effective vertical stresses after earthquake analysis -> pore water pressure built up (Plaxis)

### 12.3.1.3.1 Check Earthquake

Figure 299 and Figure 300 show the effective minimum stress  $\sigma_3$  prior and post check earthquake within Fujinuma dam fill. From these plots it can be seen that no or no significant pore water pressure was generated due to the Check earthquake.

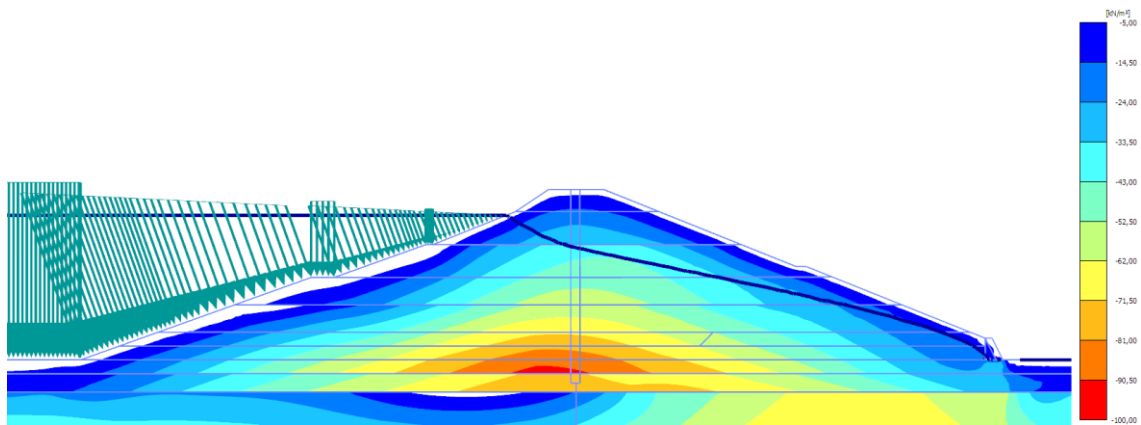


Figure 299 Effective minimum stresses prior check earthquake (NL code, Plaxis)

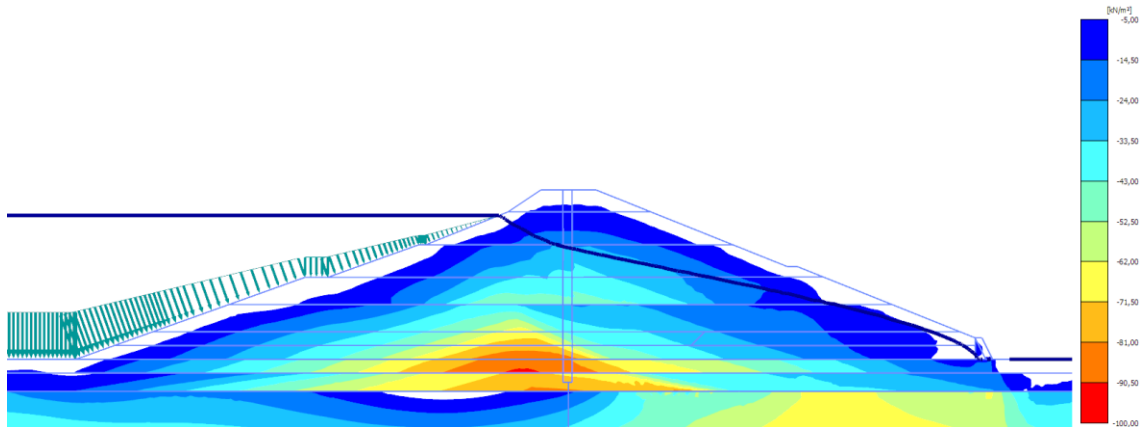


Figure 300 Effective minimum stresses after check earthquake (NL code, Plaxis)

Figure 301 plots the settlements immediately after end of Check earthquake. Figure 302 plots the statically driven post-earthquake settlement. From both plots it can be seen that the settlements are basically zero. No deformation takes place due to Check earthquake.

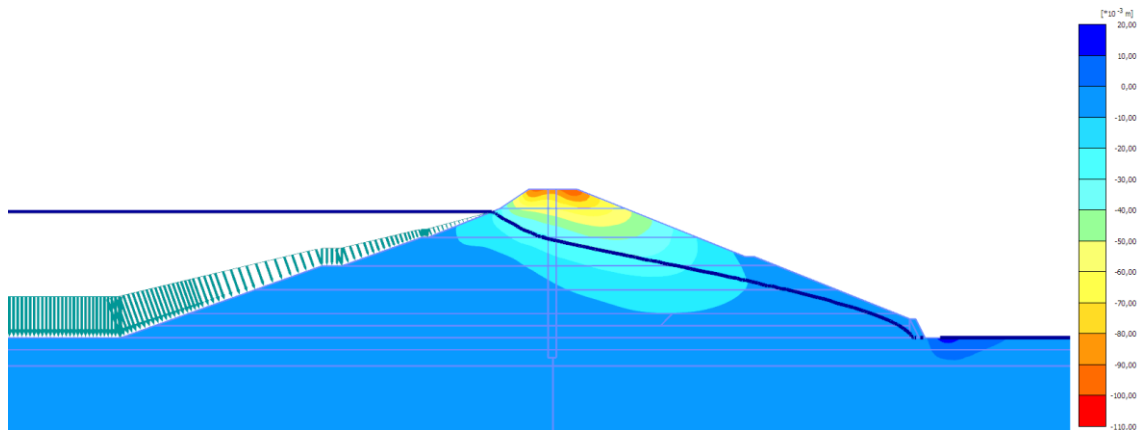


Figure 301 Settlement at end of Check earthquake (NL code, Plaxis)

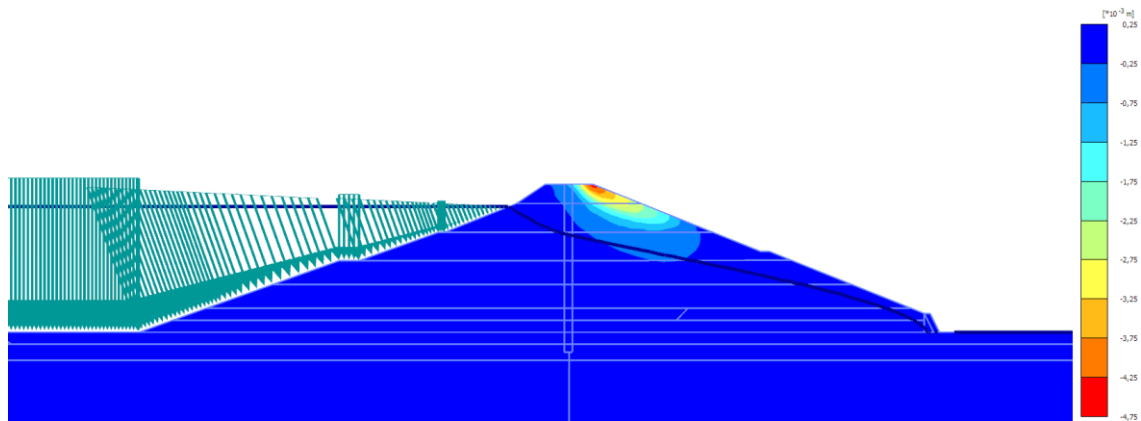


Figure 302 Post-earthquake settlement from Check earthquake (NL code, Plaxis)

#### 12.3.1.3.2 Tohoku Earthquake

Figure 303 shows the development of effective minimum stress  $\sigma_3$  within the embankment's fill zones. From the plot it becomes evident that the effective minimum pressure of brown- and greyfill came close to zero indicating liquefaction of the mate-

rial. Indirectly zones that have liquefied may be seen from Figure 304 plotting the effective minimum stresses starting from 5 kN/m<sup>2</sup>. Liquefied zones are shown white (uncolored).

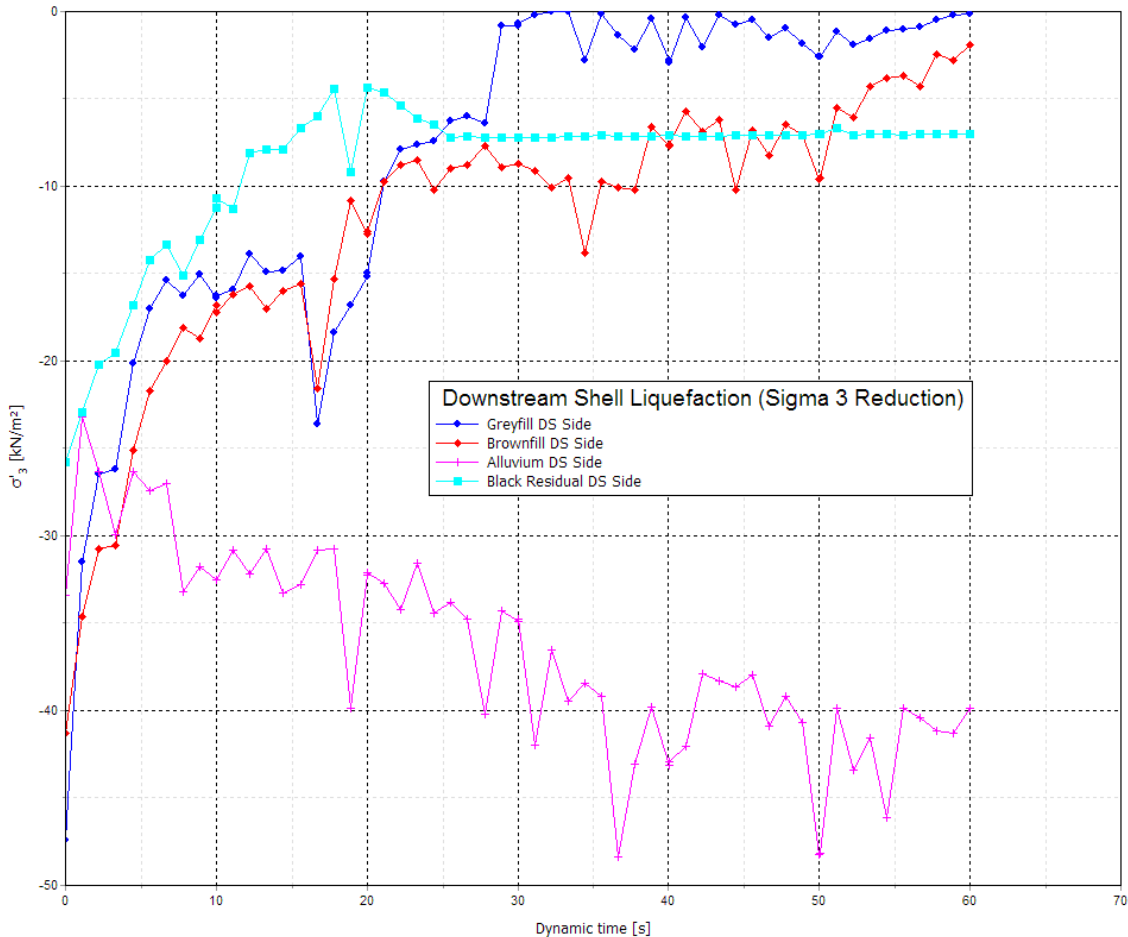


Figure 303 Liquefaction of fill zones within Fujinuma embankment after Tohoku earthquake (NL code, Plaxis)

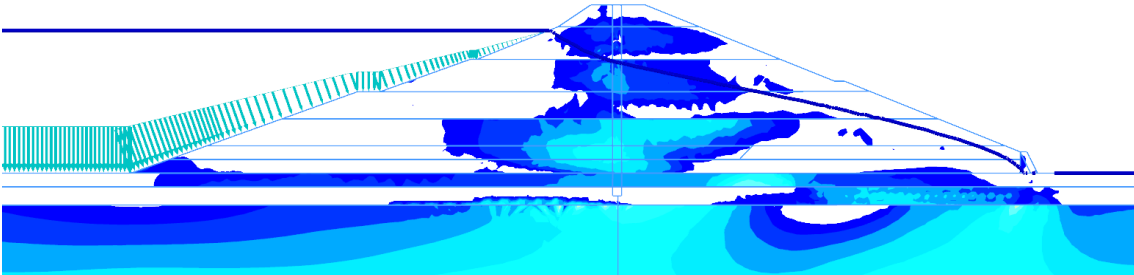
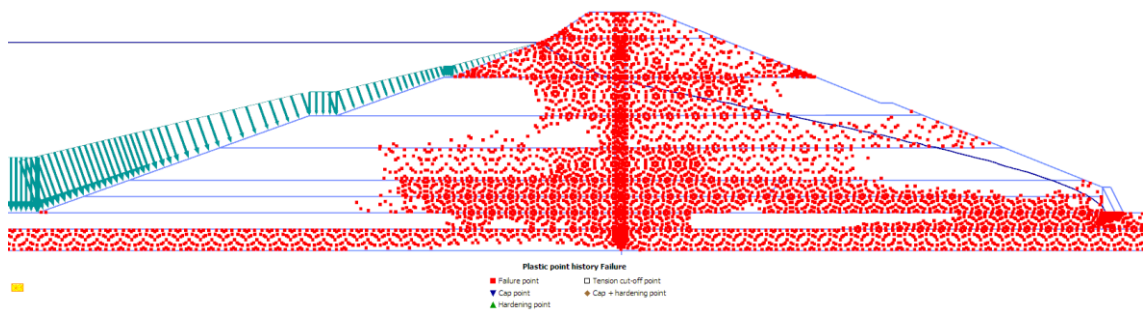


Figure 304 Liquefaction of fill zones within Fujinuma embankment after Tohoku earthquake (NL code, Plaxis)



Figure 305 plots all points where the failure criterion was reached at least once during the dynamic shaking.



**Figure 305 Failure points (red dots) where the yield criterion was reached during or at end of the dynamic calculation of Tohoku earthquake (NL code, Plaxis)**

Figure 307 plots the post-earthquake settlements in 1:1 scale. The plot shows the uncorrected settlements at end of Tohoku earthquake. Please note the base of the model at same time deforms too. Figure 306 shows the settlement and horizontal deformation at crest and at model base location. From this plot it may be followed that the maximum crest settlement is  $3.07\text{m} - 0.54\text{m} = 2.53\text{m}$ . It becomes clear that such deformations would clearly induce the dam's failure. It shall be noted that this result does only show the settlement at the end of the earthquake excitation. The result might be interpreted as follows: At the end of the earthquake the dam was by sure heavily cracked, potentially creating seepage paths but the crest itself did not settle in an order resulting in immediate over flow. However, significant liquefaction was created and statically driven forces would induce time delayed further crest settlement finally causing overflow and a dam failure. A post- earthquake analysis was added but did not find equilibrium, thus indicating ongoing dam deformation due to static forces.

The same as stated for both GeoStudio analyses holds true for the results of Plaxis. Even though this result is highly realistic (refer to Figure 110) it has to be pointed out that it is more a stroke of luck as the data available is not detailed enough to rely on the calculated deformation. The Engineer shall in general not rely on the output of deformation calculations in case of liquefiable soils. Furthermore he shall not rely on the output of dynamic deformation analysis as long as they are based on state of the art approaches.

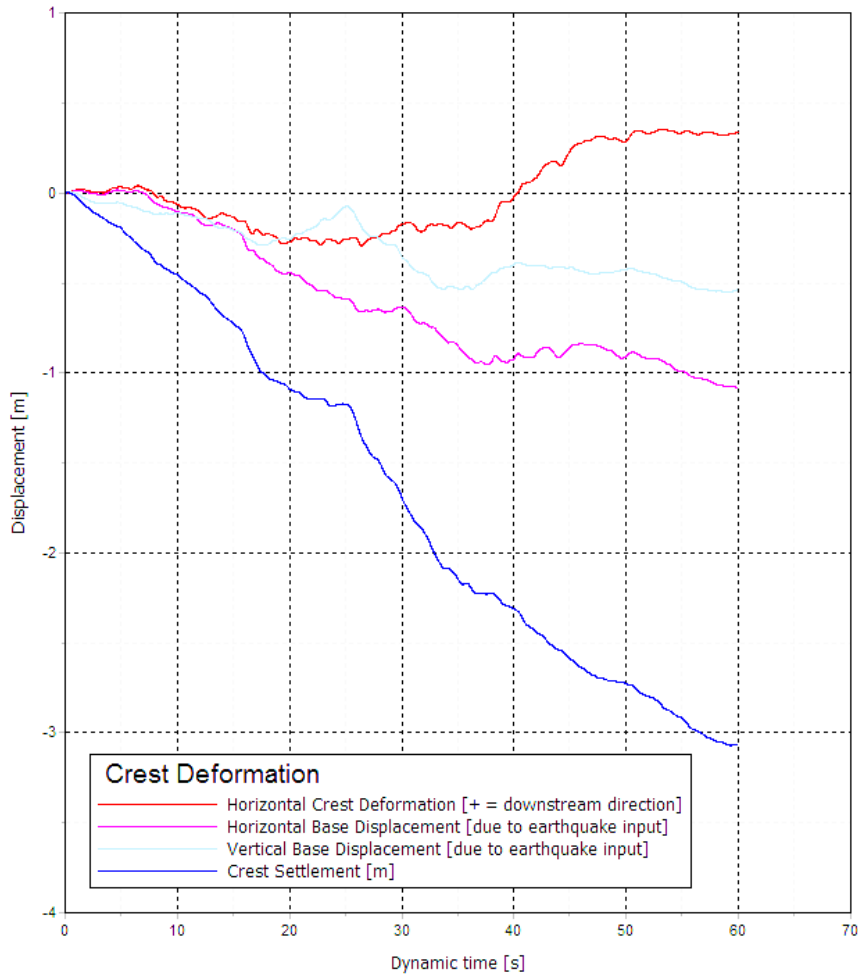


Figure 306 Settlement after Tohoku earthquake (NL code, Plaxis)

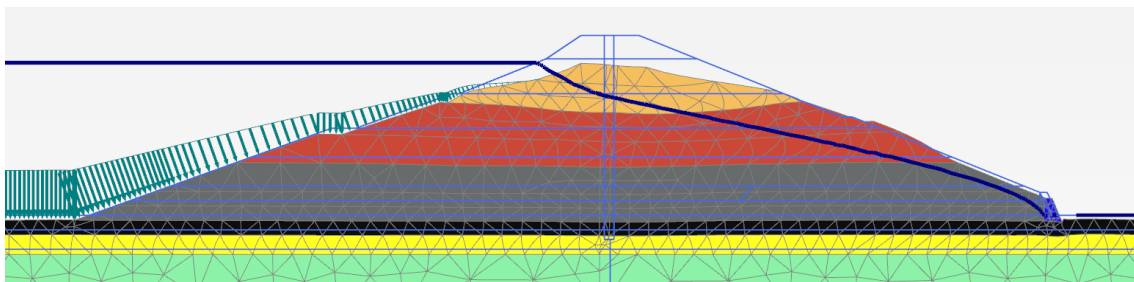
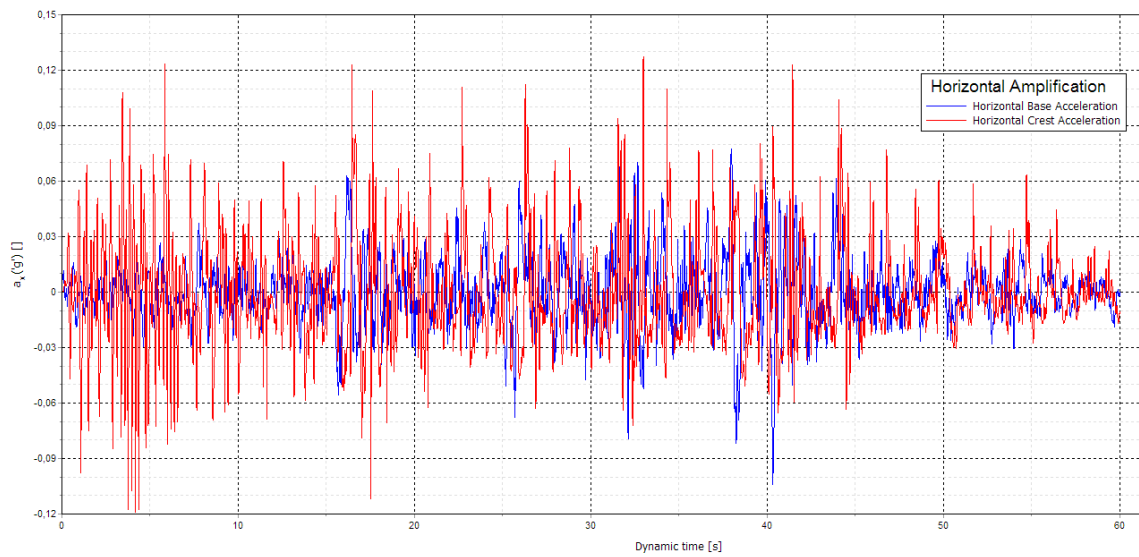


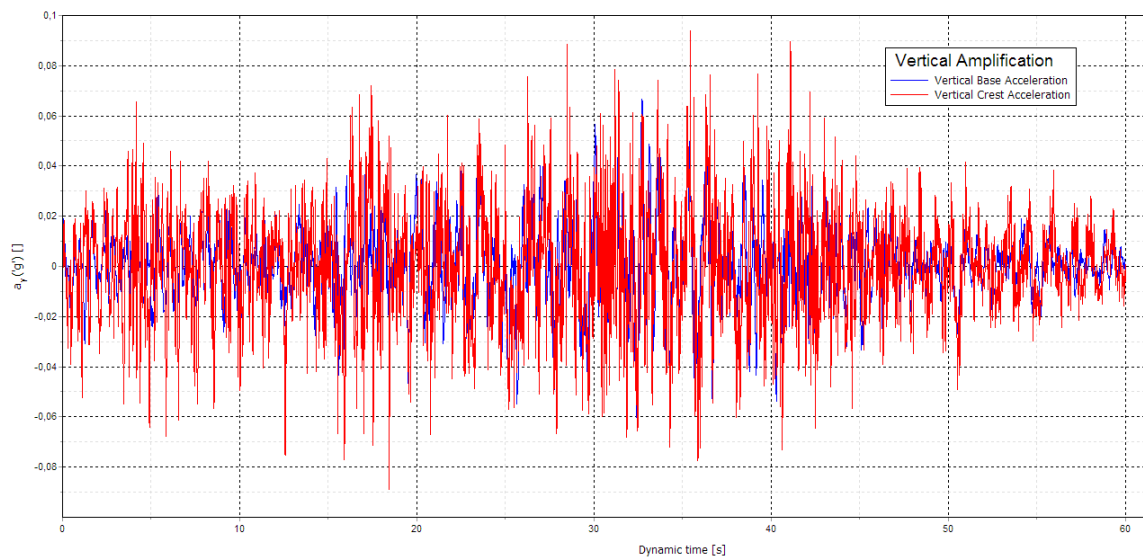
Figure 307 Settlement at end of Tohoku earthquake, deformed mesh 1:1 (NL code, Plaxis)

Figure 308 and Figure 309 plot the acceleration at base and crest location in horizontal respectively in vertical direction. The horizontal peak crest acceleration results in 0,12g whilst the vertical results in 0,094g. Referring to the results of GeoStudio EL and NL analysis the present calculation results in approximately one half of the formerly calcu-

lated peak crest accelerations. The sophisticated background of the applied soil model in Plaxis better reproduces the real soil behavior of partly liquefied ground.



**Figure 308 Horizontal crest acceleration vs. horizontal model base acceleration during Tohoku earthquake [g] (NL code, Plaxis)**



**Figure 309 Vertical crest acceleration vs. vertical model base acceleration during Tohoku earthquake [g] (NL code, Plaxis)**



## 13 Conclusions

The results generated within this thesis have to be judged by keeping in mind that the best fit material sets have first been calibrated to the Equivalent Linear method and then were applied unchanged to the Nonlinear methods. Thus possibilities for calibration of the Nonlinear methods were restricted. Although the Nonlinear methods were handicapped by this procedure, the author recognized the enormous potential of Plaxis Nonlinear models as for all three dams good results were achieved from beginning on.

The aim of this thesis was to compare the results of state of the art and newly developed procedures in calculating the dynamic behavior of embankment dams. Hence emphasis was put on creating comparable conditions whenever possible. It is the author's conviction that the Nonlinear model of Plaxis software could much better approximate the dam behavior if material parameters within a material set would have been allowed to change from one software model to the other.

It has to be pointed out that it is extremely difficult and to the author's opinion in most cases impossible to accurately calculate the final deformation of an embankment dam after a severe earthquake by the single use of the Finite Element Method alone. In all circumstances, the Engineer needs to rely and refer on empirical data.

This is especially true for soils subject to liquefaction even if perfect, undisturbed, excessive soil testing was done for all in-situ and perfectly homogenous fill materials. But this is also true for dams not subject to liquefaction. State of the art procedures may adequately reproduce the crest settlements known from empirical data, but they fail in prediction of the associated horizontal deformations.

The main purpose of this thesis was to clarify whether Nonlinear or state of the art Equivalent Analysis result in better agreement with observed behavior of three different dam types.

Description of material damping in that case turned out to be of specific interest.

Damping of the materials is well investigated in the “normal” range of 0,0001% to 0,1% dynamic shear strain. The range between 0,1% to 1% is known but the accuracy of the laboratory data is often questionable as this is the upper end of data to be measured. For higher ranges from 1% to 10% material behavior is basically untested. This range is out of typical engineering range as it would have to be avoided to ensure a structure’s adequate behavior. In case of dams that often have to be calculated for 10000 + year events, the 1% to 10% range has to be specified for the numerical analysis. As observed from embankment dams shaken by large magnitude earthquakes rockfill materials bear an enormous capacity to deal with such high accelerations. Basically this is due to the high damping the material develops if sheared. As laboratory testing lacks sufficient methods to investigate the material behavior in this range, this data needs to be collected from back analysis of case studies.

Each of the investigated constitutive models used for the present case studies has different approaches to account for material damping. The equivalent linear method in GeoStudio provides the most efficient way for the Engineer. Damping is specified via a data point function along the whole shear strain path. The input data may be manipulated in all regions of accumulated shear strain directly referring to the outcome of laboratory testing. In Nonlinear method of GeoStudio, damping is indirectly linked to the reduction of the maximum shear modulus by a simple formula that as a consequence does not provide enough capability for adapting it to natural behavior of varying soils. Formulation of Damping in Plaxis is again different for each type of constitutive model. The Generalized Hardening Soil Model introduces two input parameters. The so called Rayleigh parameters  $\alpha$  and  $\beta$  control the damping in the range of the first two Eigen frequencies (equivalence to a single degree of freedom system). Application and adoption of these important input values call for an iterative procedure which in

combination with time-consuming dynamic calculations is quite inconvenient and the effect is hard to cross check with laboratory data.

It has to be pointed out that damping is one of the important parameters that guides the dynamic behavior. Especially in case of dams prone to a significant earthquake risk, it would be good to have full control of this parameter in all ranges of shear stress. Despite its deficiencies, this is solved best by the Equivalent linear method (right now).

Referring to the stress – strain relations, it may be pointed out in a first step that the Equivalent Linear method does not provide a closed solution. Solving the dynamic problem is well separated from calculating the pore water pressure and the final deformations. Within each of these steps assumptions and significant simplifications have to be made thus resulting in strongly varying output. Due to these assumptions and the great number of material test results available in international literature, the Engineer may reach high accuracy for single points that shall be calibrated (or are already known from empirical formulae). However it is nearly impossible to end up in results that provide good agreement at several locations of interest. If at five points the observed vertical deformation was met perfectly, the observed horizontal deformation could not be calculated in an acceptable range of accuracy and vice versa. This is also true if the aim was to gain acceptable deformations at same time with pore water pressure build up.

In a second step it may be pointed out that analysis termed Nonlinear are not comparable to each other at all. The general benefit of Nonlinear analysis is that deformations are calculated in every time step, thus enabling to directly calculate the development of pore water pressure built up and the related material changes as increased damping. However the clear benefit of Nonlinear analysis can only be achieved if the analysis foots on a realistic stress – strain material models. As long as pore water pressure development is again linked to strong simplifications the Nonlinear method resulted in deficiencies compared to the Equivalent – Linear method. However, as soon as realistic stress – strain models are the basis for the nonlinear dynamic analysis for-

merly unknown good agreement at several points of interest was achieved in all calculations.

A comparison may be drawn to deformation analysis of embankment dams. The well-known Mohr –Coulomb model is very often the basis for linear elastic – ideally plastic deformation analysis. However this model cannot reflect the highly nonlinear behavior of the fill materials for all loading conditions. More sophisticated models as the Hardening Soil model much better reflect a dam's behavior but still need to be based on simplifications. One important input the hardening soil model lacks for is the shear resistance. Parameters for internal angle of friction and cohesion have to be kept constant in numerical modelling but are highly nonlinear in reality. It has to be pointed out that the Hardening Soil model is already based on 14 input parameters hence adding the nonlinear shear strength would add even more complexity but would for sure increase the models applicability to embankment dam engineering. To the authors experience much better and more reliable results may be gained from sophisticated models even if single parameters need to be estimated on typical relations to known parameters.

As all parameters in dynamic analysis of fill material vary with stress and shear strain it becomes clear that accurate modelling of the stress – strain conditions is of highest importance.

The Equivalent – Linear method in general needs to rely on additional deformation analysis to judge the permanent dynamic deformation of a dam.

Newmark's double integration method or Makdisi – Seed deformation analysis are recommended as the state of the art methods to judge the dams permanent deformations as long as liquefaction may be excluded. Post – earthquake stress – redistribution analyses are recommended if liquefaction may be triggered (ICOLD Bulletin 155). It may be stated that none of these two procedures result in a reliable deformation pattern. These two methods do only result in reliable calculation of crest settlement if their input parameters are adjusted and calibrated against empirical data.



The question then rises why a Designer should spend time and money for this analysis when a one row formula better predicts the deformation.

If horizontal crest deformation is of special interest (e.g. to design the filter width) it may be stated that these two models simply cannot forecast realistic horizontal deformations and therefore should not be used for that purpose.

To the authors practical experience it has always been interesting that completely different material sets, used in comparable situations, in different types of dams, analyzed by varying Engineers of varying cultural background, did in many cases result in permanent deformations that surprisingly were in perfect agreement with empirical formulae. If discussing such results in detail, it can be seen that the assumptions made in the background are completely different but the result is the same, i.e. the generally accepted results of empirical formulae.

The design Engineer in this case is in a bit of a bind as owners logically claim for state of the art design and unfortunately state of the art in this case are Newmark or Makdisi – Seed analysis.

The Nonlinear analysis do not call for additional 2<sup>nd</sup> step deformation analyses. The calculated result at the end of the analysis is the final permanent deformation as long as liquefaction does not occur. Post – earthquake stress – redistribution analysis do only make sense if the model is not in equilibrium at the end of the dynamic analysis, i.e. when statically driven forces cause ongoing deformation (liquefaction or significant changes in shear strength for other reasons). Even though the Nonlinear analysis and especially those that rely on sophisticated constitutive models have significant benefits the following conclusion may be drawn:

Accurate calculation of dynamic rockfill deformation is not possible same as it is not possible for all other types of analyses too (at least for those that were tested within this thesis). The simple reason is that the mechanical effects that guide these deformations are not simulated.

Dynamic deformation of rockfill is guided by densification within the inner zones whilst it is loosening of the outer, surface near material. It is not the result of defined slip surfaces. Dynamic densification is, same as the deformations during construction and impounding mainly guided by particle breakage, particle rearrangement and break down of particle edges at contact points. In general the Small Strain Hardening Soil model is suitable to describe this behavior, but it underestimates the total deformation. This is clear as the material set is calibrated to static conditions. However in dynamic conditions, the load direction at particle edges changes from uniaxial to three dimensional. Thus, resulting in increased break down of such particle edges and further more in particle rearrangement. This “plasticity” cannot accurately be simulated as long as the cyclic energy dependent strain weakening is not kept by the constitutive model.

National and international guidelines need to be adjusted to lessons learned from last decade’s earthquakes. Wide crests and unnecessary flat slopes result in cost estimations that hinder investments.

## **14 Research**

Earthquake engineering to a large extent has always been driven by empiric methods. The importance of empirically derived formulae shall not be underestimated even though numerical capabilities have significantly increased.

On the one hand it is recommended to put more emphasis on the development of empirical formulae to better predict other deformation parameters of interest as they are horizontal deformation, pore water pressure build up and so on. In many cases it would be adequate to update the existing ones to the gained knowledge of recent time.

On the other hand it is recommended to put emphasis on the development of constitutive models that can simulate the cyclic energy dependent strain weakening process of rockfill embankments.

## 15 References

- ATV–DVWK-M502, 2002. Berechnungsverfahren für Staudämme – Wechselwirkung zwischen Bauwerk und Untergrund. Deutsche Vereinigung für Wasserwirtschaft, Abwasser und Abfall eV.
- CFRD International Society, 2008. Guidelines for Design High Concrete Face Rockfill Dam, (Draft).
- Cooke, J.B., (1984). Progress in rockfill dams (18<sup>th</sup> Terzaghi lecture). *Journal of Geotechnical Engineering*. Vol. 110 (10), pp. 1383-1414.
- Cooke, J.B., Sherard J.L., 1987. *Concrete face rockfill dams: design, construction and performance*, USA: ASCE.
- Cooke, J.B., 2000. The High CFRD. In: *Concrete Face Rockfill Dams*, J. Barry Cook Volume, Beijing, China. p. 1-4.
- Douglas, K., 2002. *The shear strength of rock masses*. Thesis, (PhD). School of Civil and Environmental Engineering, The University of New South Wales, Sydney.
- Duncan, J., Wong, K. and Ozawa, Y., 1980. FEDAM: A computer program for finite element analysis of dams. USA: University of California-Berkley.
- EN-1992-1-1, 2004. Eurocode 2: Design of concrete structures – Part 1-1: General rules and rules for buildings.
- EN – 1998-1, 2004 Eurocode 8: Design of structures for earthquake resistance – Part 1: General rules, seismic actions and rules for buildings.
- Fell, R., MacGregor P., Stapledon D. and Graeme B., 2005. *Geotechnical Engineering of Dams*. The Netherlands: A.A. Balkema Publishers Leiden.
- Fitzpatric, M., Cole, B., Kinstler, F., and Knoop, B., 1985. Design of concrete faced rockfill dams, USA: ASCE Geotechnical Engineering Division, 410-434.

- Guidici, S., Herweynen, R. and Quinlan, P. 2000. HEC experiences in concrete faced rockfill dams – past, present and future, *In: International Symposium on Concrete Faced Rockfill Dams*, 18.September 2000 Beijing. ICOLD, 2000
- Hall, E., and Gordon, B., 1963. Triaxial Testing with Large-Scale High Pressure Equipment. *Laboratory Shear Testing of Soils*. ASTM, p. 329-339.
- Hunter, G., Fell, R., 2002. The Deformation Behavior of Rockfill. Australia: The University of New South Wales.
- ICOLD. 1989. Rockfill dams with concrete facing. State-of-the-art. International Committee on Large Dams, Paris. Bulletin 70.
- ICOLD, 2005. Concrete Face Rockfill Dams Concepts for Design and Construction. Draft.
- ICOLD, 2010. Selecting seismic parameters for large dams guidelines, International Committee on Large Dams, Paris. Bulletin 148.
- ICOLD, 1995. Dam failures statistical analysis. International Committee on Large Dams, Paris. Bulletin 99.
- ICOLD, 2001. Design features of dams to resist seismic ground motion, Paris. Bulletin 120.
- Kai, W. and Duncan, J., 1974. Hyperbolic stress strain parameters for nonlinear finite element analysis of stresses and movements in soil masses. USA: University of California-Berkley.
- Marsal, R., 1973. Mechanical properties of rockfill. *In: Hirschfeld, R. and Poulos, S., ed. Embankment-dam engineering Casagrande volume*. USA: John Wiley & Sons. p. 109-199.
- Meißner, H., 1991. Recommendation of the Committee on Numerical Methods in Geotechnics of the German Geotechnical Society [in German]. *Geotechnik* , 1991-14, 1-10.

Oldecop, L. and Alonso, E., 2007. Theoretical investigation of the time-dependent behavior of rockfill. *Geotechnique* 57, No. 3, 289-301. Thomas, M., (1988). Rockfill Dam Design and Analysis. In: Jansen, R.B., *Advanced Dam Engineering*. New York: Van Nostrand Reinhold, 372-381.

Plaxis,. 2009. Plaxis 2D material models manual version 9.0

Schanz, T., Vermeer, P.A., Bonnier, P.G., (1999). The hardening soil model: Formulation and verification. In: R.B.J. Brinkgreve, *Beyond 2000 in Computational Geotechnics*. Balkeman, Rotterdam: p. 281-290.

United States Society on Dams, 2007. *Strength of Materials for Embankment Dams*.

Kamalesh, K., 2008. *Basic Geotechnical Earthquake Engineering*. New Delhi: New Age International (P) Limited, Publishers.

Hawaii Dam Safety Guidelines, 2004. *Seismic Analysis & Post Earthquake Inspections (C131)*.

RAUCH, A.F., 1997. *EPOLLS: An Empirical Method for Predicting Surface Displacements Due to Liquefaction Induced Lateral Spreading in earthquakes*. Thesis, (PhD). Virginia Polytechnical Institute and State University, VA.

Boulganger, R.W., 2007. *Residual Shear Strength of Liquefied Soils*. University of California, Davis.

Suppiah, S., 2004. *Dynamic Analysis of El Infiernillo Rockfill Dam*. In: Wieland, Ren & Tan. *New Developments in Dam Engineering*. London: Taylor and Francis Group, 869 – 876.

Lang, X., Wang, X. 2009. Briefly Analyze the Influence of the May 12 Earthquake upon Qiaoqi Dam, In: 1<sup>st</sup> International Symposium on Rockfill Dams, 18. October 2009 Chengdu, China.

Feng, Z., Tsai, P.H. and Li, J.N., 2010. Numerical Earthquake Response Analysis of the Liyutan Earth Dam in Taiwan. *Nat. Hazards Earth Syst. Sci.*, 10, 2010, 1269-1280.

Davoodi, M. and Jafari, M.K., 2004. Using In-situ Dynamic Tests for Accurate Seismic Stability Evaluation of Embankment Dam. In: Wieland, Ren & Tan. *New Developments in Dam Engineering*. London: Taylor and Francis Group, 281-288.

Yu, L., Kong, X. and Xu B., 2012. Seismic Response Characteristics of Earth and Rockfill Dams, In: 15 WCEE, 2012, Lisboa.

Matsumoto, N., 2010. The Recent Earthquakes and Dam Safety in Japan, In: 8<sup>th</sup> European Club Symposium, 2010 Innsbruck. 571-576.

JCOLD, (2008). *Seismic Interpretation of Integrated Observation Data*. Draft, Preliminary.

Sasaki, T., 2014. *Current Situation of JCOLD Activity about Seismic Data*, In: ICOLD Annual Meeting, 2014, Bali.

United States Society on Dams, 2014. *Observed Performance of Dams During Earthquakes - Volume III*.

Wieland, M., Malla, S., 2002. *Seismic Safety Evaluation of a 117m High Embankment Dam Resting on a Thick Soil Layer*, In: 12<sup>th</sup> European Conference on Earthquake Engineering, 2002, London.

Zhai, E., et al., 2004. Seismic Deformation Analysis of an Earth Dam – a Comparison Study between Equivalent-Linear and Nonlinear Effective-Stress Approaches, In: 13<sup>th</sup> World Conference on Earthquake Engineering, 2004, Vancouver.

Sommerville, P., n.d.. *Characterizing Near Fault Ground Motions for the Design and Evaluation of Bridges*, Berkley.

Ambraseys, N., et al., 2002. Internet-Site for European Strong-Motion Data, European Commission, Research-Directorate General, Environment and Climate Program. Available from: <[http://www.isesd.hi.is/ESD\\_Local/Documentation/documentation.htm](http://www.isesd.hi.is/ESD_Local/Documentation/documentation.htm)>.

Day, R., 2002. *Geotechnical Earthquake Engineering Handbook*. McGraw Hill.

Ohmachi, T. and Tahara, T., 2011. *Nonlinear Earthquake Response Characteristics of a Central Clay Core Rockfill Dam*, In: Soils and Foundation No. 2, 2011, 227-238.

Kayen, R., et al., 2008. Geoengineering and Seismological Aspects of the Iwate Miyagi – Nairiku, Japan Earthquake of June 14, 2008, Geer Web Report 2008 v.1, Available from: [http://www.geerassociation.org/GEER\\_Post%20EQ%20Reports/Japan\\_2008/IwateMiyagiEQV1d.pdf](http://www.geerassociation.org/GEER_Post%20EQ%20Reports/Japan_2008/IwateMiyagiEQV1d.pdf)

Swaisgood, J.R., 2003. Embankment Dam Deformations Caused by Earthquakes, In: 2003 Pacific Conference on Earthquake Engineering.

Matsumoto, N., Sasaki, T. and Ohmachi, T., 2011. The 2011 Tohoku Earthquake and Dams, In: ICOLD 89<sup>th</sup> Annual Meeting in Lucerne, June 1, 2011.

Okamoto, T., 2004. Recent Trend for Earthquake Induced Residual Settlement of Rock-fill dam and some consideration on affecting factors, In: Wieland, Ren & Tan. *New Developments in Dam Engineering*. London: Taylor and Francis Group, 705-716.

Fowler, C. M. R. (1990). *The Solid Earth: An Introduction to Global Geophysics*. Cambridge University Press, Cambridge, England.

Pacheco, J. F., and Sykes, L. R. (1992). "Seismic Moment Catalog of Large Shallow Earthquakes, 1900 to 1989." *Bulletin of the Seismological Society of America*, vol. 82, pp. 1306–1349.

USGS., 2000. *Glossary of Some Common Terms in Seismology*. United States Geological Survey Earthquake Hazards Program, National Earthquake Information Center, World Data Center for Seismology, Denver, CO. Glossary available from: <<http://earthquake.usgs.gov/>>

USGS (2014). United States Geological Survey Earthquake Hazards Program, National Earthquake Information Center, World Data Center for Seismology, Denver, CO., Available from: <<http://earthquake.usgs.gov/>>

Yeats, R. S., Sieh, K., and Allen, C. R. (1997). *The Geology of Earthquakes*. Oxford University Press, New York.

Dadisp., 2014. DADiSP The ultimate engineering spreadsheet, Available from: <<http://www.dadisp.com>>



Penn., (n.d.). Penn State Earthquake Seismology, Pennsylvania State University, Available from: <<http://eqseis.geosc.psu.edu>>

Javelaud, E.H., et al., 2011. *Evaluation of coseismic displacements in the near-field from strong-motion seismometers*, In: 8<sup>th</sup> International Conference on Urban Earthquake Engineering, March 7-8, 2011, Tokyo.

Wieland, M., (2003). General Report Question 83 - Seismic aspects of dams, Committee on Seismic Aspects of Dam Design, In: Proceedings of 21<sup>st</sup> ICOLD Congress, Montreal, Canada

Wieland, M., (n.d.). ICOLD's revised seismic design and performance criteria for large storage dams, Available from: < <http://www.povyry.com>>

Gazetas, G. and Dakoulas, P., 1991. "Seismic analysis and design of rockfill dams: state-of-the-art." *Soil Dynamics and Earthquake Engineering* 1992, vol. 11, pp. 27–61.

Midorikawa, S., et al. (n.d.) Report on the 2008 Iwate –Miyagi-Nairiku, Japan Earthquake, Tokyo: Institut of Technology, Department of Built Environment, Available from: [www.enveng.titech.ac.jp](http://www.enveng.titech.ac.jp), Sept. 2014

Seed, H.B. and Idriss, I.M., 1971. Simplified procedure for evaluating liquefaction potential, In *Journal of the Soil Mechanics and Foundation Division, ASCE*, vol. 97, 1249-1273.

Seed, H.B., et al., 1985. The influence of SPT procedures in soil liquefaction resistance evaluations, In: *Journal of Geotechnical Engineering, ASCE*, vol. 111, 1425-1445.

Youd, T.L. and Noble, S.K., 1997. Magnitude scaling factors. NCEER Workshop on evaluation of liquefaction resistance of soils, Salt Lake City, 191-200.

Chen and Sheng-Shui, . (n.d.) Impact of the "5.12" Wenchuan Earthquake on Zipingpu Concrete Face Rock-fill Dam and its Analysis, Nanjing Hydraulic Research Institute, Nanjing, China.

Noguera, G., 2010. Maule Earthquake, a presentation to ICOLD Committee on Seismic Aspects of Dam Design, Hanoi, Vietnam, May 24, 2010

Wieland, M., 2013. STK Workshop Verhalten von Talsperren während Starkbeben, Swiss Commission on Large Dams, Bern, 08.05.2013.

Chang, F.K. and Krinitzsky, E.L. (1977). State-of-the-Art for Assessing Earthquake Hazards in the United States, US Army Engineer Waterways Experiment Station, Misc.Paper 5-73-1, Report 8, December, 58 pp.

- Turkish Dam Design Guideline, 2012. DOLGU BARAJLAR TASARIM REHBERİ. General Directorate of State Hydraulics, Ankara, 2012.
- Oh-ishi, S. 1975. Design and practice of Aratozawa dam, *Damu Nippon*, 15-47 (in Japanese).
- Vucetic, M.V., Dobry, R., 1991. Effect of soil plasticity on cyclic response. *Journal of Geotechnical Engineering*, 117, 89 - 107.
- Kazuma, M., Kataoka, S. and Uzuoka, R., 2012. Volcanic mountain area disaster caused by the Iwate – Miyagi Nairiku earthquake of 2008, Japan, In: *Soils and Foundations* 2012, 52, 168-184.
- Heaton, T. H., Tajima, F., and Mori, A. W., 1982. Estimating ground motions using recorded accelerograms. Report by Dames & Moore to Exxon Production Research Company, Houston, TX.
- Harder, L.F., et al., 2011. Preliminary observations of the Fujinuma dam failure following the March 11, 2011 Tohoku offshore earthquake, Japan. GEER Association report No. GEER-25a-preliminary.
- Matsumoto, Norihisa (2011), "Amended 4<sup>th</sup> Quick Report on Dams," Japanese Committee on Large Dams, April 4, 2011.
- NIED Database., National Research Institute for Earth Science and Disaster Prevention, K-Net & Kik.Net Earthquake Database, Available from: [www.bosai.go.jp](http://www.bosai.go.jp), Dec. 2014.
- JCOLD, 2012. Review of the cause of Fujinuma-ike dam failure –Summary report–, Japanese Committee on Large Dams, Tokyo, 2012.
- EERI, 2011. Special earthquake report - learning from earthquake events - geotechnical effects of the Mw 9.0 Tohoku earthquake, Available from: [www.eqclearinghouse.org](http://www.eqclearinghouse.org), Dec. 2014.
- Ono, K., et al., 2011, Possible earthen dam failure mechanisms of Fujinuma reservoir due to the Great East Japan Earthquake of 2011. *Hydrol Res Lett* 2011; 5. 69 –72.
- Charatpangoon, B., et al., 2014, Dynamic analysis of earth dam damaged by the 2011 off the Pacific coast of Tohoku earthquake. *Soil Dynamics and Earthquake Engineering*, 64, 50-62.

Bureau, G., Volpe, R. L., Roth, W. H. and Udaka, T., 1985. *Seismic analysis of concrete face rockfill dams*. Concrete Face Rockfill Dams – Design, Construction and Performance, American Society of Civil Engineers, p479-508.

Pells, S. and Fell, R., 2003. Damage and cracking of embankment dams by earthquake and the implications for internal erosion and piping. In: Proceedings 21<sup>st</sup> ICOLD, Montreal, Canada.

Kramer, S. L., 1996. Geotechnical earthquake engineering. Prentice Hall Upper Saddle River, New Jersey

Marcuson, W. F., 1981. *Moderator's report for session on earth dams and stability of slopes under dynamic loads*. In: Proceedings International Conference on Recent Advances in Geotechnical Earthquake Engineering and Soil Dynamics. St. Louis Missouri, 1175.

Terzaghi, K., 1950. *Mechanisms of landslides*. Harvard University, Department of Engineering.

Gazetas, G., 2012. *Some presumptions on the nature of base excitation may erroneously affect the response of strong inelastic systems*. In: Proceedings 15<sup>th</sup> World Conference on Earthquake Engineering, Lisbon, Portugal.

Hynes-Griffin, M. E. and Franklin, A.G., 1984. Rationalizing the seismic coefficient method. Paper No. G.L. 84-13, US Army Engineer Waterways Experiment Station, Vicksburg, Mississippi

Abrahamson, L. W., Lee, T.S., Sharam, S. and Boyce, G. M., 2002. Slope stability and stabilization methods, Wiley Interscience Publication, John Wiley & Sons, Inc.

FEMA – 65, 2005. Federal guidelines for dam safety – earthquake analysis and design of dams, U.S. Department of Homeland Security.

Fujiwara, H., et al., 2003, Strong-motion observation networks of NIED: K-NET and KiK-net, National Research Institute for Earth Science and Disaster Prevention, Japan.

NIED - Strong motion seismograph networks, National Research Institute for Earth Science and Disaster Prevention 3-1 Tennodai, Tsukuba, Ibaraki 305-0006, Japan. Available from: <[http:// www.kyoshin.bosai.go.jp/](http://www.kyoshin.bosai.go.jp/)>.

Jeon, S., 2008. *Dynamic and cyclic properties in shear of tuff specimens from Yucca Mountain, Nevada*. Thesis, (PhD). Graduate School of the University of Texas, Austin.

BWG 2003. Sicherheit der Stauanlagen – Basisdokument zu dem Nachweis der Erdbbensicherheit. Berichte des Bundesamt für Wasser und Geologie – Sektion Talsperren; Schweiz.

Ohmachi, T., 2009. Recent Topics related to seismic safety of dams. *Journal of Japan Society of Dam Engineering*, Vol.19 (2), P94-103.

Shimamoto, K., et.al., 2008. Damage to dams caused by the 2008 Iwate / Miyagi inland earthquake (Quick Report). *Journal of Japan Society of Dam Engineering*, Vol.18 (1), P4-9.

Guan, Z. 2009. Investigation of the 5.12 Wenchuan earthquake damages to the Zipingpu water control project and an assessment of its safety state, *Science in China Press*, Vol. 52 (4), 820-834.

Zou, D., et al., 2012. Numerical simulation of the seismic response of the Zipingpu concrete face rockfill dam during the Wenchuan earthquake based on a generalized plasticity model, *Computers and Geotechnics*, 49 (2013), 111-122.

Zou, D., et al., 2012b. Numerical simulation on slabs dislocation of Zipingpu concrete face dam during Wenchuan earthquake based on a generalized plasticity model. In: *Proceedings 15<sup>th</sup> World Conference on Earthquake Engineering*, Lisbon, 2012.

Xiao, F., 2012. Did the Zipingpu dam trigger China's 2008 earthquake, *Probe International*, 2012.

- Chen, S., Huo, J., and Zhang, W., 2008. Analysis of 5.12 Wenchuan earthquake on Zipingpu concrete face rockfill dam, Chinese Journal of Geotechnical Engineering, Vol 30 (6).
- Zeping, X., 2009. Performance of the Zipingpu CFRD during the Wenchuan earthquake, Hydro Power and Dams, Vol 3, 2009.
- Kong, X., et al., 2012. Study of seismic wave input of Zipingpu concrete face rockfill dam during Wenchuan earthquake, Rock and Soil Mechanics, Vol 33 (7), 2012.
- Liu, A. ,et al., 2001. Equivalent number of uniform stress cycles for soil liquefaction analysis, Journal of Geotechnical and Environmental Engineering, Vol 127 (12), 705-712.
- Bray, J., et al., 2004. Liquefaction susceptibility of fine-grained soils, In: Proceedings of 11<sup>th</sup> ICSDEE / 3<sup>rd</sup> ICEGE, Berkeley, 655-662.
- Seed, B., Lee, K., 1965. Studies of the liquefaction of sands under cyclic loading conditions, University of California, Berkely.
- LEE, W., Ishihara, K., Chen, C., 2012. Liquefaction of silty sand – preliminary studies from recent Taiwan, New Zealand and Japan earthquakes, In: Proceedings of the International Symposium on Engineering Lessons Learned from the 2011 Great East Earthquake, Tokyo, Japan, 747-758.
- Shamsher, P., Vijay, K., 2006. Liquefaction of silts and silty – clay mixtures, College of Engineering and Science, Clemson University, South Carolina, Available from: <[http://www.ces.clemson.edu/UsTaiwanWorkshop/Paper\\_SDEE/SDEE\\_Shamsher%20Prakash.pdf](http://www.ces.clemson.edu/UsTaiwanWorkshop/Paper_SDEE/SDEE_Shamsher%20Prakash.pdf)>
- DeAlba, P., Chan, C.K., Seed, H.B., 1975. Determination of soil liquefaction characteristics by large-scale laboratory tests, Report EERC 75-14, Earthquake Engineering Research Center, University of California, Berkeley.

Martin, R., Fin, L., Seed, B., 1974 Fundamentals of liquefaction under cyclic loading, University of British Columbia, Department of Civil Engineering, Soil Mechanics Series No. 23.

Tho, T., Hai, D., Du, N., 2011. Correlation of the laboratory and in-situ deformation moduluses of sandy clay, Geotechnicke problem linivych stavieb, Bratislava, 2011.

Chu, H., Vucetic, M., 1990. Settlement of compacted clay under cyclic direct simple shear loading, Civil Engineering Department University of California, Los Angeles.

Wang, W., 1979. Some findings in soil liquefaction, Water Conservation And Hydroelectric. Power Science Research Institut, Beijing, China.

Seed, B., Idriss, I., 1982. Ground motions and soil liquefaction during earthquakes, EERI Monograph, Berkeley, California.

JCOLD, 2014. Acceleration records on dams and foundations No. 3, Japan Commission on Large Dams.

Seed, B., Wong, R., Idriss, I., Tokimatsu, K., 1984. Moduli and damping factors for dynamic analyses of cohesionless soils, College of Engineering, University of California, Berkeley.

Newmark, N., 1976. Effects of earthquake on dams and embankments, Milestones in Soil Mechanics, 109-129, Reprinted from Fifth Rankine Lecture, Geotchnique, Vol. 15 (2), 139 -160.

Gasparini, D., Vanmarcke, E., 1976. Simulated earthquake motions compatible with prescribed response spectra. Massachusetts Institute of Technology, Department of Civil Engineering, Cambridge, Massachusetts.

## **16 Certification**

I certify that the ideas, designs and experimental work, results, analyses and conclusions set out in this PhD thesis are entirely my own effort, except where otherwise indicated and acknowledged.

I further certify that the work is original and has not been previously submitted for assessment in any other course or institution, except where specifically stated.

---

Place, Date

---

Signature